Inaugural dissertation

for

obtaining the doctoral degree

of the

Combined Faculty of Mathematics, Engineering and Natural Sciences

of the

Ruprecht - Karls - University

Heidelberg

Presented by

Diplomate Engineer Athanasios Alexandros Tsengenes

born in: Athens, Greece

Oral examination: 06 October 2025

Computer-Aided Drug Design of Small-Molecule Neurotrophin Mimetics

Referees: Prof. Dr. Rebecca C. Wade
Prof. Dr. Christian Klein

Contents

Abbreviations

AA	All-atom
AD	Alzheimer’s disease
ADAM17	α disintegrin and metallopeptidase domain
ADME	Absorption, distribution, metabolism and excretion
AKT	Ak strain transforming
ALS	Amyotrophic lateral sclerosis
APBS	Adaptive Poisson-Boltzmann Solver
ASA	Accessible surface area
ATP	Adenosine triphosphate
BB	Backbone
BBB	Blood brain barrier
BDNF	Brain-derived neurotrophic factor
BEX3	Brain expressed X–linked protein 3
BLAST	Basic Local Alignment Search Tool
BPM	Binding protein microtubule-organizing centre
CAP	c-Cbl associated protein
CARC	Cholesterol-recognition amino acid consensus
CARV	Carvacrol
CER	Ceramide
CG	Coarse-grained
CN	Central nervous system
CNS	Ciliary Neurotrophic Factor
COG	Center of geometry
COM	Center of mass
CRAC	Cholesterol-recognition amino acid consensus
CRD	Cystein-rich domain
CREB	cAMP response element binding protein
CTF	C-terminal fragment
CV	Collective variable
DD	Death domain
DFT	Density functional theory
DHEA	Dehydroepiandrosterone
DHF	Dihydroxyflavone
DPC	Dodecylphosphocholine
DPPC	1,2-dipalmitoyl-sn-glycero-3-phosphocholine
DPPE	1,2-dipalmitoyl-sn-glycero-3-phosphoethanolamine
DPR	Detergent-to-protein molar ratio
DRG	Dorsal root ganglion
EC	Extracellular
ECD	Extracellular domain
ECL	Extracellular linker
EGFR	Epidermal Growth Factor Receptor
ENT	EuroNeurotrophin
ERK	Extracellular signal–regulated kinase

FES	Free energy surface
FRET	Fluorescence resonance energy transfer
GFCK	Growth factor cystine-knot
GIRK	G-protein-coupled inwardly rectifying potassium
HB	Hydrogen bond
HD	Huntington’s disease
HEK293	Human Embryonic Kidney 293
HERG	Human ether-a-go-go-related gene
HI	Hypoxic–ischaemic
HIE	Hypoxic–ischaemic encephalopathy
HITS	Heidelberg Institute for Theoretical Studies
IC	Intracellular
ICD	Intracellular domain
ICL	Intracellular linker
ICV	Intracerebroventricular
IFD	Induced Fit Docking
ITN	Innovative Training Network
JM	Juxtamembrane
JNK	c-Jun N-terminal kinase
KDE	Kernel density estimate
LLPE	2-linoleoyl-sn- glycero-3-phosphoethanolamine
LTD	Long-Term Depression
LTP	Long-Term Potentiation
MAG	Myelin-Associated Glycoprotein
MAPK	Mitogen-activated protein kinase
MBGI	Myelin-based growth inhibitors
MC	Monte Carlo
MCM	Molecular and cellular modeling
MD	Molecular dynamics
MW	Molecular weight
ND	Neurodegenerative diseases
NGF	Nerve Growth Factor
NGFR	Nerve Growth Factor Receptor
NHRF	National Hellenic Research Foundation
NMR	Nuclear Magnetic Resonance
NPW	Non-polarizable water
NRADD	Neurotrophin receptor alike DD protein
NRAGE	Neurotrophin receptor interacting melanoma associated antigen homolog
NRH2	Neurotrophin receptor homologue 2
NRIF	Neurotrophin receptor interacting factor
NSM	Neutral sphingomyelin
NT	Neurotrophin
OMgp	Oligodendrocyte myelin glycoprotein
PAPC	1-palmitoyl-2-arachidonoyl-sn- glycero-3-phosphocholine
PC	Phosphocholine
PCA	Principal Component Analysis
PD	Parkinson’s disease

PDB	Protein databank
PE	Phosphoethanolamine
PI	Phosphatidylinositol
PI3K	Phosphoinositide 3-kinase
PIP2	Phosphatidylinositol 4,5-biphosphate
PKA,B,C	Protein kinase A,B,C
PLPS	1-palmitoyl-2-linoleoyl-sn-glycero-3-phospho-L-serine
PME	Particle Mesh Ewald
PNS	Peripheral nervous system
POPC	1-palmitoyl-2-oleoyl-sn-glycero-3-phosphocholine
POPE	1-palmitoyl-2-oleoyl-sn-glycero-3-phosphoethanolamine
POPI	1-palmitoyl-2-oleoyl-sn-glycero-3-phosphoinositol
POPI25	1-palmitoyl-2-oleoyl-sn-glycero-3-phosphoinositol 4,5-bisphosphate
POPS	1-palmitoyl-2-oleoyl-sn-glycero-3-phospho-L-serine
PS	Phosphoserine
RIP	Regulated intramembrane proteolysis
RMSD	Root mean squared deviation
RMSF	Root mean squared fluctuation
RMSIP	Root mean squared inner product
RTK	Receptor tyrosine kinase
SAPI	1-stearoyl-2-arachidonoyl-sn-glycero-3-phosphoinositol
SASA	Solvent accessible surface area
SC	Side chain
SCI	Spinal cord injury
SM	Sphingomyelin
SNFG	Symbol Nomenclature for Glycans
SP	Standard precision
SSM	N-stearoyl sphingomyelin
STD	Saturation Transfer Difference
TACE	Tumor necrosis factor-α converting enzyme
TM	Transmembrane
TMD	Transmembrane domain
TNF	Tumor necrosis factor
TNFR	Tumor necrosis factor receptor
TNFRSF	Tumour necrosis factor receptor superfamily
TRADD	TNF receptor associated death domain
TRAF	TNFα receptor-associated factor
WT	Wild-type
XP	Extra precision

Summary

Neurotrophins (NTs) are growth factors that regulate key functions of the nervous system. This is achieved through binding to four cell surface receptors. The capacity of NTs to modulate different functions of the nervous system has made them appealing as therapeutics for neurodegenerative disorders. However, due to their large size, administration to patients requires invasive methodologies. As a result, small molecule NT mimetics that can bind to NT receptors have emerged as a solution. In this thesis, I have performed computer-aided drug design of novel small-molecule NT mimetics that act as NT receptor agonists. Specifically, I tested with molecular docking the potential binding sites of the lead steroidal compound BNN-27, which is a known TrkA agonist and computationally evaluated several BNN-27 derivatives with the goal to prioritize some of them for organic synthesis. I also performed virtual screening of 9200 compounds synthesized at University of Caen (UNICAEN), from which I identified several fragments that could be used as substituents of BNN-27. From those, eight fragments were determined as TrkA binders via STD-NMR. I performed a further optimization of the best-scoring fragment and proposed the six most promising compounds for organic synthesis. I also performed extensive mechanistic studies of BNN-27 analogues that were identified experimentally as TrkA and TrkB NT receptor agonists. I showed via Molecular Dynamics (MD) simulations that the compounds inserted readily in the membrane, which suggested that the molecules might bind to the transmembrane (TM) domain of the NT receptors. Consequently, I used docking and MD simulations to probe for small molecule binding in the TM domain of TrkA and compared with calculations done on TrkB. The simulations showed non-specific transient interactions between the compounds and the TM helices of both TrkA and TrkB, while the simulations that started with the compounds at the interface of the TM helices showed dissociation of the small molecules and diffusion in the membrane. This suggests that additional experimental data would be needed to shed light into the NT mimetic mechanism. Additionally to the small-molecule modeling, I performed mechanistic studies of the p75 NT receptor. I performed simulations of the glycosylated extracellular (EC) domain of the p75 receptor, which showed the glycan shielding of the protein is minimal, and instead the glycans might interfere with the binding kinetics of the NTs to the p75 receptor, which is known to be different than for the rest of the NT receptors. Then, I studied the dimerization of the TM helices of p75 with coarse-grained MD simulations. A range of interhelical crossing angles was observed which probably corresponds to the scissors-like movement that is expected to happen upon receptor activation. Finally, I modeled for the first time the

full-length homodimeric structure of the p75 receptor with its glycans present and a NT bound. I inserted the whole structure in a neuronal-like membrane and simulated it. The simulations showed that the EC domains of p75 approach and lie on the membrane, while the intracellular (IC) domains also come close and interact with the membrane. Interestingly, in some replica simulations the two death domains, which are initially in contact in a presumably inactive state, dissociate from each other, an event expected to occur upon p75 activation. This is accompanied by a shorter distance between the TM helix C-termini. Thus, in this thesis, a potential activation event of the p75 receptor is presented for the first time in atomic detail, with an allosteric signal propagated through the TM helices to the IC domains. The neuronal membrane also seems to be involved in the observed activation events. Overall, this thesis suggests some novel NT mimetics and reveals the dynamics of the p75 NT receptor in a membrane, which can guide future studies of these systems for the treatment of neurodegenerative disorders.

Zusammenfassung

Neurotrophine (NTs) sind Wachstumsfaktoren, die wichtige Funktionen des Nervensystems regulieren. Dies wird durch die Bindung an vier Zelloberflächenrezeptoren erreicht. Die Fähigkeit der NTs, verschiedene Funktionen des Nervensystems zu regulieren, hat sie als Therapeutika für neurodegenerative Erkrankungen interessant gemacht. Aufgrund ihrer Größe erfordert die Verabreichung an Patienten jedoch invasive Methoden. Daher haben sich NT-Mimetika in Form kleiner Moleküle, die an NT-Rezeptoren binden können, als Lösung erwiesen. In dieser Arbeit habe ich ein computergestütztes Wirkstoffdesign für neuartige niedermolekulare NT-Mimetika durchgeführt, die als NT-Rezeptor-Agonisten wirken. Insbesondere habe ich mit molekularem Docking die potenziellen Bindungsstellen der führenden Steroidverbindung BNN-27 getestet, die ein bekannter TrkA-Agonist ist, und mehrere BNN-27-Derivate rechnerisch ausgewertet mit dem Ziel, einige von ihnen für die organische Synthese zu priorisieren. Außerdem führte ich ein virtuelles Screening von 9200 Verbindungen durch, die an der Universität Caen (UNICAEN) synthetisiert wurden, und identifizierte mehrere Fragmente, die als Substituenten von BNN-27 verwendet werden könnten. Davon wurden acht Fragmente mittels STD-NMR als TrkA-Binder bestimmt. Ich führte eine weitere Optimierung des Fragments mit der besten Bewertung durch und schlug die sechs vielversprechendsten Verbindungen für die organische Synthese vor. Außerdem führte ich umfangreiche mechanistische Studien an BNN-27-Analoga durch, die experimentell als TrkA- und TrkB-NT-Rezeptor-Agonisten identifiziert wurden. Mit Hilfe von Molekulardynamiksimulationen (MD) konnte ich zeigen, dass sich die Verbindungen leicht in die Membran einfügen, was darauf hindeutet, dass die Moleküle an die Transmembrandomäne (TM) der NT-Rezeptoren binden könnten. Daraufhin habe ich mit Hilfe von Docking- und MD-Simulationen die Bindung kleiner Moleküle in der TM-Domäne von TrkA untersucht und mit Berechnungen an TrkB verglichen. Die Simulationen zeigten unspezifische, vorübergehende Wechselwirkungen zwischen den Verbindungen und den TM-Helices sowohl von TrkA als auch von TrkB, während die Simulationen, die mit den Verbindungen an der Schnittstelle der TM-Helices begannen, eine Dissoziation der kleinen Moleküle und eine Diffusion in der Membran zeigten. Dies deutet darauf hin, dass zusätzliche experimentelle Daten benötigt werden, um den NT-mimetischen Mechanismus zu erhellen. Zusätzlich zur Modellierung der kleinen Moleküle habe ich mechanistische Studien des p75-NT-Rezeptors durchgeführt. Ich führte Simulationen der glykosylierten extrazellulären (EC) Domäne des p75-Rezeptors durch, die zeigten, dass die Glykanabschirmung des Proteins minimal ist, und dass die Glykane

stattdessen die Bindungskinetik der NTs an den p75-Rezeptor stören könnten, die sich bekanntermaßen von der der übrigen NT-Rezeptoren unterscheidet. Anschließend habe ich die Dimerisierung der TM-Helices von p75 mit grobkörnigen MD-Simulationen untersucht. Es wurde eine Reihe von interhelikalen Kreuzungswinkeln beobachtet, die wahrscheinlich der scherenartigen Bewegung entsprechen, die bei der Aktivierung des Rezeptors erwartet wird. Schließlich habe ich zum ersten Mal die homodimere Struktur des p75-Rezeptors in voller Länge modelliert, wobei die Glykane vorhanden sind und ein NT gebunden ist. Ich fügte die gesamte Struktur in eine neuronenähnliche Membran ein und simulierte sie. Die Simulationen zeigten, dass die EC-Domänen von p75 sich der Membran nähern und auf ihr liegen, während die intrazellulären (IC) Domänen ebenfalls in die Nähe der Membran kommen und mit ihr interagieren. Interessanterweise dissoziieren die beiden Todesdomänen, die sich in einem vermutlich inaktiven Zustand zunächst berühren, in einigen Nachbildungssimulationen voneinander, was bei einer Aktivierung von p75 zu erwarten ist. Dies geht mit einem kürzeren Abstand zwischen den C-Termini der TM-Helix einher. In dieser Arbeit wird also zum ersten Mal ein potenzielles Aktivierungsereignis des p75-Rezeptors im atomaren Detail dargestellt, bei dem ein allosterisches Signal durch die TM-Helixen zu den IC-Domänen weitergeleitet wird. Auch die neuronale Membran scheint an den beobachteten Aktivierungsvorgängen beteiligt zu sein. Insgesamt schlägt diese Arbeit einige neuartige NT-Mimetika vor und zeigt die Dynamik des p75-NT-Rezeptors in einer Membran auf, was für künftige Studien dieser Systeme zur Behandlung neurodegenerativer Erkrankungen von Nutzen sein kann.

1 Introduction

1.1 Neurotrophins: regulators of Neurotrophin receptors

Neurotrophins (NTs) are a family of functionally and structurally related proteins of the central and peripheral nervous systems (CNS, PNS), which are secreted from neurons, glia and various tissues of the nervous system. Although these factors were initially described as promoting survival and outgrowth of developing neurons to guarantee appropriate innervation of target tissues, now it is well known that they also partake in different stages of the maintenance of the nervous system[1] as well as the regulation of neuronal function and apoptosis.[2–4] In mammals, four NTs have been identified: the Nerve Growth Factor (NGF), the Brain-Derived Neurotrophic Factor (BDNF), the neurotrophin-3 (NT-3) and the neurotrophin-4/5 (NT-4/5).

The four NTs are initially produced as *pre-proproteins*, which are converted to pro-neurotrophins, after cleavage of an N-terminal signal peptide. Pro-NTs are further processed by proteases to afford the mature, homodimeric NTs, with a size of 12–13 kDa and monomer length of 118–129 amino acids.[2,3]

The NGF is the member of the family that spearheaded the research around NTs. It was discovered to be responsible for the survival and maturation of developing sensory and sympathetic neurons in the PNS.[5,6] NGF was found to promote the survival of some but not all sensory neurons,[1] which eventually led to the discovery of the rest neurotrophic factors.[7] BDNF was discovered as a trophic factor for placode-derived sensory neurons.[8] Later NT-3 and NT-4/5 were found to be expressed mainly in the brain.[9–13]

The discovery of NGF led to the investigation of the receptors that mediate its actions through studies in sympathetic neurons[14] and PC12 cells.[15,16] Initially, the p75 receptor was identified by two independent laboratories,[17,18] and was thought as the only receptor of NGF. However, it was found later that the family of the Tropomyosin Receptor Kinases (Trk), TrkA, TrkB and TrkC, which are receptor tyrosine kinases, also bind NGF and the other neurotrophins.[19–21] Nowadays, it is known that each NT binds preferentially to a certain Trk receptor: NGF binds to TrkA, BDNF and NT-4/5 both bind to TrkB, and NT-3 binds to TrkC. Based on the cellular context, these interactions can activate different signaling pathways.[2,3]

All pro-NTs and NTs can bind to the p75 receptor, but only mature neurotrophins bind to a specific Trk receptor each. Neurotrophins bind to p75 with similar affinities of about 10^{-9} M but with somewhat different kinetics.[21] The interactions of NTs with their receptors can affect neuronal survival and differentiation, neurite outgrowth, and synaptic plasticity.[22] Next, I focus on reviewing the structure, signaling mechanisms and functional consequences of the signaling of NT receptors on the CNS and PNS. Special focus is put on the p75 receptor, since this is the receptor which I studied mechanistically in this thesis.

In addition to their physiological role, NTs have also been associated with neurological disorders, such as Alzheimer's disease, Parkinson's disease, epilepsy, and cancers of the CNS, etc. The investigation of the molecular mechanisms of NTs may lead to solutions that will help in the treatment of human nervous system diseases.

1.2 The p75 pan-neurotrophin receptor

The p75 receptor is a Type I transmembrane glycoprotein receptor which means that its N-terminus is outside the cell while the C-terminus is inside. p75 has a molecular weight of 75 kDa. Although it was originally characterized as the NGF receptor, today p75 is classified as the 16th member of the Tumour Necrosis Factor Receptor Superfamily (TNFRSF).[23] Members of TNFRSF participate in several biological responses ranging from cell death to cell survival. The superfamily is divided in two major groups on the grounds of the presence or not of a specific domain in the intracellular region called the *death domain*. Receptors without a death domain are called *survival receptors* and include TNFR2, RANK, TACI, and others. Receptors containing a death domain are called *death receptors* and include TNFR1, Fas, p75 and others.[24] Members of the TNFR superfamily do not have enzymatic activity, i.e. they are non-catalytic receptors. Instead, activation takes place by recruiting signaling adaptor proteins to the intracellular regions.[25]

Since the p75 receptor lacks a catalytic domain, it was thought at first to function as a binding partner for TrkA, facilitating the association with NGF and inducing activation of TrkA.[26] However, there were several indications that p75 serves other purposes. The receptor is expressed widely in developing peripheral neurons, and within the CNS.[27] It is expressed in a variety of cell types as neural stem cells, astrocytes, oligodendrocyte precursors, Schwann cells and glia.[1,27,28] p75 is also expressed in several nonneural tissues during development, such as kidney and muscle.[27,29] In addition, the upregulation of p75 in injury suggests its functional role in such conditions[30] Finally, there are particular amino acid sequences of the intracellular domain of p75, that are highly conserved across species.[31,32] Further study of p75 has revealed that it regulates an array of cellular responses, including cell survival, cell cycle, neurite outgrowth, myelination, synaptic function,[1] but also cell death and apoptosis in the absence of Trk receptors.[33]

The signaling that is facilitated by p75 depends on both the cellular context as well as the presence of different co-receptors and ligands, with which complexes are formed, as in the cases of sortilin/pro-NGF in cell death[34] or TrkA/NGF in survival.[35] The p75 receptor also experiences Receptor Intramembrane Proteolysis (RIP). As a result, the intracellular domain (ICD) of p75, which has signaling properties of its own, is released.[36]

1.3 Structural and functional profile of neurotrophins and their receptors

Structure of neurotrophins

Neurotrophins share approximately 50% sequence similarity, and form non-covalently bound homodimers with highly homologous structure. However, even though they generally exist as homodimers, at least some NT monomers are able to form heterodimers with other NT monomers.[1] The structures of NGF, NT-3, and NT-4 homodimers and of NT-3/BDNF and NT-4/BDNF heterodimers have been solved, showcasing this.[37–41]

As soon as the biologically active forms of NTs are secreted in the extracellular space, these stable homodimers are formed and operate as signal-inducing molecules. Interestingly, secreted forms of pro-NTs can exhibit opposing biological effects compared to those mediated by mature NTs.[42] This suggests that proteolytic processing of pro-NTs controls the direct downstream signalling effect.[43]

Neurotrophins contain a tertiary fold structure known as *"cystine-knot*" (Figure 1.1), which consists of three disulphide bonds between cysteines. The cystine-knot fold superfamily has the feature of two pairs of antiparallel β-strands bundled through these three disulfide bridges.[44]

The X-ray crystal structure of NGF was first solved in the 90s.[37,45] The NGF monomer comprises seven β-strands, creating three antiparallel pairs of β-strands (Figure 1.1). The central hydrophobic core of the NGF monomer is formed by the cystine-knot motif i.e., the two pairs of twisted, antiparallel β-strands (labeled β1–β4). A reverse turn (loop III) is on one side of this region, and three β-hairpin loops (loops I, II, and IV) are on the other side. The cystine-knot motif and hydrogen bonds among side chains create the hydrophobic core and lead to the final three dimensional structure of NGF and neurotrophins.[37,45]

NGF is a non-covalent head-to-head homodimer. The main core of each monomer consists of β-strands that maintain its conformation. The residues that form the β-strands constitute the hydrophobic core and are highly conserved, while the loops are highly variable. Two parallel NGF homodimers interact through hydrophobic interactions, which leads to a high association constant for the two homodimers. Distinctive features of NGF are its long, disordered loops (I, II, III, and IV) (Figure 1.1), important for binding to NT receptors. Variable regions are located in the three β-hairpin loops I, II and IV, and the reverse turn loop III.[46]

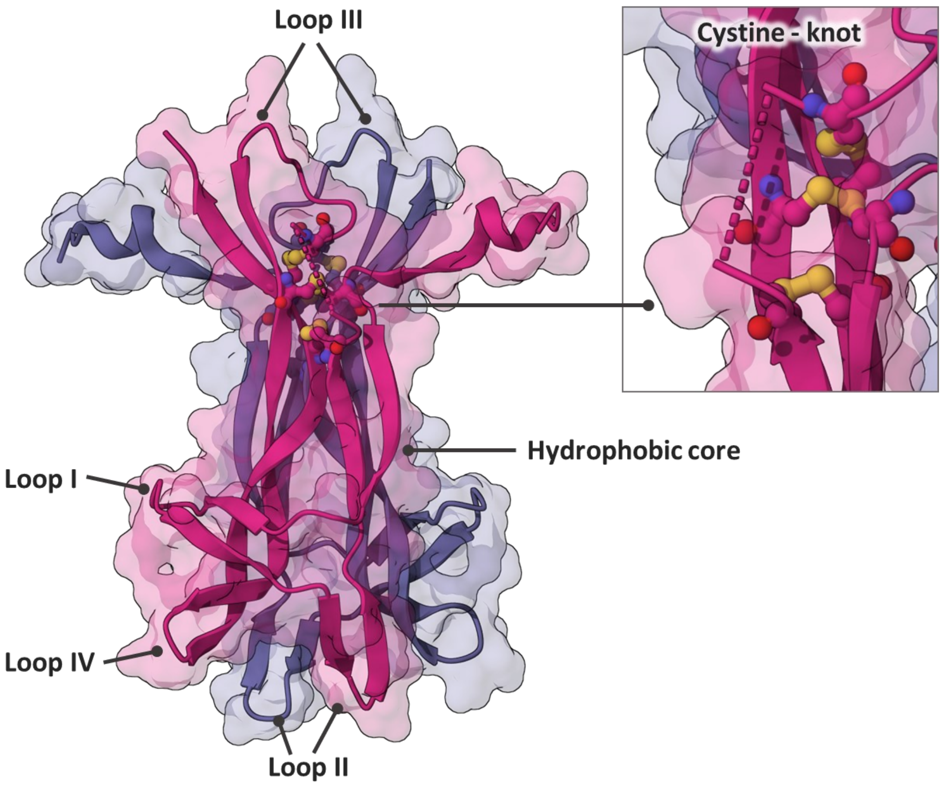

Figure 1.1: X-ray structure of NGF (PDB ID: 2IFG)[47] in cartoon representation with molecular surface. The two NGF monomers are shown in magenta and purple colors, and the position of the loops, the hydrophobic core and the cystine-knot are marked.

Structure of neurotrophin receptors

There are two groups of receptors to which NTs bind, the Tropomyosin receptor kinase receptors (Trks) and the p75 NT receptor (p75), with different signalling pathways occurring, that lead to different physiological responses.[23] Both the Trks and the p75 receptors are type I single-pass transmembrane glycoproteins of 140 and 75 kDa, respectively. They both have an extracellular (EC), a transmembrane (TM) and an intracellular (IC) domain(Figure 1.2). The Trk receptors are receptor tyrosine kinases (RTKs), which means that they have a kinase domain in their IC segment with phosphocatalytic activity. The p75 receptor is a Tumour Necrosis Factor Receptor (TNFR) and it instead has a death domain intracellularly with no catalytic activity.[48–50]

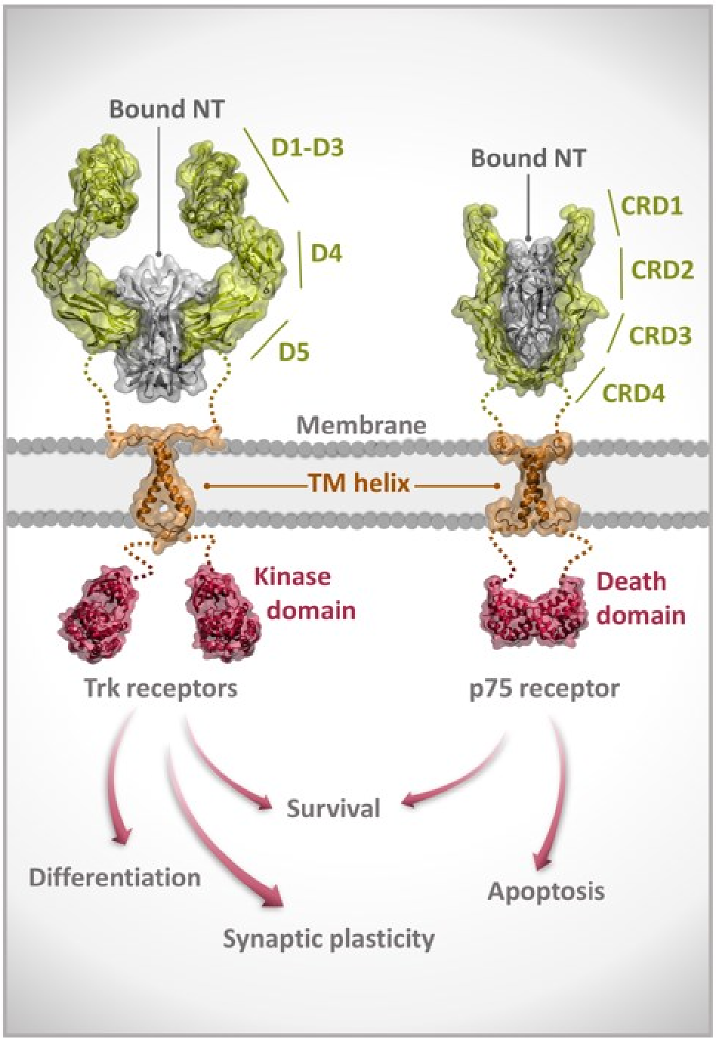

Figure 1.2: Full-length structural representation of the Trk (left) and p75 (right) receptors with NTs bound.[51] The structured parts of the receptors as well as the NTs are shown in cartoon representation with molecular surface. The EC segment of Trk receptors comprises five domains (D1–D5), while that of p75 four cysteine-rich domains (CRD1-CRD4). Both possess an α-helical TM domain. The IC segment of Trk contains a kinase domain, while that of p75 a death domain. Upon NT binding, the receptors are activated, leading to a diverse set of signaling cascades. In this figure I created the schematic structure of p75.

The EC domain of the Trks comprises an N-terminus signal peptide, which is 32 amino acids long and is cleaved, and five structured subdomains. Starting from the N-terminus, there are three grouped subdomains, D1-D3, with D1 and D3 being cysteine-rich regions, while D2 – which is located between the other two – is a leucine-rich repeat (Figure 1.2 and Figure 1.3). After the D1-D3 group, there are two immunoglobulin (IgG)-like subdomains, D4 (Ig-C1) and D5 (Ig-C2) (Figure 1.2 and Figure 1.3). The subdomains of the structured EC segment of the Trks are glycosylated (Figure 1.3). The NT binds in the homodimeric state of the receptor, and specifically in the D5 domain (Figure 1.2 and Figure 1.3). After the D5 domain, there is a disordered linker connecting the structured EC part with the TM α-helix (Figure 1.2). Another disordered linker – the juxta-membrane (JM) domain – connects the TM domain with the IC kinase domain.

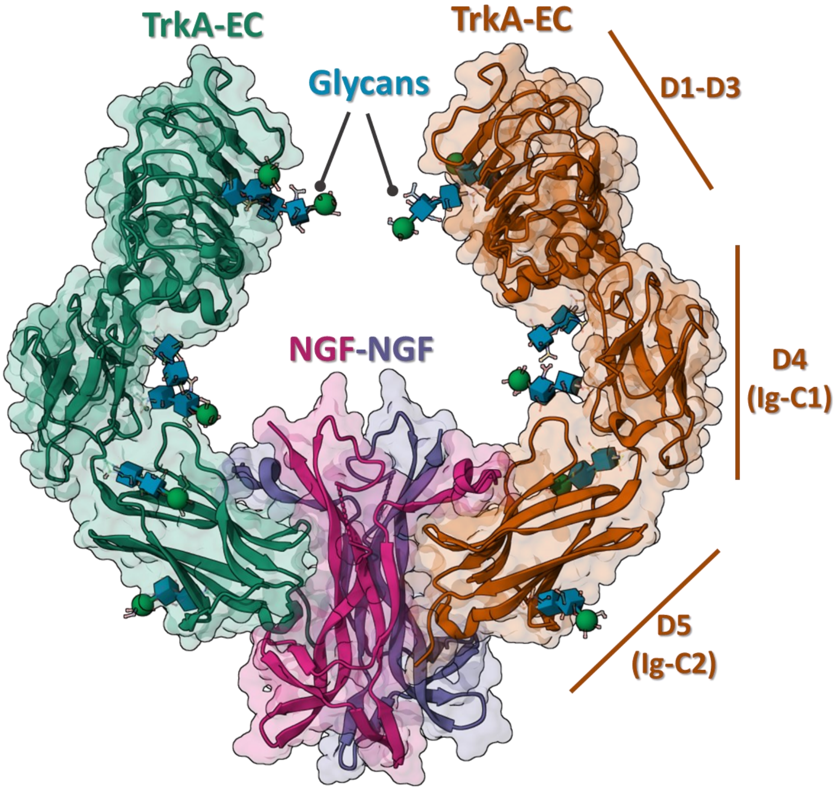

Figure 1.3: Crystal structure of the TrkA-EC homodimer bound to NGF (PDB ID: 2IFG)[47] depicted in cartoon representation with molecular surface. The two TrkA monomers are shown in green and orange colors, while the two NGF monomers in magenta and purple. Also shown are the solved N-glycans of the structure, in stick and 3D-Symbol Nomenclature For Glycans (3D-SNFG) representations. The blue cubes and green spheres correspond to N-acetyl glucosamine (GlcNac) and mannose (Man), respectively.

The p75 receptor is also composed of a 28-amino acid signal peptide, which is cleaved, followed by four cysteine-rich domains (CRD1-CRD4) (Figure 1.2), a structure common in the TNFR family.[52] The extracellular region of p75 is almost identical in all the three known crystal structures of p75-EC complexed with NGF, NT-3 and pro-NGF (p75-EC:NGF,[53,54] p75-EC:NT-3,[55] and p75-EC:pro-NGF[56]) (Figure 1.4). The p75-EC is made up of all four CRDs, in an elongated structure (Figure 1.2 and Figure 1.4). Twelve pairs of disulfide bonds ("disulfide ladder") are evenly spaced along the p75-EC inducing a rigid structure in the EC domain rather than a flexible one, despite the presence of several loops (Figure 1.5).[25,45]

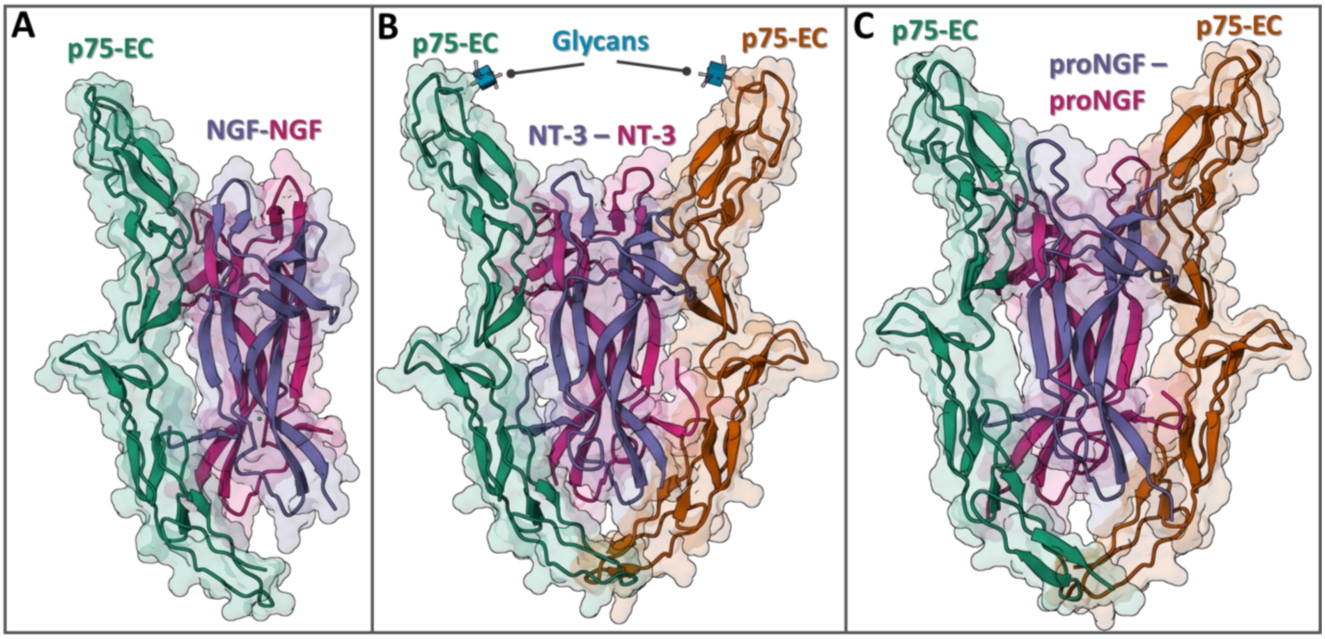

Figure 1.4: Crystal structures of p75 bound to different NTs. (A) NGF homodimer (magenta-purple) in complex with the full extracellular p75-EC monomer (green) (PDB ID: 1SG1).[53] (B) NT-3 homodimer (magenta-purple) in complex with the p75-EC homodimer (green-orange) (PDB ID: 3BUK).[55] (C) Pro-NGF homodimer (magenta-purple) in complex with the full extracellular p75-EC monomer (green) (PDB ID: 3IJ2).[56] All proteins are depicted in cartoon representation with molecular surface. The N-glycan from the 3BUK structure is shown in stick and 3D-Symbol Nomenclature For Glycans (3D-SNFG) representations. Only the first sugar is solved shown as a blue cube corresponding to N-acetyl glucosamine (GlcNAc).

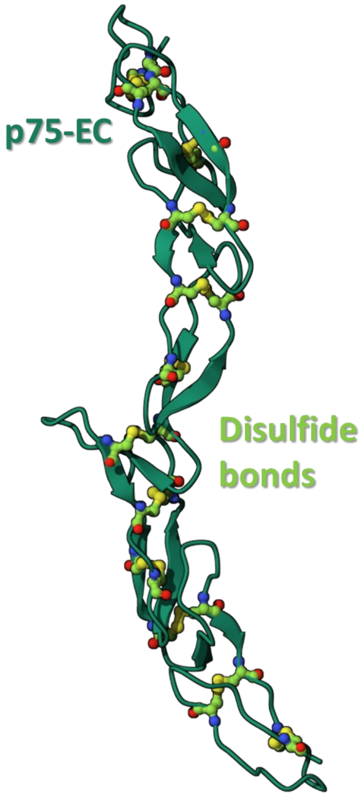

Figure 1.5: "Disulfide ladder" in the EC domain of p75. Crystal structure of p75-EC in green carton representation with the twelve disulfide bonds in light green ball and stick representation (PDB ID: 1SG1).[53]

Because of the dimeric nature of NTs, and the 2:2 stoichiometry of p75-EC:NT-3, and p75-EC:pro-NGF complexes observed by X-ray crystallography,[55,56] it is proposed that the p75-homodimer probably represents the active form of the receptor, despite the existence of a crystal structure of monomeric p75-EC bound to NGF.[53] The identification of a constitutively formed disulfide-linked p75-homodimer in the absence of NTs was an important step in that direction.[57] Full-length p75 homodimers disulfide-linked through the highly conserved Cys 257 (rat numbering) in the TM domain were reported in 2009.[57,58] In 2016, the NMR structure of the p75-TM helical homodimer was solved.[59] The structure shows that the TM domain of p75 forms covalent dimers bonded at the Cys 257 (Figure 1.6).

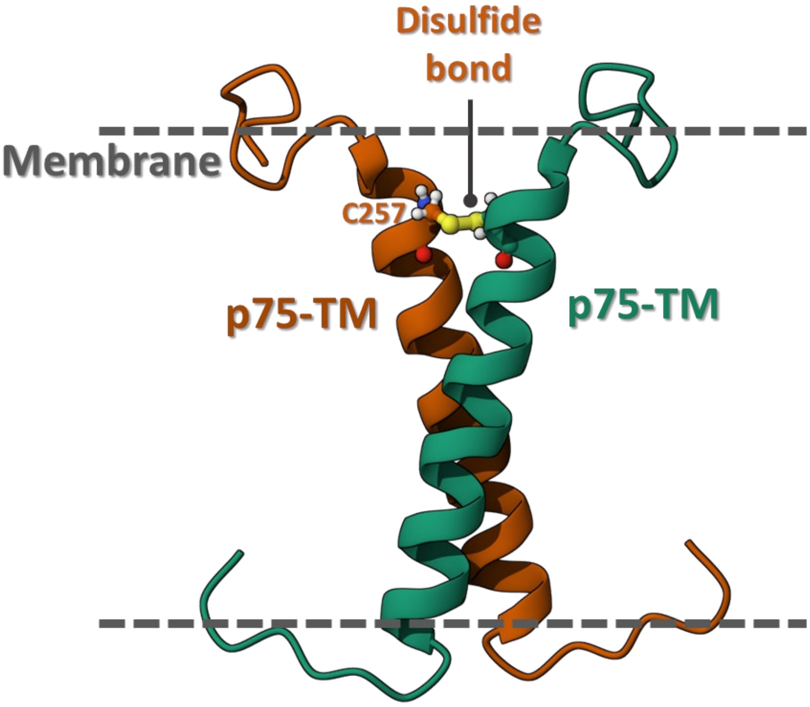

Figure 1.6: Disulfide-linked p75-TM homodimer. NMR structure (PDB ID: 2MIC)[59] of the TM α-helices of the p75 homodimer in cartoon representation (green-orange) and the disulfide bond at C257 in ball and stick representation. The TM region is demarcated with dashed lines.

The p75-IC domain is composed of two different regions. A flexible, intrinsically disordered region of about 60 residues presenting no secondary structure, called the juxta-membrane domain (JM), and a region that comprises the death domain (DD).[25,48] The relaxation kinetics of the entire p75-IC was determined and found that p75-JM is flexible even when linked to the TM and DD domains.[25,60] No interaction between the p75-JM and the p75-DD was found. Nevertheless, the p75-JM domain contains several motifs that mediate downstream signaling through binding with adaptor proteins like, NRIF,[61] SC-1,[62] TRAF4,[63] and TRAF6.[64]

A 29-amino acid linker in the p75-JM, called the *Chopper domain*, has been found to induce rapid cell death.[32] When the Chopper domain binds to the plasma membrane by a lipid anchor, it can induce cell death activity. Cys 279 of p75-JM is post-translationally modified by palmitoylation, and this cysteine may be responsible for the recruitment of a cell death-inducing machinery, if the Chopper domain remains membrane bound or in certain cholesterol- and sphingolipid-rich microdomains known as lipid rafts.[65]

The most interesting structure of p75-IC domain is the type II death domain (p75-DD). The first structure determined was that of rat p75-DD, as a monomer in pure water by NMR spectroscopy.[66] It is composed of six antiparallel *α*-helices labeled α1 through α6, including a helical Greek-key motif, anN-terminal 3_{10} helix and a C-terminal tail of seven amino acids (Figure 1.7).[66]

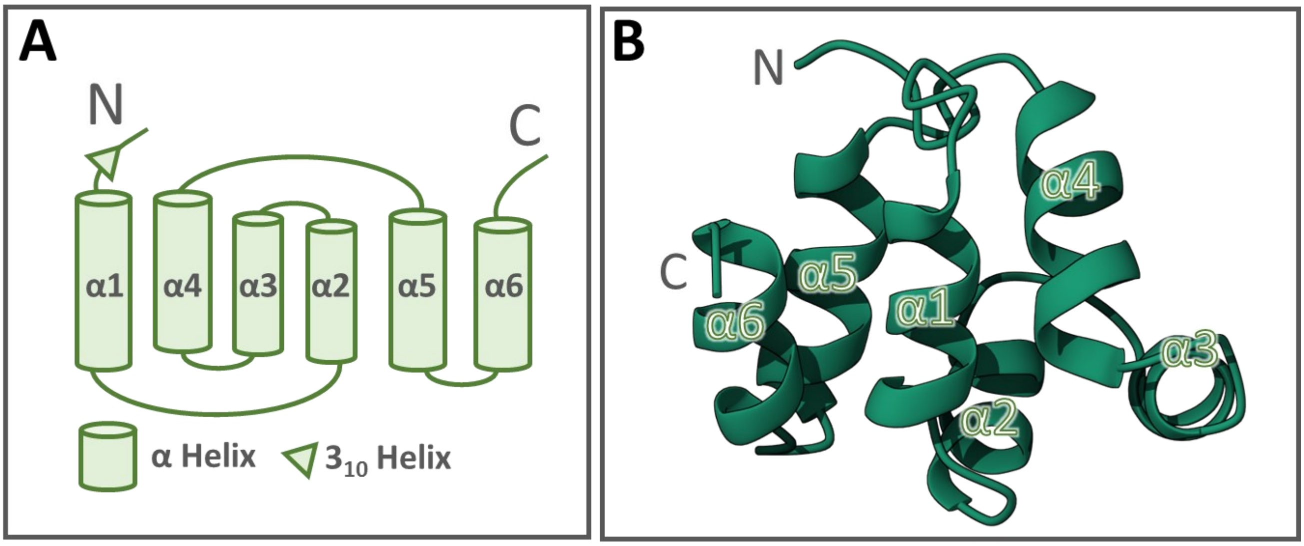

Figure 1.7: Structure of the p75 death domain. (A) Topology of monomeric p75-DD. (B) Solution NMR structure of the monomeric rat p75-DD (PDB ID: 1NGR).[66]

The structure of the rat p75-DD was the second one solved after Fas-DD, confirming that in the DD superfamily, the 3D folding of the DD is more conserved than its protein sequence.[25] In contrast to Fas-DD, which was able to self-associate under near-physiological conditions,[67] no self-association of the p75-DD was observed under the same conditions.[25,66] Although the structure of the p75-JM domain is completely flexible and disordered *in vitro*, an asymmetric non-bonded p75-DD dimer[68] and a symmetric non-bonded self-associated dimer[69] were observed in crystals and in a buffer solution containing phosphate ions (pH 8.0) respectively. In 2015, the NMR structure and the binding interface of the dimer of p75-DD was revealed.[70] It was confirmed that phosphate ions are necessary at pH 6.9 for the p75-DD dimer to be formed and not when other buffered molecules were present, suggesting that phosphate ions may stabilize the dimer structure.[70] The structure of the symmetric p75-DD homodimer reveals the existence of low-affinity interactions involving residues in helix α3 and the α1–α2 and α3–α4 loops.[25,70]

The DDs in the p75-DD homodimer use the residues in the α3 helix, making this complex a new type of homotypic interaction compared to the other members of the DD superfamily.[48,67]

Glycosylation of neurotrophin receptors

The NT receptors are glycoproteins, which means that they have covalently attached sugar moieties, called glycans. Two types of glycans exist: N-glycans, which bind to the side-chain N atom of asparagines, and O-glycans, which bind to the side-chain O atom of serines or threonines.[71] In most cases, N-glycans can be found in Asn-X-Ser/Thr sequences (with “X” denoting any amino acid except Pro), although not all such Asn residues are N-glycosylated.[71] On the other hand, no specific sequences for O-glycans have been identified, but instead there is a preference for certain residues such as Pro that has been observed near the serines/threonines to which the O-glycans bind.[71] There are three types of N-glycans in eukaryotic cells: (1) oligomannose, (2) complex and (3) hybrid. All three types share a common core sequence, Manα1-3(Manα1-6)Manβ1-4GlcNAcβ1–4GlcNAcβ1–Asn-X-Ser/Thr, and differ on how they extend it: in oligomannose the core is extended by additional Man residues bound to the ones of the core; in the complex type by a Fuc bound to the first GlcNac and “antennae” initiated by GlcNAc bound to the Man of the core; and in the hybrid type by additional Man residues bound to the Man of the Manα1-6 arm of the core and one or two GlcNAc-initiated antennae at the Manα1-3 arm (Figure 1.8).

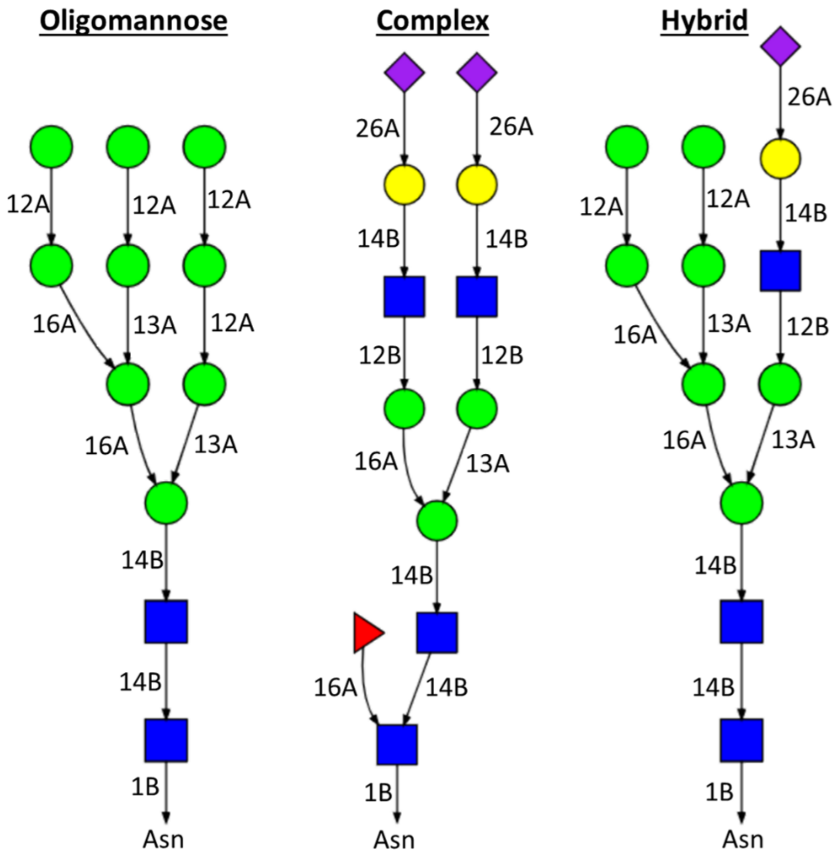

Figure 1.8: Structures of the three types of N-glycans in Symbol Nomenclature for Glycans (SNFG) representation, with their common core enclosed in a dashed-line box.[71] The numbers in each glycosidic bond signify the atoms of the two sugars forming it, while the letters A and B the configuration (alpha or beta, respectively) of the anomeric carbon. The blue boxes correspond to N-acetyl-glucosamine (Glc-NAc), the green circles to mannose (Man), the yellow circles to galactose (Gal), the purple rhombus to sialic acid (Neu5Ac) and the red triangle to fucose monosaccharides (Fuc). Figure adapted from Christina Athanasiou.[72]

The p75 neurotrophin receptor has been identified to have both N- and O- glycosylation oligosaccharides in its extracellular (EC) segments, with a single N-glycan close at the very N-terminal Cysteine-rich domain (Asn 60) and several O-glycans (the exact number is not known) at the linker connecting the EC and transmembrane (TM) domains.[73–80] In contrast, the Trk receptors are known to have multiple N-glycosylation sites at their EC domains without O-glycans present.[47,74,78] The EC domain of TrkA has 13 putative sites, with only 9 of them being actually glycosylated,[80] and 6 of them determined in an x-ray structure of TrkA.[47] TrkB has 12 putative sites with only 10 positions being actually glycosylated and known.[74,78] There is also evidence of glycosylation presence in the pro-domain of pro-neurotrophins.[81–83] The single N-glycosylation of p75 has a complex glycan type,[73] while its O-glycans in the linker were found to contain sialic acids and have this core: Galβ1-3GalNAc-O-Ser/Thr.[84] The exact role of the N-glycosylation in p57 is not clear, as its deletion does not have any effect on receptor cell partitioning as found for TrkA.[75,80] On the other hand, the O-glycosylation has been suggested to help with the proper folding on the EC linker[76,84] and the apical sorting of p75.[75–77] The exact glycan types on TrkA and TrkB are not known, except for the existence of sialic acid.[85,86]

Structure-function relationship of the p75 receptor

The p75 receptor is responsible for inducing signal transduction through binding directly with extracellular ligands including all neurotrophins,[53–55] pro-neurotrophins,[56] amyloid-beta (Aβ) peptide,[67,87,88] or indirectly with members of a subclass of myelin-derived growth inhibitory proteins like MAG (Myelin-Associated Glycoprotein), Nogo-A and OMgp (Oligodendrocyte myelin glycoprotein).[45,89] Also, p75 can function together with the TrkA, TrkB and TrkC neurotrophin receptors.[89–92] The two types of receptors can signal *synergistically*, *independently* or *antagonistically* to each other in different cellular contexts.[67,93]

p75-TrkA complex formation increases affinity of TrkA for NGF

p75 signaling is mostly mediated by ligand binding, but other structural factors can also influence these signals. Trk receptors and p75 bind NTs with similar affinity ($K_d \approx 10^{-9}$ M).[94] However, in sensory neurons and PC12 cells that express endogenously both receptors, p75 is acting as a co-receptor for Trks.[35] The affinity of NGF for TrkA has been shown to increase in the presence of p75, leading to high-affinity binding sites for NGF ($K_d \approx 10^{-11}$ M) and enhanced specificity of Trks for cognate NTs.[35,95] This interaction of Trks with p75 increases their affinity for NTs while at the same time it can lead to reduced ligand-dependent Trk internalization and degradation.[96,97] The co-expression of TrkA and p75 and their synergistic association is able to modulate TrkA to obtain increased sensitivity to lower concentrations of NGF.[35,98] This function of p75 is very important for developing neurons where limited amounts of neurotrophins are present and could be the leading idea in the design of therapeutic molecules targeting diseases where TrkA expression is limited.[23,99] It has been reported that co-expression of p75 also increases the affinity and specificity of TrkB for BDNF, in A293 cells.[96,100]

After decades of research, it is now clear that p75's ability to increase the affinity of Trks with NTs can impact cell fate *in vivo*. Nevertheless, the mechanism of Trk–NT interaction modulation by p75 remains unknown. The significance of this interaction in development, cell maintenance, and the response to disease where NTs or Trk receptor expression is altered, make it important to understand how high-affinity binding sites are achieved.[23]

p75 receptor undergoes Regulated Intramembrane Proteolysis (RIP)

The p75 receptor belongs to a group of proteins which includes among others amyloid precursor protein, Notch, and ErbB4 receptor tyrosine-protein kinase, that undergo RIP (Regulated Intramembrane Proteolysis).[89,101,102] RIP is a two-step procedure yielding two soluble fragments: the cleaved EC domain of p75 and a cytosolic fragment corresponding to the IC domain. First, the α-secretase TACE/ADAM17 (tumor necrosis factor-α converting enzyme/α-disintegrin and metallopeptidase domain) cleaves within the EC linker between the EC and TM domains, thereby shedding the p75-EC and yielding a C-terminal fragment tethered to the cell membrane.[102–104] The second step involves presenilin-dependent γ-secretase cleavage within the TM domain and release of the soluble p75-IC fragment into the cytoplasm.[23,103] After three decades of studying the process, it is well understood that each cleaved fragment serves a distinct functional purpose, with the p75-IC acquiring signaling capacity in relation with the ligand and co-receptor interactions.

RIP of p75 enhances TrkA receptor high-affinity binding for NGF

Several studies have demonstrated that p75 receptor RIP enhances Trk signaling.[105–108] The IC domain fragment is the modulating factor that stimulates functional outcomes associated with TrkA high-affinity binding mode for NGF.[106] On the other hand, PC12 cell assays have shown reduced NGF affinity and shorter neurite outgrowth function upon NGF stimulation at the presence of a p75 mutant, which is unable to undergo RIP, compared to wild type.[23,32]

Particularly, several studies indicate that the p75-TM and the chopper domain of p75-IC appear to be both sufficient and necessary to mediate high-affinity TrkA/p75 receptor complex formation.[23,65,105,106] It is recognized that both pro-neurotrophins and mature neurotrophins increase p75 subsequent processing by α-secretase TACE/ADAM17 and γ-secretase.[107–112]

Implication of ligand binding in stoichiometry and activation of p75

Despite the vast number of structural and biochemical studies, a globally accepted mechanism for p75 activation by ligands is still a matter of discussion. The question of stoichiometry of the p75 receptor still remains a matter of debate. The association of p75 with its ligands is still elusive, since monomeric, dimeric, and trimeric structures have been reported complexed with its cognate ligands. Isolated p75 exists mainly as a monomer up to 2.5 mM,[66] in pure water or a non-phosphate buffer.[57,66,70,113] It can also exist in monomeric and dimeric forms in phosphate buffer with weak affinity ($K_d \approx 50$ µM).[66] However, the homodimerization affinity of the real system anchored in the cell membrane can differ.[67] Even before the p75 receptor was identified, NGF was known to be a non-covalent dimer in a complex with other proteins.[114,115] Cross-linking experiments suggested later that a dimer of p75 is associated with a dimer of NGF.[16,116] Based on crystallographic studies it was shown that the cysteine-rich repeats CRD2, CRD3, and CRD4 of p75-EC constitute the binding sites of cognate ligands.[53,55]

On the cell surface, p75 exists as a homodimer that binds NTs in a 2:2 stoichiometry, as revealed by the crystal structures of p75-EC bound to NT-3 and pro-NGF.[55,56] However, p75 was shown to be also able to bind NGF in a 1:2 stoichiometry.[53] Although this 1:2 stoichiometry between ligand-receptor complex has been proposed to be the outcome of using non-glycosylated p75 in that study,[55] it was also shown that glycosylated p75 can form both an asymmetrical and a symmetrical receptor-ligand complex.[56] Thus, it was proposed that asymmetrical ligand binding may be an intermediate step towards a symmetrical 2:2 receptor/ligand complex.[56,117] However, it remains still unclear whether the asymmetric complex possesses the ability to signal.[117]

As described above, the cross-talk between the p75 and TrkA receptors creates high-affinity binding sites for NTs. Initially it was proposed that NGF dimer binds a p75/TrkA high affinity site complex-formation.[35] However, the proposed ternary complex between NGF, TrkA, and p75 has never been observed via structural biology techniques. In addition, NGF and NT-3 have antiparallel orientations in the available crystal structures of the NGF/TrkA-EC,[47] and NT-3/p75-EC[55] binary complexes. Comparison of the 2:2 NT-3/p75-EC complex structure and the crystal structure of NGF/TrkA-EC complex, shows that there are mutually exclusive binding sites on the ligand dimer.[55] It is therefore impossible for a p75/NT/TrkA ternary complex to form high-affinity binding sites or even an instantaneous intermediate binding state through interactions between EC domains of the receptors. This brings into the question: how a ternary complex could assemble.[47] The findings suggest that the p75 ligand-binding site on TrkA can potentially lead to an altered conformation of TrkA in the presence of fragmented p75.[23]

Concerning the activation of p75 leading to recruitment of downstream signaling effectors, it has been suggested that in the absence of ligands, and even before receptor activation by NTs or other signal stimulating ligands, the p75-DD could form a rather stable dimer through weak homotypic interactions in cellular context.[57,70,118] This homodimerization affinity of the p75-DD could prevent exposure of binding regions for signaling proteins prior to receptor activation in response to extracellular signals. The disulfide bond at the TM helices was considered the determinant factor for functional p75-DD.[59] Without the formation of this disulfide bond, p75-DD may be independent of p75-TM movements, leading to lack of response to NGF stimulation, after binding to the EC domain.

It was proposed that the p75-TM dimer is formed via a conserved cysteine residue in the TM domain (Cys 256 in human numbering, corresponding to residues Cys 257 in rat and Cys 259 in mouse sequences), which plays the role of a scissor's fulcrum, facilitating a pivotal conformational change propagated from the p75-EC domain to the IC domain upon ligand binding.[57] Mutating the Cys 256 has been shown to abolish NT-mediated apoptosis by p75 in neurons and a mouse model.[110] FRET assays also showed that the IC domains of p75 dissociate upon NGF binding, which is not possible in the C256A (C257A in the study that used the rat p75) mutant.[57] This suggested that the disulfide bond in the highly conserved cysteine residue functions as the pin in the scissors. When the disulfide bond is deleted, relative movements at one end cannot be propagated to the other. However, unlike normal scissors, it was suggested that as the EC domains come closer together, the IC domains separate, like a ''snail-tong'' utensil.[57]

Upon ligand binding, like NGF, the putative p75-EC dimer undergoes conformational changes from an open to a closed state,[53,57] which propagate to the TM and IC domains, leading to IC domain separation and exposure of regions for binding of DD-interacting proteins.[57] The p75-DD can partake in and regulate different signaling cascades by interacting with different molecules intracellularly.[67] This model of allosteric regulation of the p75-DD is proposed for different cellular contexts, including neuron and cancer cells,[67] even though it has been challenged by the flexibility of the p75-JM and Chopper domains.[60] According to this report, it is unclear how the flexible p75-JM region can allow propagation of conformational changes from the p75-EC to the IC domain.[57,67]

In a recent study an alternative model for receptor activation was proposed. In this study, upon NGF stimulation, p75 monomers preferentially concentrate into membrane microdomains, like lipid rafts, with Cys 256 and Gly 265 residues (human numbering) playing a crucial role in this compartmentalization.[113] Also, in another recent study it was claimed that the ''snail-tong'' model is not supported by experimental data, as there is no interaction between the DDs of p75 in any cellular context and the model should be revised.[119] Another model of functioning p75 was proposed suggesting that p75 dimerization requires a "helper" protein, with ligand binding leading to "helper" release, allowing p75 dimer to interact with IC-interacting proteins.[119] Although members of the TNFR family usually initiate downstream transduction signalling through trimerization and higher-order oligomerization, it seems that experimental data remains inconclusive regarding the role of p75-DD self-association for receptor function.[119]

It is possible that the p75 function is a multivariable problem. Different cell context imposes a different functional behavior of p75. Cellular types are differentiated in terms of lipid composition, glycosylation profile, existing adaptor proteins and chaperone proteins. p75 has been found in association with different plasma membrane proteins like Sortilin, LINGO1 protein, Nogo-R1 receptor not to mention the Trk receptors family and their ligands and adaptor proteins. All these variables taken into account affect p75 stoichiometry, adapted conformation, and signaling profile. It is known that conformational alterations can change receptor's localization,[57] and ligand binding.[53] Another important variable is the expression level of p75. The receptor is up-regulated in many cell types after injury or disease and its expression is triggered by inflammation or tissue damage.

p75-DD heterotypic complexes with signal effectors

The p75 receptor does not possess any catalytic activity, however there are several protein-binding sites in the p75-IC domain, which are implicated in the initiation of signaling through p75.[120–122] The p75-DD is the main feature involved in contacts with interactor molecules. Nevertheless, there are also several motifs within the p75-IC domain, which are mostly related to the chopper domain, able to mediate downstream signaling through binding with adaptor proteins.[123]

In 2015, two complex structures of p75-DD with Rho-GDI (for the RhoA pathway), and RIP2-CARD (for the NF-κB pathway) were disclosed.[70] Structural calculations in the complex structure of p75-DD/Rho-GDI suggest that Rho-GDI could potentially bind the small GTP-binding protein RhoA forming a trimeric complex of p75-DD/Rho-GDI/RhoA in solution due to non-competing binding sites of the p75-DD and RhoA on the Rho-GDI surface.[67,70] The second structure of the p75-DD/RIP2-CARD complex provided a structural mechanism for the p75-mediated NF-κB pathway through RIP2-CARD, and it is the first described heterotypic complex between different proteins of the DD family.[67,70]

After these two described complexes, in recent years a variety of adaptors have been identified that interact with p75-DD and lead to signaling in different cell types. These adaptors include TRADD (TNF receptor associated death domain), p45 (also known as neurotrophin receptor homologue 2: NRH2, or neurotrophin receptor alike DD protein: NRADD), calmodulin, p38β2 a mitogen-activated protein kinase (MAPK), BEX3 (brain expressed X–linked protein 3, also known as p75-associated cell death executor: NADE), NRIF (neurotrophin receptor interacting factor), RanBPM (ran-binding protein microtubule-organizing center) and others.[67] However, the structures of the complexes between these adaptors and the p75-DD are for most of them still not solved. Thus, p75-DD functions as an intracellular interaction and signaling hub for the modulation of different downstream signaling regulators.

In a more recent study the structure of p75-DD bound to TRADD-DD has been reported.[124] In this study, the DD interaction interface between the p75-DD and TRADD-DD is mainly formed by helices α1, α6, and the α3-α4 loop of the p75-DD, and by helix α5, and the α2-α3, and α4-α5 loops (a characteristic β-hairpin motif), of the TRADD-DD.[124] TRADD is a multi-functional adaptor protein, consisting of two domains connected by a long linker peptide.[67,125,126] It has multiple interacting proteins and is involved in different and divergent signaling pathways, including NF-*κ*B mediated survival pathway,[124] but also apoptosis through mitogen-activated protein kinase (MAPK) activation.[127,128]

Interaction of p75 with Sortilin, LINGO proteins and Nogo receptor

Sortilin is a multitask protein implicated in the physiology of the nervous system,[34] but also in neurodegenerative disorders and colorectal and other cancers.[129] Sortilin has been shown to associate with p75 and induce neuronal apoptosis through binding with pro-NGF,[130] and pro-BDNF.[131,132] The structure of the ternary complex p75/pro-NTs/Sortilin is not completely solved. In 2012, part of the interface between p75 and Sortilin to a few residues within their EC domains were reported.[36] Previously it was established that pro-NGF binds both Sortilin and the mature form of p75-EC in a 1:2:1 complex.[56]

Neural axons of the central nervous system are unable to regenerate upon injury due to the repulsive action of myelin inhibitors, such as MAG, Nogo-A and the OMgp.[89] These inhibitors bind and signal through a receptor/co-receptor complex that comprises the Nogo-R1 receptor, the LINGO-1 trans-membrane protein and p75. The stimulated complex is triggering intracellular downstream signaling that inhibits re-growth of axons.[133] A structure of p75 in complex with NgR1 or LINGO-1 has not been reported yet.

Neurotrophin receptor function in lipid rafts

NT receptors have been detected to localize to membrane compartments on the cell surface that are ordered and have higher concentrations of cholesterol and sphingolipids. These compartments have been called in the literature lipid rafts.[134–138] The p75 receptor partitions in lipid rafts, which is modulated by the cAMP-dependent protein kinase A (PKA).[139] Also, the shedding mechanism of p75 is affected by its localization in raft domains.[140]

For the TrkA receptor, it has been shown that translocation to lipid rafts enabled by association with flotillin and the adapter protein c-Cbl-associated protein (CAP), is necessary for the activation of the ERK sugnaling mechanism.[141] Deletion of the interacting domains of CAP does not allow TrkA translocation to rafts and consequently ERK activation. Caveolin proteins that are localized in lipid raft domains have been aslo identified to regulate NGF activity by partitioning the TrkA and p75 NT receptors together with other membrane proteins related to NT signaling.[142]

Binding of BDNF to TrkB leads to transolation if the latter to lipid rafts, an effect that can be hindered by TrkB kinase inhibitors.[143] Rafts also regulate TrkB signalling related to neurotransmitter release and synaptic response to tetanus.[143] Hypoxic conditions can distort TrkB presence in lipid rafts, which can ben restrored by vitamin E uptake.[144]

Spingolipids whose concentration is higher in lipid raft microdomains have been found to associate with and activate the NT receptors. The GM1 ganglioside can bind to and activate the TrkA receptor,[145–147] which leads to enhanced NGF-mediated TrkA phosphorylation and promotes neurofilament expression and neurite outgrowth.[148] Ceramide lipids can also activate TrkA and enhance its dimerization.[149] Also, upon impaired GM1 production ion cells, TrkA localization in the cell membrane is hindered.[150] Regarding the interaction of GM1 with TrkA, it has been found that GM1 can only recognize the glycosylated form of TrkA[151] and that the sugar moieties of GM1 are needed for TrkA-mediated neurodifferentiation.[152] Activation of the TrkB receptor by GM1 has been also reported and associated with neuroprotection.[153] It has been also suggested that activation of NT receptors by GM1 is due to increased NT expression and release.[154]

1.4 Neurotrophin signaling through p75

Investigation of the signaling mechanisms of the p75 receptor has been proven a challenging task.[89,121] p75 has two main functions: it modulates signaling of Trks and other receptors and initiates autonomous signaling cascades that regulate survival or apoptosis.[100] It plays an important role in the regulation of cell death during neuronal development and in the responsive mechanism to nervous system injury. Depending on the cellular context, p75 signaling also modulates myelination by Schwann cells, synaptic plasticity, neurite growth, cell-cycle regulation, long-term potentiation (LTP) in hippocampal neurons, and modulates the invasiveness of tumor cells.[121]

During development, p75 is widely expressed throughout the CNS, though it is down-regulated after developmental completion. In the adults, it is found only in a few neuronal populations in the brain. Stimuli of p75, such as NTs, are important for development as they regulate neuronal growth, differentiation and death.[89]

Evidently, p75 participates to multiple signaling complexes. It associates with several co-receptors, including the Trk receptors, Sortilin, Nogo-receptor, LINGO-1 and others, while mediating the response to multiple ligands, including NTs, pro-NTs, MAG (myelin-associated glycoprotein), NogoA, OMgp (oligodendrocyte myelin glycoprotein) and others. However, the mechanisms by which p75 facilitates the downstream responses are still not completely understood.

As described above a number of adaptor proteins have been identified to bind to the p75-IC domain, including NRIF (neurotrophin receptor-interacting factor), TRAF6 (TNFα receptor-associated factor 6), Rho-GDI, NADE (p75-associated death executor), TRADD (TNF receptor associated death domain), NRAGE (the neurotrophin receptor interacting melanoma associated antigen homolog), RIP2 (receptor-interacting factor 2), the actin bundling protein Fascin in melanoma cells, and several others.[155]

p75 facilitates survival independently or by modulating Trk receptor signaling

As discussed before, p75 interacts with the Trks through the cytosolic and transmembrane domains. To facilitate this function, p75 adopts the role of a co-receptor that improves Trk affinity and specificity for NTs. Specifically, the high-affinity binding site is generated by a complex of TrkA and p75, and the presence of p75 enhances ligand specificity as well as the binding affinity of NGF for TrkA.[35] When this high-affinity binding complex is formed it ultimately enhances TrkA tyrosine-kinase signaling.

Subsequent studies have shown that p75 can also restrict the binding affinity of TrkA for NT-3, and it relaxes the specificity of TrkC for NT-3.[3] Induction of p75-expression in sympathetic neurons can reduce axonal growth by NT-3 and promote neuronal survival and differentiation induced by NGF.[156]

Trk–p75 receptor complexes have different signaling capabilities than those of Trk dimers alone. TrkA can activate the ERK/MAPK pathway in the absence of p75, but both receptors are required for PI3K/Akt pathway activation. This might explain why TrkA dimer activation alone is able to assist neurite outgrowth, whereas p75 presence is necessary for complete outgrowth and long-term survival.[157] There have been several alternatives proposed regarding the mechanism of modulation of Trk activity by p75.[23]

In certain cases, and predominantly during development, p75 can also independently induce survival. NGF binding to p75 has been shown to promote survival of developing neocortical sub-plate neurons,[158] sensory neurons,[159] and cultured Schwann cells.[160] The activation of the transcription factor, NF-κB, is one of the best-characterized anti-apoptotic signaling pathways. This involves the recruitment of RIP2 and TRAF6 adaptor proteins, or TRADD interactor, to the p75-IC domain after NT binding leading to activation of NF-κB, a factor that controls DNA transcription promoting cell survival and synaptic plasticity.[121,161]

p75 displays a pro-apoptotic function in the absence of Trks

In the absence of the Trk receptors, NTs activate cascades regulating apoptosis, via the p75 receptor. The ability of p75 to promote cell death has been illustrated initially in transgenic animal models as have been thoroughly reviewed in the literature.[100,121,155,162] Nowadays, it is well-established that, in response to ligand binding, p75 induces programmed cell death in a wide variety of neuronal and non-neuronal cell types,[125] including sympathetic neurons,[163,164] motor neurons,[165] hippocampal neurons,[166] oligodendrocytes,[167] Schwann cells,[168] and other types of cells.[169,170]

Based on several studies, the p75 receptor has been recognized as a critical regulator of developmental apoptosis, as have been demonstrated in basal forebrain,[171] superior cervical ganglion,[163] and spinal cord.[172] This apoptotic role of p75 during development has been well characterized in sympathetic neurons.[1,99,163] However, p75 is down-regulated during the adulthood when it is found only in a few neuronal populations in the CNS.

Since p75 has no enzymatic activity, it requires the recruitment of IC adaptors that link the receptor to downstream apoptotic cascades. For this purpose, the p75-DD contains several potential motifs for interactions with signaling adaptors.

p75 induces cell death through activation of the mitochondrial cascade

The apoptotic cascade of p75 involves the release of cytochrome c from mitochondria and activation of the intrinsic caspase cascade. The triggering event of this pathway involves the activation of the stress kinase JNK (c-Jun N-terminal kinase). Like many members of the TNF receptor superfamily, p75 activates JNK, a signal necessary for p75-induced apoptosis.

Ligand binding to p75 leads to activation of Rac, which is an activator of JNK.[173] Several p75-interacting adaptor proteins have been proposed to link p75 with Rac and consequently to JNK activation: such as NRAGE, TRAF6, and NRIF.[174] Genetic deletion of these proteins prevented p75 from activating JNK, showing their contribution to this pathway.[175]

It has been shown that JNK activation can induce cell death via mechanisms that can depend or not on transcription. JNK activates the transcription factor c-Jun through phosphorylation. Further downstream events include activation of both p53 and p73,[176] resulting in transcriptional up-regulation of an array of genes encoding pro-apoptotic factors, including Bad and Bim, and mitochondrial translocation of Bax.[1,177] This event leads to release of mitochondrial cytochrome c and activation of caspases 9, 6 and 3.[121,178–181] Furthermore, JNK directly phosphorylates a number of proteins belonging to the Bcl-2 family, which inhibits pro-survival members – such as Bcl-2 itself[182] – and activates pro-death members – such as Bim[183] and Bad.[184] The end result is the mitochondrial release of cytochrome c and the caspase-dependent apoptosis.[185]

Another mechanism that has been implicated in p75 regulation of JNK activation, involves the production of the lipid signaling molecule ceramide. Ligand binding to p75 has been shown to trigger the activation of acidic sphingomyelinase, which results in generation of ceramide.[186] A known downstream effect of elevated levels of ceramide is that of JNK activation.[1,187] It has been shown that ceramide couples p75 to JNK phosphorylation. In a study where cultures of hippocampal neurons were used, activation of p75 led to upregulation of ceramide, stimulation of JNK, and cell death.[1,188] Several other IC adaptors are known to bind p75 and mediate its apoptotic signaling, such as NADE[189] and Necdin.[190]

p75 undergoing regulated intramembrane proteolysis (RIP) induces apoptosis

p75 is distinguished from other members of the TNFR superfamily as it undergoes RIP (Regulated Intramembrane Proteolysis), a mechanism first described in HEK293 cells transfected with the receptor.[103,191] As described TACE/ADAM17, first cleaves the EC region of p75 producing a 24 kDa membrane-bound C-terminal fragment (CTF).[192] After the release of the soluble EC domain, the rest of p75-CTF is further cleaved in the JM region by the γ-secretase complex, releasing a 19 kDa IC segment.[50,193] TACE/ADAM17 acts on the receptor before p75 cleavage by γ-secretase, as TACE inhibition can prevent γ-secretase induced receptor cleavage.[193,194] RIP of p75 is based on a ligand-dependent mechanism as shown in sympathetic neurons,[110,194] Schwann cells,[109] and cerebellar neurons.[195] Nevertheless, it is uncertain, whether ligand-binding activation of p75 always leads to RIP.

Release of the p75-IC domain facilitates transport to the nucleus of associated factors such as NRIF, an event required for p75-mediated apoptotic signaling. RIP of p75 is a possible mechanism of NRIF translocation from the surface-bound p75-IC domain to the nucleus, as it was demonstrated in sympathetic neurons.[110] NRIF translocation to the nucleus is dependent on TRAF6-mediated ubiquitination. TRAF6 ubiquitinates NRIF after p75 ligand binding, while blocking ubiquitination of NRIF leads to inhibition of p75-mediated apoptosis.[196] The fact that p75 cleavage is required for NRIF ubiquitination, suggests that p75 proteolysis facilitates: (1) NRIF/TRAF6 interactions leading to ubiquitination of NRIF, necessary for nucleus entrance; and (2) the oligomerization of TRAF6, which promotes JNK activation.

In some cell types, p75-CTF alone can induce cell death.[1] As reported before, overexpression of p75-CTF is able to promote apoptosis of dorsal root ganglion neurons (DRG).[32,65] It was demonstrated that overexpression of the p75 chopper domain promotes apoptosis through an increase in PIP2 (phosphatidylinositol 4,5-bisphosphate). PIP2 then activates GIRK (G-protein-coupled inwardly rectifying potassium) channels, causing a reduction of internal potassium that eventually initiates the APAF1-dependent cell death pathway.[112,117,123]

Although cell death regulation seems to be partially dependent on p75 RIP, the ability of the receptor to regulate neurogenesis and neural progenitor cell migration, also appears to be dependent on p75-RIP.[117] In peripheral tissues, p75 has been demonstrated to be tumorigenic, and to promote metastasis, specifically following intramembrane cleavage.[197] Nevertheless, in other cases p75 acts as a tumor suppressor by mediating cell death in cancer cells.[198]

pro-NT binding to p75/Sortilin complex induce cell death

Several studies have shown that pro-NTs, which do not activate the Trks,[199] bind with high affinity to p75 and can initiate apoptosis even when Trks are present. Thus, it is well-established that pro-NTs can act as agonists of p75 signaling.[30,131,200,201] Pro-NT apoptosis happens though their binding to a complex of p75 with its co-receptor Sortilin.[34,131] Sortilin, which is a member of the Vps10p family, comprising also SorLA, SorCS-1, SorCS-2, and SorCS-3, is a type I TM receptor with multiple functions.[202]

Pro-NTs bind to Sortilin and p75 with their pro-domain and mature domain, respectively, therefore enabling the association of these two receptors acting as a cross-linker, creating a ternary complex which leads to initiation of programmed cell death.[34,100,131] *In vivo* studies with animal models have shown that Sortilin is necessary for retinal ganglion neuron death from p75.[34,203,204] However, Sortilin may not be necessary for p75-mediated cell death occurring during the developmental time period of these neurons. But loss of Sortilin does delay age-related degeneration of these neurons.[203] This suggests that pro-NTs play a role in the aging of sympathetic neurons, but are not involved in early development.

The emerging question is: what is the purpose of a receptor that promotes neuronal survival in response to NT binding (Trk), and another receptor that initiates neuronal death in response to pro-NTs (p75)? Binding of NTs to the Trk receptors sustains survival during development, and also regulates neuronal function during adulthood. On the other hand, pro-NTs induce apoptosis through p75 during injury or disease; when expression of p75 is increased. Thus, NTs being present during normal development, seem to promote physiological function and survival of the nervous system, but under pathological conditions, increase of pro-NTs and expression of p75 stimulate a signaling pathway that leads to cell death.

The signaling pathways activated by the p75/Sortilin complex are still not known. Sortilin might facilitate pro-NT binding to p75, or it can aid other proteins to regulate or activate p75 signaling pathways. NRIF has been implicated upon pro-NGF stimulation.[100] It has been shown that Sortilin mediates the internalization of pro-NGF and it is possible to facilitate p75 retrograde signaling through incorporation of the receptor to “signaling endosomes”.[34] p75 has been found in internalized endosomes associated with NRAGE and necdin.[205] Recently it has been proposed that Sortilin modulates pro-BDNF activation of p75 leading to neuronal apoptosis through the mitochondria-caspase cascade.[206]

Signaling of p75/Nogo-R/LINGO-1 complex restricts axonal regeneration

The formation of the complex between p75 and the Nogo-R (glycophosphatidylinositol-linked) receptor, a protein with no IC domain, is different from that of p75 and Sortilin.[207,208] Nogo-R binds MBGIs (myelin-based growth inhibitors), including Nogo-A, MAG (myelin-associated glycoprotein), and OMgp (oligodendrocyte myelin glycoprotein).[100] These interactions promote the association of the Nogo-R with p75 and another TM protein termed LINGO-1.[209]

Whereas pro-NGF simultaneously engages Sortilin and p75 for signaling, MBGIs bind to Nogo-R only. When pro-NGF binds p75, the latter then binds to the guanine-nucleotide-exchange protein Kalirin9, and to Rho-GDI (the Rho guanine dissociation inhibitor), relieving the small GTP-binding protein RhoA from its inhibition, resulting to its activation. This activation cascade is distinct from that in pro-apoptotic stimulation.[210] This signaling pathway requires cleavage of the p75, although it is not clear how receptor processing facilitates the cascade. The formation of this complex and the activation of RhoA causes reorganization of the actin-cytoskeleton, promotes growth cone collapse of injured neurons and restricts axonal regeneration and axonal growth.[174,211]

1.5 p75 in neurodegeneration

Neurological disorders are complex diseases, with multiple risk factors, causes, treatments and outcomes. They present many molecular and morphological alterations suggestive of impairment in cellular plasticity and pliability. Aging has been associated with many neurodegenerative diseases, including Huntington's disease (HD), Parkinson's disease (PD), Alzheimer's disease (AD), Amyotrophic lateral sclerosis (ALS). In the past decades, substantial demographic change has been observed particularly in the western world. The aged population is increasing with an accelerating rate, driven by a decline in birth rates and astonishing improvement in life expectancy.[212]

Neurotrophins regulate growth, survival, differentiation of neurons and the creation of connections with other neurons or axon regeneration after nerve injury, maintaining this way the structures and functions of the CNS.[213,214] Imbalance in the expression and function of NTs and their receptors is regarded as a main contributor involved in many neurological disease pathogenesis, including the above mentioned neurodegenerative diseases, but also cerebrovascular diseases such as stroke.[215,216] Despite the efforts that have been made to develop drugs for the treatment of nervous system disorders, no significantly effective drug is available partly due to poor knowledge of their pathogenic mechanisms at molecular level.[217]

As previously discussed, p75 has been implicated in contradictory tasks such as cell death and survival depending on its interactions with other proteins and the cell type.[218] p75 plays a key role in the development of the CNS and in the pathogenesis of several neurological diseases,[219,220] cerebrovascular insufficiency,[221] and neuropsychiatric disorders,[222] by regulating axonal degeneration, neuronal death, synapse damage, and tau hyperphosphorylation.

p75 and Alzheimer's disease (AD)

AD is a complex CNS neurodegenerative disease with pathological changes of cortical and hippocampal neurons, amyloid β-protein (Aβ) aggregation-formed plaques, and tau protein hyper-phosphorylation-induced neurofibrillary tangles, which is clinically shown by deficits in learning and cognitive function, especially memory.[223] The expression of p75 is increased in the cortex[224] and hippocampus[225] of AD patients. Aβ in addition to NTs and pro-NTs is a p75 ligand,[226] and neurotoxic Aβ oligomers can directly interact with the p75-EC domain.[88] Significant evidence demonstrated the roles of p75 in the regulation of neurotoxicity and the production, deposition and elimination of senile plaques in AD.[217,227] The p75-EC domain has been detected in the serum and cerebral spinal fluid of AD patients, proving that p75-EC can be used as a specific biomarker monitoring AD progression.[228]

It is suggested that p75 may have a double effect on Aβ metabolism: p75 signaling can increase the production of Aβ, which may exacerbate AD pathology; in contrast, shed p75-EC domain can bind Aβ, reducing its ability to aggregate and be deposited in the brain. In the absence of p75, the end result is the increase of Aβ deposition and AD pathology, suggesting that it is the effect of the shed p75-EC domain that is the strongest of the two, and also that the clearance of Aβ plays a big role in the development of AD. The above adds to the evidence that p75 constitutes a valid target to combat AD.[229]

p75 and amyotrophic lateral sclerosis (ALS)

ALS is a chronic gradually paralyzing and fatal neurodegenerative disorder,[230] which can involve various neurons from upper motor neurons (brain, brainstem and spinal cord) to lower motor neurons (cranial nuclei, anterior horn cells of the spinal cord) and lower motor neuron-innervated muscles of the trunk, head, face, and extremities.[217,231] The p75 has been involved in cell autonomous or non-autonomous aspects of ALS.[232] Motor neuron death has been triggered by astrocytes in the spinal cord of SOD1 mice, via p75 signaling.[233] Additional studies are needed to investigate the possible role of p75 in the cognitive impairments associated with ALS.[217]

p75 and Parkinson's disease (PD)

Parkinson's Disease (PD) is a neurodegenerative disease with clinical symptoms including static tremor, bradykinesia, myotonia and postural gait disorders accompanied by non-motor symptoms such as depression, constipation and sleep disorders.[217,224] Degeneration and death of dopaminergic neurons which lead to decrease of dopamine, is one of the main characteristics of PD.[234] The specific underlying mechanisms leading to degeneration and death of dopaminergic neurons remain unclear.[217] Genetic susceptibility, environment, ageing and oxidative stress are potential reasons. p75 specifically has been found to be implicated in the neuronal death of dopaminergic neurons, as well as in the pathogenesis and progression of PD. [217,235]

p75 and Huntington's disease (HD)

HD is an neurodegenerative disorder that causes the progressive degeneration of nerve cells in the brain.[230,236] Patients suffering from HD exhibit clinical symptoms such as deficits in learning and memory and motor symptoms.[237] Memory-dysfunction processes in multiple brain regions are found to contribute to HD memory impairments.[236,238] Data from several studies demonstrate p75 as a negative regulator of memory impairments and synaptic dysfunction associated with HD.[230,236,239]

p75 and cerebrovascular diseases

Hypoxic–ischaemic (HI) brain injury can be caused after cardiac arrest or acute hypotension. It is a significant cause of mortality in adults as well as in newborns.[217] Upregulation of p75 in cholinergic interneurons in mouse striatum after focal cerebral ischemia, is found to exert a neuroprotective effect in adult rat models of middle cerebral artery occlusion. [217,240] This highlights the role of p75 in HI brain injury and stroke. In another study, blocking p75 and its related Nogo co-receptor promotes neuronal survival in mouse models.[230,241] Several other studies propose the significant role of p75 and of neurotrophins in cerebrovascular disease pathology.[242,243]

p75 and spinal cord injury (SCI)

The lack of effective therapies for SCI, stresses the need for novel targets for therapeutic intervention. Myelinating oligodendrocytes have been identified as a target that can improve functional recovery after SCI, since increasing survival of oligodendrocytes could potentially spare many more axons.[244] The p75 is a crucial factor for the death of oligodendrocytes following spinal cord injury, a mechanism mainly mediated by pro-NGF.[30] In response to myelin inhibitory molecules, p75 was shown to act as a co-receptor for NgR and thereby activate RhoA.[208,217] Studies have focused on the development of small molecules that cross rapidly the blood–brain barrier, to specifically block p75.[245,246]

p75 and Schizophrenia

Schizophrenia is a mental disease manifested by hallucinations, delusions and disordered thought, as well as impairment in cognitive functions such as attention and memory.[247,248] BDNF signaling has been suggested to contribute to the pathophysiology of schizophrenia.[230] A study has shown that a large proportion of schizophrenia patients had the V66M polymorphism in pro-BDNF, a polymorphism known to affect BDNF secretion and short-term episodic memory located at hippocampus.[249,250] Pro-BDNF is known to interact with p75 and to facilitate Long-Term Depression (LTD) and Long-Term Potentiation (LTP). Previous work has emphasized that the interactions between BDNF and p75, as well as p75 and Lingo-1, are critical for modulating learning and cognitive function which are attenuated in schizophrenia.[247,251,252]

1.6 Neurotrophin mimetics

The ability of NTs to affect the survival or apoptosis of neuronal cells, as well as their reduced expression in some neurological conditions, makes them potentially interesting molecules for the treatment of neurodegenerative diseases.[253–255] Attempts to use them as therapeutics have shown difficulty of NTs to cross the blood-brain barrier (BBB) and target the diseased tissues, while they can only be administered with invasive procedures and cause side effects.[256–265] To remedy this, small molecule NT mimetics that can elicit similar to NT function, have been explored as an alternative and are discussed here.

Previous studies have investigated the ability of small molecules to bind to p75 receptor and initiate p75-related signaling. Specifically, compounds EVT901, LM22A-24, LM11A-31 and THX-B have been shown to bind p75 and decrease cell death of different types of neurons.[242,266,267] Also, compound BNN27 has been also detected to activate p75 and hinder neuronal apoptosis.[268] The latter, as well as its natural analogue dehydroepiandrosterone (DHEA) are TrkA agonists and can rescue neuronal cells avoiding hyperalgia.[269,270] Analogues of BNN27, ENT-A010 and ENT-A013, have been identified within the EuroNeurotrophin consortium as selective agonists of TrkA,[271,272] while ENT-A011 is a selective agonist of TrkB.[273] BNN20 has anti-apoptotic, antioxidant, and anti-inflammatory effects via TrkB signaling.[274] Other agonists of TrkA, the gambogic amide, MT2, talaumidin, the peptidomimetic D3 and Carvacrol (CARV) can rescue neuronal cells from apoptosis, enhance survival and neurite outgrowth.[269,275–279] Agonists of TrkB, such as a peptide mimicking BDNF, the dipeptide GSB-106, compounds LM22A-4, deoxygedunin and 7,8-dihydroxyflavone (7,8-DHF), have been also shown promote neuronal survival, promote axon regeneration and prevent cell death in neurodegenerative disease models.[280–286]

1.7 Computational approaches on neurotrophins and mimetics

The elucidation of the activation mechanism of NT receptors remains challenging, despite the wealth of experimental data available regarding the functions and roles of receptor sub-domains. The complexity arises partly due to the inherent localization of these transmembrane receptors within membrane compartments, posing limitations for study using conventional structural biology techniques. Moreover, the intricate nature of their signaling cascades, spanning both survival and apoptotic pathways, presents obstacles in fully comprehending their precise responses to external stimuli. Similarly, the mechanisms underlying the activation or modulation of NT receptors by existing NT mimetics remain poorly understood. Consequently, the ongoing debate pertains not only to the mode of action, whether they function as direct or indirect modulators of neurotrophin receptors, but also to their precise effects.[287]

Computational methodologies are frequently employed to elucidate processes that are challenging to explore experimentally, primarily due to constraints in spatial and temporal observations. Among the prevalent computational techniques utilized for investigating biomolecules and their dynamic behaviors, Molecular Dynamics (MD) simulations hold prominence. In a study examining the stability of complexes, MD simulations were applied to model the binding of TrkA-D5 in complex with peptide mimetics of the N-terminal loop of NGF, which act as TrkA agonists.[288] The simulations highlighted specific peptide residues forming salt bridges with TrkA, implicating their role in the binding process.[288] Additionally, all-atom simulations of the TrkA-D5/NGF complex, coupled with Poisson-Boltzmann electrostatic calculations, revealed the presence of water-mediated hydrogen bonds between NGF and TrkA, potentially influencing the overall dynamics of the complex.[289]

MD simulations of the N-terminal region of the TrkA-JM in proximity to a membrane demonstrated the penetration of three residues into the membrane, in a conformation of this disordered region that was stabilized through interactions with PIP_2 lipids.[290] The resulting reduction in the flexibility of the JM domain suggests a potential role in TrkA activation. MD simulations together with free energy calculations have been also performed to investigate the mechanisms underlying allosteric TrkA-kinase inhibitor binding.[291] Simulations were also applied to find possible ATP-binding sites in the TrkA-NGF and p75-NGF complexes.[292] Simulations of the TrkA and p75 TM domains revealed that p75 binding to TrkA leaves TrkA-TM residues exposed for engagement in the active state of TrkA-TM, suggesting a possible mechanism for the high-affinity binding sites of NGF in TrkA in the presence of p75.[293]

MD simulations have shown that the TrkB-TM homodimer can be stabilized at a 20% membrane cholesterol concentration. Conversely, lower and higher cholesterol concentrations led to unstable arrangements.[294] Another MD simulation study by the same researchers disclosed that cholesterol might be possible to bind to the reversed cholesterol-recognition amino acid consensus (CARC) motif of TrkB-TM.[295] Experimental verification of cholesterol binding was established through mutagenesis studies.[294] Docking of antidepressant (fluoxetine) and psychedelic drugs to TrkB-TM determined specific amino acids as crucial for binding, and these findings were experimentally validated with point mutagenesis.[294] Simulations of the TrkB-TM/fluoxetine complex within membranes demonstrated that fluoxetine can stabilize the helices in a configuration that does not depend on cholesterol levels.[294] In another study, it was reported that psychedelic drugs can also bind to the TrkB-TM domain, on distinct but partially overlapping sites from the antidepressant drugs.[296]

In addition to MD simulations, various other computational techniques have been employed for the investigation of NTs and NT receptors. Normal mode and dynamical network analysis on the TrkA-D5/NGF-R221W complex showed that the point mutation on NGF can attenuate the collective motions and diminish the coupling of the complex.[297] Such alterations may contribute to the observed reduction in signal transduction associated with nociception. Quantum mechanical calculations suggested that the N-terminal TrkA-EC can bind a zinc ion.[298] Additionally, metadynamics simulations were utilized to reconstruct the free energy surface of the TrkA-EC/NGF complex.[298] Finally, molecular docking and MD simulations have been used to investigate the binding of DHEA and BNN-27 small molecules to TrkA and p75.[268,270]

1.8 Scope of the thesis

As mentioned before neurotrophin mimetics can offer a solution to the poor pharmacological profile of NTs and be used as a treatment for neurological disorders. The EuroNeurotrophin ITN project,[299] in the context of which this thesis has been carried out, was focused on the molecular modeling and computer-aided design of small organic molecule NT mimetics. This thesis contains the computer-aided drug design work on the DHEA-analogues that were tested in the consortium. This will be presented in chapter 3, right after the introduction of the introduction of the methods that I employed in the thesis in chapter 2. Chapter 3 also contains the screening of small-molecule fragments from the UNICAEN library of molecules, as well as mechanistic studies of the compounds and their interaction with the NT receptors and the cell membrane. Since the molecular basis of NT receptor activation is still unknown, computational studies were performed within the EuroNeurotrophin consortium to elucidate the receptor activation, which can further guide small-molecule design targeting specific mechanisms. In this thesis, the p75 NT receptor has been investigated. Chapter 4 will present the glycosylation effects on p75-EC domain, while chapter 5 will present the homodimerization states of p75-TM helical domains in micelles and bilayers. Finally, chapter 6 will present the modeling of the full-length glycosylated p75 structure bound to a NT and its simulation in a complex neuronal membrane model. Conclusions about the NT mimetics and the mechanism of action of the p75 receptor will be finally discussed.

2 Introduction to computational methods

2.1 Introduction to molecular modeling

The term molecular modeling pertains to the construction of models and usage of computation to study the structure and function of molecular systems. Even though simple molecular modeling studies can be performed without the usage of computer, on small systems, state of the art computational methodologies have allowed for the study of much larger and complex systems. Molecules consists of atoms which are further split in electrons and nuclei. The explicit incorporation of electrons in mathematical models is dealt by quantum mechanical methods, which are limited though by the size of the molecular system that can be used in calculations. An alternative solution to this is the usage of molecular mechanics, which assumes that the energy of a system is a function of nuclei only. This becomes possible from the Born-Oppenheimer approximation, which explains that electron motion can follow the change of nuclear positions, due to the much smaller mass of electrons. Thus, each atom is depicted as a point charge centered at the atomic nucleus position. The interactions between atoms are modeled by a set of simple functions and parameters, such as Coulomb's law for the electrostatic interactions. These functions and parameters consist the force field and will be explained in more detail in the next section.[300–304]

2.2 Potential energy surface and force fields

The energy of a molecular system is described by the potential energy surface (PES) which dependents on all the possible atomic arrangements in a system. The PES can be broken down to several functional forms that describe the various types of interactions between two atoms. These functional forms comprise constants which change based on the atom pair, and the whole set of constants consists a molecular mechanics force field. The PES functional forms, also call force field terms, consist of bonded and non-bonded terms based on whether they describe the interaction between covalently attached or not atoms, respectively (Figure 2.1). The bonded terms contain the stretching of bonds, the angle bending, the rotation around single bonds, called torsion, as well as the out of plane movement of one atom out four bonded atoms, called improper torsion (Figure 2.1 A-D). The non-bonded terms are used for the description of the electrostatic and van der Waals interactions (Figure 2.1 E-F).

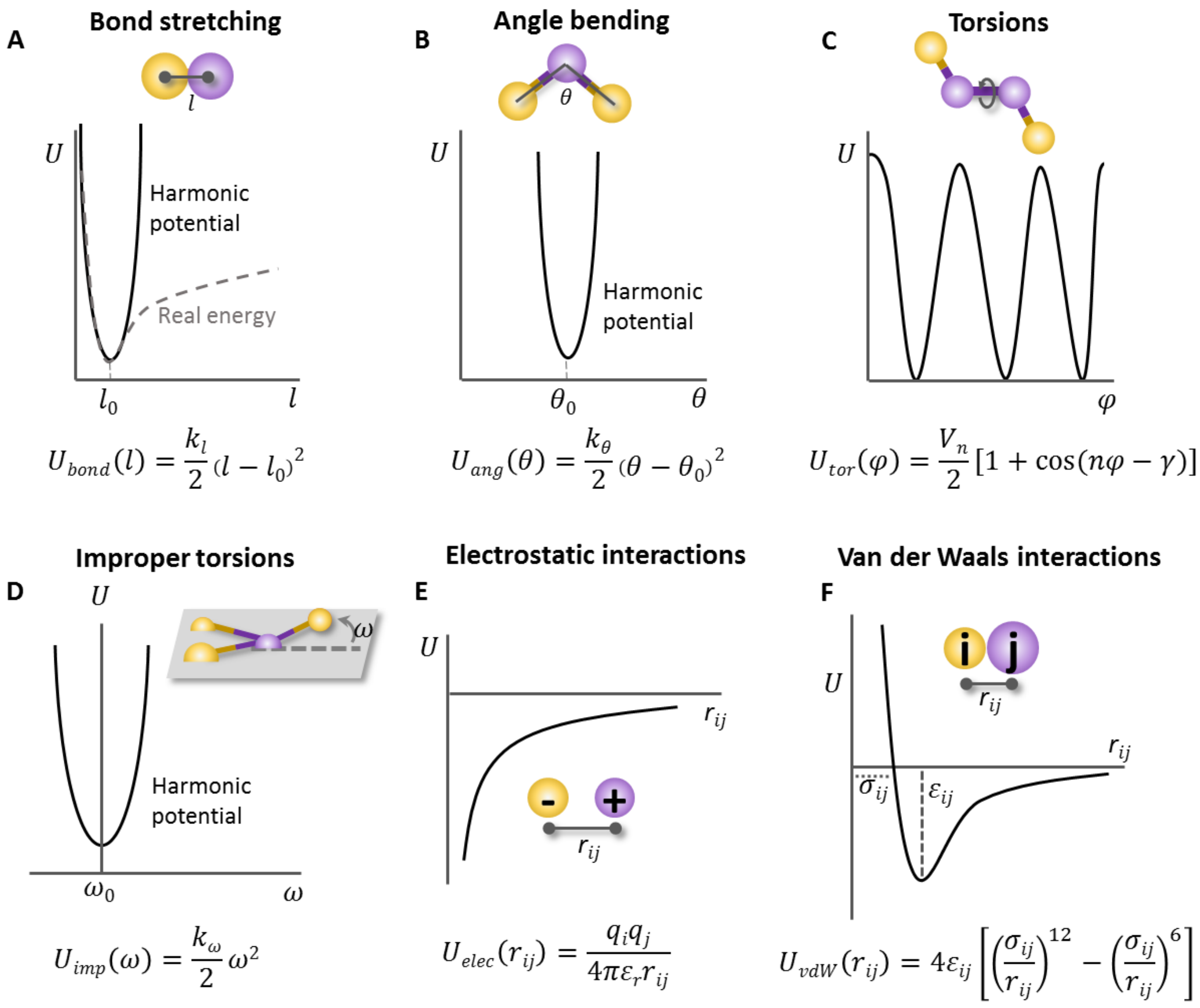

Figure 2.1: Set of most commonly used mathematical models to describe the interactions among atoms in molecular force fields. The functions can describe bonded (A)-(D) and non-bonded interactions (E)-(F). Figure adapted from Christina Athanasiou.[72]

The movement of the stretching of a bond between two atoms can be described mathematically by the simple model of a harmonic potential, or otherwise Hooke's law which can reasonably describe the behavior of the bond energy close to the equilibrium bond length (Figure 2.1 A). The bending of an angle among three atoms and the improper torsions of four atoms in the same plane can also be described by a harmonic potential (Figure 2.1 B,D). The dihedral torsions, i.e. the rotation around a bond can be described by a cosine function due to its periodic nature (Figure 2.1 C). Finally, the non-bonded terms of electrostatic and van der Waals interactions are modeled by Coulomb's law and the Lennard-Jones potential (Figure 2.1 E,F).

A major advantage of molecular mechanics force fields is their additive behavior, i.e. the possibility to develop parameters for molecules or part of molecules separately and then use them in combination on complex systems consisting of multiple molecules. This has allowed the modeling of more and more complex molecular systems with a variety of chemical components. This can lead to quite large systems with many degrees of freedom to be calculated corresponding to the interactions between all the particles in the system. Most force fields describe the interactions between atomic particles, and thus they are called atomistic, or all-atom, force fields. However, the calculation of all the interactions among atoms in a large molecular system can be computationally intensive reaching the limits of the available computational resources at a researcher's disposal. A solution to this can be offered by the so called coarse grained (CG) force fields, which model several atoms together as a single particle. This reduces the number of particles in a system and thus the degrees of freedom allowing for the modeling of larger systems or simulation of longer timescales. A deeper explanation of how simulation methods work will follow in the next sections.

One of the most widely used CG biomolecular force fields is the Martini force field. This was originally developed for lipids and thus membrane systems, but was soon expanded for the modeling of other biomolecules, such as proteins, DNA, RNA, sugars, even small molecule therapeutics.[305–310] The Martini force field usually models four heavy atoms as a single bead, allowing this way a significant reduction of the number of atoms in a system. One of its many applications has been the study of transmembrane helix dynamics from cell surface receptors in multiple lipid environments, such as micelles and membranes.[311–315] Therefore, it was chosen also for the study of the transmembrane domain of p75 NT receptor in this thesis. At the time that the simulations of this thesis were performed the Martini 2.2 was the latest version of the force field.[316] However, in the meantime of the PhD, a new version came out, the Martini 3, with improved parameters for bead interactions as well as some advanced features, such as the possibility to model hydrogen bonds.[317] One of the caveats of Martini 3, as described in a collaborative manuscript, was an imbalance in the protein-water Lennard-Jones interactions which does not allow transmembrane helices to be incorporated in the lipid environment of self-assembled micelles and membranes. We solved this issue by a down-scaling factor of 0.1 of the Lennard-Jones interactions between protein and water.[318] This allowed us to use it for the simulation of the transmembrane helices of NT receptors.[51] However, in this thesis I will be focusing only in the simulations with Martini 2.2, which I have performed.

After having discussed the different terms of force fields and the different levels of representation that they can offer, the next step is to explain how force fields can used in molecular dynamics (MD) simulations. The various steps and main methodological concepts of MD simulations will be presented in the subsequent sections.

2.3 Energy minimization

The PES of a molecular system consists of several hills and valleys. When performing molecular mechanics calculations in a molecular system, an important first step is bringing the system at a minimum point in the potential energy surface, i.e. at the bottom of a valley. This makes the system stable and any movement away from the minimum leads to configurations of higher potential energy. For location of minima in the PES, also called stationary point, energy minimization algorithms are used which are able to minimize the potential energy function. In molecular mechanics that deal with large atoms, calculation of the PES is very challenging as it depends on a high number of variables, which are the Cartesian coordinates of all the atoms, or more generally particles, in a system. On the other hand, calculating the potential energy at a single point is simple. Thus energy minimization algorithms work by iteratively evaluating the potential energy at different points of the PES, by moving the system by specific steps. The mode of movement in the PES can differ among the various energy minimization algorithms. Also, due to the high number of variables, numerical rather than analytical methods are used, which modify the atomic coordinates to produce lower energy configurations until a minimum is reached.

Two commonly used algorithms, which are also employed in this thesis, are the *steepest descent* and the *conjugate gradient* methods. The steepest descent method works by calculating the potential energy at the initial point, and at points away from it by a small step and moves the system in the direction where the energy decreases by the maximum. Thus it moves downhill from the steepest path. A limitation of steepest descent is that each step is orthogonal to the previous, even if it is not the optimum route to the minimum, which has as a consequence to take a lot of time to converge to the minimum once it is close to it. On the other hand, the conjugate gradient method is able to take successive steps that are “conjugate”, and so not in right angles to each other, avoiding this way the oscillatory movement that steepest descent demonstrates in long narrow valleys. It is common to combine the two algorithms, starting with a steepest descent calculation to move fast close to the minimum, and the use conjugate gradient to converge to it.

2.4 Molecular dynamics simulations

Energy minimization methods that were just discussed allow the generation of single configurations of a system of minimum energy. This can be potentially used for the estimation of thermodynamic properties through statistical mechanics methods, given that all the energy minima in the PES of a system can be identified. This is very difficult, if not impossible for the large biomolecular systems of interest. Simulation methods can enable the study of such systems by considering only a small unit of the real system which is replicated. The simulation of such units of the system can allow the calculation of structural ensembles and thermodynamic properties. Also, the time dependent behavior of a system can be examined to obtain transitions from one configuration to another. The latter is possible with molecular dynamics (MD) simulations, which have been employed in the current thesis and will be discussed here.

As explained earlier, the potential energy of a system can calculated with a force field, giving the energy experienced by each atom or particle. This has as a consequence the action of a force on every particle which can be calculated by differentiating the potential energy on that particle with respect to the Cartesian coordinates of the particle. From the Newton’s second law, the acceleration can be calculated from the force with second-order ordinary differential equation. Solving that equation can afford the new coordinates of the particle and the trajectory at which the system evolves with time. The integration of the second-order ordinary differential equations for each particle is done numerically and two common algorithms that are used for such purpose are the *leapfrog* and the *Verlet*.

In the leapfrog algorithm the velocities are first calculated at $t+\Delta t/2$, where Δt is the integration time step, usually equivalent to one or two femtoseconds. The initial velocities are then used to calculate the positions of the particles at $t+\Delta t$. Therefore, this algorithm gives velocities that leap over the positions and positons that leap over the velocities. The Verlet algorithm takes the position and acceleration at time t as well as the position at time t-Δt to calculate the new position at t+Δt. This way the Verlet algorithm provides the positions, velocities and accelerations simultaneously at each time step.

When running an MD simulation several steps need to take place. First, the appropriate force field for a particular system needs to be chosen. Then, an initial model, i.e. the initial coordinates of all the atoms, of the system has to be created with a configuration which is close to state of interest, e.g. active or inactive state of a protein. An energy minimization step is then conducted to bring the system to a local minimum and thus start the simulation from a stable configuration. Subsequently, an equilibration phase takes place, which might consist of several steps, where the system is gradually heated to room or physiological temperature for biomolecular systems, and is allowed to relax in the statistical ensemble of choice. It is common for the heating step to be done in the NVT ensemble, where the number of particles (N), the volume (V) and the temperature (T) remain constant, and then switch to the NPT ensemble, where the number of particles (N), the pressure (P) and the temperature (T) are constant. Several thermodynamic and structural properties are usually monitored during equilibration to ensure stability. Next, the production phase is performed, for biomolecular systems most often in the NPT ensemble, and the dynamical behavior of the system is then analyzed at the time intervals, or frames, in which the system coordinates are saved. An initial first analysis is to examine how much the system changes during the production simulation from the initial configuration, or if any unexpected events take place. Finally, thermodynamic or structural properties of interest are calculated to answer specific biological or chemical questions.

Accurate calculation of thermodynamic properties, such as the free energy, requires adequate sampling of all configurations in the phase space. Ideally, in MD simulations all these configurations could be sampled, but instead mostly lower energy states are visited leading to poor convergence of the simulations and inaccurate calculation of the thermodynamic properties. A way to increase sampling in conventional MD simulations is to increase the simulation time or run multiple replica simulations starting from different initial velocities or even configurations of the system. This can require significant computational resources and still might not guarantee increased sampling. A solution to this if offered by *enhanced sampling* methods which increase the energy of the system of bias it to visit regions of the phase space of higher energy.

Metadynamics is one of the most commonly used enhanced sampling methods and it works by depositing energy in the form of Gaussian potentials at specific reaction coordinates, or collective variables (CVs), that constitute the slow degrees of freedom of the system.[319] This way the slow motions can be sampled at shorter simulation times as the system is forced to explore them, reducing the simulation time, or simply making it possible to sample configurations that otherwise would be energetically inaccessible. Metadynamics gives also a direct way to calculate the free energy along a CV, as this corresponds to opposite of the sum of Gaussian potentials deposited during the simulation. It is also possible to assess convergence, as eventually the system appears to oscillate at the space of the biasing CV and demonstrate a diffusive behavior, i.e. sampling of all physically possible CV values, indicative of convergence. There is also the possibility to calculate the free energy as a function of other variables than the biasing CV, after taking into account the bias potential that was used to access the different variable values, through a method known as *reweighting*.

One limitation of the conventional metadynamics methodology is the difficulty to reach convergence as, once diffusion over CV space is achieved, it keeps depositing Gaussian potentials which lead to wrong free energy estimation. A solution to this was offered by *well-tempered metadynamics*,[320] which has been also used in this thesis. In this metadynamics variant, the height of the Gaussian potentials decreases in regions of the CV space that have been already sampled. Once the height is very small, this is an indication of convergence and the simulation can be stopped. As it will be explained in chapter 5, in this thesis, well-tempered metadynamics has been used with the coarse grained Martini force field to study the dimerization free energy of the p75 transmembrane domain, as shown previously for the Epidermal Growth Factor Receptor (EGFR).[314]

2.5 Molecular docking

In chapter 3 of this thesis, I have performed structure-based design of small molecule neurotrophin mimetics. For this purpose, a first step was to predict the small molecule - receptor complexes. This task is usually tackled computationally with molecular docking. This is a technique that, given a specific protein structure and a binding site on it, it creates conformations, or poses, of a ligand attached to the binding site, also called pocket. This is achieved by a series of steps that sample multiple orientations and conformations of the ligand in the protein pocket and then scores each one of the ligand configurations with a scoring energy function. The molecular docking tool that I used in this thesis is the Glide tool of the Schrodinger Suite.[321–324] This docking algorithm treats the protein as a rigid body and the ligand as flexible allowing rotations around rotatable bonds. The geometrical and physical properties of the protein binding site, such as the position of the hydrogen bond donors and acceptors, are represented by a 3-dimensional grid, and the ligand shape and size are compared to that grid. The different ligand poses are generated and filtered through a series of hierarchical steps. These are different for the standard precision (SP) and the extra precision (XP) protocols of Glide, with the first one employing an approximate positioning of the whole ligand structure in the pocket, while the second one positioning first the more rigid parts of the ligand, such as rings, and then growing it bond-by-bond. The two protocols also differ in their scoring functions, with the XP docking score penalizing mismatches in the ligand-receptor complementarity. After the generation of the initial poses, the ligand-receptor complexes are first scored with the OPLS-AA force field,[325] and then energy minimized with the OPLS4 force field.[326] Finally, the poses are scored with the Glide docking score, which has several terms describing ligand-protein interactions, such as hydrogen bonds, electrostatic and can der Waals interactions, while it also takes into account desolvation effects.

3 Computational studies of neurotrophin mimetics

3.1 Introduction to neurotrophin mimetics

Neurodegenerative diseases (ND), like Alzheimer's Disease (AD) and Parkinson's Disease (PD), are prevalent in developed societies worldwide, without any existing cure. To combat this type of disease, neurotrophins (NT) – growth factor proteins which partake in different aspects of survival, development and function of neurons – have been tested as treatment of NDs, since low levels of NTs have been observed in some of them. Studies have shown NTs to be able to prevent or slow the progression of NDs,[253–255] which has led to the proposal of NTs as therapeutic agents. However the administration of NTs is restricted by their poor pharmacokinetic properties, their inability to penetrate the blood-brain barrier (BBB) – due to their size – and to selectively target the affected neurons.[261] To circumvent this, their administration has been performed via invasive procedures, such as intracerebroventricular (ICV) injection,[258,262] a practice which has been reported to cause side effects; most notably pain.[256,257,259,260,263–265] The aforementioned issues render the use of NTs as drugs prohibitive.

An alternative approach, which could address the shortcomings of NTs, is the development of small organic molecules that act as neurotrophin mimetics and potentiators, with favorable pharmacokinetic properties, i.e. the ability to penetrate the BBB and selectively target the proteins of interest, as well as ease of administration – all mainly due to their smaller size. Scientists from the EuroNeurotrophin (ENT) consortium have previously developed an agonist of TrkA and p75 NT receptors, called BNN-27, which is a C17-spiroepoxyl derivative of dehydroepiandrosterone (DHEA), and is able to promote neuronal survival.[268–270] The EuroNeurotrophin consortium focused on the development of novel derivatives of BNN-27, with the aim of achieving selectivity towards the NT receptors and improved potency and metabolic profile.

To aid in this goal, I performed molecular docking and physicochemical property prediction for the compounds designed by my collaborators, as well as designed novel compounds of my own, starting from a library provided by Prof. Christophe Rochais from the University of Caen Normandie (UNICAEN).

Furthermore, I investigated the mechanism of action of the steroidal derivatives through Molecular Dynamics (MD) simulations for the proposed binding sites and for possible membrane penetration.

3.2 Methodology

Lead compound binding site validation

Before starting the docking studies of BNN-27[269] analogues, I needed to replicate the proposed binding poses of BNN-27 in TrkA.[270] I used molecular docking to place BNN-27 in the two proposed binding sites in TrkA, sites 1a and 1b (Figure 3.2)[270] I employed the Protein Preparation Wizard tool (Schrödinger, LLC)[327] to prepare the protein structure prior to docking. The protein preparation procedure assigns bond orders, adds missing hydrogens, and creates disulfide bonds. Moreover, it performs and optimizes the hydrogen bond assignment. This optimization is done by re-orienting hydroxyl and thiol groups, waters, asparagines, glutamines and histidines, and by selecting the most fitting protonation state for histidines, aspartic acids and glutamic acids, and the most fitting tautomeric states for histidines (for a given pH value). Lastly, it removes unimportant waters (waters that do not form many hydrogen bonds with the protein and/or the ligand), and performs a restrained energy minimization of the structure.

Since the proposed binding sites are located in the interface of TrkA-D5 and NGF complex, I used the crystal structure of the human TrkA-D5:NGF complex (PDB ID: 1WWW). I prepared the structure using the aforementioned procedure, and I removed all waters. For the identification of possible binding sites, I used the SiteMap tool (Schrödinger, LLC).[328,329] SiteMap uses a grid-based method over the whole protein structure, and identifies empty space near the protein surface that can be a cavity. Afterwards, it characterizes the areas of these sites as hydrophobic or hydrophilic. In order to perform docking, a grid box needs to be generated over an area of the protein, to specify the binding site for docking. Since there is no native ligand bound in the crystal structures used, and because the sites identified by SiteMap tend to be large, I set up manually multiple different binding sites and sizes of them, by setting the Cartesian coordinates of the center each time.

I generated the grid box with the Glide software[321,330] and set the size so that ligands with length up to 20 Å can be docked, while an inner box for the placement of the center of the ligand had the default side length of 10 Å in x, y, z (except in cases where mentioned). While the receptor is kept frozen during docking, rotation of all hydroxyl and thiol groups inside the grid box was allowed. I performed docking with the 3 different docking protocols provided by Glide (Schrödinger Suite): SP (single precision),[321,330] XP (extra precision),[323] and IFD (induced-fit docking).[331–333] SP places the molecule as a whole in the binding site, while trying to optimize its position and energy score by performing translations and rotations of the whole molecule and of individual atoms. XP anchors the parts of the molecule with fewer degrees of freedom (e.g. individual rings or ring systems) to the specified binding site, and then builds the rest of the molecule rotatable bond by rotatable bond, while trying to optimize its position and energy score. IFD performs a softened-potential docking (van der Waals radii scaling) first, then adjusts the backbone and residue side chains of the protein, to accommodate the ligand pose, and then performs a final, regular docking to the adjusted binding site of the protein. The ligand sampling for all docking runs was flexible (changes in ligand conformation are allowed), and the force field used was OPLS3e. For site 1a, I performed multiple docking runs using different setups of the binding site and the protocols SP, XP or IFD, as can be seen in Table 3.1. For site 1b, the grid box was centered based on the pocket predicted by SiteMap, and the protocol followed was XP.

Table 3.1: Parameters for various docking runs in site 1a of 1WWW. (*) I set the grid box around selected residues: Tyr79, Thr81, Thr83, His84, Arg103 (NGF chain V), Ser19 (NGF chain W), His297, His298, Trp299, Asn349, Gln350 (TrkA-D5 chain X).

Docking run No.	Grid box center coordinates (Å)	Inner box dimensions (Å)	Glide protocol
1	(18,0 , 5,0 , 0,0)	10x10x10	SP
2	(18,0 , -2,0 , 0,0)	10x10x10	SP
3	*	10x10x10	SP
4	*	10x10x10	XP
5	(17,5 , -4,0 , 2,5)	15x10x11	SP
6	(17,5 , -4,0 , 2,5)	15x10x11	XP
7	(17,5 , -4,0 , 2,5)	8x7x9	SP
8	(17,5 , -4,0 , 2,5)	8x7x9	XP
9	(24,0 , 0,0 , 15,5)	10x9x13	SP (symmetric 1a)
10	(24,0 , 0,0 , 15,5)	10x9x13	XP (symmetric 1a)
11	*	10x10x10	IFD (no side-chain trimming)
12	*	10x10x10	IFD (with side-chain trimming)

I also tested the binding of BNN-27 to TrkB, to validate the low affinity with this target, as BNN-27 cannot activate the TrkB receptor. For the docking of BNN-27 to TrkB, I used the 1HCF crystal structure, which comprises the D5 domain of the extracellular part of TrkB receptor bound to NT-4 neurotrophin. First, I performed protein preparation again with the Protein Preparation Wizard tool. Then, I performed grid generation at sites 1a and 1b with the Glide software, where the binding pocket was specified and hydroxyl and thiol groups of the receptor in the pocket area were allowed to rotate. The binding pocket was defined by the center of mass of the residues that are given in the publication that describes binding sites 1a and 1b in TrkA.[270] I determined the corresponding residues in the TrkB structure by alignment of TrkB to the TrkA crystal structure. The residue matching between TrkA and TrkB is presented in Table 3.2. Then, I prepared BNN27 with the LigPrep[334,335] tool of Schrödinger, and performed docking to 1HCF crystal structure with the Glide tool.

Table 3.2: Identification of residues in sites 1a and 1b in the TrkB structure from superposition on TrkA.

Site 1a 1WWW (TrkA – NGF)	Site 1a 1HCF (TrkB – NT-4)	Site 1b 1WWW (TrkA – NGF)	Site 1b 1HCF (TrkB – NT-4)
Thr81	Lys91	Ile31	Leu33
His84	Gln94	Arg103	Arg114
Trp299	Trp301	Val321	Ile323
Leu348	Leu348	Asn323	Asn325
Asn349	Asp349	Asn355	Asn355
Glu350	Asn350	-	-

Steroid analogues with three-membered-17-spirocyclic substituents

I created a virtual library of 78 BNN-27 analogues with three-membered-17-spiro substitutions, designed for future synthesis by NHRF. I prepared the library with LigPrep, generating the E and Z isomers and the two different stereochemistries of the cyclopropyl moiety. I analyzed all ligands with QikProp[336] to compute their absorption, distribution, metabolism and excretion (ADME) properties (Table 3.3).

Table 3.3: Recommended QikProp property ranges for drug-like molecules.[336] Dipole: computed dipole moment of the molecule; donorHB: estimated number of hydrogen bonds that would be donated by the solute to water molecules in an aqueous solution (values are averages taken over a number of configurations, so they can be non-integer); acceptorHB: estimated number of hydrogen bonds that would be accepted by the solute from water molecules in an aqueous solution (values are averages taken over a number of configurations, so they can be non-integer); QPlogPo/w: predicted

octanol/water partition coefficient; QPlogHERG: predicted IC_{50} value for blockage of HERG K^+ channels; QPPCaco: predicted apparent Caco-2 cell permeability in nm/sec (Caco-2 cells are a model for the gut-blood barrier – QikProp predictions are for non-active transport); QPlogBB: predicted brain/blood partition coefficient (QikProp predictions are for orally delivered drugs so, for example, dopamine and serotonin are CNS negative because they are too polar to cross the blood-brain barrier); QPPMDCK: predicted apparent MDCK cell permeability in nm/sec (MDCK cells are considered to be a good mimic for the blood-brain barrier – QikProp predictions are for non-active transport); # metabolites: number of likely metabolic reactions.[1]

QikProp	Range Value
Dipole	1.0 – 12.5
DonorHB	0.0 – 6.0
AcceptorHB	2.0 – 20.0
QPlogPo/w	-2 – 6.5
QPlogHERG	< -5
QPPCaco	< 25 poor > 500 great
QPlogBB	-3 – 1.2
QPPMDCK	< 25 poor > 500 great
# metabolites	1 - 8

I docked the library of molecules to the following crystal structures: the TrkA-D5 receptor homodimer in complex with NGF homodimer (PDB: 1WWW),[337] and TrkB-D5 receptor homodimer bound to NT-4 homodimer (PDB: 1HCF).[338] I prepared all structures with the Protein Preparation Wizard of Schrödinger. I docked the compounds to sites 1a and 1b on the TrkA and TrkB receptors. For docking, I used the SP and XP protocols of Glide. The best compounds from XP, based on their docking scores, were subjected to Induced Fit Docking (IFD). IFD allows for some flexibility of the residues in the pocket, resulting in better accommodation of the ligands. I chose one IFD pose for further analysis in a Molecular Dynamics (MD) simulation. I used the Desmond[339] tool (Schrödinger, LLC) to run the simulation. I solvated the system consisting of the TrkA:NGF complex with the molecule bound, using the TIP3P water

---

[1] The following metabolic reactions contribute to the # metabolites descriptor: 1) aromatic OH oxidation, 2) enol oxidation, 3) benzylic-like H → alcohol, 4) allylic H → alcohol, 5) secondary alcohol → ketone, 6) primary alcohol → acid, 7) tertiary alcohol E1 or SN1, 8) amine dealkylation, 9) ether dealkylation, 10) pyridine C2 hydroxylation, 11) aniline NH → NOH or NCOR, 12) low IP—easily oxidized, 13) alpha hydroxylation of cyclic ether, 14) sulfoxide → sulfone, 15) alpha hydroxylation of carbonyl, 16) alpha, beta dehydrogenation at carbonyl, 17) thiol SH → SSR, SR, 18) para hydroxylation of aryl, 19) aryl sulfide → S=O, 20) reduction of aryl nitro to amine, 21) oxidative deamination of primary amine.

model, in an orthorhombic box with size 10 Å from the solute to the end of the box and I added Na^+ and Cl^- ions for neutralization. I ran the simulation in the NPT ensemble for 50 ns at temperature 310 K and pressure 1.01325 bar. I used the OPLS3e force field. I used the default Nose-Hoover and Martyna-Tobias-Klein thermostat and barostat, respectively.

Steroid analogues with six-membered-17-spirocyclic substituents

I created a virtual library of 18 BNN27 analogues with six-membered-17-spiro substitutions, designed for future synthesis by NHRF, and prepared it using LigPrep. This resulted in 24 output molecule structures. I docked all analogues to the frame at 26 ns of the aforementioned MD simulation of the TrkA:NGF complex, which has a more spacious binding pocket of site 1b than the initial crystal structure. I centered the grid box at (18.0 , -2.0 , 27.0), I set the inner box edge length to 10 Å in all x, y, z directions, and selected that rotation of all hydroxyl and thiol groups be allowed. I carried out docking using the SP and XP protocols of Glide. I selected fifty poses to be sent to post-docking minimization, while a maximum of five was set to be reported per input ligand. The output poses from the SP run were 110, while from the XP run were 96. From the poses of the two docking runs, I did not consider for analysis poses that were outside of the pocket, poses that had exposed methyl groups, and poses that were inverted (the six-membered-17-spiro substituents were outside the pocket). After visual inspection of the poses from the two docking runs, I identified four molecules that had plausible binding modes in both runs and deemed them suitable to be prioritized in organic synthesis.

Fragment compounds

I performed virtual screening of a library of 9200 compounds synthesized in UNICAEN provided to me as a structure file. The screening involved several steps (Figure 3.1). In the first step I filtered the molecules for a maximum molecular weight of 300 g/mol. For this I used the Canvas tool (Schrödinger, LLC),[340,341] and it resulted in 3656 output molecules. Then, I used LigPrep for the generation of protonation states at pH = 7.0 ± 0.5 and possible stereoisomers, setting a maximum of 100 stereoisomers per ligand to be produced, which satisfies up to 6 chiral centers. The number of output ligands was 7114. Subsequently, I performed docking of the ligands in site 1b of the crystal structure of the TrkA-D5:NGF complex (PDB ID: 1WWW). I set the grid box center coordinates to (x, y, z) = (15, 0, 22) (1WWW crystal structure coordinates), which is found in site 1b, and I selected the option of 2 output poses per ligand. The number of output poses from this step was 18633. I discarded poses with a docking score higher than -3 kcal/mol, and this resulted in 8806 poses, which were subjected to a QikProp run for calculation of physicochemical properties. I applied the following filters to the 8806 poses: (1) logP ≤ 3.5, (2) number of H bond acceptors greater than 1 but not more than 4, (3) maximum number of rotatable bonds was set to 4, (4) maximum number of H bond donors was set to 4. As QikProp cannot process molecules that have Boron, these molecules were not considered for further analysis. This resulted in 3668 poses, from which I kept only the poses that were docked precisely in site 1b, leading to 832 poses. Subsequently, I performed structural fingerprint similarity and clustering using Canvas. For the calculation of the fingerprints, I chose the dendritic fingerprint type, as well as the Daylight atom types and 64-bit precision. For the similarity, I used the Tanimoto index to compare all the poses against themselves. For the clustering, I used the average linkage method and 179 clusters were created. After visual inspection of the poses within each cluster, as well as consideration of the docking scores, I selected 21 molecules as potential hits.

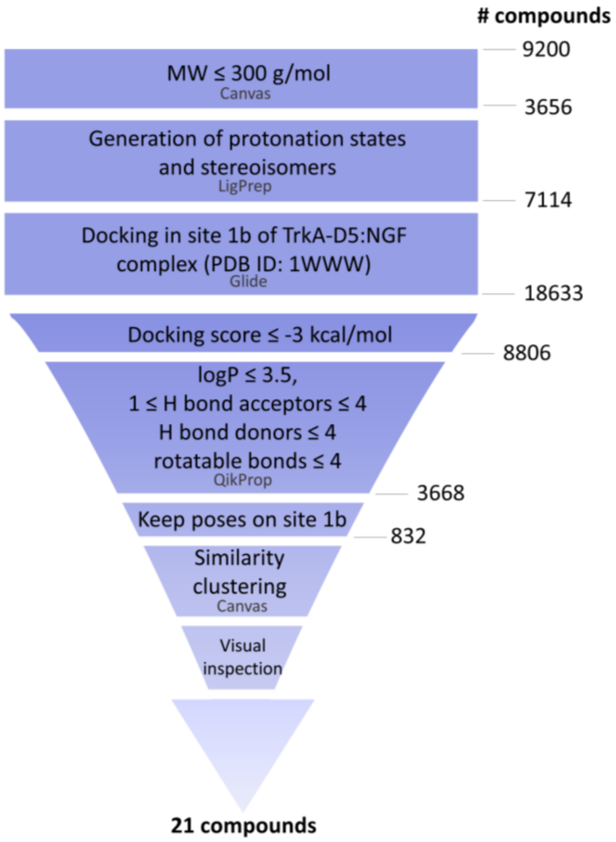

Figure 3.1: Virtual screening steps of a library of 9200 fragment compounds synthesized in UNICAEN.

Mechanistic studies

For a set of compounds that were verified experimentally to be active against TrkA and TrkB I performed an additional, more extensive series of mechanistic studies with MD simulations. The mechanistic studies were done in collaboration with Christina Athanasiou[72] from the Molecular and Cellular Modeling (MCM) group at the Heidelberg Institute for Theoretical Studies (HITS), who did all the mechanistic studies on TrkB, while I did the calculations on TrkA.

For this purpose, we started by creating the models of the protein domains where the compounds were possible to bind. I used the X-ray structure of TrkA-D5 homodimer bound to the NGF homodimer (PDB ID: 1WWW)[337], while for TrkB the TrkB-D5 homodimer bound to the neurotrophin-4/5 (NT-4/5) homodimer (PDB ID: 1HCF)[338] was used by Christina Athanasiou. I modeled the following missing residues with the AutoModel class of MODELLER v.9.23[342] : (1) on NGF: S122, P182 – S187, A237 – A241 (residue numbers correspond to the UniProt sequence of human NGF, UniProt ID: P01138), while Christina Athanasiou modeled the following missing residues: (2) on NT-4/5: : N145 – G150 and G207 – A210 in chain A and G81 – E84, N145, R209 and A210 in chain B (residue numbers correspond to the UniProt sequence of human NT-4/5, UniProt ID: P34130), (3) on TrkB-D5 the 1st 3 residues were mutated from the cloning to the wild-type sequence. On NGF, I built the missing loop P182 – S187 with the known specific conformation from crystal structures and I used the structure of human NGF from PDB ID: 5JZ7[343] as a template with homology modeling and the AutoModel class of MODELLER v.9.23. Christina Athanasiou did a similar approach for the N145 – G150 loop on NT-4/5 for which I used the structure of human NT-4/5 from PDB ID: 1B98[344] as a template.

Once I had the protein models without any missing residues or atoms, I prepared them with Protein Preparation Wizard[345,346] of Schrödinger Suite v.2020, which assigns bond orders, adds hydrogens, creates disulfide bonds, assigns protonation states at pH 7 with PROPKA,[347] optimizes the H-bond network and performs an energy minimization with the OPLS3e force field[348] with restraints on heavy atoms at mean squared deviation (RMSD) not higher than 0.3 Å. For subsequent docking studies, apart from the TrkA-D5 and TrkB-D5 models, we also used the TrkA and TrkB transmembrane (TM) helical dimers, which are presented in chapter 4, for molecular dynamics (MD) simulations with the compounds. Again, I ran simulations with TrkA and Christina Athanasiou ran the simulations with TrkB.

Molecular docking of experimentally determined BNN-27 analogues

I performed docking calculations of the compounds studied experimentally in the EuroNeurotrophin consortium to the TrkA receptor with NGF bound. Similar calculations were run for TrkB bound to NT-4/5 by Christina Athanasiou.[72] The first step was to identify possible binding sites in the TrkA-NGF model structure, for which I used the SiteMap tool[328,349,350] of the Schrödinger Suite. Several pockets were predicted and I chose sites 1a and 1b, as it was previously suggested by STD-NMR that BNN27 binds at the interface of TrkA and NGF,[270] and the compounds are analogues of BNN27 and are shown in Table 3.4. These compounds were synthesized by Alessia Latorrata, and tested experimentally on functional and cell assays by Thanasis Rogdakis and Despoina Charou in the EuroNeurotrophin consortium.

Table 3.4: Neurotrophin mimetics discovered by the EuroNeurotrophin consortium. Experimental validation with functional and cell assays done by Thanasis Rogdakis and Despoina Charou: phosphorylation of TrkA (pTrkA), AKT (pAKT) and ERK1/2 (pERK1/2) and cell survival in TrkA expressing cells. Similar for TrkB expressing cells. Data provided by Alessia Latorrata, unpublished except for ENT-A011[273] and ENT-A013E/Z[272].

		TrkA				TrkB		
Compound code	**Structure**	**pTrkA**	**pAKT**	**pERK1/2**	**Cell survival**	**pTrkB**	**pAKT**	**Cell survival**
BNN-27	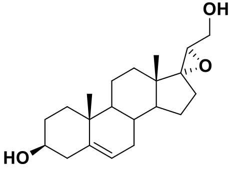	yes	yes	yes	yes	no	no	no
ENT-A011[273]	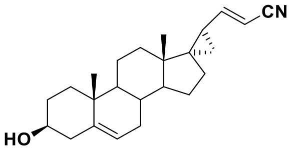	no	no	no	no	yes	yes	yes
ENT-A013E/Z[272]	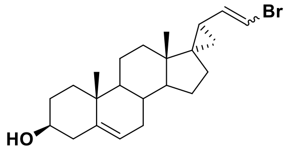	yes	yes	yes	yes	no	no	no
ENT-A040	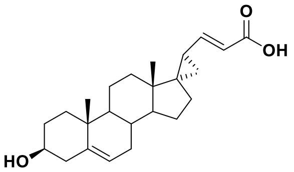	yes	yes	yes	yes	no	no	no

ENT-A044	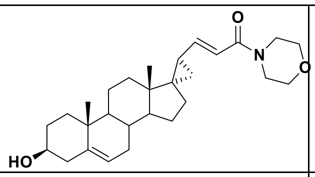	no	no	no	no	yes	yes	yes
ENT-A045	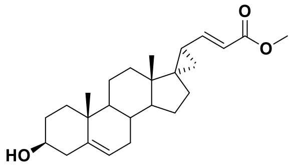	no	no	no	no	yes	yes	yes
ENT-A061	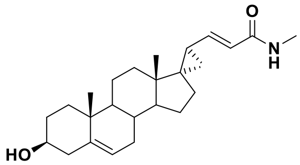	no	no	no	no	yes	yes	yes

For the docking calculations, I built grids describing the physicochemical properties of the protein pockets 1a and 1b in both symmetric sites of the TrkA-NGF dimer. During grid preparation, I defined the serine, threonine and tyrosine residues to be able to rotate their hydroxyl groups to form H-bonds during the docking calculations. I built the grids with the Glide tool[321,323,324,330]of the Schrödinger Suite. Then, I built the 3D structures of the small molecules in Table 3.4 with Maestro[351] and prepared them with the LigPrep tool[352] of the Schrödinger Suite. I performed docking calculations in both symmetric sites 1a and 1b of the TrkA-NGF dimer with the standard precision (SP) and extra precision (XP) protocols of Glide[321,323,324,330] of the Schrödinger Suite. I also performed induced fit docking in site 1a, which is more confined, with the Induced Fit Docking (IFD) tool[331,332,353,354] of the Schrödinger Suite. Similar steps were done by Christina Athanasiou for the docking of the compounds on the TrkB-NT-4/5 complex. I also docked compounds ENT-A011, ENT-A013E/Z and BNN-27 at the interface of the TM helices of TrkA, while the same was done on TrkB by Christina Athanasiou. I visualized all structures with VMD v.1.9.3.[355]

Molecular dynamics (MD) simulations of experimentally determined BNN-27 analogues

I ran MD simulations of compounds ENT-A011, ENT-A013E/Z and BNN27 bound to TrkA, while the same was done on TrkB by Christina Athanasiou. Specifically, I simulated the complexes of these compounds with the TrkA-D5/NGF complex and the TM helices of TrkA, which I created with the previously mentioned docking calculations. The summary of simulations is shown in Table 3.5. For the models of the compounds bound in the EC-D5 domain of TrkA, I tested both symmetric sites of 1a and 1b pockets. For the models of the compounds bound in the TM domain of TrkA, I used as starting configurations the docked compounds at the interface of the active TrkA-TM helices, while I started some simulations with 10 compounds placed around the inactive state of the TrkA-TM helices. I did this because it has been suggested that the drug fluoxetine acts through binding at the interface of the active state of the TM helices of TrkB,[294] while there is no information about how small molecules might bind in the inactive TM helices of TrkA or TrkB. I also tested the effects of the lipid environment and I tried both POPC or POPC:cholesterol 6:4 membranes. The exact simulation protocol for the EC domain simulations is presented in detail in chapter 4, while the simulation protocol for the TM systems is the same as the one presented in chapter 6 for the full-length p75 system. For each system, 3 replica simulations of ~300 ns were run. I did all structural visualization with VMD v.1.9.3.[355]

Table 3.5: Summary of simulations with small molecules bound to the EC and TM domains of TrkA and TrkB. When distance restraints were applied in the TM helices it is denoted as "Dist. Rest.". For each system, 3 replica simulations of ~300 ns were run.

Receptor	Domain / binding site	NT	Compound	# of Compounds	Environment
TrkA	D5 – site 1a	NGF	ENT-A011	2	Solution
			ENT-A013E		
			ENT-A013Z		
			BNN27		
	D5 – site 1b		ENT-A011		
			ENT-A013E		
			ENT-A013Z		
			BNN27		
	D5		-	-	
	TM – inactive	-	ENT-A011	10	POPC
			ENT-A013E		
			ENT-A013Z		
			BNN27		
			cholesterol		
	TM – active		ENT-A011	1	
			ENT-A013E		
			ENT-A013Z		
			BNN27		
			ENT-A011		POPC:cholesterol 6:4
			ENT-A013E		
			ENT-A013Z		
			BNN27		
TrkB	D5 - site 1a	NT4/5	ENT-A011	2	Solution

			ENT-A013E		
			ENT-A013Z		
			BNN27		
			ENT-A045		
	D5 – site 1b		ENT-A011		
			ENT-A011 - IFD		
			ENT-A013E		
			ENT-A013Z		
			BNN27		
			ENT-A045		
	D5		-	-	
	TM – inactive	-	ENT-A011	10	POPC
			ENT-A013E		
			ENT-A013Z		
			BNN27		
			cholesterol		
	TM – active		ENT-A011	1	
			ENT-A013E		
			ENT-A013Z		
			BNN27		
			ENT-A011		POPC:cholesterol 6:4
			ENT-A013E		
			ENT-A013Z		
			BNN27		
	TM – active – Dist. Rest.		ENT-A011		POPC
			ENT-A013E		
			ENT-A013Z		
			BNN27		
			ENT-A011		POPC:cholesterol 6:4
			ENT-A013E		
			ENT-A013Z		
			BNN27		

I also ran MD simulations to investigate the propensity of the compounds to enter the membrane from the solvent environment. For this purpose, I started the simulations with 10 compounds placed close to the membrane in the solvent phase and monitored whether the compounds would enter the membrane spontaneously. The same simulations but with 1 compound molecule close to the membrane than 10 were ran by Christina Athanasiou. The membrane permeability simulations are summarized in Table 3.6.

Table 3.6: Summary of simulations for membrane permeability.

Compound	# of Compounds	Environment
BNN27	1	POPC
ENT-A011		
ENT-A013E		
ENT-A013Z		
cholesterol		
DHEA		
DHEAS		
BNN27	1	POPC:cholesterol 6:4
ENT-A011		
ENT-A013E		
ENT-A013Z		
cholesterol		
DHEA		
DHEAS		
BNN27	10	POPC
ENT-A011		
ENT-A013E		
ENT-A013Z		
cholesterol		
BNN27	10	POPC:cholesterol 6:4
ENT-A011		
ENT-A013E		
ENT-A013Z		
cholesterol		

3.3 Results

Lead compound binding site validation

I performed molecular docking calculations to validate the proposed from the literature binding site of the lead compound BNN27. It has been suggested that BNN27, which is C17-spiroepoxy derivative of DHEA and is an agonist of TrkA and p75 receptor, binds at the interface of NGF and TrkA-D5 by Saturation Transfer Difference Nuclear Magnetic Resonance (STD-NMR) assays.[270] In the same publication, two potential binding sites, named 1a and 1b, were identified computationally at the interface of NGF and TrkA-D5. The two sites are shown in Figure 3.2.

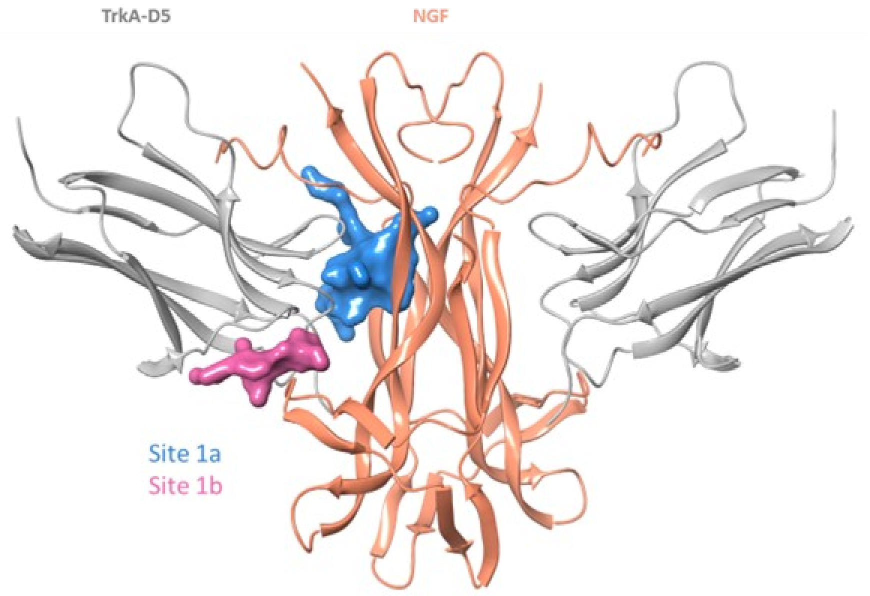

Figure 3.2: Binding sites 1a and 1b at the interface of the D5 domain of TrkA (TrkA-D5) and NGF. TrkA is shown in gray ribbon representation, while NGF in orange. The surface representation of the two binding sites showcases the volume of the pockets.

The first step of understanding how BNN27 works upon binding to TrkA would be to identify the changes that happen during this process, i.e. the interactions formed between ligand and receptor, and the conformational changes of the ligand and the protein. Thus, a starting point would be to try to simulate binding of the ligand in the proposed binding sites. Then, by observing the aforementioned changes, design of optimized analogues can be made possible. For this purpose, I performed computational docking to investigate the binding of BNN27 to TrkA sites 1a and 1b. For site 1a, I performed multiple docking calculations using different setups for the binding site and the protocols of Single Precision (SP) and Extra Precision (XP) of Glide or Induced-Fit Docking (IFD) of the Schrödinger Suite v.2020.

None of the SP and XP docking runs were able to place BNN27 inside the pocket of site 1a. I tested this for both symmetric 1a sites in structure 1WWW,[337] since it is a homodimer. Thus, I concluded that site 1a in the X-ray structure is not spacious enough for BNN27 to fit in. As a solution to this issue, I used the IFD protocol, with which I was able to dock BNN27 inside the 1a pocket (Figure 3.3A), with the output poses seeming plausible and having better docking scores than plain docking. For site 1b, docking was able to place BNN27 in the site (Figure 3.3B). In both cases, the output pose is similar to the proposed ones,[270] however the ligand in both cases is placed in such a way that it has the hydrophobic methyl groups of the steroidal part exposed to the solvent, which raises entropy-related concerns. Moreover, the Glide XP docking score of -3.9 kcal/mol that was reported was not satisfying.

The docking poses of BNN27 to TrkB showed a specific binding mode in site 1a (Figure 3.4A), whereas docking in site 1b resulted in various poses with low docking score (Figure 3.4B). On the other hand, docking to TrkA showed a more consistent pose of BNN27 to site 1b. This may be an indication that site 1b is a specific binding site of BNN27 to TrkA.

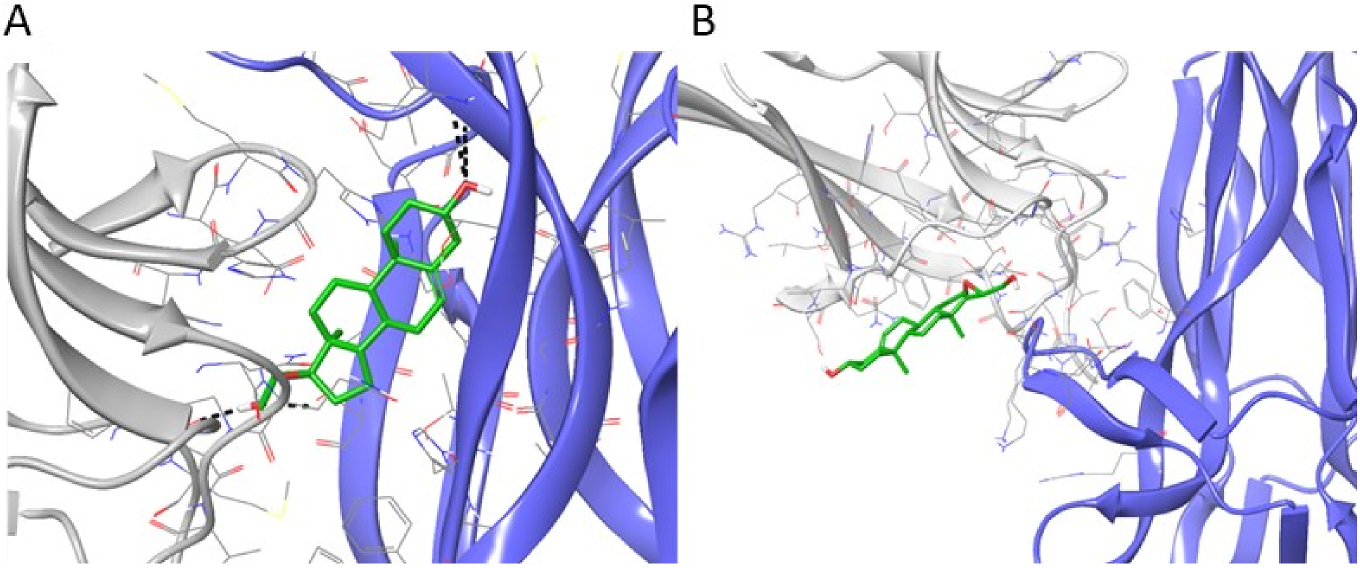

Figure 3.3: Molecular docking of BNN27 to TrkA-D5:NGF complex (PDB ID: 1WWW). TrkA is shown in gray ribbon representation, while NGF is blue. (A) Binding pose of BNN27 inside the pocket of site 1a obtained with IFD. Four hydrogen bonds are formed between BNN27 and receptor (shown as black dotted lines). (B) Binding pose of BNN27 in site 1b obtained with XP docking.

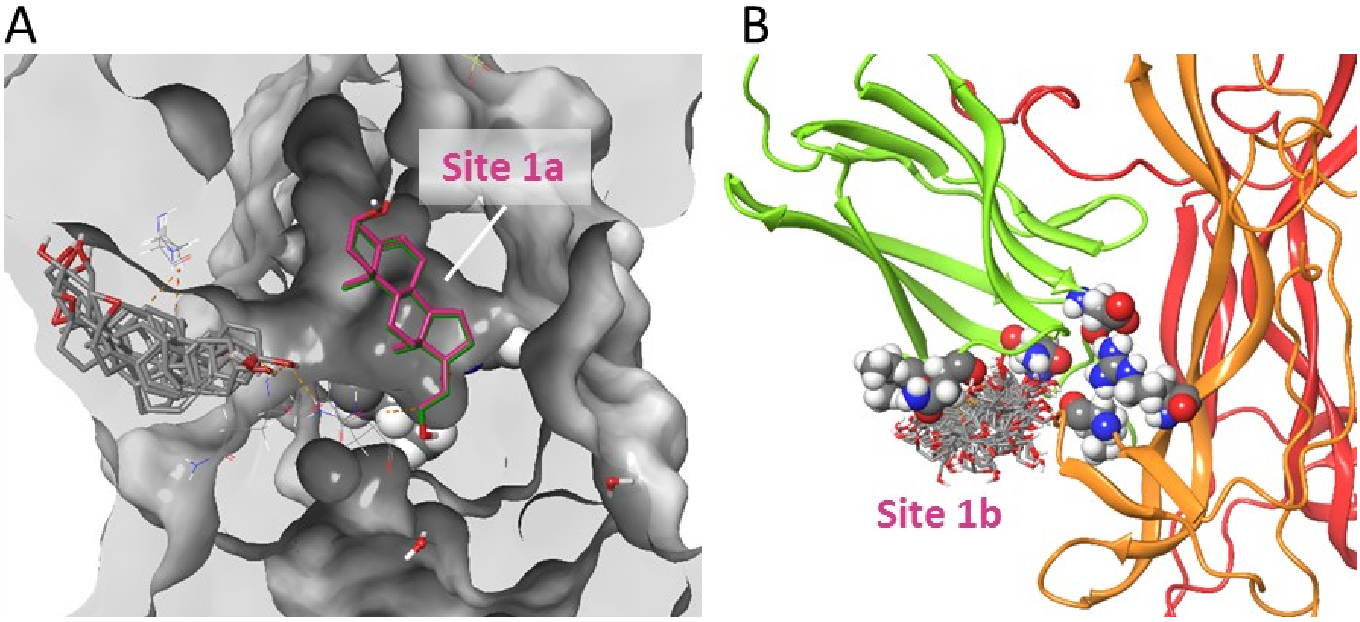

Figure 3.4: Molecular docking of BNN27 to TrkB-D5:NT-4/5 complex (PDB ID: 1HCF). (A) Docking poses of BNN27 to equivalent site 1a on TrkB. The BNN27 in pink tube representation shows the pose inside site 1a, whereas the rest of the poses in gray show docking poses of lower scores in the entrance of the pocket. (B) Docking poses of BNN27 in site 1b.

Steroid analogues with three-membered-17-spirocyclic substituents

I created a virtual library of 78 BNN27 analogues with three-membered-17-spiro substitutions, which contained the already synthesized and tested compounds BNN20, BNN23 and BNN27,[269] as well as compounds planned to be synthesized by NHRF partner of the EuroNeurotrophin consortium. Out of all compounds, BNN27 and BNN23 have an epoxide ring C17 substituent, while the rest have a cyclopropyl ring.

I docked the compounds to sites 1a and 1b of TrkA-D5:NGF, using the SP and XP protocols of Glide, as well as the IFD to the most promising compounds from XP. The docking scores for the best compounds are presented in Table 3.7 and their structures in Figure A.1.

Table 3.7: BNN-27 analogues with three-membered-17-spiro substitutions with the highest SP and XP docking scores in TrkA-D5:NGF (sorted by XP score).

Compounds	SP Docking score (kcal/mol)	XP Docking score (kcal/mol)
ENT-A021_Z	-4.895	-4.758
ENT-A031_E	-4.914	-4.593
ENT-A030_Z	-4.720	-4.351
ENT-A021_E	-4.813	-4.183
ENT-A020_E	-5.132	-4.154
ENT-A010	-4.513	-3.922
ENT-A028_Z	-4.052	-3.769
ENT-A029_Z	-4.459	-3.748
ENT-A027_E	-4.864	-3.651
ENT-A040_Z	-3.929	-3.547
BNN27	-4.051	-3.342
ENT-A016_Z	-3.863	-3.327
BNN27-cyclopropyl	-3.996	-3.391

I chose compound ENT-A027_E docked to site 1b of TrkA to be simulated with MD, since it showed good interactions with the residues of the receptor, good XP and IFD scores and good QikProp properties. During the 50 ns of the simulation, the phenol moiety interacts mostly with the proteins, while the steroid core remained solvent exposed. A schematic of detailed ligand interactions with the protein residues during the simulation is shown in Figure 3.5. Interactions that occurred between the compound and the TrkA and NGF proteins are presented as occupancy percentages. As seen in Figure 3.5, the phenol moiety of the molecule creates the most interactions with the protein and it is the ligand part that stabilizes the whole molecule in the pocket. Therefore, this phenol group may be employed as a fragment for future drug design approaches.

Docking to the TrkB receptor with protocols SP and XP did not give conclusive results, with compounds that had good SP scores, performing poorly in XP. The best poses from XP were subjected to IFD calculation, but the resulting poses were either too solvent exposed or did not create many interactions.

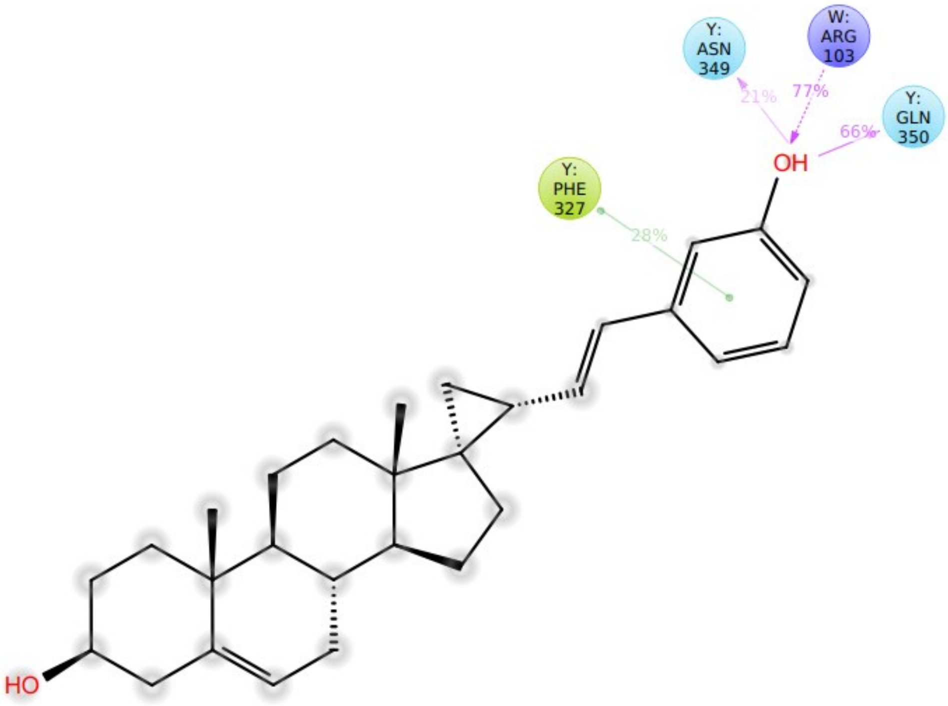

Figure 3.5: Interaction occupancy between compound ENT-A027_E and the TrkA-D5 and NGF proteins throughout the simulation time. TrkA-D5 is chain Y and NGF is chain W.

Steroid analogues with six-membered-17-spirocyclic substituents

I docked a library of 18 BNN27 analogues to site 1b of the TrkA-D5:NGF complex from the frame at 26 ns of the MD simulation mentioned in the previous section, which is the time when the C17 substituent entered deeper into the pocket and thus the cavity is larger at that frame. I eliminated output ligand poses from the SP and XP docking that were placed outside of the pocket or had methyl groups exposed to the solvent from further analysis. Four molecules had favorable poses in both SP and XP protocols. The 2D structures and their corresponding XP docking scores are presented in Table 3.8.

Table 3.8: 2D structures of best-scoring compounds with their XP docking scores.

Nr	2D structure	XP Docking score (kcal/mol)
1	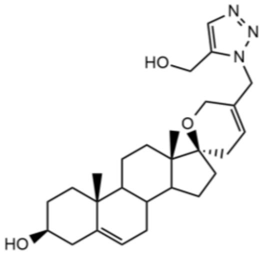	-5.6
2	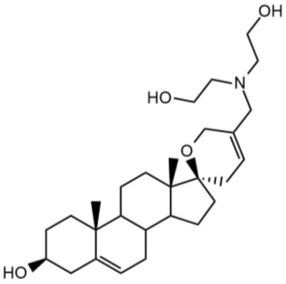	-6.2
3	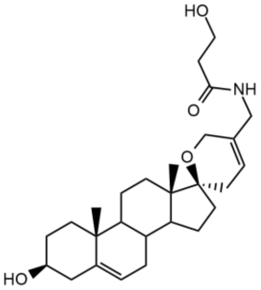	-5.0
4	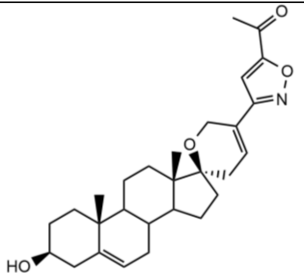	-3.8

The four ligands exploit the crevice deep inside the pocket at site 1b, in contrast to other ligands that were placed in the solvent exposed area of the pocket. All ligands are able to form interactions with NGF (hydrogen bonds shown in Figure 3.6) and TrkA (mainly van der Waals interactions), thus having the potential to stabilize the TrkA-NGF complex. I proposed these molecules to be prioritized in subsequent organic synthesis efforts.

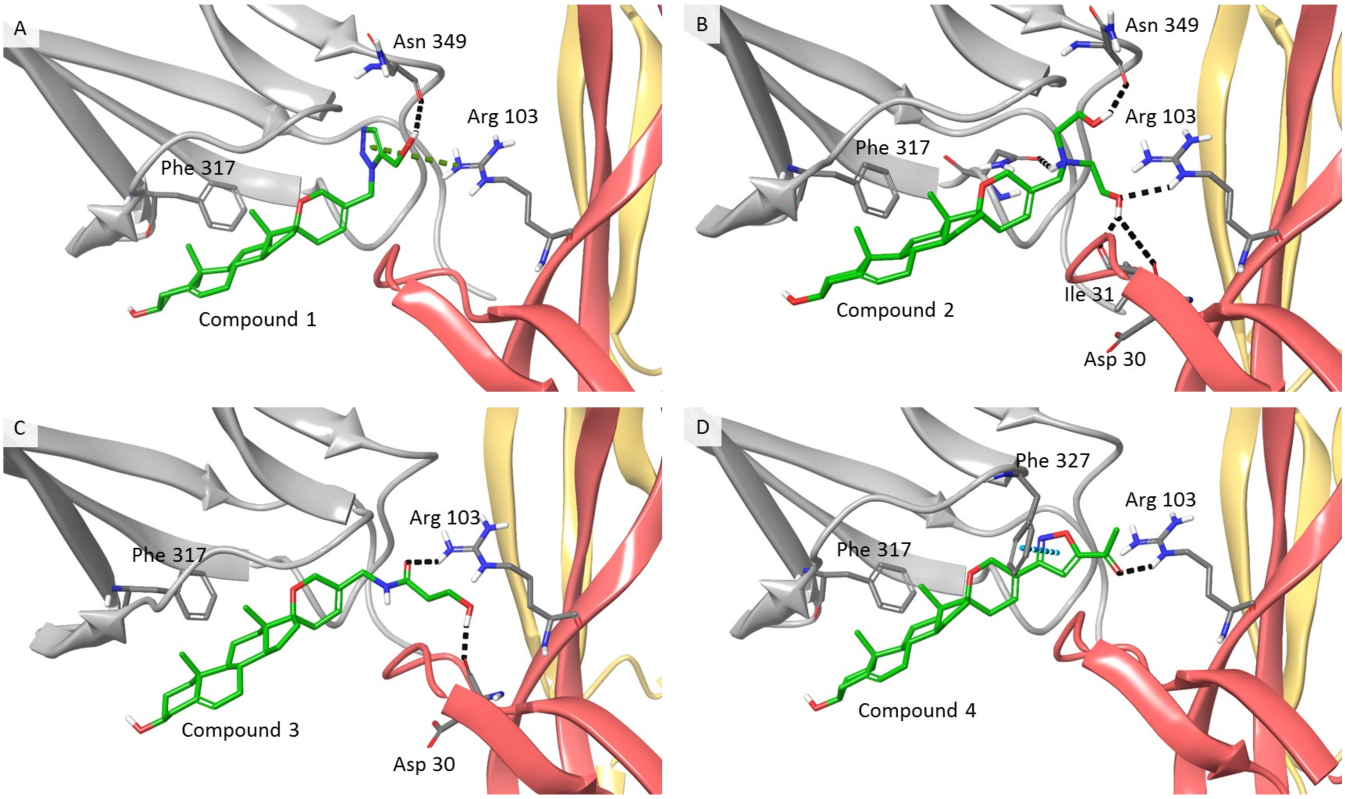

Figure 3.6: Docking poses of the best four compounds. Hydrogen bonds are shown with dashed black lines. The ligands and representative interacting residues are shown in stick representation. TrkA-D5 is shown in grey ribbon representation, while the NGF dimer is depicted in orange and yellow ribbon representations (different color for each NT monomer).

Fragment compounds

I performed virtual screening of a library of 9200 compounds synthesized in UNICAEN. I filtered and docked the fragments to site 1b of the TrkA-D5:NGF complex and after a series of filters presented in the methods section, I selected the 21 compounds shown in Table A.1 as potential hits. The binding poses of these compounds are shown in Figure A.2. I chose the best poses based on their docking scores and on whether the binding poses were deemed plausible during visual inspection. Also, I considered desirable the formation of H bonds and other energetically strong interactions during the selection process, since these interactions will play a key role in the selectivity of the compounds for TrkA. From those 21 fragment compounds, 11 were tested with STD-NMR by Dr. Maria Zervou, NHRF, Greece for TrkA-D5 binding, as the rest were either insoluble or not readily available in the UNICAEN library. Out of the 11 compounds, 8 were identified from STD-NMR as binders of TrkA-D5 (Figure 3.7).

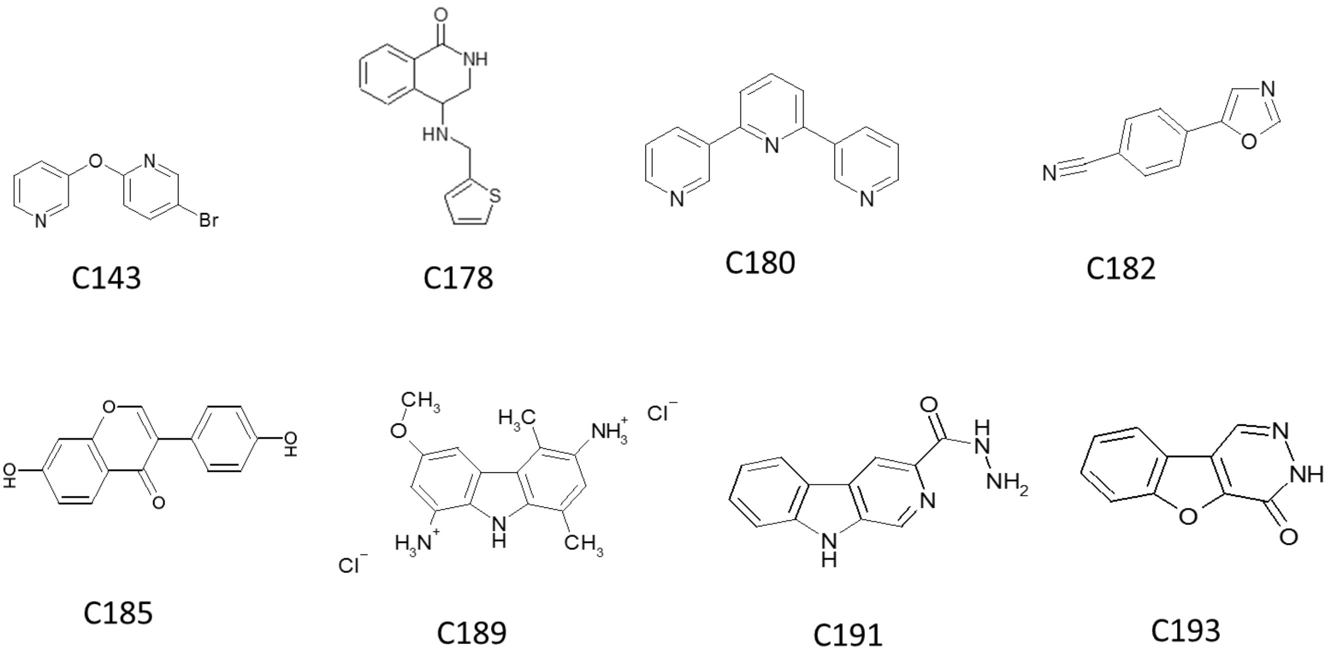

C143 C178 C180 C182

C185 C189 C191 C193

Figure 3.7: UNICEAN fragments identified by STD-NMR by Dr. Maria Zervou, NHRF, Greece as TrkA-D5 binders. The codes were given to each compound by the UNICAEN partners when the compounds were sent to be tested by STD-NMR.

From the eight UNICAEN library fragments identified by STD-NMR as TrkA-D5 binders, C178 had the best docking score (-5.6 kcal/mol), when docked to site 1b of TrkA. The docked pose of C178 shows the formation of a pi-pi interaction between the hydro-isoquinolinonyl and Phe 317 of TrkA, as well as two hydrogen bonds with the backbone of Asn 323 of TrkA (Figure 3.8). Additionally, the amine group forms two hydrogen bonds, one with Asn 355 of TrkA and one with Lys 32 of NGF (Figure 3.8). These strong interactions help in the stabilization of the pose in the binding site, while also offering potential selectivity for TrkA. The thienyl, on the other hand, does not contribute any strong interactions, and thus the pose lacks a stabilizing interaction in the inner part of the binding site. An improved compound would be one that possesses the hydro-isoquinolinonyl and amine parts of C178, but has a substitute for the thienyl group, in order to form a strong interaction, thus further stabilizing the pose. It is important, though, that the strong interactions of C178 are also retained.

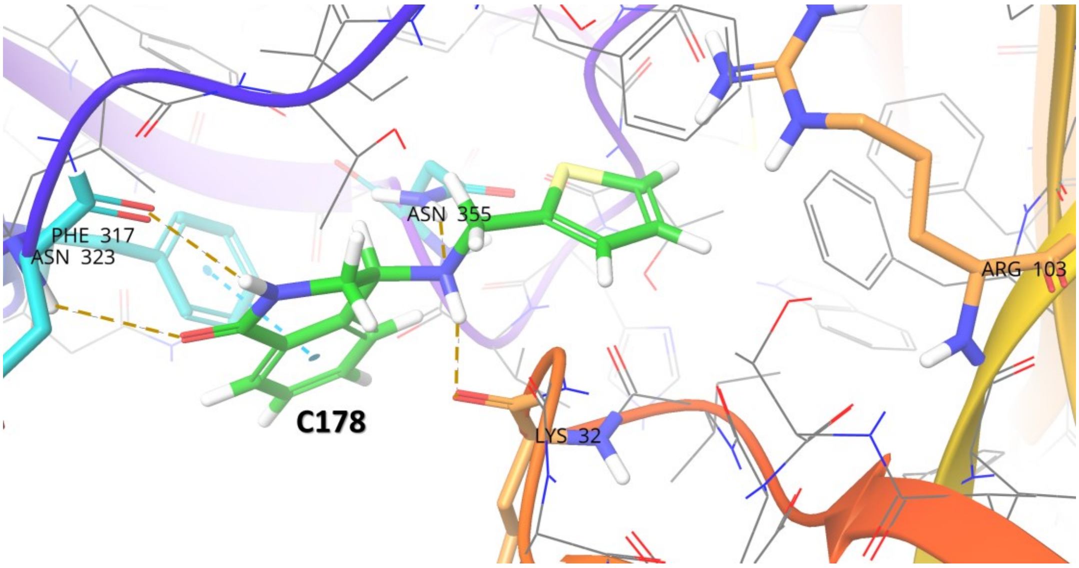

Figure 3.8: Docked pose of C178 in site 1b of TrkA. TrkA is shown in purple, while NGF is shown in yellow or orange. The ligand is shown with green-colored carbons. The pi-pi interaction with Phe 317 of TrkA is depicted as a cyan dashed line, while the hydrogen bonds with Asn 323 and Asn 355 of TrkA and Lys 32 of NGF are shown by brown dashed lines.

For the aforementioned reason, I substituted the thienyl part by a diverse set of groups via R-group enumeration, yielding a set of 226 compounds, which then I docked to site 1b of TrkA. In order to select compounds with docking score around or better than that of C178, I considered only compounds with a docking score of -5 kcal/mol or better and also positive predicted logP. Afterwards, I carried out visual inspection to keep only those that possessed the pi-pi interaction and hydrogen bonds of C178, but also had strong interactions in the substitute R-group. This resulted in 27 compounds. I docked the selected compounds to TrkB, in the site that is equivalent to site 1b of TrkA (the two receptors share the same secondary structure). The goal in this case was to identify compounds that showed docking scores in TrkB of the same magnitude as that in TrkA, and eliminate them as non-selective. Any compound with a docking score of -4 kcal/mol or better in TrkB (which translates to 1 kcal/mol or smaller difference from the docking scores in TrkA, which were -5 kcal/mol or better) was eliminated from the final set of compounds. The above procedure resulted in six compounds, which I proposed for synthesis as potential TrkA-specific binders (Figure 3.9).

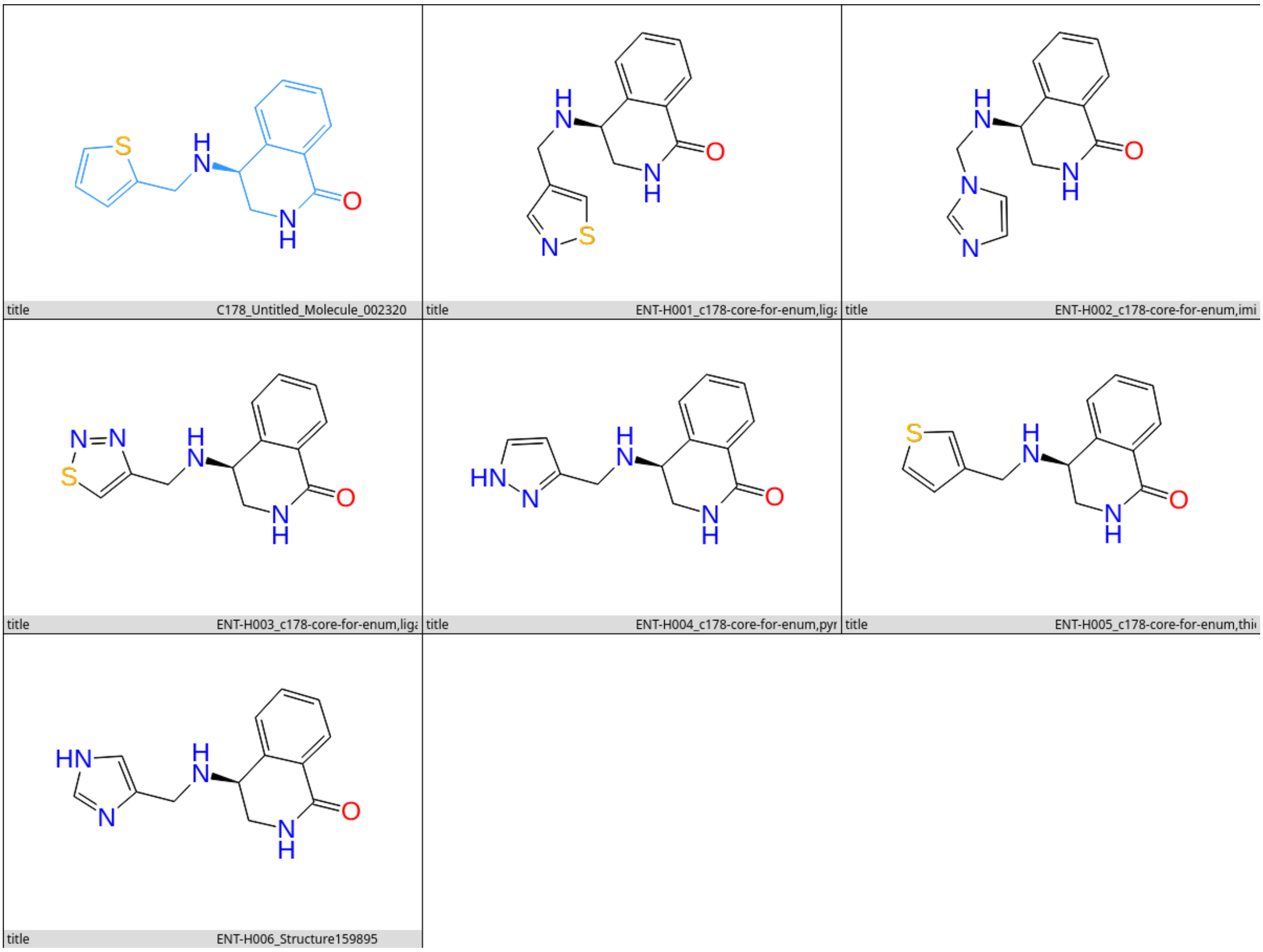

Figure 3.9: The 2D structures of C178 and its six proposed optimized derivatives. C178 is shown first, with cyan-colored carbons. The derivatives are coded as ENT-H001 to ENT-H006, in the order shown here.

The six proposed C178 derivatives all have five-membered aromatic rings as their substitute R-group, which mediate the formation of strong interactions with either TrkA or NGF (Figure 3.10). At the same time, the strong interactions of C178 with TrkA and NGF are preserved, with the exception of ENT-H002 which lacks only one hydrogen bond, the one with Asn 355 of TrkA. The docking scores are in the range of -5.2 kcal/mol to -6.3 kcal/mol. Regarding interactions, ENT-H001, ENT-H002 and ENT-H006 form extra hydrogen bonds with Arg 103 of NGF; ENT-H003 forms an extra hydrogen bond with Asn 355 of TrkA; ENT-H004 forms an extra hydrogen bond with Lys 32 of NGF; ENT-H005 forms an extra pi-cation interaction with Arg 103 of NGF.

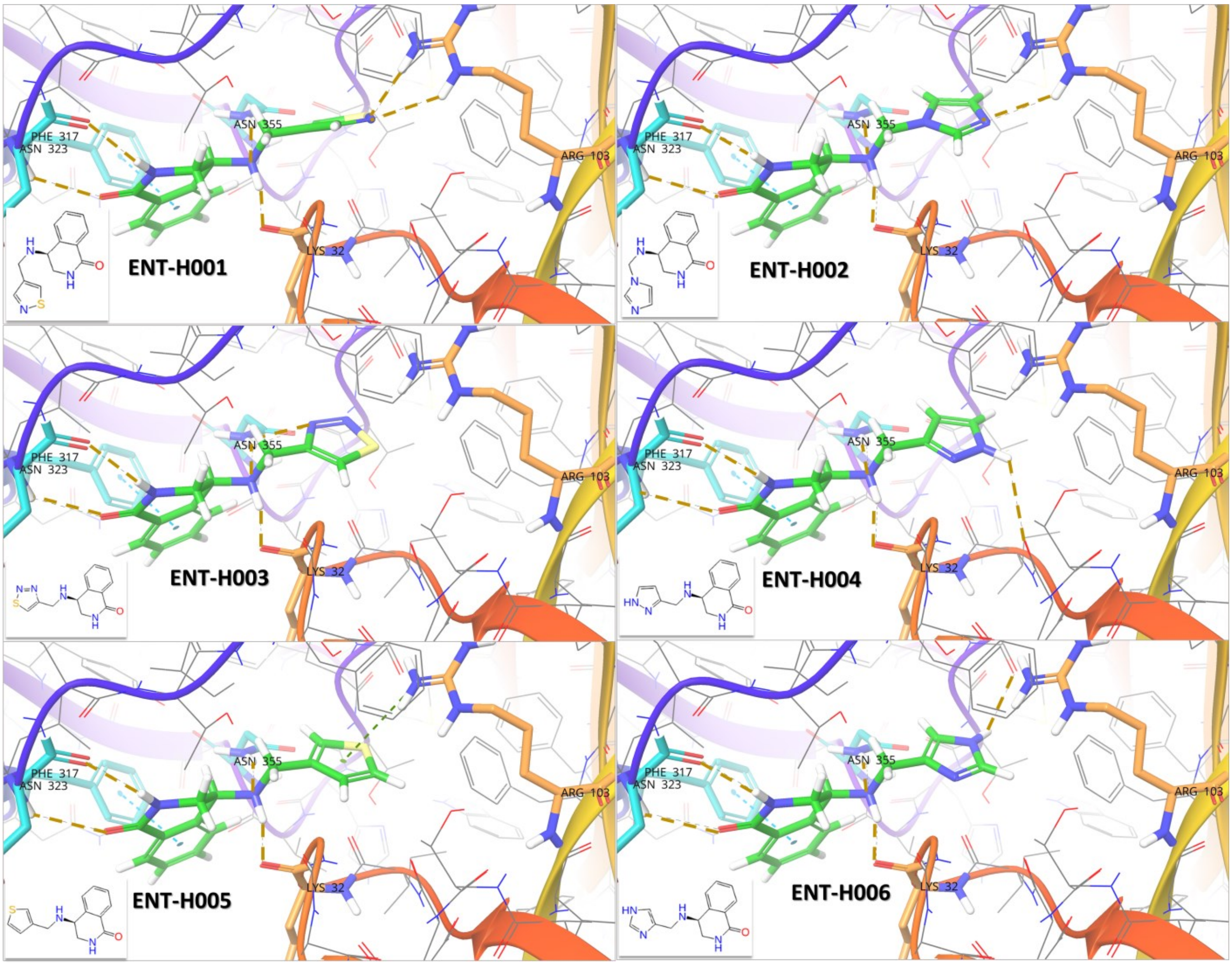

Figure 3.10: Docked poses of the six proposed, optimized C178 derivatives in site 1b of TrkA. The order is the same order as in Figure 3.9. TrkA is shown in blue or purple colors, while NGF in yellow or orange. The ligands are shown with green-colored carbons. The pi-pi interaction is depicted as a cyan dashed line; the hydrogen bonds as orange dashed lines; the pi-cation interaction as a green dashed line.

Prediction of the physicochemical properties of the C178 derivatives was also carried out (Table 3.9). All predicted values are within the recommended range (Table 3.10), except for the predicted permeability of Caco-2 and MDCK cell lines (models of the gut-blood and blood-brain barriers, respectively), where the predicted values do not offer a clear answer. This, in combination with the

QPlogP values, shows that the compounds may be too hydrophilic for passive permeability, requiring the introduction of more hydrophobic groups in the next steps of optimization.

Table 3.9: XP docking scores and predicted physicochemical properties for C178 and the proposed derivative compounds. MW (molecular weight – in g/mol); HBd (hydrogen bond donors); HBa (hydrogen bond acceptors); QPlogP (octanol/water partition coefficient); QPPCaco (permeability of the Caco-2 cell line, non-active transport – model for the gut-blood barrier – in nm/sec); QPPMDCK (permeability of the MDCK cell line, non-active transport – model for the blood-brain barrier – in nm/sec); #metab (number of likely metabolic reactions); QPlogKhsa (binding to human serum albumin).

Compound	XP score (kcal/mol)	MW (g/mol)	HBd	HBa	QPlogP	QPPCaco	QPPMDCK	#metab	QPlogKhsa
C178	-5.599	258	2.0	4.0	2.2	369	325	5	0.0
ENT-H001	-6.315	259	2.0	5.0	1.5	185	185	4	-0.2
ENT-H002	-6.044	242	2.0	6.0	0.9	177	84	3	-0.3
ENT-H003	-5.725	260	2.0	6.0	0.8	99	95	4	-0.3
ENT-H004	-5.622	242	3.0	5.5	0.6	97	44	4	-0.3
ENT-H005	-5.476	258	2.0	4.0	2.2	387	398	5	0.0
ENT-H006	-5.228	242	3.0	6.0	0.5	114	52	4	-0.4

Table 3.10: Recommended values of the predicted physicochemical properties.

QikProp property	Recommended values
Molecular Weight (g/mol)	130 – 725
Hydrogen-bond donors	0.0 – 6.0
Hydrogen-bond acceptors	2.0 – 20.0
QPlogP	-2.0 – 6.5
QPPCaco	<25 poor, >500 great
QPPMDCK	<25 poor, >500 great
Metabolic reactions	1 – 8
QPlogKhsa	-1.5 – 1.5

Mechanistic studies

For some of the compounds discovered within the EuroNeurotrophin consortium as agonists of TrkA and TrkB receptors,[272,273] I performed mechanistic studies involving MD simulations. Specifically, I docked the compounds in Table 3.4 at the interface of NGF with TrkA-D5, or placed around the TM helices of TrkA and I ran membrane permeability MD simulations of 10 compound molecules placed close to the membrane. The same was done on TrkB and with 1 molecule close to the membrane for the membrane permeability simulations by Christina Athanasiou. I present here all results for comparison. A summary of the simulated systems is shown in Figure 3.11.

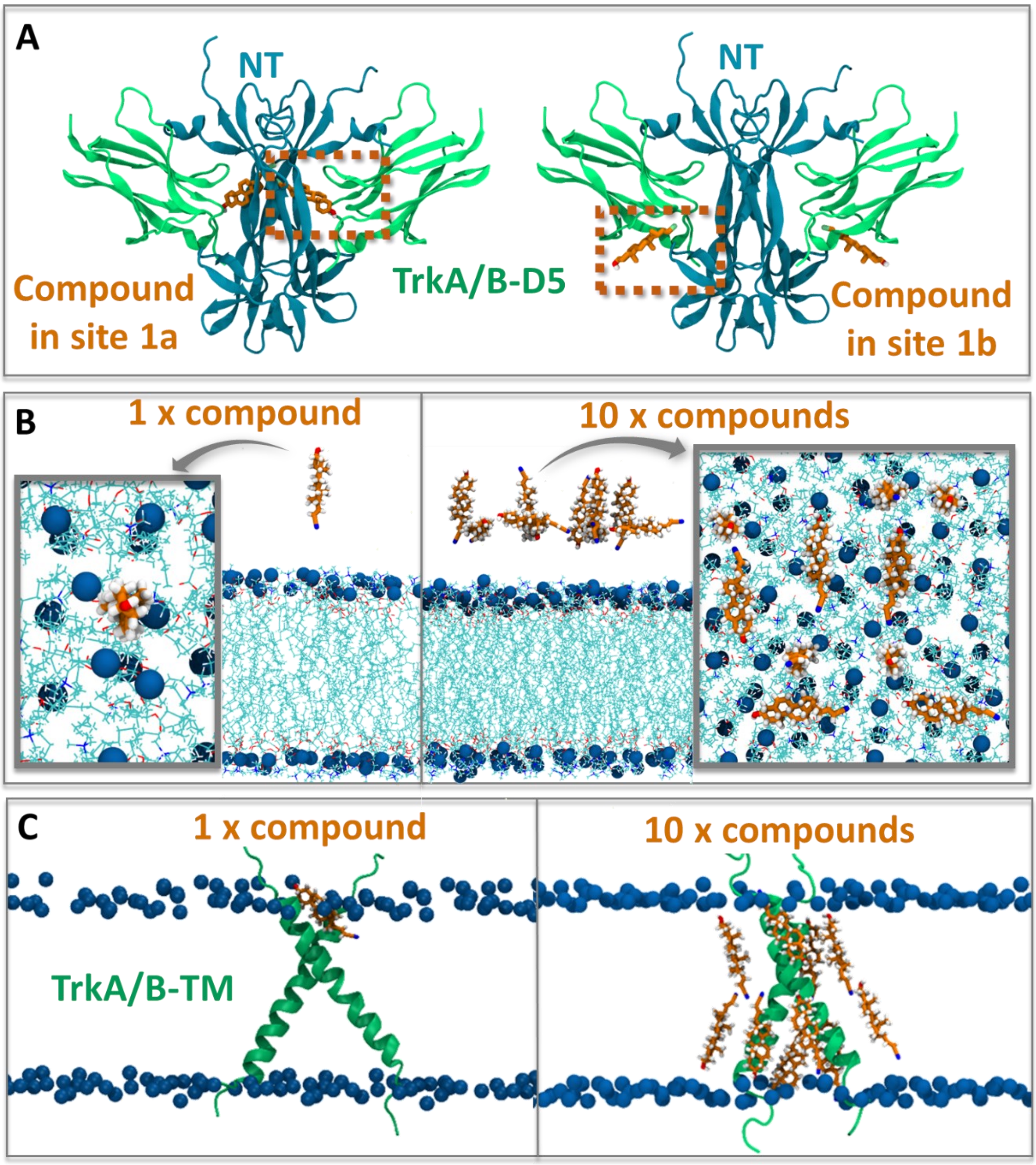

Figure 3.11: Summary of various systems with compounds. (A) Docked compounds at the interface NGF with TrkA-D5 and NT-4/5 and TrkB-D5. (B) Membrane permeability systems with 1 or 10 compound

molecules close to the membrane. (C) TM TrkA and TrkB systems with 1 compound docked at the interface of the TM helices or 10 compound molecules placed around the TM helices. I ran the simulations with TrkA and the 10-molecule membrane permeability simulations, while all calculations with TrkB and the 1-molecule membrane permeability simulations were done by Christina Athanasiou.[72] Figure partially adapted from Rogdakis et al.[272] For this figure, I created subfigure (A) and the 10-compound part of subfigure (B).

For the systems with EC-D5 domains of TrkA and TrkB and the corresponding compounds that bind selectively to each receptor, the results are shown in Figure 3.12 and Figure 3.13. The docking poses show an overall complementarity of the small molecules with the binding sites. The poses in site 1a show multiple possible binding modes of the steroid moiety, suggesting reduced stability in the binding. The poses is site 1b are partially exposed to the solvent, with the 3β-hydroxyl pointing to the solvent and the C17 substituents pointing deep to the protein pocket, providing an explanation for the variety in function of the different substituents. The docking models for compounds ENT-A013E/Z and ENT-A011 have been published.[272,273]

I also ran MD simulations starting from the docked poses to examine the stability of the models. In several of these simulations the compounds detached from the binding sites, which means that the initial models are not stable, or even the selected binding sites at the interface of neurotrophin and receptor are not the highest-affinity binding sites of the compounds. It might be that there are other binding pockets with which the compounds have higher affinity and thus can account for the observed function of the compounds on the receptors, i.e. the activation and phosphorylation of the receptors.

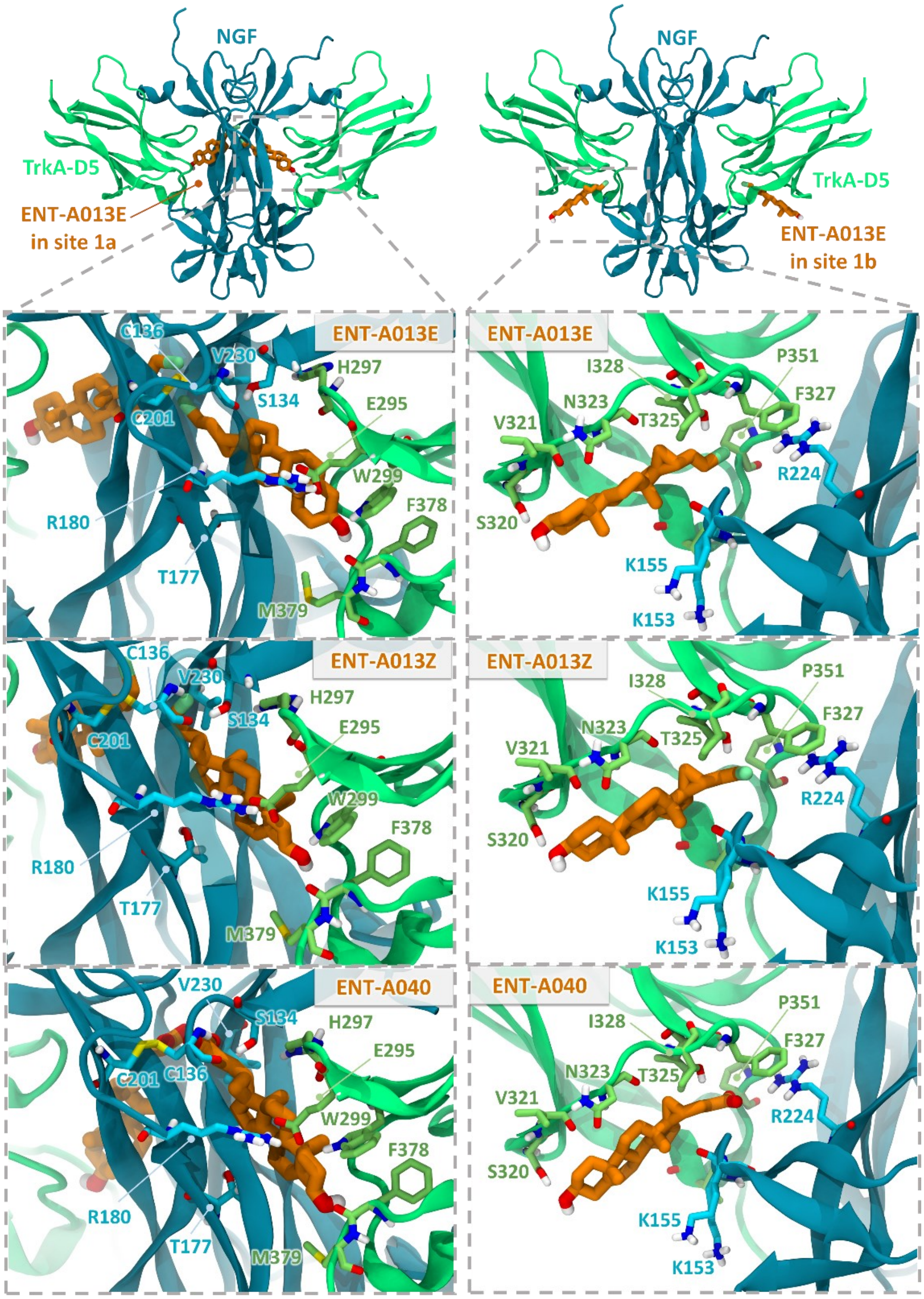

Figure 3.12: Docked binding modes of ENT-A013E/Z and ENT-A040 compounds bound at the interface of NGF with TrkA-D5. The poses in both symmetric sites of 1a and 1b are shown. NGF and TrkA-D5 are shown in green- and blue-ribbon representation, respectively, while the compounds are in orange stick representation. Figure partially adapted from Rogdakis et al.[272] I have fully created this figure and the docked poses.

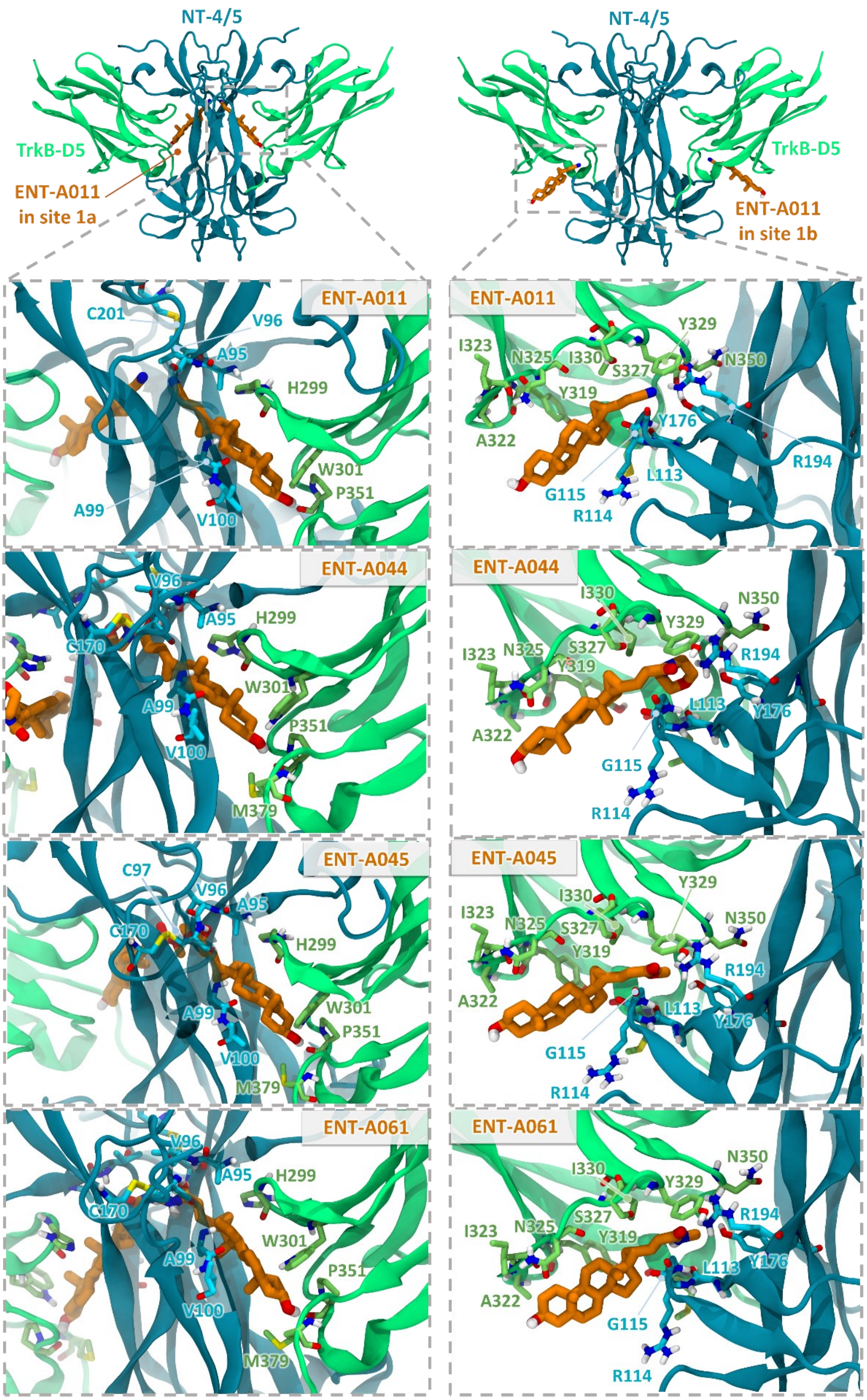

Figure 3.13: Docked binding modes of ENT-A011, ENT-A044, ENT-A045 and ENT-A061 compounds bound at the interface of NT-4/5 with TrkB-D5. The poses in both symmetric sites of 1a and 1b are shown. NGF

and TrkA-D5 are shown in green- and blue-ribbon representation, respectively, while the compounds are in orange stick representation. The calculations and figure were made by Christina Athanasiou.[72] Figure partially adapted from Charou et al.[273]

Since the docking and MD simulations of the compounds in the EC domains of TrkA and TrkB did not produce clear results on the compound binding site, together with consideration of the steroid core of the compounds, similar to that of cholesterol that is naturally found on cell membranes, I decided to investigate the possibility of the compounds entering in the membrane and interacting with the TM domain of the receptors. Thus, I placed 10 compound molecules close to POPC or POPC:cholesterol 6:4 membrane bilayers and ran MD simulations to observe whether they would be incorporated in the membrane environment (Figure 3.14, right). The same simulations but with 1 compound molecule instead of 10 were ran by Christina Athanasiou (Figure 3.14, left). Both types of simulations showed the compounds spontaneously entering the membrane bilayer. In the single molecule simulations, the compounds entered the membrane very fast. Control simulations with cholesterol showed that the compounds have a tendency to penetrate the membrane faster than cholesterol. The simulations with 10 compound molecules close to the membrane showed that they first create aggregates in the solvent phase and then they are able to enter the membrane as aggregates. When the aggregates have entered the membrane phase they dissociate and diffuse in the membrane (Figure 3.14, right).

The propensity of the compounds to readily penetrate the cell membrane suggests that they might act on the TM domain of the NT receptors. This would be similar to the behavior of the antidepressant drug fluoxentine as well as psychedelic drugs that were found to bind to the TM domain of TrkB.[294,296] To test this hypothesis, I docked single compounds at the interface of the TM helices of TrkA and simulated them with MD simulations, or I started simulations with 10 compound molecules around the TM helices of TrkA. The same work was done on TrkB by Christina Athanasiou. The simulations showed non-specific transient interactions between the compounds and the TM helices of both TrkA and TrkB, while the simulations that started with the compounds at the interface of the TM helices showed dissociation of the small molecules and diffusion in the membrane. No particular difference was also observed between the two membrane models POPC or POPC:cholesterol 6:4, although the second is more rigid and thus diffusion of the compounds in it was slower. The lack of a clear binding site might mean that more than one binding sites can act synergistically, or even that the activity of the compounds is due to an indirect effect through interaction with other types of proteins.

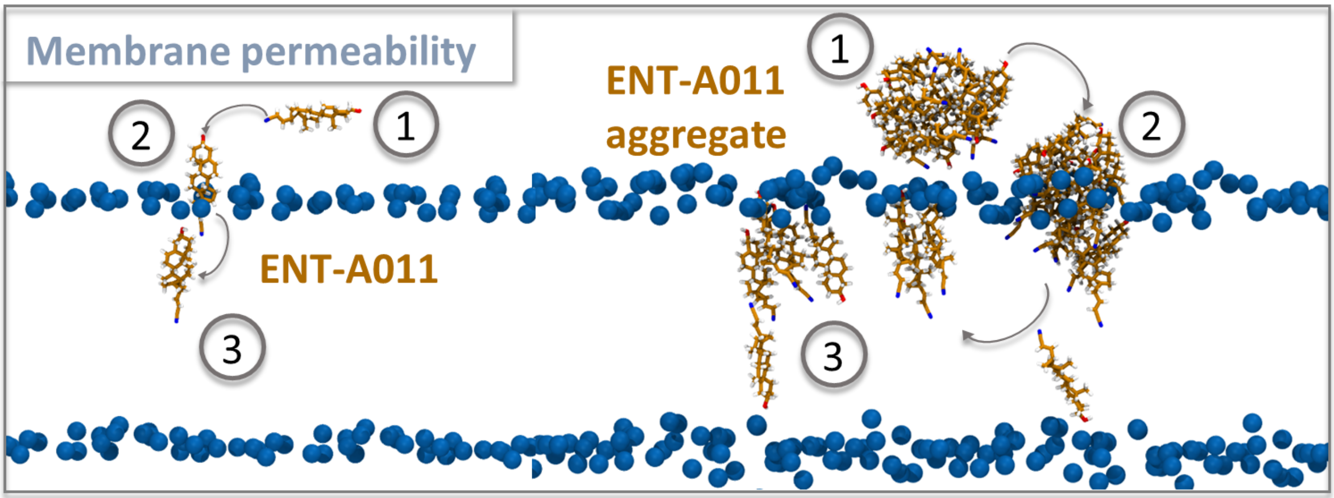

Figure 3.14: Molecular systems used for the membrane permeability simulations. Left: One molecule is placed close to the membrane. Right: Ten molecules are placed close to the membrane. The several steps of compound entrance to the membrane as a monomer or aggregate are shown in superposition. Figure created by Christina Athanasiou.[72]

3.4 Conclusions

The work presented in this chapter entailed the molecular modeling and design of novel NT mimetics agonists of the NT receptors. First, I focused on the lead steroidal compound BNN27, which is a TrkA agonist and was previously suggested to bind at the interface of TrkA and NGF, at two potential binding sites. Here, I also identified the two proposed sites 1a and 1b, and performed molecular docking studies of BNN27 in both of them. For docking to site 1a, which is more confined, I had to use a docking protocol which allowed for flexibility of the protein side chains and allowed accommodation of the compound. For site 1b, standard rigid-protein docking was able to place BNN27 in the pocket. This work set the docking protocols that I used for the rest of the BNN27 analogues as well. I performed similar docking studies for the equivalent sites at the interface of TrkB and NT-4/5, which showed variability in the poses in site 1b. Given that BNN27 activates TrkA and not the TrkB receptor, site 1b might be a specific binding site of BNN27 to TrkA. This could be tested by site-specific mutagenesis in site 1b and binding assays.

Subsequent work involved the creation of a virtual library of 78 already-planned BNN-27 analogues with three-membered-17-spiro substitutions, which I docked to sites 1a and 1b. I chose one of the most promising compounds to perform MD simulations, which revealed that the phenol moiety of the molecule creates the most interactions with the protein. This work suggested that this phenol group could be employed as a fragment for future drug design approaches. I also created a virtual library of 18 already-planned BNN27 analogues with six-membered-17-spiro substitutions, which I docked in a conformation of TrkA bound to NGF that had a more spacious site 1b. This was important for the bulkier six membered-17-spiro substitutions, and it allowed for the identification of four ligands that exploited the crevice deep inside the pocket at site 1b. I suggested all four compounds to be prioritized in subsequent organic synthesis efforts.

Next, I performed virtual screening of a library of 9200 compounds synthesized in UNICAEN, using a series of filters, which led to the selection of 21 fragment compounds to be tested experimentally. From those 21 fragment compounds, 11 were tested with STD-NMR for TrkA-D5 binding, and 8 were identified as binders. I used the binder with the best docking score, compound C178, as a template to design derivatives that could introduce stronger interactions with the residues at site 1b of TrkA. Through R-group enumeration, I designed 226 derivatives, which I subsequently docked to TrkA and TrkB, in order to identify those that would have potential selectivity for TrkA. This yielded six compounds that I proposed for synthesis and testing. These compounds form strong interactions with residues of TrkA or NGF, in site 1b, stabilizing their docked poses. Physicochemical property prediction showed values within the recommended ranges, however these molecules seem to be too hydrophilic to cross membranes by themselves. Introduction of hydrophobic groups should be the goal for the optimization of these compounds, after testing, which was not completed during the course of the current PhD thesis.

Functional studies of TrkA and TrkB receptors that were performed within the EuroNeurotrophin network, identified some small-molecule TrkA and TrkB agonists. I performed more extensive mechanistic studies in this set of compounds aiming to understand their selectivity for TrkA and TrkB. I docked the compounds at sites 1a and 1b of TrkA, Christina Athanasiou did the same for TrkB, and performed MD simulations, which showed that the compounds can spontaneously dissociate from these binding sites, indicating weak binding to these sites.

Since the docking and MD simulations of the compounds in the EC domains of TrkA and TrkB did not produce clear results on the compound binding site, together with consideration of the steroid core of the compounds, similar to that of cholesterol that is naturally found on cell membranes, I decided to investigate the possibility of the compounds entering in the membrane and interacting with the TM domain of the receptors. I performed MD simulations with compounds close to the membrane which showed spontaneous incorporation of the compounds to the membrane bilayer either as single molecules or as aggregates which then diffuse within the membrane. Interestingly, control simulations with cholesterol showed that the compounds have a tendency to penetrate the membrane faster than cholesterol. This suggests that the compounds can readily penetrate the membrane and potentially interact with the TM domain of the receptors. A limitation of this work is that the NT receptors are localized in neuronal membranes which are much more rigid than those simulated here, and thus it might be more difficult for the compounds to penetrate more rigid membrane. However, this might mean that they just need more time, as more complex POPC:cholesterol 6:4 membrane simulations also showed slower entering of the compounds in the membrane.

The propensity of the compounds to readily penetrate the cell membrane suggests that they might act on the TM domain of the NT receptors. This would be similar to the behavior of the antidepressant drug fluoxentine as well as psychedelic drugs that were found to bind to the TM domain of TrkB.[294,296] To test this hypothesis, I ran MD simulations with the compounds docked or close to the TM domain of TrkA and the same was done on TrkB by Christina Athanasiou. The simulations showed non-specific transient interactions between the compounds and the TM helices of both TrkA and TrkB, while the simulations that started with the compounds at the interface of the TM helices showed dissociation of the small molecules and diffusion in the membrane.

Overall, the mechanistic studies showed that the investigation of the binding site and mode of action of neurotrophin mimetics is far from trivial. STD-NMR data suggest binding at the EC domain, however the currently proposed binding sites lead to unstable binding poses. Furthermore, the propensity of the compounds to enter the cell membrane suggests possible action through the membrane environment and the TM domains of the receptors, however no specific binding site on the TM helices was detected with MD simulations. It might be possible the existence of more than binding site which act synergistically for the activation of the receptors. Also, accumulation of high compound concentrations in the cell membrane might alter the microenvironment of the membrane, which in turn leads to activation of the receptors. In fact it is known that NT receptors translocate to lipid rafts upon activation,[139,141,143] which shows that the lipid background plays a role in receptor function. Finally, the experimentally observed activity of NT mimetics on NT receptors might be an indirect effect resulting from binding to other proteins that interact with NT receptors. Consequently, it becomes evident that further exploration of the interaction between the compounds and receptors is needed to identify the actual binding site and mode of action of NT mimetics.

4 Glycosylation in the p75 receptor

4.1 Neurotrophin receptor glycosylation

A common attribute of cell surface receptors, including single pass transmembrane receptors such as p75, is the presence of covalently bonded oligosaccharides, often called glycans, in their extracellular segments. These glycosylation sites are post-translational modifications occurring during the protein expression and are important for proper protein folding, function as well as cell partitioning. Based on the amino acid that the glycans are attached, they can be categorized to N- and O- glycans, with conjugation of the N atom of Asn residues, or the O atom of Ser and Thr residues, respectively.[71]

The p75 neurotrophin receptor has been identified to have both N- and O- glycosylation oligosaccharides in its extracellular (EC) segments, with a single N-glycan close at the very N-terminal Cysteine-rich domain and several O-glycans (the exact number is not known) at the linker connecting the EC and transmembrane (TM) domains.[73–80] In contrast, the Trk receptors are known to have multiple N-glycosylation sites at their EC domains without O-glycans present.[47,74,78] There is also evidence of glycosylation presence in the pro-domain of pro-neurotrophins.[81–83] The single N-glycosylation of p75 has a complex glycan type,[73] while its O-glycans in the linker were found to contain sialic acids and have this core: Galβ1-3GalNAc-O-Ser/Thr.[84] The exact role of the N-glycosylation in p57 is not clear, as its deletion does not have any effect on receptor cell partitioning as found for TrkA.[75,80] On the other hand, the O-glycosylation has been suggested to help with the proper folding on the EC linker[76,84] and the apical sorting of p75.[75–77]

Experimental structural biology methods, such as x-ray crystallography, often require removal of glycosylation from the protein structure during sample preparation, to increase resolution, as glycans are very flexible and have a lot of structural variability and they tend to decrease the X-ray diffraction quality of the crystals or even hinder crystal formation.[356,357] This renders the structural investigation of glycan effects on protein structure quite challenging. A solution to this can be offered by Molecular Dynamics (MD) simulations, which allow explicit atomistic modeling of every type of glycan in any selected glycosylation site and investigation of the dynamical behavior of a protein of interest with glycans attached to it. Increased spectroscopy data regarding the type and site of glycans have led to more computational studies taking into account glycosylation in their glycoprotein models.[358–361] In this chapter, I have modeled and performed MD simulations of the glycosylated and non-glycosylated EC domains of p75 receptor and compared differences in receptor structure and dynamics due to the addition of glycans.

4.2 Methodology

Protein & glycosylation modeling

Due to the lack of an experimental structure for the human p75-EC domain, I used the structure of the Rattus norvegicus (rat) p75-EC, after alignment of its sequence to the human one, which showed a sequence identity of ca. 92%. I performed the sequence alignment using Clustal Omega 1.2.4[362] via UniProt.[363] I selected the crystal structure of the complex of the rat p75-EC domain homodimer and the human NT-3 homodimer (PDB ID: 3BUK).[55] This structure contains the rat p75-EC domain residues 32-190 (31-189 in human — corresponding to UniProt entries P07174 and P08138, respectively), an N71S mutation in the rat p75-EC domain, which results in the serine residue present in the human sequence, and the human NT-3 residues 143-253. It thus comprises (with a few missing residues) the full length of the structured parts of the p75-EC domain and NT-3. I processed the structure using the Schrödinger Suite 2020,[351] by mutating the residues that were different in rat to the human ones using Maestro, and then I prepared the protein (bond order assignment, optimization of hydrogen-bond network, restrained energy minimization) using the Protein Preparation Wizard.[351] This structure was missing the p75-EC residues 29-30 and the NT-3 residues 139-142 and 254-257 in each monomer. I modeled these residues using MODELLER 9.23.[364] The resulting model lacked hydrogen atoms, so the protonation states were predicted using PROPKA 3.4.0[365] via PDB2PQR 3.4.0.[366] For the simulations, I modeled the p75-EC domain at three different states: (1) as a homodimer in complex to NT-3, (2) as a monomer in complex with NT-3 and (3) as a monomer alone.

Regarding the glycosylation of p75, it is known that each monomer has one complex N-glycan of composition $Hex_5HexNac_4dHex_1NeuAc_2$ (Hex: Hexose, HexNac: N-Acetylhexosamine, NeuAc: N-acetylneuraminic acid) (Figure 4.1) at Asn 60.[73] p75 has also several O-glycosylation sites, which are located at the linker between the EC and transmembrane (TM) domains.[76,77,367] However, in this chapter I have only modeled the structured EC domains of p75, so the O-glycosylation is not present. The glycans were built using CHARMM-GUI.[368] I built the three states of p75-EC mentioned above with the presence or absence of glycans.

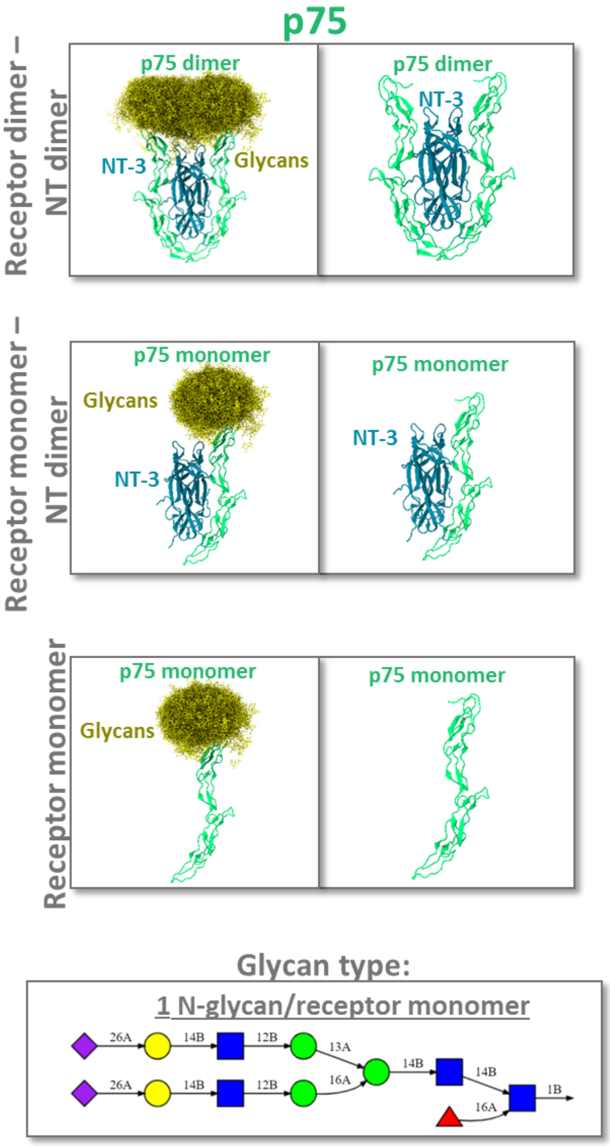

Figure 4.1: States of p75-EC simulated in this chapter: (1) p75-EC as a homodimer in complex to NT-3, (2) as a monomer in complex with NT-3 and (3) as a monomer alone. The proteins, p75-EC and NT-3, are depicted in green and blue cartoon representations, respectively, while the N-glycan at Asn 60, is shown in yellow stick representation and in multiple conformations, as sampled from the simulations. The box at the bottom shows the type of complex N-glycan that was modeled with the shapes and colors meaning as follows: the blue boxes correspond to the N-acetyl-glucosamine, the green circles to the

mannose, the yellow circles to the galactose, the purple rhombus to the sialic acid and the red triangle to the fucose monosaccharides.

Molecular dynamics (MD) simulations

I used CHARMM-GUI to insert the glycoprotein into an orthorhombic simulation box, solvate it in water with 150 mM NaCl, and prepare it for MD simulation using the CHARMM36m force field and the GROMACS engine. I repeated this process to build six systems in total: the p75-EC homodimer in complex with NT-3 with and without glycans, the p75-EC monomer in complex with NT-3 with and without glycans, and the p75-EC monomer alone with and without glycans (Figure 4.1).

For all simulations, I used the GROMACS v.2020 MD engine,[369] and the CHARMM36m as force field.[370] The simulation protocol that I followed consisted of a steepest-descent energy minimization, an NVT and NPT equilibration steps with gradual removal of restraints and one NPT production run. I performed the NVT equilibration step at 310 K for 500 ps with restraints on protein backbone atoms of 400 kJ/(mol·nm^2) force constant and restraints on the protein side chains of 40 kJ/(mol·nm^2) force constant. Then, I ran the NPT equilibration at 310 K and 1 atm for 500 ps with restraints on protein backbone and side chain of 200 kJ/(mol·nm^2) and 20 kJ/(mol·nm^2), respectively. Finally, I performed the production run for 500 ns with the systems totally unrestrained and ran three replica simulations per system starting from different initial velocities (Table 4.1).

For thermostat and barostat I used the Nosé-Hoover[371,372] and Parrinello-Rahman[373,374], respectively. I used a coupling constant of 5 ps and isotropic pressure with $4.5 \cdot 10^{-5}$ compressibility. I used a 1 fs time step in the first equilibration step and then 2 fs for the second step, while I saved frames every 100 ps. For the treatment of the non-bonded electrostatic interactions I chose the Particle Mesh Ewald (PME)[375,376] with a cutoff distance at 1.2 nm, while for the calculation of non-bonded van der Waals interactions I chose a cutoff of 1.2 nm and a switching distance of 1.0 nm. All hydrogen-containing bonds were fixed with the LINCS algorithm.[377]

Table 4.1: Summary of p75-EC systems that I simulated with or without glycans.

System No	Protein	Glycosylation	Replicas	Production Time/Replica (ns)
1	p75 EC-dimer, NT-3 dimer	+	3	500
2		-	3	500
3	p75 EC-monomer, NT-3 dimer	+	3	500
4		-	3	500
5	p75 EC-monomer	+	3	500
6		-	3	500

Simulation analyses

At the end of each replica simulation I performed a set of post-processing analyses, with the fixing of periodic effects being with the *gmx trjconv* tool of GROMACS being the first step. I rendered all protein structures presented in this thesis with VMD 1.9.3.[355]

Root mean square deviation (RMSD), root mean square fluctuation (RMSF) & radius of gyration (Rg)

I performed RMSD calculations on the protein structures with the MDAnalysis Python library.[378,379] Specifically, I calculated the RMSD of each protein backbone during the simulations with respect to the initial structure, after having aligned first all frames to protein backbone of the first frame. I also calculated the internal RMSD of each subdomain backbone of p75-EC, after alignment to the backbone of the same sub-domain at the first frame. I plotted the RMSD values with the Matplotlib Python library,[380] while I calculated and plotted their density distributions with the Seaborn Python library.[381]

In order to monitor the fluctuations of the residues during the simulations, I performed RMSF calculations with MDAnalysis. For this, I aligned first the Cα atoms of the EC domains to an average structure from the simulations and then I calculated the RMSF of each residue Cα from that average structure. I also examined the RMSF of the oxygen atoms that are part of the sugar rings in each of the glycans. I plotted the RMSF values with Matplotlib and Seaborn.

I performed a radius of gyration calculation of the EC domains again with MDAnalysis, after having aligned each of the systems to the backbone of the p75-EC domains at the first frame of the simulations. I performed the plotting with Seaborn.

Solvent accessible surface area (SASA)

I chose to investigate the effect of glycan shielding of the p75-EC domain by performing SASA calculations with the *measure sasa* method of VMD 1.9.3.[355] I measured the SASA of the protein with and without taking into account the presence of the glycans and estimated the difference between the two. I also performed the calculation with several radii of probe, i.e. 1.4, 2, 3, 4, 5, 6, 7, 8, 9 and 10 Å, to take into account binding of molecules of various sizes.

I used the *measure sasa* method to also calculate the interface area between the p75-EC domains and the NT-3 and examine whether the glycan participates in this interface. For this purpose, I calculated the SASA of the p75-EC domain with the glycan with and without taking into account the presence of NT-3. By subtracting the values from the two calculations, I retrieved the SASA of the interface. I repeated this for the simulations that did not have glycans present and then compared the interface areas in the presence or absence of the glycan. Higher interface area in the presence of the glycan would mean that the glycan participates at the interface.

Principal component analysis (PCA)

Upon visualization of the simulation trajectories, I noticed a movement of the D1 domain of p75-EC with respect to the D2-D4. Therefore, I chose to quantify this intrinsic motion and examine whether it is influenced by the presence of the glycan by performing a PCA analysis on the D1 domain using MDAnalysis. For this purpose, I aligned all the simulation frames to the backbone of the D2-D3 domains and performed the PCA calculation on the coordinates of D1 backbone atoms. I plotted the values of the 1st and 2nd principal components with Seaborn.

Distances and angles between domains

For the systems that had the p75-EC homodimers in complex with the NT-3, I examined the distances between the centers of geometry (COG) of the different sub-domain monomers of p75, i.e. the D1-D1, D2-D2, D3-D3 and D4-D4 distances. I compared how these distances change in the presence or absence of the glycans. For this analysis, I used MDAnalysis and the numpy.linalg.norm function of the Numpy library.[382] I also calculated the angles formed by the COGs of the D1-NT-D1, D2-NT-D2, D3-NT-D3 and

D4-NT-D4 domains. I did this analysis every 100 frames and plotted the results in violin plots with Seaborn.

Hydrogen bonds & dihedral angles (χ1) of the glycan

In order to investigate whether the glycan at Asn 60 engages in any specific interactions, such as hydrogen bonds (as expected from the multiple H-bond acceptors in sugars), I calculated the H-bonds that it forms with its surrounding during the simulations with the HydrogenBondAnalysis class of MDAnalysis. I visualized with Matplotlib the residues that form H-bonds with either of the glycans at the two symmetric positions for more than 1% of the simulation frames.

I also performed an analysis of the χ1 dihedral angle of the Asn 60 that bears the glycan, both in the replica simulations with and the without the glycan to check the glycan influence at the conformation of that residue. For this, I used MDAnalysis to calculate the χ1 dihedral angle in all frames and plotted the results with Seaborn.

4.3 Results

As mentioned in the introduction, in this chapter I have modeled and performed MD simulations of the glycosylated and non-glycosylated EC domains of p75 receptor and compared differences in receptor structure and dynamics due to the addition of glycans. I modeled and simulated the p75-EC domain in three states: (1) as a homodimer in complex to NT-3, (2) as a monomer in complex with NT-3 and (3) as a monomer alone, always with and without glycans. Initial visualization of simulation trajectories showed that only the N-terminal part of the p75-EC can be shielded by the single N-glycan at Asn 60 position, while it seems to also have minimal interactions with NT-3. The cloud of glycan conformations appears to block the entrance at the upper region of the receptor, which might affect NT binding kinetics. Kinetic studies have shown that NTs dissociate from p75 at different rates, with NGF>NT-3≫BDNF.[22] Additionally, even though the Trks and p75 interact with NTs with similar dissociation constants in the nanomolar range, the binding kinetics are different, with NGF attaching to and dissociating from the Trks slower than p75.[383]

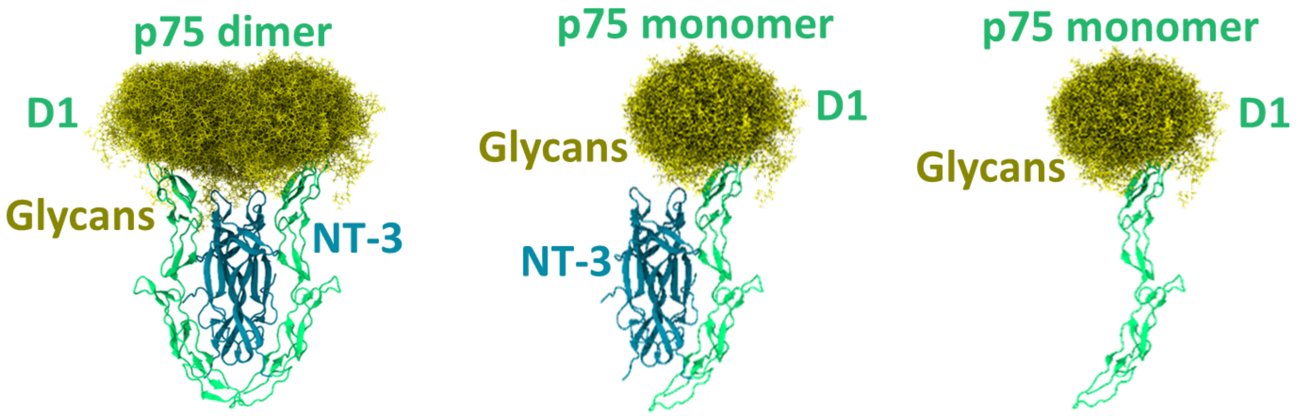

Figure 4.2: States of p75-EC simulated in this chapter: (1) p75-EC as a homodimer in complex to NT-3, (2) as a monomer in complex with NT-3 and (3) as a monomer alone. Only the glycosylated systems are shown with the multiple glycan conformations from the simulations. The p75-EC and NT-3 are depicted in green and blue cartoon representations, respectively, while the N-glycan at Asn 60, is shown in yellow stick representation and in multiple conformations sampled in the simulations.

Figure 4.2 shows that the cloud of glycans and thus glycan conformations are not influenced by the oligomeric state of the proteins. After visualization, I performed a quantitative analysis of the simulations. First, I monitored the root mean square deviation (RMSD) of the protein backbone with respect to the initial structures as a function of time (Figure 4.3). The results do not show any significant difference between the glycosylated and non-glycosylated systems, with only dimer-dimer and monomer-dimer systems exhibiting slightly higher peak in the RMSD population values for the glycosylated states. Interestingly, the systems with the p75-EC as a monomer alone show more fluctuations in the RMSD values, which suggests that NT might stabilize the EC domain of p75. Overall, the RMSD values are below 10 Å, which indicates deviation from the initial crystal structure, but not large conformational changes.

For more granularity, I calculated the RMSD values for each of the sub-domain of the p75-EC after alignment the domain itself, to observe the internal domain deviations from the initial structure (Figure 4.4). The results show low RMSD values for most of the domains, except for the D1 domain, which can exceed the 5 Å in RMSD and it seems to account for the higher that 3 Å RMSD values in the full-EC domain RMSD calculations (Figure 4.3). The D1 domain is located in the N-terminus of the p75-EC segment, and it appears to be less stable than the rest of the p75-EC domains. To investigate further the reason for the high RMSD values in the D1 domain, I took a closer look at the sampled conformations of this domain.

In Figure A.3, I have visualized the differences in the conformation of the D1 domain, which lead to the high RMSD values. The high RMSD values originate in the N-terminal linker of D1, which is disordered and seems to be quite flexible. Interestingly, the region of the D1 domain where the N-glycan is attached, has a more stable conformation, although this also fluctuates. Overall, the rest of the p75-EC domains have a stable conformation, despite the several disordered regions. This stability is probably conferred by the 12 disulfide bonds in the EC domain of p75, which form a disulfide bond ladder (Figure 4.5).

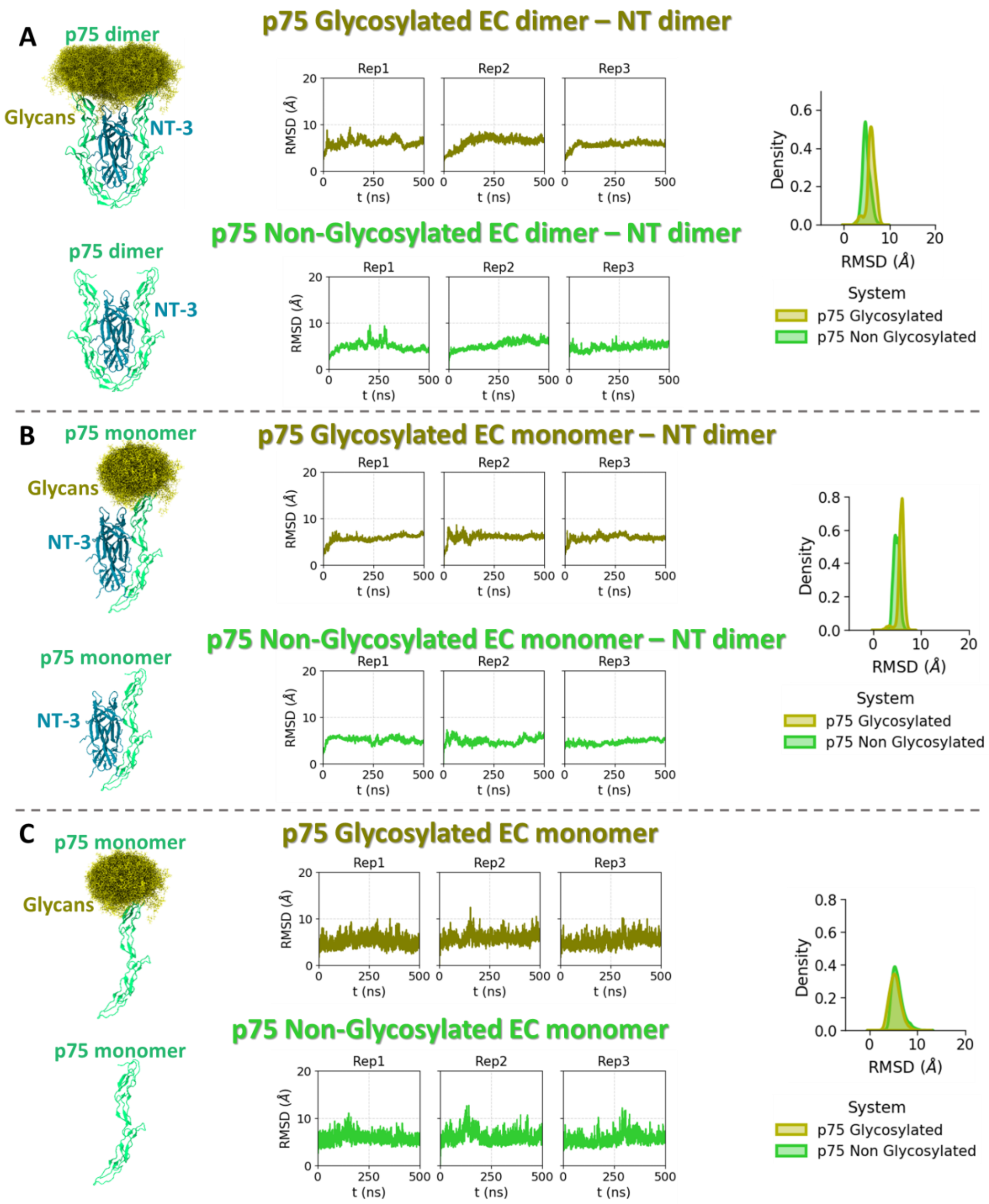

Figure 4.3: Summary of RMSD calculation results for the (A) p75-EC as a homodimer in complex to NT-3, (B) as a monomer in complex with NT-3 and (C) as a monomer alone, with and without glycans. The structural representations are the same as in Figure 4.1. The RMSD values are presented as an evolution with time (middle plots) and as probability densities for all the replicas together in the glycosylated and non-glycosylated systems (right plots).

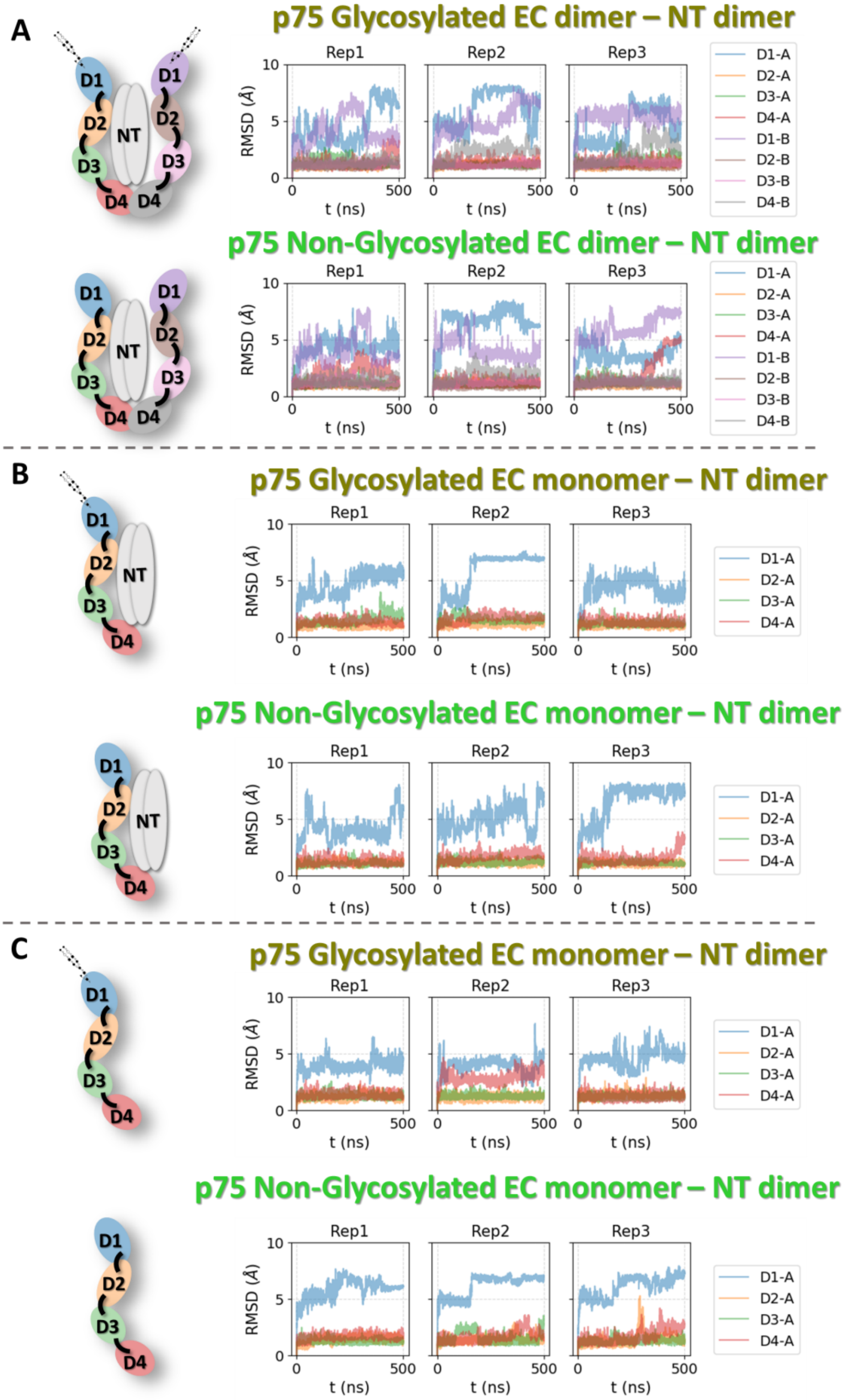

Figure 4.4: Summary of sub-domain RMSD calculation results for the (A) p75-EC as a homodimer in complex to NT-3, (B) as a monomer in complex with NT-3 and (C) as a monomer alone, with and without

glycans. The RMSD values are presented as an evolution with time for each of the domains, after alignment to each domain.

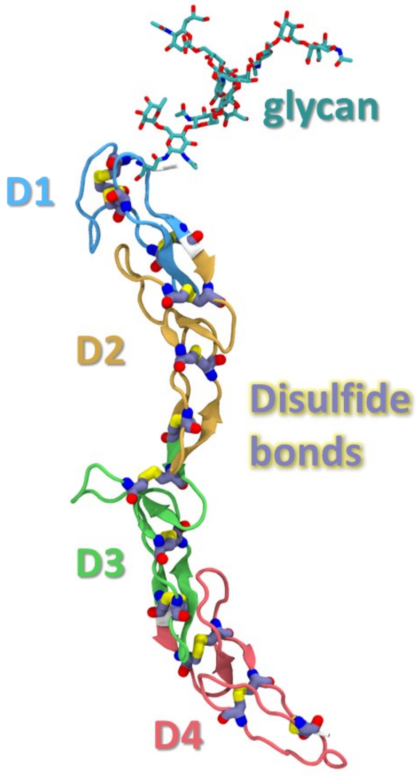

Figure 4.5: Disulfide bond ladder in the structure of p75-EC (from PDB ID: 3BUK). The D1-D4 domains are shown in cartoon representation with the same colors as in Figure 4.4. The disulfide bonds are shown in licorice representation.

Next, I analyzed the root mean square fluctuation (RMSF), which is a metric showing the average fluctuation of each of the protein residues during the simulations (Figure 4.6). The results show that the glycosylated and non-glycosylated systems behave in the same way, as shown before by RMSD. In all systems, the N-terminal region of the D1 domain displays the highest RMSF values, which corresponds to the disordered region that was previously shown to change conformation during the simulations in the RMSD calculations (Figure A.3). Comparison of the RMSF for the several oligomerization states shows that, for the “p75-EC monomer” system, residues 90-130 from D2 and D3 domain have higher RMSF values than for the “p75-EC dimer/NT-3 dimer” and “p75-EC monomer/NT-3 dimer” systems. However, there is no difference between the glycosylated or not forms for this system. Another interesting point is that the glycosylation at Asn 60 does not affect the fluctuations at this residue, as the RMSF values for the glycosylated or not systems are the same at this residue. This is in agreement with the higher RMSD values that were calculated for this system (Figure 4.3). In the case of the NT-3, highest RMSF values occur in the N- and C-terminal regions, which have disordered loops and are very flexible. In addition to the protein residue RMSF, I also calculated average RMSF values for each of the glycan in the systems (Figure 4.7). The N-glycan at N60 has RMSF values of ~10-12 Å in all oligomerization states of p75-EC, with a tendency for higher values observed in the "p75-EC monomer/NT-3 dimer" system.

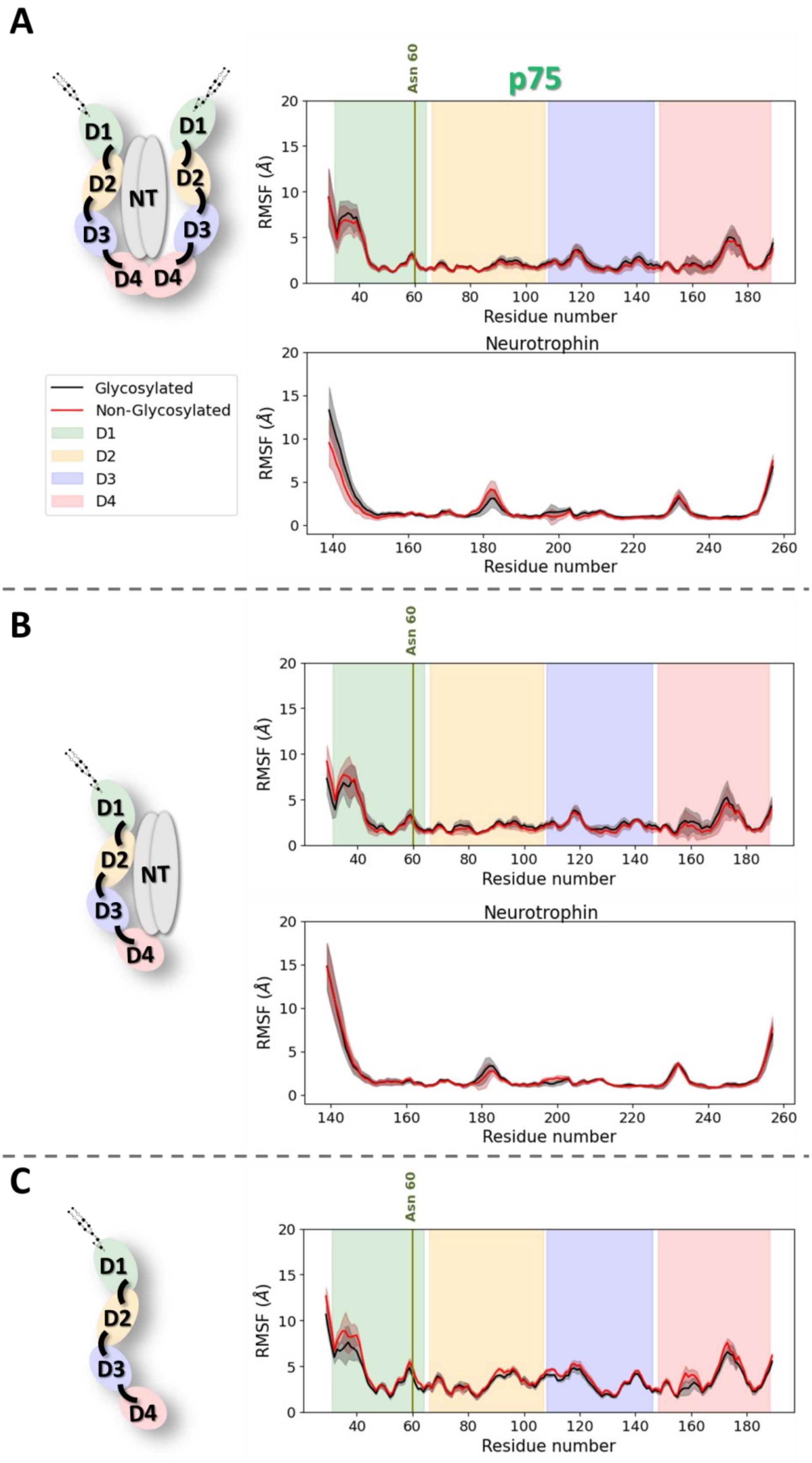

Figure 4.6: Summary of RMSF calculation results for the (A) p75-EC as a homodimer in complex to NT-3, (B) as a monomer in complex with NT-3 and (C) as a monomer alone, with (black) and without (red)

glycans. The RMSF for each residue was calculated as an average from the three replica simulations and the standard deviation at each point is shown with shadowed areas. The different domains of p75-EC are color coded and the glycosylated Asn 60 is indicated with a vertical line.

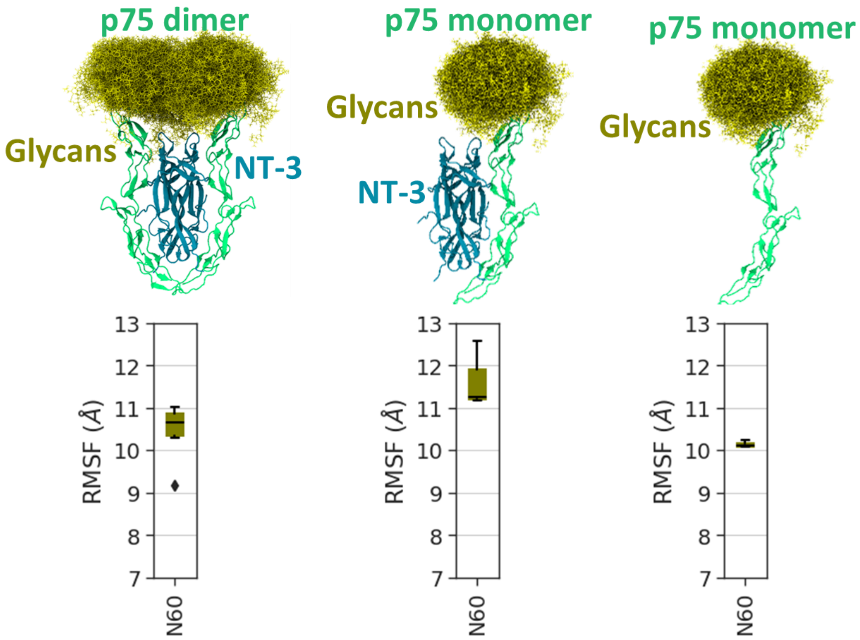

Figure 4.7: Distribution of RMSF values for the glycan at N60 in box plots. The RMSF was calculated after alignment to an average structure of the D1 domain during the simulations. The coordinates of the oxygen heteroatom at each sugar ring were used for the RMSF calculation.

Next, I investigated the effects of the glycan presence in the surface exposure of the proteins. For this purpose, I ran accessible surface area (ASA) calculations using probes of varying radii, from 1.4 to 10 Å, which corresponds to molecules of different sizes, such as water, small molecules and proteins. This allows to understand how much of the protein surface is actually accessible to interact with such type of molecules. As shown in Figure 4.8, the overall protein shielding from the glycan at Asn 60 is not very high, probably because of the single glycan, which points away from the surface of the protein as revealed by visualization of the simulation trajectories. Increase of the size of the probe seems to have a larger effect on the glycan shielding, reaching up to 7% of the protein ASA, which suggests that the binding of larger proteins rather than small molecules in the area proximal to the glycan may be more disturbed. The small bars for standard deviation suggest similar configurations and thus agreement among all replicas.

Subsequently, I calculated the contact area of the p75-EC domains with the bound NT-3 and how this is changes by the presence of the glycan. This analysis was done only for the systems in which NT-3 was present, i.e. the “p75-EC dimer/ NT-3 dimer” and “p75-EC monomer/ NT-3 dimer” systems. The results are presented in Figure 4.9. Comparison of contact area between receptor and NT with and without taking into consideration the presence of glycans shows exactly the same results. This shows that the N-glycan does not interact with the NT-3. Comparison of the p75-EC dimer system with the monomer one, shows that the contact area is slightly smaller in the monomer system, although this difference is probably not significant. In case this captures a real effect, it could mean that the packing between NT and receptor is a bit higher in the dimeric system, which might be facilitated through interactions of the two N-glycans with each other, as will be shown later, at the two N60 residues present in p75-EC homodimer.

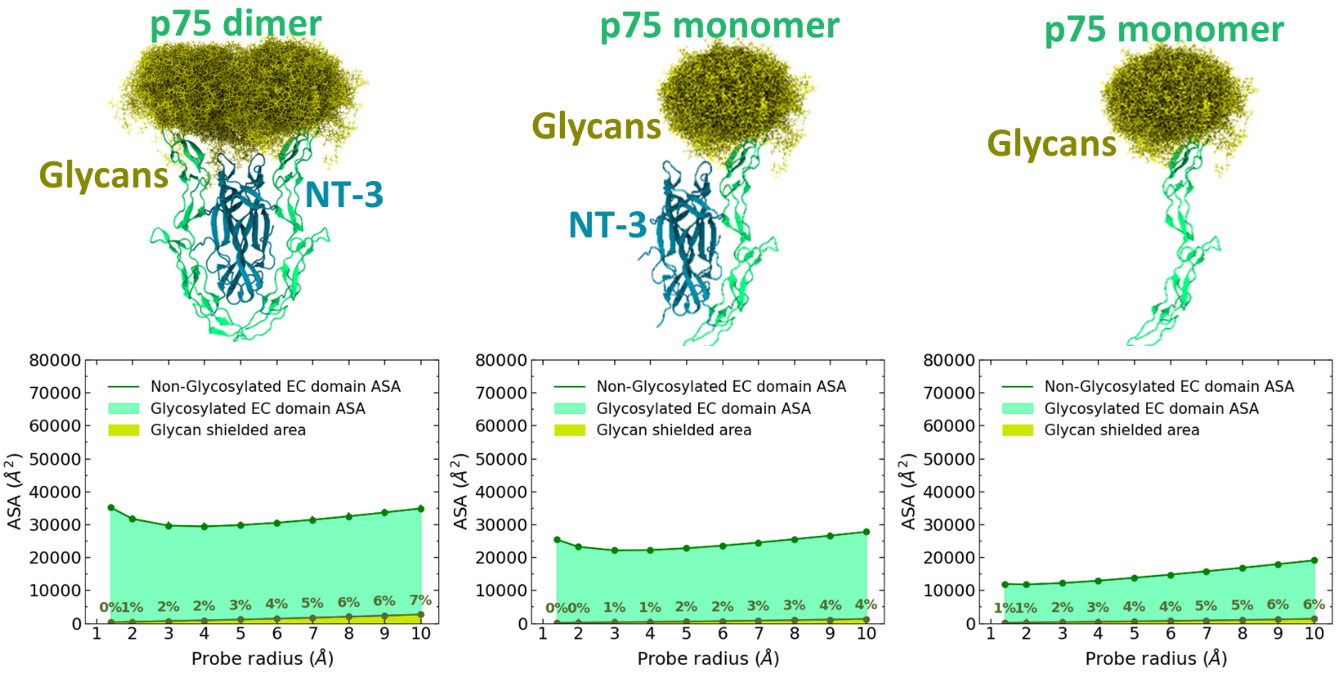

Figure 4.8: Summary of the accessible surface area (ASA) of the proteins to estimate the shielding by the glycan at Asn 60. The systems are presented in this order: p75-EC as a homodimer in complex to NT-3, as a monomer in complex with NT-3 and as a monomer alone. The ASA of the proteins without the glycans is shown with the green line, while the area that is shielded by the glycans when they are present

in shown in yellow. The remaining accessible area that is not shielded by the glycans is shown in light green and the percentage of the overall surface that is shielded by the glycans in written in the graph for the different probe radii. I used different probe radii of 1.4 to 10 Å to estimate how much of the protein surface is "seen" by molecules of different sizes, from water to small molecules and proteins.

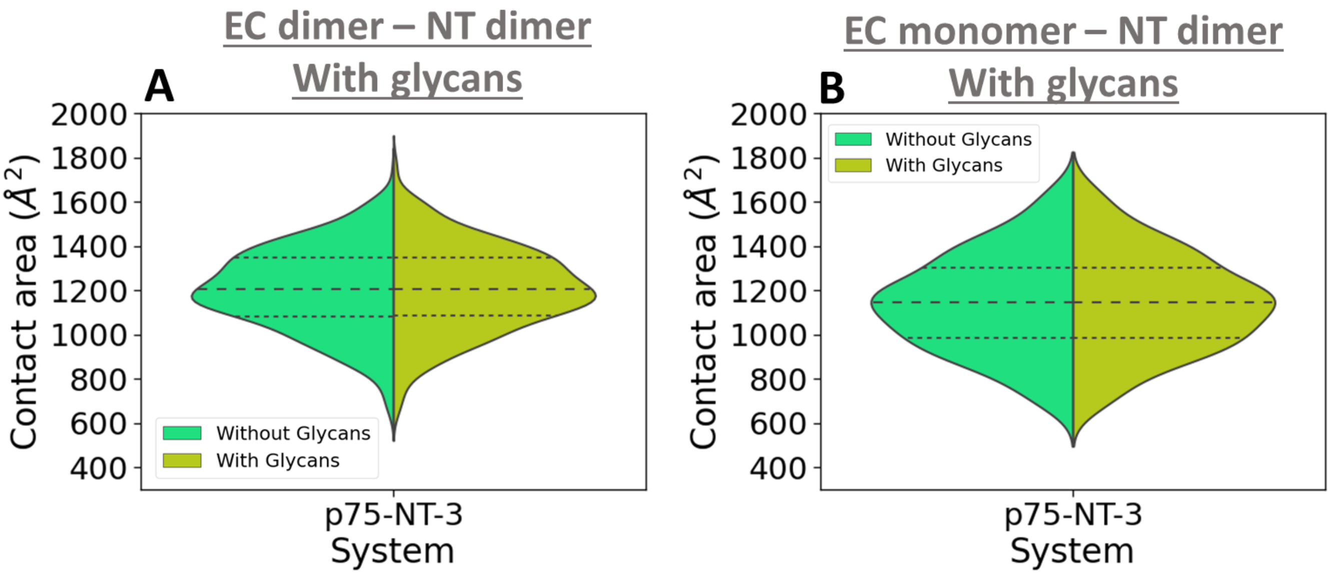

Figure 4.9: Calculated contact area between the p75-EC domain with the NT-3 shown as distributions. Only the systems with (A) p75-EC as a homodimer in complex to NT-3 or (B) as a monomer in complex with NT-3 were used for this calculation as only in these systems NT-3 was present. In both cases, the contact area between the two proteins in the presence and absence of the glycan is shown in yellow and green, respectively.

As a next step, I calculated the radius of gyration of the p75-EC domains for the glycosylated or not systems (Figure 4.10). Small radius of gyration values indicate a more compact protein structure, while higher values suggested more extended conformations. The results showed that the glycosylated and not systems are very similar in terms of radius of gyration distributions. Only in the "p75-EC monomer/NT-3 dimer" system there is perhaps a difference with slightly higher radius of gyration values being sampled for the glycosylated systems. The apparent stability in the values of the radius of gyration suggests rigidity in the structure of the p75-EC domains, which might be due to the disulfide bond ladder that was previously discussed (Figure 4.5).

Subsequently, I examined the distances between pairwise p75-EC domains and the angles formed by each of the domain monomers and the NT-3 and checked for any differences between glycosylated and not systems (Figure 4.11). The average distances of the D1-D1, D2-D2 and D4-D4 domains from the two p75 monomers are a bit lower for the non-glycosylated systems, while the distance between the D3-D3 domains is slightly higher for the non-glycosylated system, although this difference is probably negligible. The angles follow similar patterns to the distances. These results indicate that the two p75-EC monomers are a bit more distant when the two N-glycans at N60 are present, which might happen for the two glycans to be accommodated within the two p75-EC monomers.

As a final comparison between the glycosylated and not systems, I performed Principal Component Analysis (PCA) to investigate the intrinsic motions of the proteins. I specifically calculated the principal components of the movement of the D1 domain of p75-EC which showed to fluctuate more compared to the other domains (Figure 4.12). For this, I aligned first the trajectories to the D2-D4 domains. Comparison of the 1st and 2nd principal components for the glycosylated and non-glycosylated systems shows similar behavior. The “p75-EC monomer” system seems to cover more PC1 space, which might be due to the increased fluctuations observed before (Figure 4.6). In the way that this PCA analysis was performed, i.e. separately for each replica simulation, the PC1 and PC2 are not necessarily the same in all replica simulations. Thus, to compare the PCs between different replicas, I calculated the dot products between the PC1s and PC2s from the various replicas (Figure A.4). The results showed that in some cases the PCs were pointing towards the same direction (positive dot products) between the glycosylated and non-glycosylated systems, while in other cases they were pointing in opposite directions (negative dot products), or were even perpendicular to each other (close to zero dot products). I also examined the time evolution of the 1st and 2nd principal components. The results are shown in Figure A.5. The systems visit the same PC1-PC2 space at all times of the simulation, which is probably facilitated by the narrow space that is explored by the system, consistent with the previously discussed rigidity of the p75-EC domain.

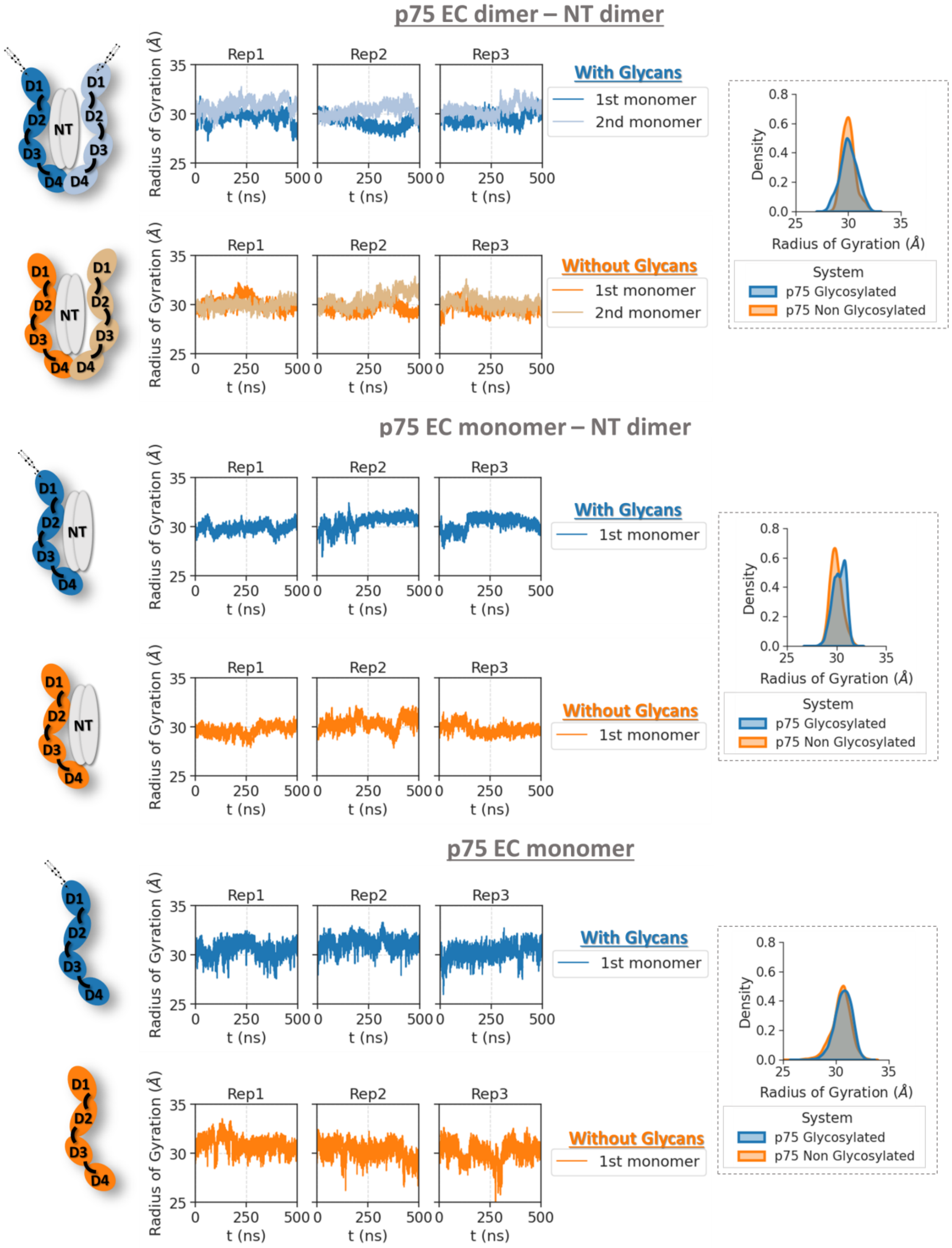

Figure 4.10: Time evolution and distribution of the radius of gyration values for the systems of p75-EC as a homodimer in complex to NT-3, as a monomer in complex with NT-3 and as a monomer alone, with

(blue) and without (orange) glycans. For the system of p75-EC as a homodimer in complex to NT-3, the radius of gyration was calculated for both p75-EC domains separately.

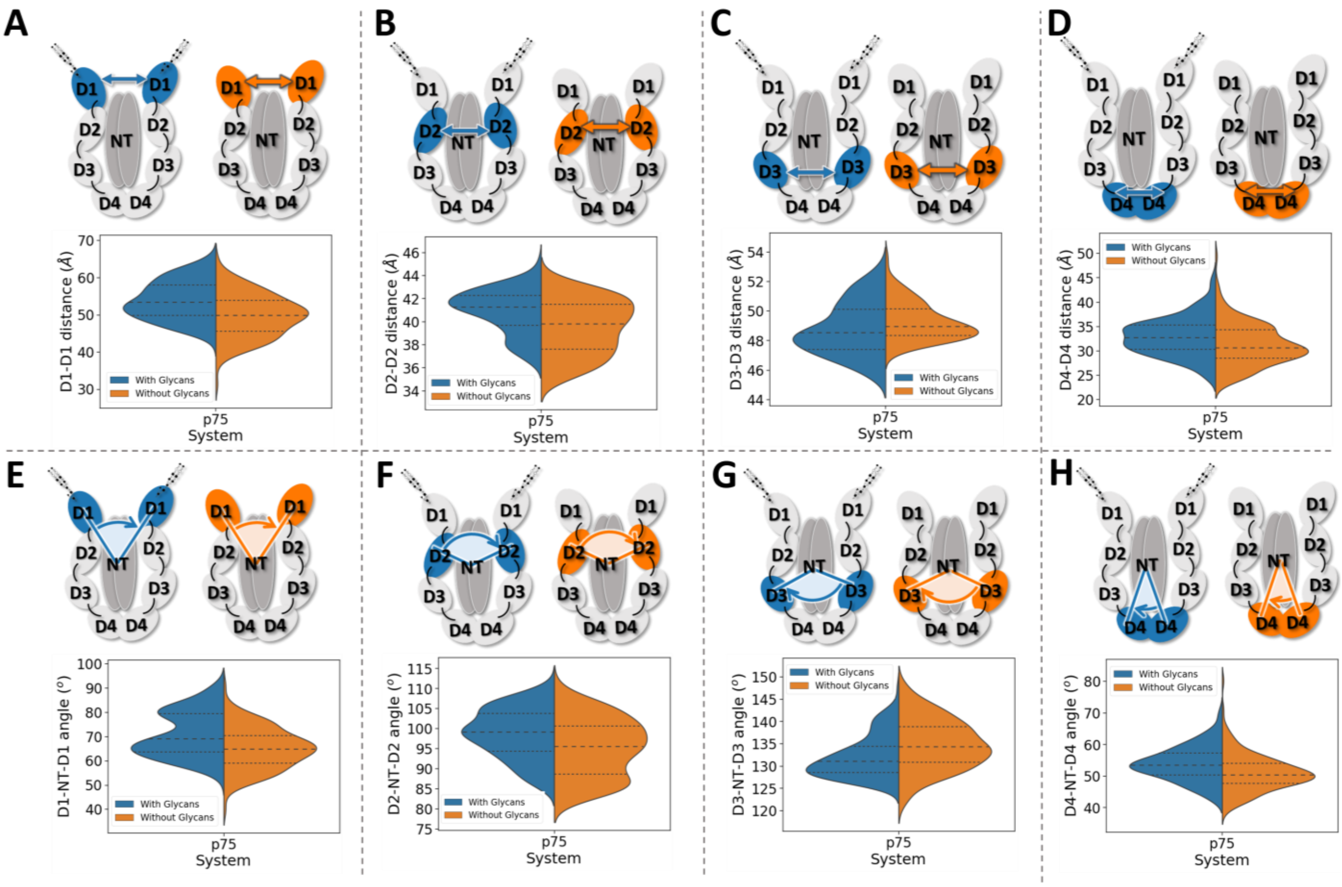

Figure 4.11: Calculated distributions of the distances and angles between the four p75-EC domains. (A)-(C) Distances between the COGs of D1-D1, D2-D2, D3-D3 and D4-D4 domains, in the presence (blue) and absence (orange) of glycans. (E)-(H) Angles defined by the COGs of D1-NT-D1, D2-NT-D2, D3-NT-D3 and D4-NT-D4 domains.

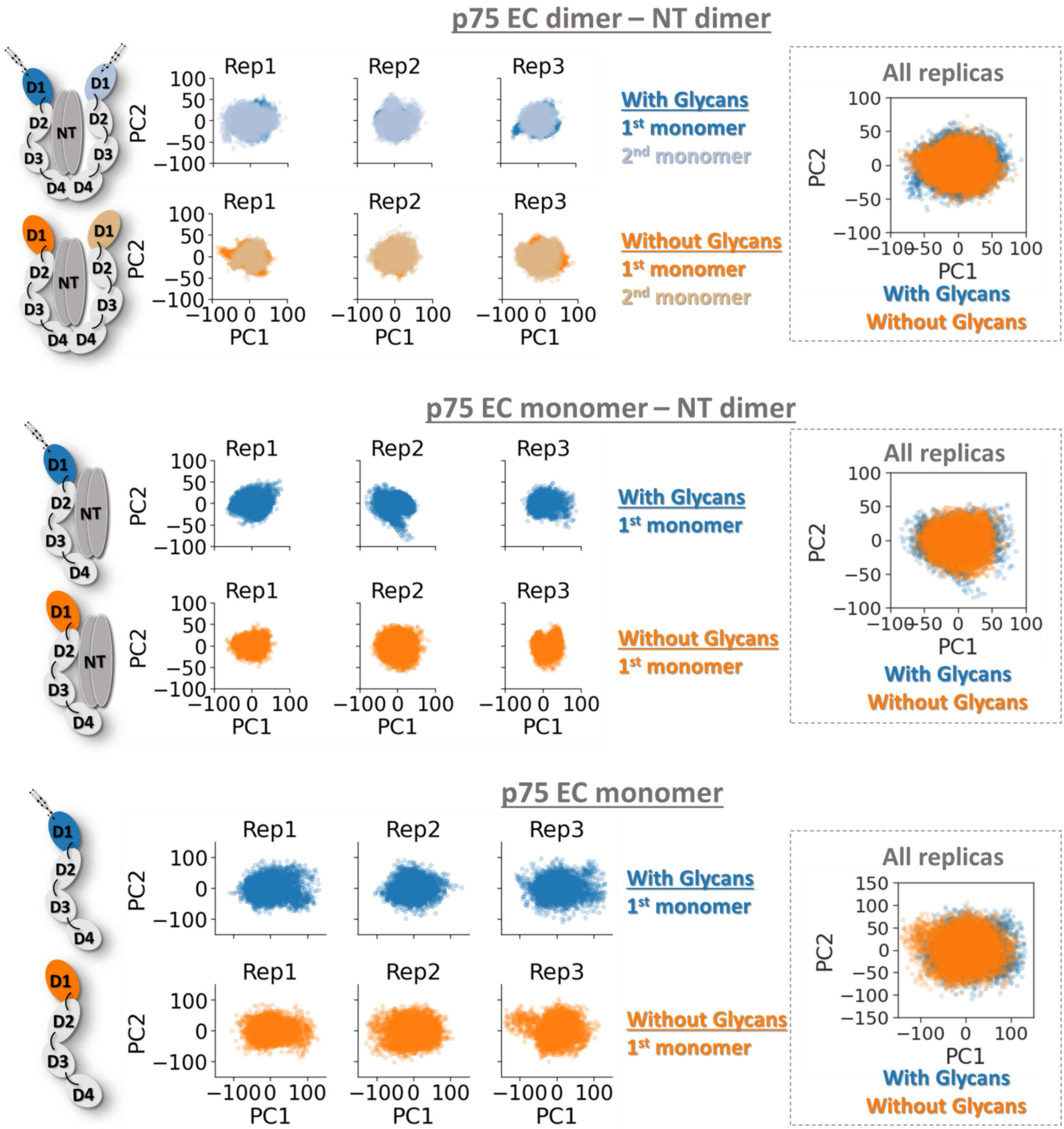

Figure 4.12: Principal component analysis (PCA) of the D1 domain of p75-EC after alignment to the rest of the domains for the glycosylated (blue) or not (orange) systems. Only the 1st and 2nd principal components are visualized.

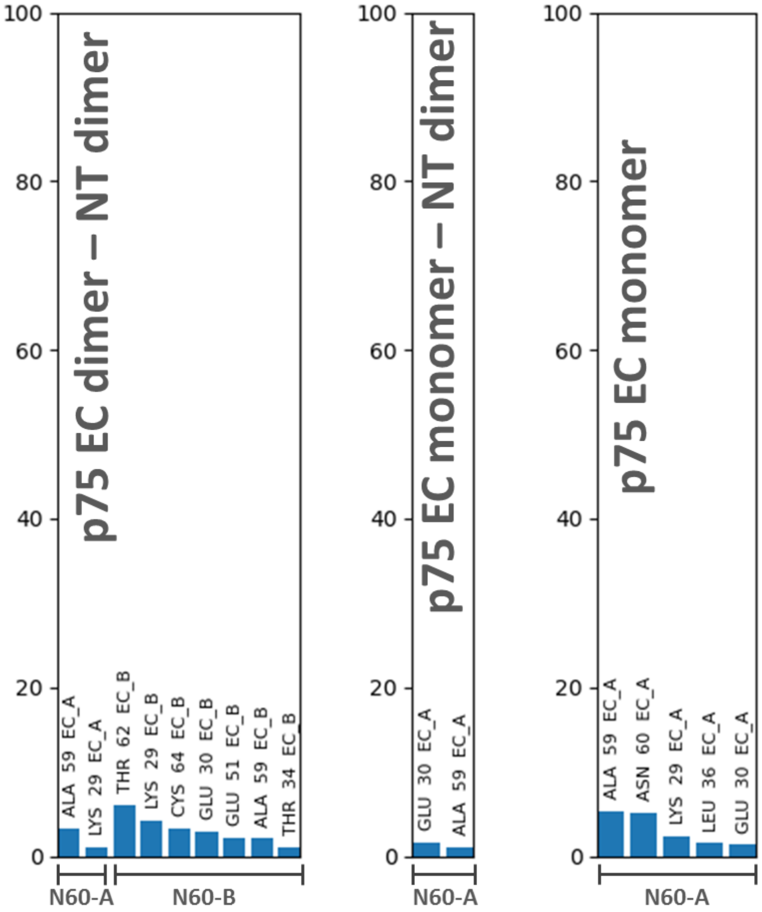

Figure 4.13: Percentage of contacts between the glycan at N60 and the protein amino acids in the three different glycosylated p75 systems. The x-axis shows the exact glycan at N60 from the two p75-EC monomers (A and B) and the y-axis the percentage of simulation frames that this glycan interacts with other residues, shown vertically on top of each bar.

Finally, I analyzed the interaction contacts between the glycan at N60 position and the protein amino acids (Figure 4.13), with a contact occurring when a heavy atom from the glycan is within 4.5 Å distance from a heavy atom in the protein. This analysis shows that the glycan interacts mostly with charged or polar residues, with the most common contacts being with Ala 59 (possibly due to the proximity to Asn 60 where the glycan is attached), as well as Lys 29 and Glu 30. I also examine the different conformations of the Asn 60 side chain with and without the glycan attached to it. For this purpose, I calculated the χ1 dihedral angle of N60 for the glycosylated and not p75 systems (Figure A.6). However, no difference was observed for the residue in the presence or not of the glycan.

The N-glycan at Asn 60 from one p75-EC monomer seemed to interact also with the same glycan from the second monomer in several simulation snapshots, with a visualization of this interaction shown in Figure 4.14. The glycans in this conformation interacting with each other can potentially block the NT from dissociating from p75, which might affect its binding kinetics. Also, the interacting glycans might help with the overall avidity of the complex and stabilize it in this dimer of homodimers state.

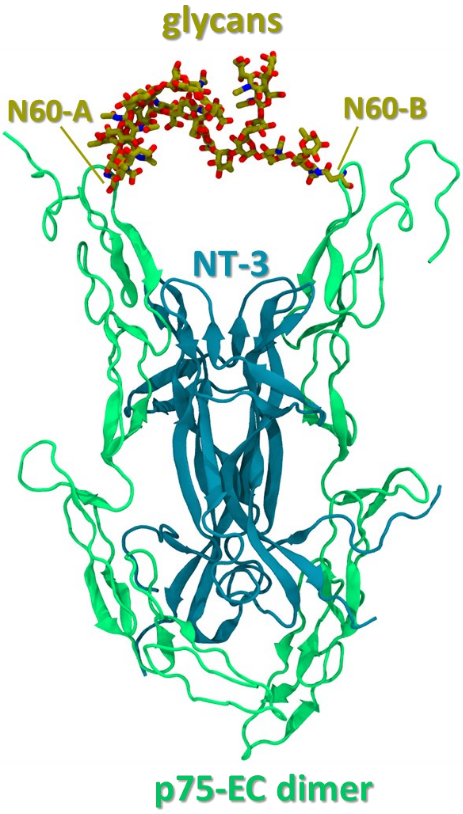

Figure 4.14: Interactions between the complex glycans at N60 from the two p75-EC monomers in a snapshot at 150 ns of the 1st replica. The p75-EC and NT-3 are shown in cartoon representation in green and blue colors, respectively. The complex glycans at N60 from the two p75-EC monomers, together with the N60 residue, are shown in licorice representation in dark yellow color.

4.4 Conclusions

In this chapter, I have modelled and simulated the glycosylated and non-glycosylated states of the extracellular (EC) domain of the p75 receptor, as a homodimer bound to NT-3, as a monomer bound to NT-3 and as a monomer alone. For the position and type of the single N-glycan present in the p75-EC structure I used experimental information[76,77,367] and build the atomistic models. To achieve reliable statistics from the MD simulations, I ran three replica simulation for each system, with each replica spanning a 500 ns time window.

From the simulation trajectories it became apparent that only the very N-terminal part of the p75-EC can be shielded by the single N-glycan at Asn 60 position, while it seems to also have minimal interactions with NT-3, as revealed also by contact area calculations. The cloud of glycan conformations appears to block the entrance at the upper region of the receptor, which might affect NT binding kinetics, which have been experimentally indicated to be different for the p75 compared to the Trk receptors.[383] The glycan shielding of the proteins, as estimated by ASA calculations, was low, probably because of the single glycan, which points away from the surface of the protein as revealed by visualization of the simulation trajectories. Bigger sizes of the probe that was used for the ASA calculations seemed to have a more apparent, but still small, glycan shielding up to 7% of the protein ASA, suggesting that the binding of larger proteins in the area proximal to the glycan may be more disturbed than that of small molecules.

Analysis of stability of the EC domains of p75 in the various systems, revealed considerably stable conformations, with the initial crystal structures being preserved during the simulations. This was shown by various types of analysis, such as RMSD, RMSF, radius of gyration and PCA, and it can possibly be attributed to the disulfide bond ladder created by 12 disulfide bonds in the p75-EC domain. The only regions of the p75-EC segment that was relatively flexible in the simulations was the N-terminal region of the D1 domain, which is disordered. The same analyses also showed that the D2 and D3 domains fluctuate more in the absence of NT. Additional analysis of the distances between the various p75-EC domains from the two p75 monomers in the homodimeric state of the receptor, showed that shorter distances occurred in the non-glycosylated state of the homodimer, which might happen for the two glycans to be accommodated within the two p75-EC monomers.

Finally, calculations of interaction contacts between the complex N-glycan at Asn 60 and the protein amino acids revealed interactions mostly with charged or polar residues, with the most common contacts being with Ala 59 (possibly due to the proximity to Asn 60 where the glycan is attached), as well as Lys 29 and Glu 30. In the homodimeric p75-EC simulations, the glycans from the two monomers interacted with each other, suggesting a potential blocking of the NT from dissociating from p75, which might affect its binding kinetics. Also, the interacting glycans might help with the overall avidity of the complex and stabilize it in this dimer of homodimers state.

5 Transmembrane p75 dimerization

5.1 Introduction to transmembrane p75 helix dimerization

Signal transduction by p75 is thought to occur through NT binding and exposure of binding sites on the receptor accessible for binding to other proteins.[155] Although several oligomerization states of p75 have been described in the literature, the model of receptor dimerization for activity prevails.[57,113,118,384–386] In fact, disulfide-linked receptor dimers pre-exist in the membrane before activation.[57] Only when NT homodimers bind in the extracellular (EC) domains of p75 and induce dimerization of it,[16,54–56] is the receptor activated.[57] The disulfide bond, which is located at C257 in the transmembrane (TM) domain of p75, is required for receptor signaling in response to NT binding, allowing the propagation of conformational changes from the EC to the intracellular (IC) domains.[57] The conformational changes that lead from an inactive to the active state of the receptor have been imitated by cysteine-scanning mutagenesis, which led to the formation of active disulfide-linked dimers.[384] Cysteine point mutations were introduced in the EC linker that connects the EC and TM domains. Out of all the tested mutations, mutants P242C, T248C, T249C and D250C resulted in constitutive receptor activity in the absence of NT.[384]

The TM domain of p75 stabilizes the receptor dimers with a disulfide bond between the helix monomers, at Cys 257 (Figure 5.1A), which is important for NGF signaling.[57] The TM dimer structure of the wild-type (WT) p75, as well as that of the functionally inactive p75-C257A mutant, have been solved with Nuclear Magnetic Resonance (NMR) in dodecylphosphocholine (DPC) lipid micelles (Figure 5.1B,C).[387] The p75-WT dimer is stabilized by the C257-C257 disulfide bond, but also by van der Waals interactions of L260, V264, V265 and π-stacking of F273 and W276. The crossing angle is 36°. C257 is at the interface of the p75-WT dimer even under reducing conditions, and thus in the absence of the disulfide link, but in this case the free energy of dimerization is -0.9 kcal/mol, which is quite weak.[387] Thus, the disulfide bond seems to be important to stabilize the weak dimer.

The p75-C257A mutant forms dimers through the $A^{262}xxxG^{266}$ motif on the opposite side of the α-helix from C257 (Figure 5.1D). This type of motifs are commonly found at the interface of TM helices.[388–390] However, in contrast to similar GxxxG-like motifs that form right-handed dimers, p75-C257A forms a left-handed arrangement, with crossing angle 66°. Residues A269, Y270 and F273 also participate in the interface. The AxxxG motif is not at the interface of the WT p75 dimer in the NMR structure, which means that it is probably not relevant for receptor function. However, mutagenesis studies showed that the AxxxG motif is important for intramembrane p75 proteolysis by γ-secretase.[387] Chemical crosslinking experiments revealed that the C257A mutant can still form homodimers in the membrane through non-covalent interactions.[57] Mutation of the Gly 266 from the AxxxG motif to an Ile abolishes the dimer formation in the cell membrane, indicating that the AxxxG motif is indeed at the TM helix interface in the full-length mutant p75-C257A or at least plays an indirect effect.[57] The free energy of dimerization of the mutant is -1.8 kcal/mol, which is stronger than the non-disulfide linked p75-WT.[387]

Fluorescence resonance energy transfer (FRET) experiments showed that NT binding to p75 tagged with the fluorophores at the C-terminus, i.e. in the death domains, leads to a conformational change of the receptor that depends on the presence of the disulfide bond at C257.[57] Decrease in FRET upon NT binding indicated dissociation of the death domains, and it is proposed that p75 undergoes a scissors-like movement in which the C257-C257 bond plays the role of the fulcrum.[57]

All these experimental data demonstrate the key role of the TM domain of p75 receptor for its function, and thus in this chapter of the thesis, I have studied the dynamics of the WT and C257A p75 homodimers in lipid micelles and bilayers, using coarse-grained and atomistic, unbiased and enhanced sampling molecular dynamics (MD) simulations. The main goal was to investigate the conformation landscape of the TM helices of p75 WT and C257A mutant, and their potential implications in receptor signaling. Part of this work has been published in a preprint article at the time of writing the thesis.[51]

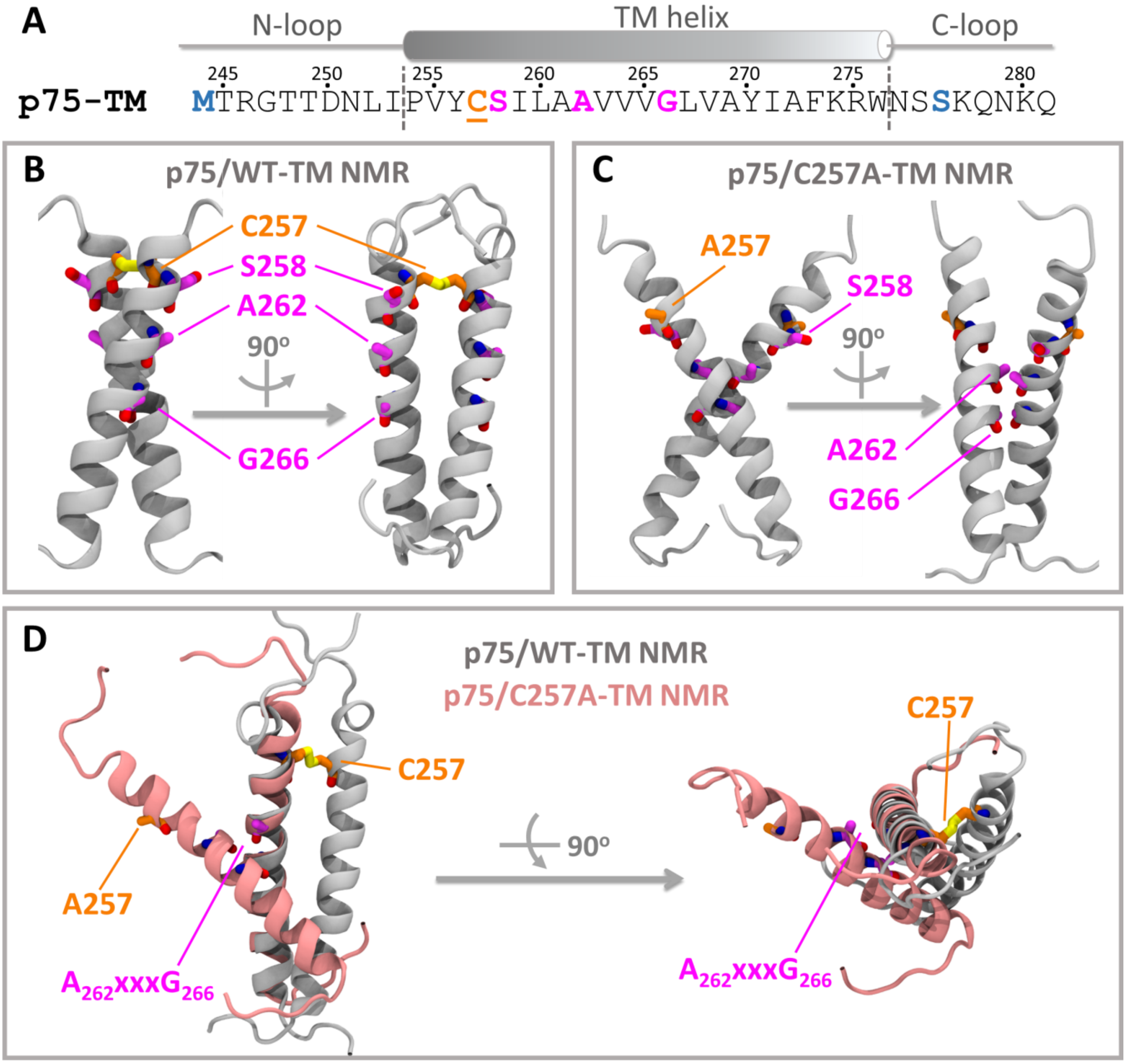

Figure 5.1: Overview of simulated protein structures. (A) Sequence of the p75-TM receptor used in the simulations. The TM helical part from the p75 NMR structures (PDB IDs: 2MIC and 2MJO)[387] is shown with the dashed lines. Also shown are the N- and C-terminal loops solved in the NMR structures. The Cys 257 residue in p75, which is mutated to Ala in the NMR structure of p75 (PDB ID: 2MJO), is underlined and colored orange. Mutated residues in the NMR sequence with respect to the human p75 are colored blue. Residues from the GxxxG-like motifs are depicted in magenta. (B-C) Cartoon representations of the (B) p75-WT (PDB ID: 2MIC) and (C) p75-C257A (PDB ID: 2MJO) NMR structures. The GxxxG-like motifs and C257A are shown in magenta and orange licorice representation, respectively. (D) Alignment of p75-

WT and p75-C257A TM NMR structures on one of the two helices for comparison. Figure partially adapted from Athanasiou et al.[51] In this figure, I created subfigures (B), (C), and (D).

5.2 Methodology

Coarse-grained (CG) simulations

I simulated the TM sequences of the p75-WT (Figure 5.1A) and the p75-C257A mutant. As initial models for the simulations, I used the NMR structures of the p75-WT and p75-C257A TM homodimers, with PDB IDs 2MIC and 2MJO,[387] respectively (Figure 5.1B,C,D).

I performed coarse-grained (CG) molecular dynamics (MD) simulations using the Martini 2.2[309,310] force field, of the p75-WT and p75-C257A TM homodimers (Systems 1-2, Table 5.1) in self-assembled dodecyl-phosphocholine (DPC) micelles (Figure 5.2). This micellar environment corresponds to the conditions in which the two NMR structures were solved. I performed all-atom to coarse grained conversion with the martinize.py script. To enforce the helical secondary structure of the TM helices and allow at the same time the N-terminal and C-terminal linkers to be flexible, I applied an elastic network model on the TM helices during the simulations. I chose an elastic force constant of 500 kJ/(mol·nm2) and a distance cutoff range of 5-9 Å for the harmonic restraints of the elastic network. I built the simulation box by placing the TM helices together with 100 DPC lipids at random initial positions. This was chosen from the detergent-to-protein molar ratio (DPR) of 50:1 used for determining the NMR structures of p75-TM.[387] I solvated the simulation box with a ration 9:1 of the non-polarizable water model (NPW) and the anti-freeze water type (WF). For system neutralization, I added Na+ and Cl− ions for a final ionic strength of 150 mM.

Table 5.1: Overview of simulations I performed for the p75-TM systems. I conducted simulations for the p75-WT and p75-C257A TM dimers. The simulation types are all-atom (AA), coarse-grained (CG) and coarse-grained metadynamics (CG-MetaD) simulations.

System No.	Protein	Lipid environment	Simulation type	Replicas	Time/Replica (µs)
1	p75-WT TM	DPC micelle	CG	10	20
2	p75-C257A TM	DPC micelle	CG	10	20
3	p75-WT TM	DPC micelle	AA	3	0.5
4	p75-C257A TM	DPC micelle	AA	3	0.5
5	p75-C257A TM	POPC bilayer	AA	1	0.45
6	p75-C257A TM	neuronal bilayer	AA	1	0.19
7	p75-C257A TM	POPC bilayer	CG-MetaD	1	144

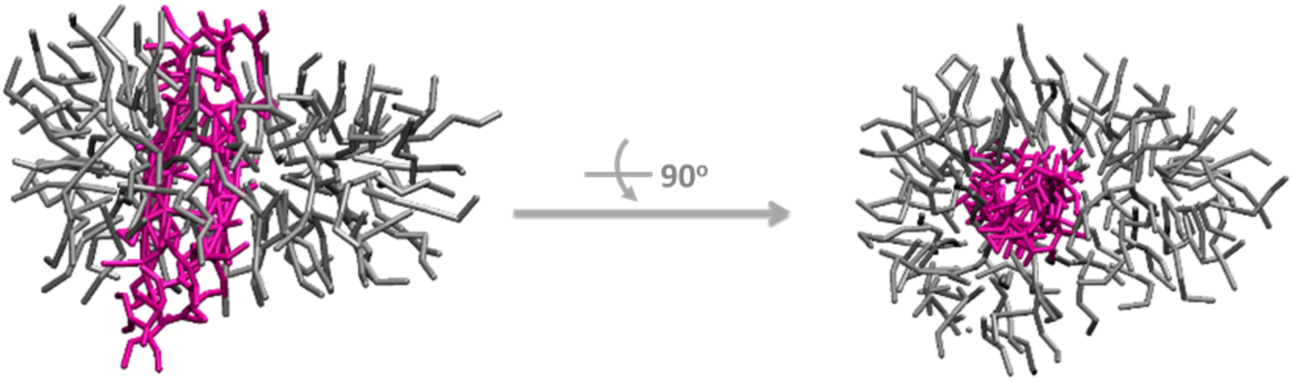

Figure 5.2: p75-TM domain dimer in a DPC micelle in CG representation. The DPC lipids are shown in CG grey licorice representation, whereas the p75-TM dimer is shown in magenta.

For all simulations, I used the GROMACS v.2020 MD engine[369] and I followed an equilibration protocol consisting of a steepest-descent energy minimization and a NPT equilibration for 2 µs with restraints in the backbone of the helices of 4000 kJ/(mol·nm^2) force constant. These constraints keep the initial arrangement of the helices, which corresponds to the NMR structures 2MIC and 2MJO,[387] and allows the self-assembly of the DPC lipids in micellar forms around the helices. I monitored the self-assembly of the micelles with the radius of gyration of the lipids (Figure A.7). I performed the NPT equilibration simulations at 310 K and 1 bar with the velocity rescale thermostat[391] and the Berendsen barostat[392] with a coupling constant of 4 ps and isotropic pressure coupling with $4.5\cdot10^{-5}$ bar^{-1} compressibility. For Coulomb and van der Waals interactions, I used a 1.1 nm cutoff distance. I performed a total of 20 replica equilibration simulations for both p75-WT and p75-C257A systems, starting from different velocities and lipid positions. Then, I chose 10 replicas that had formed micelles and I progressed them to production simulations (Figure A.7).

I ran NPT production simulations for 20 µs each (Systems 1-2, Table 5.1) at 310 K and 1 bar with the velocity rescale thermostat with a coupling constant of 1 ps, and the Parrinello-Rahman barostat,[373,374] with a coupling constant of 12 ps and isotropic pressure coupling with $3\cdot10^{-4}$ bar^{-1} compressibility. For Coulomb and van der Waals interactions, I used a 1.2 nm cutoff distance. For all CG simulations, I used a 20 fs time step.

Atomistic simulations in micelles

To assess the effectiveness of the CG simulation sampling, I ran also some test all-atom (AA) MD simulations of the p75-WT and p75-C257A systems in DPC micelles (Systems 3-4, Table 5.1). I ran 3 replica AA simulations, and as starting configurations I used the last frames from 3 CG replicas by back-mapping to AA level, using a CG-to-AA map created by Christina Athanasiou in the MCM group of HITS gGmbH (

Figure A.8) and the backward.py script.[393] As for the CG simulations, I performed the AA simulations also with the GROMACS v.2020.[369] For all AA simulations I used the CHARMM36m force field.[370]

I followed an equilibration protocol consisting of a steepest-descent energy minimization, one NVT and three NPT equilibration steps, for 200 ps and 1 ns respectively. I employed a gradual removal of restraints from force constant of 4000 kJ/(mol·nm^2) to 1000 kJ/(mol·nm^2) for the backbone and from 2000 kJ/(mol·nm^2) to 500 kJ/(mol·nm^2) for the side chains. I used the Berendsen[392] thermostat for all equilibration steps, except for the last for which I used the Nosé-Hoover thermostat.[371,372] Similarly, I used the Berendsen barostat for all equilibration steps, except for the last for which I used the Parrinello-Rahman barostat.[373,374] As time steps, I used 1 fs for the 1st equilibration step and 2 fs for the subsequent ones. I chose a coupling constant of 5 ps and isotropic pressure coupling with $4.5\cdot10^{-5}$ bar^{-1} compressibility. For Coulomb interactions, I employed the Particle Mesh Ewald (PME)[375,376] summation for the treatment of long range electrostatics with a cutoff distance of 1.2 nm, and for van der Waals interactions I used a force-switch function, that changes the shape of the force between the range of

1.0 and 1.2 nm. I used the Linear Constraint Solver (LINCS) algorithm[377] to fix the length of bonds with hydrogens. After the equilibration, I performed 3 production replica simulations of 500 ns (Systems 3-4, Table 5.1) using the same parameters as for the last equilibration step, although without any restraints.

Atomistic simulations in membranes

Additionally to the AA simulations in DPC micelles, I also ran some test simulations in membranes to investigate the influence of the lipid environment in the p75-C257A TM dimer stability. As membranes I used a pure 1-palmitoyl-2-oleoyl-sn-glycero-3-phosphocholine (POPC) membrane and a complex neuronal bilayer (Systems 5-6, Table 5.1). I will describe in more detail the exact neuronal membrane composition in Chapter 6. For the building of the TM systems in the membranes I used the Membrane Builder of CHARMM-GUI,[394] with which I also added NaCl at neutralization and ionic strength 150 mM. Again, I used GROMACS v.2020 for all simulations and the CHARMM36m force field. I ran several equilibration steps for proper membrane behavior, consisting of two energy minimizations with steepest descent and conjugate gradient, one NVT equilibration at 310 K for 200 ps with 1 fs time step, and 4 NPT equilibrations at 310 K, 1 bar for 1, 2, 4 and 5 ns each. In all equilibration steps, I used restraints on heavy atoms that were gradually decreased in the various steps, from 4000 kJ/(mol nm^2) to 1000 kJ/(mol nm^2). The detailed equilibration protocol of atomistic membranes can be found in Chapter 6. During equilibration I used the Berendsen thermostat and barostat, with a 5 ps coupling constant, semi-isotropic pressure coupling and $4.5 \cdot 10^{-5}$ bar^{-1} compressibility. For Coulomb interactions, I employed the Particle Mesh Ewald (PME)[375,376] summation for the treatment of long range electrostatics with a cutoff distance of 1.2 nm, and for van der Waals interactions I used a force-switch function, that changes the shape of the force between the range of 1.0 and 1.2 nm. I used the Linear Constraint Solver (LINCS) algorithm[377] to fix the length of bonds with hydrogens. At the end of the equilibration protocol, I ran a production simulation for 450 and 190 ns for the POPC and neuronal membranes, respectively (Systems 3-4, Table 5.1). For production I used the same parameters as for the last equilibration step except for the thermostat and barostat which were the Nosé-Hoover[371,372] and Parrinello-Rahman,[373,374] respectively.

Coarse-grained metadynamics (CG-MetaD) simulations

To estimate the dimerization free energy of the TM helices of p75-C257A, I ran well-tempered metadynamics[320] in the CG level with Martini 2.2 and in a POPC membrane. I used the insane script[395] to put the protein in POPC bilayer and ran the same equilibration protocol presented before for the CG simulations. For the CG-MetaD simulation I used GROMACS v.2020 patched with Plumed v.2.7.[396] I used the interhelical distance as the collective variable (CV) (Figure 5.3A), a Gaussian potential of width 0.05 nm, initial height 0.05 kJ/mol that decreases over time, deposition steps 5000 and f=10 bias factor. Similar MetaD parameters were shown before successful in estimating the dimerization free energy of the EGFR TM helices.[314] I used the same MD parameters as for the unbiased CG simulations discussed before, with the exception of the semi-isotropic pressure coupling for the membrane system. I ran the CG-MetaD simulation for 144 μs.

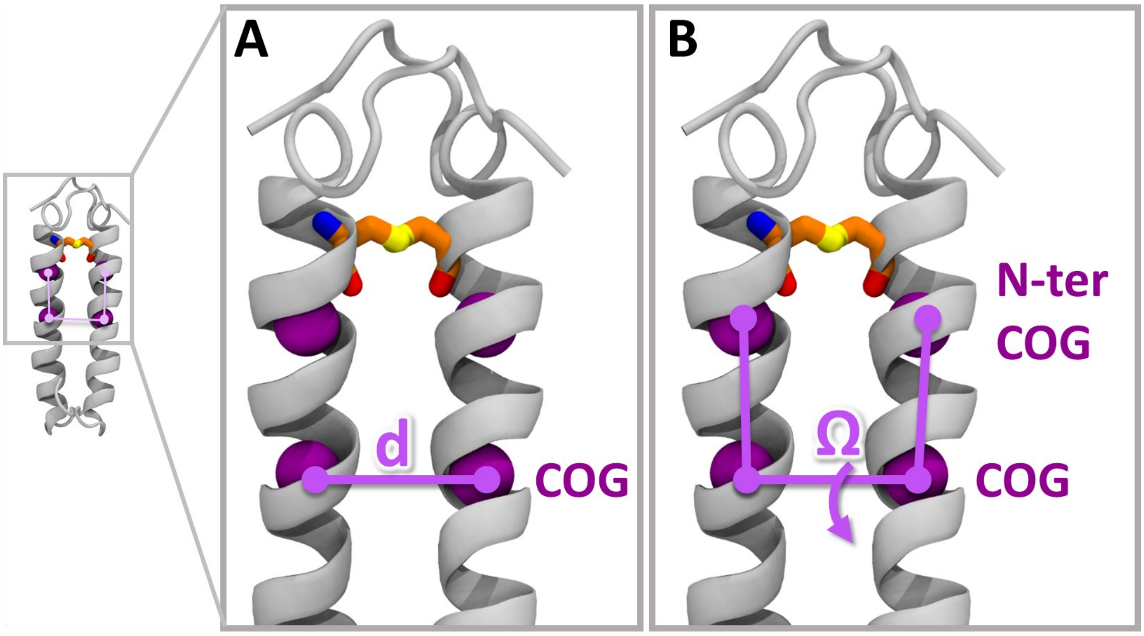

Figure 5.3: Order parameters of TM helices. (A) Interhelical distance (d) used as collective variable (CV) in the CG-MetaD simulation. For the definition of the distance I chose the centers of geometry (COG) of the backbone beads (middle purple spheres). (B) Interhelical crossing angle (Ω) defined by COGs of the helix backbone particles and the COGs of the N-terminal halves of the helices.

Analysis of simulations

At the end of each replica simulation I performed a set of post-processing analyses, with the fixing of periodic effects being with the *gmx trjconv* tool of GROMACS being the first step. For the multiple replica simulations in CG level, I concatenated all replica trajectories in a single trajectory and analyzed it as one to consider the whole of the TM arrangements sampled in the simulations. I also performed a rigid-body alignment to the backbone of one of the helices in the 1st frame of the simulations. I rendered all protein structures presented in this thesis with VMD 1.9.3.[355]

Geometric helix parameters

For the analysis of the helical arrangements during the simulations I used six geometric parameters: (1) the interhelical distance (d) defined by the centers of geometry (COG) of the backbone beads (Figure 5.3A), (2) the interhelical crossing angle (Ω) defined as a dihedral by COGs of the helix backbone particles and the COGs of the N-terminal halves of the helices (Figure 5.3B), (3), (4) the rotation around the axis of each helix, mentioned later as phase and position, defined as a dihedral by the COG of the N-terminal half of one of the helices, the COGs of the backbone particles of the two helices and the COG of Ala 262 which is part of the AxxxG motif in p75, and finally (5), (6) the distance between the N- and C-termini of the helices. I calculated these parameters in all simulation frames using the MDAnalysis[378,379] and the numpy.linalg.norm function of the Numpy library.[382] I visualized the geometric parameter distributions during the simulations with Kernel Density Estimation (KDE) plots using the seaborn.kdeplot function of Seaborn.[381]

TM helix contact analysis

I analyzed the contacts between all the residues of the TM helices by defining a contact when two CG particles are within 6 Å distance. For the calculation I used MDAnalysis and the Pandas[397,398] and Matplotlib[380] python libraries for data manipulation and visualization.

CG-MetaD analysis

I performed a series of evaluation analyses of the CG-MetaD simulation to assess its convergence. Specifically, I monitored the time evolution of the CV and the Gaussian height to ensure a diffusive behavior of the CV and a reducing height over time. Additionally, I monitored the time evolution of the free energy surface as a function of the CV which should converge to a specific profile and not change much with time. I also calculated the dimerization free energy over time which should reach a plateau or fluctuate around a specific value with time. For the dimerization free energy I defined the bound and unbound states with d < 1.5 nm and d > 1.5 nm, respectively. Finally, I performed calculation of the free energy error with block analysis, which should reach a plateau as the block size increases. I calculated the error every 10 blocks. I ran all these analyses with Plumed. As an analysis of the CG-MetaD simulation, I estimated the free energy surface as a function of the six geometric parameters mentioned before, by applying a reweighting protocol that gives the Boltzmann distribution of variables different from the biased CV. I calculated the histograms of the reweighted variables and their conversion to free energy with Plumed.

5.3 Results

The p75 receptor is found in a disulfide-linked homodimeric state in the cell membrane prior to activation.[57] The disulfide bond is positioned in the TM helices which are covalently bound at C257, as determined in the NMR structure of p75-WT TM dimer.[387] This disulfide bond is necessary for NT-induced receptor activation.[57] Thus, a conformational change in the TM helices is expected to take place during receptor activation. The existence of the disulfide bond, which holds the helices tightly bound, does not make obvious what this conformational change is. This, in combination with the existence of a totally different arrangement of the TM helices when the disulfide bond is missing, as in the case of the p75-C257A mutant,[387] render further investigation of the p75 TM domain dynamics important. For this reason, I performed Molecular Dynamics (MD) simulations of the p75-WT and p75-C257A TM dimers to investigate any differences in their dynamical behavior.

I decided to perform coarse-grained (CG) MD simulations with the Martini force field, which has been previously used in multiple studies of biomolecular system simulations and has successfully captured the configurations of TM helical dimers from different proteins.[311,313–315,399] In CG force fields multiple atoms are represented as one bead, with the Martini force field modeling four heavy atoms as one bead. This reduces significantly the size of the simulated systems and allows for longer simulation times and thus better sampling.

I simulated the NMR structures of p75-WT and p75-C257A mutant TM helical homodimers in self-assembled dodecyl-phosphocholine (DPC) micelles. I chose DPC micelles as this is the lipid environment used for the NMR structures.[387] I performed 10 simulation replicas of 20 µs each for each of the systems. I evaluated the various arrangements of the helices in the simulation with Kernel Density Estimates (KDE) of six order parameter distributions. These parameters have been found adequate to describe the various TM arrangements. The parameters were 1) the interhelical distance (d) defined by the centers of geometry (COG) of the backbone beads, (2) the interhelical crossing angle (Ω), (3), (4) the rotation around the axis of each helix, mentioned as phase and position, and finally (5), (6) the distance between the N- and C-termini of the helices. The results are shown in Figure 5.4 and Figure 5.6 for p75-WT and p75-C257A, respectively.

During the CG simulations of p75-WT (Figure 5.4) the helices were covalently bonded with the disulfide linkage at C257. This reduces the degrees of freedom of the arrangements that can be adopted by the helices, especially the rotation around them. This is revealed by the root mean squared deviation (RMSD) and crossing angle calculations in Figure A.9 which are stable during the simulations. This is also evident by the very narrow, single maximum that was explored in the phase-position space (Figure 5.4 phase-position heatmap). The d-Ω heatmap also shows that only one maximum was sampled, but in this case a bit more exploration is observed, with the interhelical distance taking values between 7.5 and 9.5 Å and the crossing angle ranging from -45^o to -30^o, corresponding to right-handed helical arrangements as the NMR structure. The NMR arrangement is at the center of the maximum, which shows that it corresponds to a stable configuration. Visual comparison of the NMR structure with the simulation arrangements (Figure 5.4 figures within heatmaps) shows that, during the simulations, arrangements similar to the NMR structure were sampled, with some rotation around the disulfide bond giving smaller or larger Ω values, corresponding to a scissors-like movement. This leads to variations in the N-ter and C-ter interhelical distances as well, which range at 14-21 Å and 9-13 Å, respectively. This movement especially in the C-ter helical distance might be important for transferring the activation signal intracellularly.

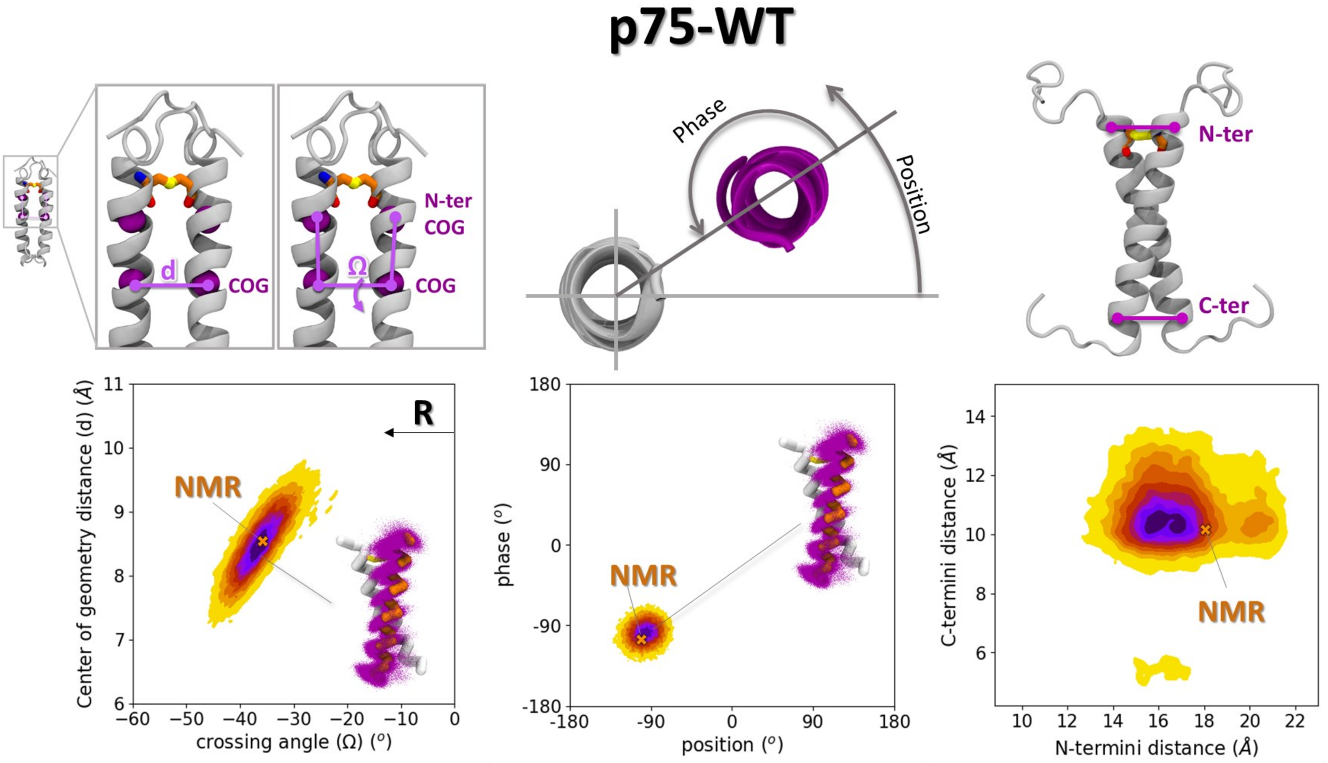

Figure 5.4: Analysis of p75-WT TM homodimer arrangements from CG simulations. Density distribution plots are shown for the six geometric parameters that I chose to describe the TM helix arrangements: interhelical distance, crossing angle (Ω), phase and position, and N- and C-termini distance. Negative crossing angle values correspond to right-handed helical arrangements ("R"). The NMR structure is shown in the orange cross. Within the heatmaps, the helical arrangements that correspond to the maxima are visualized as follows: after alignment of the helical dimer to the 1st helix of the NMR structure, the 1st helix backbone is visualized in white licorice representation, the 2nd helix backbone of the NMR is shown in orange licorice representation, and the 2nd helix backbone from the simulation snapshots that correspond to the maximum is shown in purple dot representation.

Subsequently, I analyzed the residues of the TM helices that are found at the interface in the maximum that occurred in the d-Ω heatmap (Figure 5.4). For this, I extracted the simulation frames that correspond to this maximum and ran a contact analysis between the two helices (Figure 5.5). I calculated the interactions between the two helices as contacts, with a contact defined by two CG beads from two residues being at 6 Å or less distance. The results are shown in Figure 5.5, and they revealed mostly homotypic interactions between the helix monomers, i.e. interactions involving the same residue from the two helices, which coincide with the residues that participate in the NMR interface (Figure 5.5, underlined residues). This is in agreement with the heatmaps in Figure 5.4, which showed that the NMR interface was preserved during the simulations.

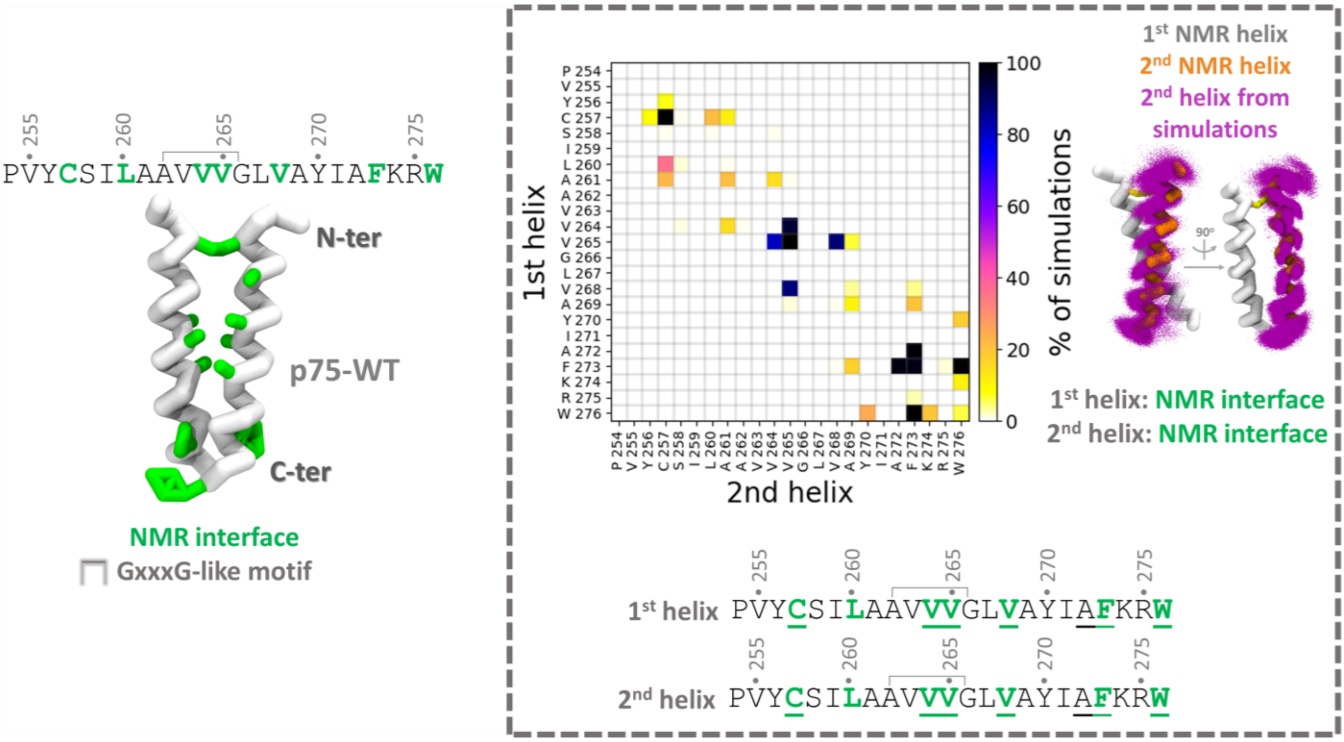

Figure 5.5: Contact analysis of p75-WT TM helices. Left: p75-WT TM NMR structure (PDB ID: 2MIC) in CG representation. Interface residues are shown in green, while the GxxxG-like motif is indicated with bracket. Right: I analyzed the helical arrangements from the maximum in the d-Ω heatmap (Figure 5.4) for their contacts. The contact map between the helix residues presents the occupancy during the ten replica simulations. The highest interacting residues are underlined in the sequences, while the residues at the p75-WT NMR interface are colored green. A visualization of the simulation arrangements (purple) is shown in alignment to the 1st frame (white, orange), i.e. the NMR structure.

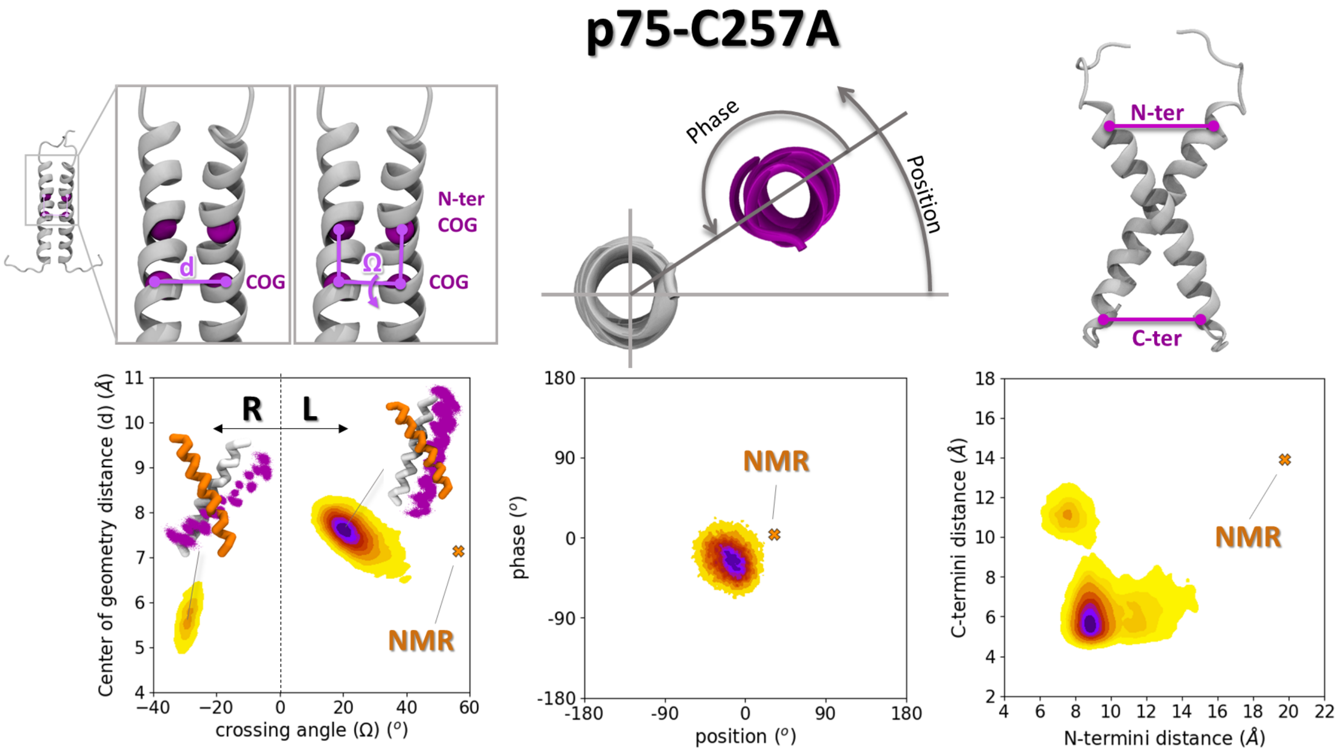

Figure 5.6: Analysis of p75-C257A TM homodimer arrangements from CG simulations. Density distribution plots are shown for the six geometric parameters that I chose to describe the TM helix arrangements: interhelical distance, crossing angle (Ω), phase and position, and N- and C-termini distance. Negative crossing angle values correspond to right-handed helical arrangements (“R”) and positive values to left-handed helical arrangements (“L”). The NMR structure is shown in the orange cross. Within the heatmaps, the helical arrangements that correspond to the maxima are visualized as follows: after alignment of the helical dimer to the 1st helix of the NMR structure, the 1st helix backbone is visualized in white licorice representation, the 2nd helix backbone of the NMR is shown in orange licorice representation, and the 2nd helix backbone from the simulation snapshots that correspond to the maximum is shown in purple dot representation.

I did the same analysis calculations for the p75-C257A TM dimer in the CG simulations. The RMSD and crossing angle calculations indicate some deviation from the initial NMR structure (Figure A.10). I also analyzed the order parameters with 2D heatmaps (Figure 5.6) as for p75-WT. The d-Ω heatmap shows that two maxima were sampled with interhelical distances around 5.5 and 7.5 Å and negative and positive crossing angles, corresponding to right- and left-handed helical arrangements of ca. -30° and

30^{o} crossing angles, respectively. Interestingly, the NMR arrangement is not located in any of the two maxima in this 2D space. This means that the system deviated from the NMR structure, which occurs as unstable during the CG simulations. In the phase-position space only one maximum occurred, which apparently encompasses the arrangements from both maxima in the d-Ω heatmap. Close to 0^{o} values in phase and position indicate that the A262, which is part of the AxxxG motif, is found at the interface of the helices. The N-ter and C-ter interhelical distance heatmap shows smaller distance compared to the NMR structure, which suggests more parallel helices. As for the d-Ω heatmap, the NMR arrangement is not located at any maximum in the phase-position or the N-ter and C-ter interhelical distance heatmaps.

I performed the same contact map analysis for the two p75-C257A maxima in the d-Ω heatmap, as I did for p75-WT. The results are presented in Figure 5.7. I post-processed the frames from each of the two maxima in the d-Ω plot. In the 1st and most populated maximum, the helices interact through the A^{262}xxxG^{266} motif as in the case of the p75-C257A mutant NMR structure. Residues from the whole length of the TM helices were shown to participate at the interface of the helices, which suggests a more parallel arrangement compared to the NMR structure, which was also suggested by the smaller crossing angle and N-ter and C-ter interhelical distances in Figure 5.6. Next, I analyzed the arrangements that correspond to the 2nd maximum in the d-Ω 2D heatmap, which involve left-handed helical arrangements in contrast to the right-handed NMR structure. The contact analysis showed that the A^{262}xxxG^{266} motif of the p75-C257A mutant NMR structure is preserved in this maximum as well, while interactions in the whole length of the helices suggest a parallel helix configuration. Overall, even though the exact arrangement of the helices in the p75-C257A NMR structure was not preserved during the CG simulations, the two new arrangements that occurred bear the A^{262}xxxG^{266} motif at their interface, as the NMR structure. However, since this mutant cannot have functional activity, this motif at the interface probably does not correspond to a biologically relevant state.

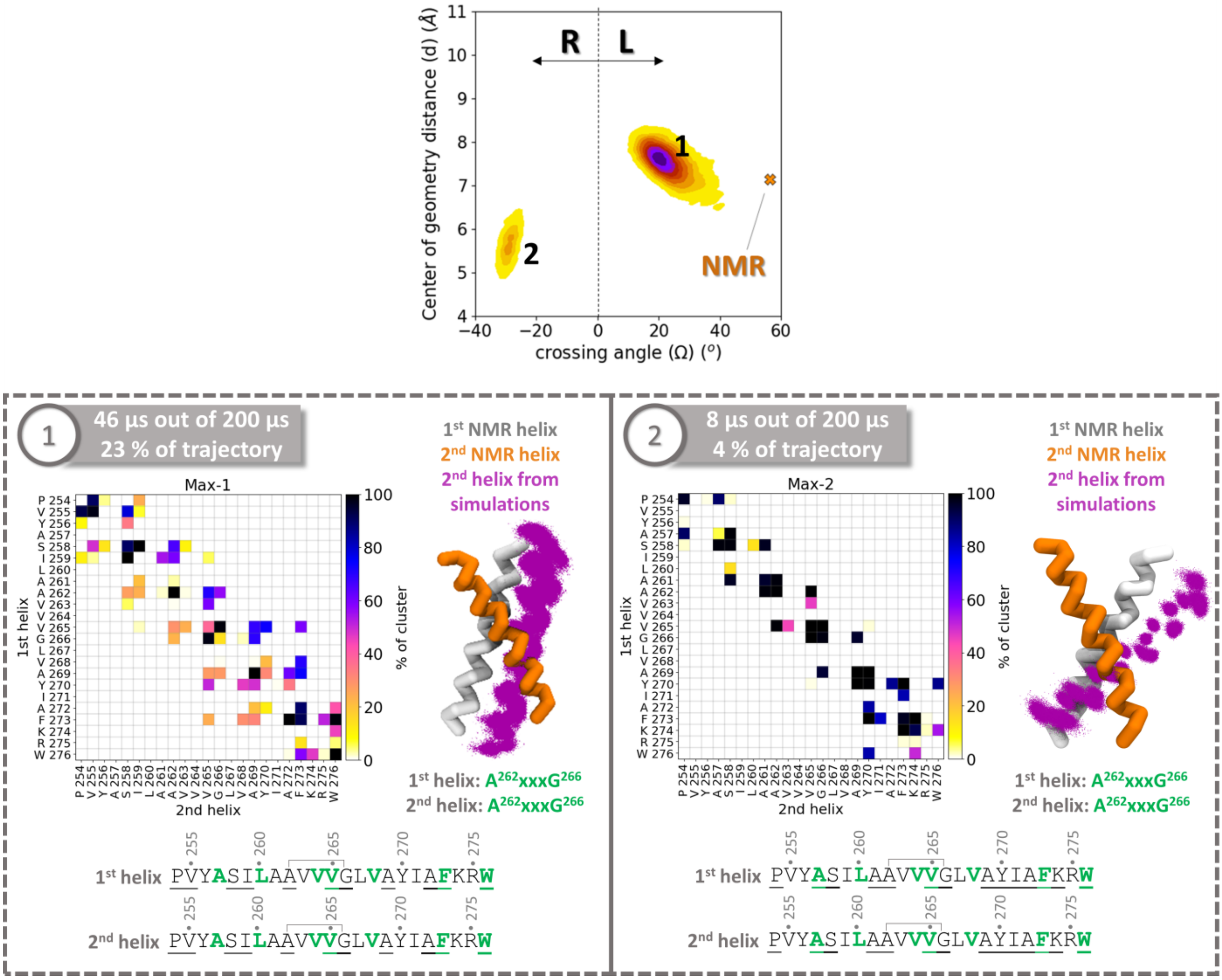

Figure 5.7: Contact analysis of p75-C257A TM helices. The top plot shows the two maxima in the d-Ω 2D heatmap and the boxes at the bottom show the contact analysis of the frames corresponding to each maximum. The highest interacting residues are underlined in the sequences, while the residues at the p75-WT NMR interface are colored green. A visualization of the simulation arrangements (purple) is shown in alignment to the 1st frame (white, orange), i.e. the NMR structure.

The lack of stability of the p75-C257A TM NMR structure, raised the question of the suitability of the CG force field to model all the important interactions that are present in the helical homodimer. For this reason, I decided to test the stability of the NMR structure in an atomistic representation, which retains more chemical information compared to the CG Martini force field. For this purpose, I simulated the p75-WT and p75-C257A TM homodimers in DPC micelles using the all-atom (AA) CHARMM36m force field. I performed 3 replica simulations of 500 ns each for each system. The heatmaps of these simulations are presented in Figure A.11 and Figure A.12. The analysis showed that also in atomistic level of representation the p75-C257A NMR structure is unstable and does not correspond to the configuration maxima (Figure A.12). The atomistic simulations of the p75-WT (Figure A.11) showed that the NMR structure is located in a maximum in the phase-position heatmap and not in the d-Ω space, in which higher interhelical distances were sampled in the AA simulations.

In order to also examine the influence of the DPC micelle environment, compared to the native environment of the cell membrane, in the arrangements of the p75-C257A homodimer, I performed test AA simulations in membranes. Specifically, I performed one simulation of the p75-C257A NMR structure embedded in a pure POPC membrane and one simulation in a more complex neuronal membrane, which contained a combination of 19 lipid species. Because I performed single replica simulations in membranes, I analyzed them with RMSD calculations to compare them with the NMR structure, and I did not create the 2D heatmaps, as they would require more extensive sampling. The results are presented in Figure 5.8 and they show deviation from the NMR structure, which is depicted with high RMSD values.

The deviation from the NMR structure in the p75-C257A atomistic simulations in micelles and membranes demonstrates that the NMR structure does not correspond to an energy minimum, and raises questions about the NMR structure conditions. For this reason, in the subsequent enhanced sampling simulations of the p75-C257A mutant that I performed, I used the CG Martini force field.

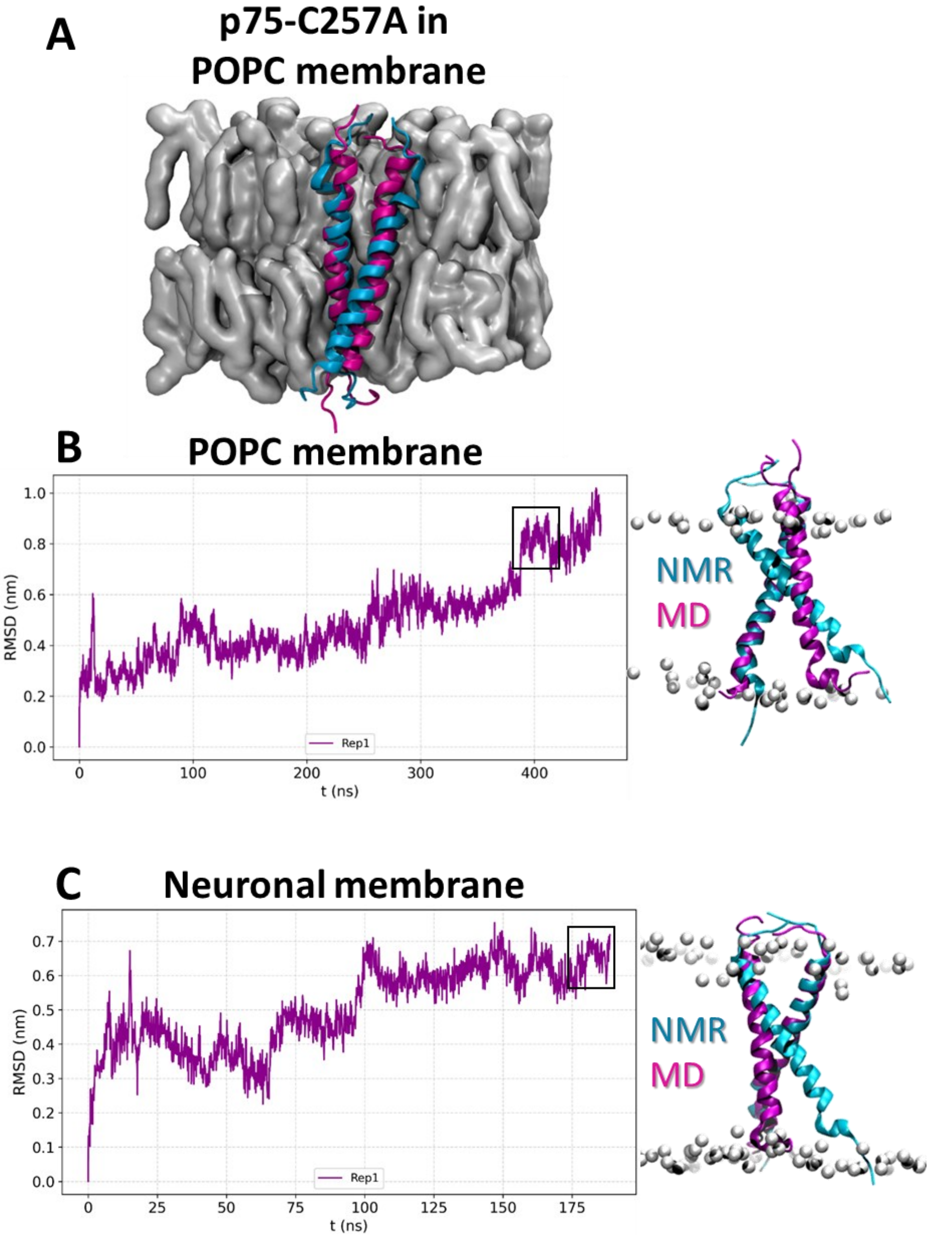

Figure 5.8: Analysis of p75-C257A AA simulations in membranes. (A) Atomistic presentation of p75-C257A in a POPC membrane. A structure from an MD snapshot (magenta) is shown in alignment to the NMR structure (cyan) to demonstrate the deviation from the initial (NMR) configuration. (B),(C) RMSD calculations with respect to the NMR structure of the p75-C257A in POPC and neuronal membrane. The black box indicates the time range from which a snapshot is visualized in the figure next to each plot. In the figures, the NMR structure is shown in cyan ribbon representation, the frame from the simulation in magenta ribbon representation and the P atoms of the membrane in white vdW representation. Different structure occurred in the POPC and neuronal membrane simulations, which shows incomplete

sampling, which is expected in such sort simulation times. Both simulations are used here to demonstrate the instability of the NMR structure in various lipid environments.

Subsequently, I ran enhanced sampling well-tempered metadynamics at the CG level (CG-MetaD) simulations to achieve a more complete sampling of the helix arrangements of p75-C257A and to calculate the binding free energy. I did this only for the p75 mutant, because the WT dimer is covalently bonded and thus the unbinding event cannot be simulated. In metadynamics simulations, Gaussian potentials bias a collective variable (CV) of choice and allow more extensive sampling of that CV. For this system, I chose the interhelical distance, d, as the CV to be biased in order to sample bound (low d values) and unbound (high d values) states of the TM dimer.

I first monitored the convergence of the CG-MetaD simulations with the time evolution of the CV, the Gaussian height, the dimerization free energy and the free energy error over block size, with block analysis (Figure 5.9). The time evolution of the CV (d) shows diffusion, with multiple CV values being sampled corresponding to both bound ($d < 1.5$ nm) and unbound ($d > 1.5$ nm) states (Figure 5.9A). The height of the Gaussian potentials that are added with time should decrease for the simulation to be converged in well-tempered metadynamics. For p75-C257A, the height decreases over time, without though reaching zero, which suggests the simulation is close to convergence, but has not reached it yet. (Figure 5.9B). The evolution of the free energy as a function of CV and the free energy of dimerization over time are also shown to be close to convergence (Figure 5.9C,D). The free energy error seems to also be close to a plateau (Figure 5.9E).

The dimerization free energy of the p75-C257A TM dimer was calculated from the CG-MetaD simulation to be $\Delta G_{bind} = -70 \pm 0.35$ kJ/mol (-16.7 ± 0.1 kcal/mol). For the literature, the experimental apparent dimerization free energy is -1.8 kcal/mol,[387] indicating that the binding free energy is over-estimated, in accordance with the over-aggregating tendency in the Martini 2.2 force field for protein-protein interactions.[309,310]

Next, I analyzed the TM helix configurations during the CG-MetaD simulation with the same six geometric parameters that were used before (Figure 5.10). Multiple regions of the six parameter space are explored during the CG-MetaD simulation, with the bound only TM arrangements showing some preference for specific regions of the phase-position.

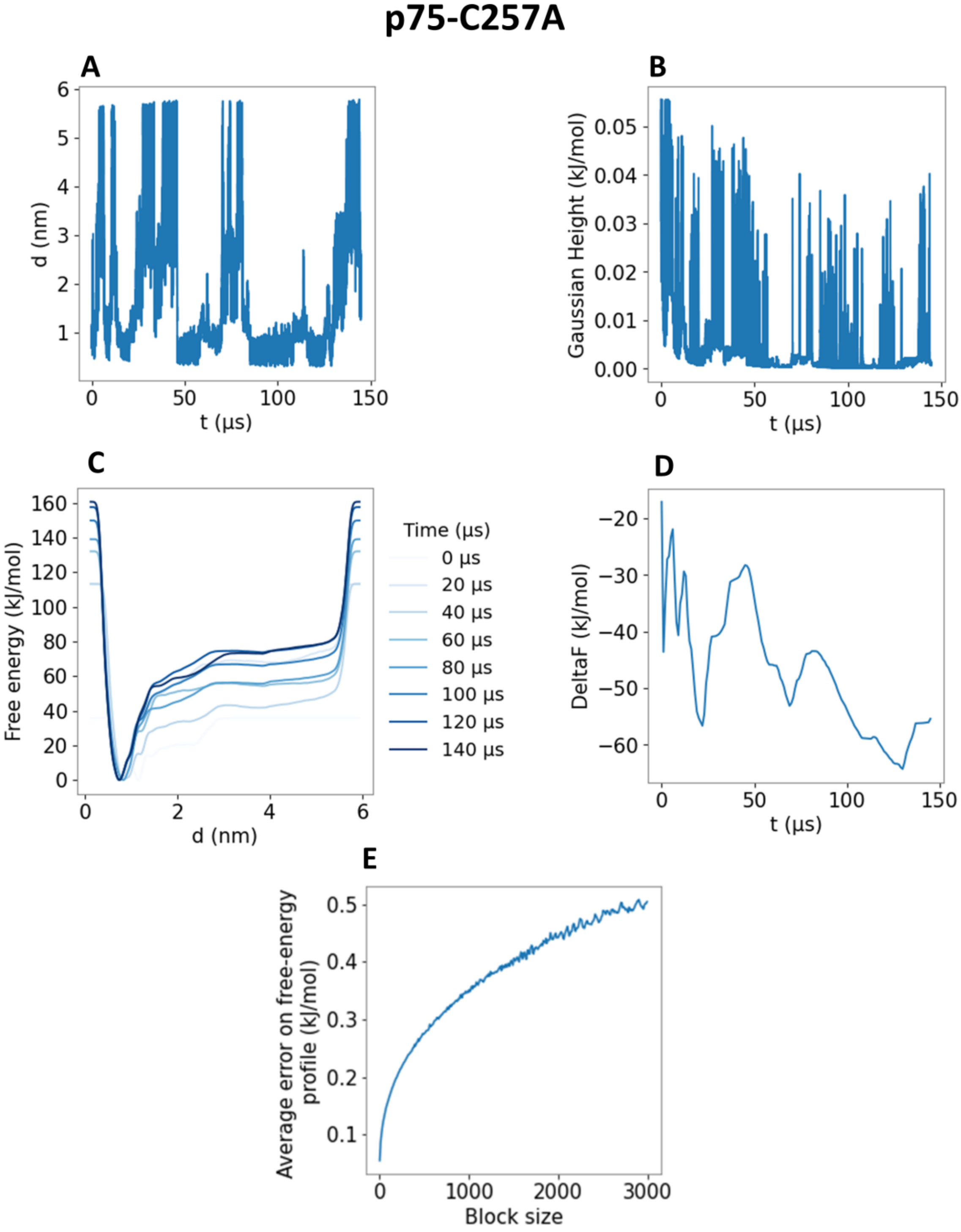

Figure 5.9: Evaluation of CG-MetaD simulation convergence.[51] Time evolution of (A) the CV, (B) the Gaussian height, (C) the free energy surface as a function of the CV, (D) the dimerization free energy and (E) the free energy error over block size from the block analysis. For the dimerization free energy, I defined the bound and unbound states with d < 1.5 nm and d > 1.5 nm, respectively. I created all plots and subfigures.

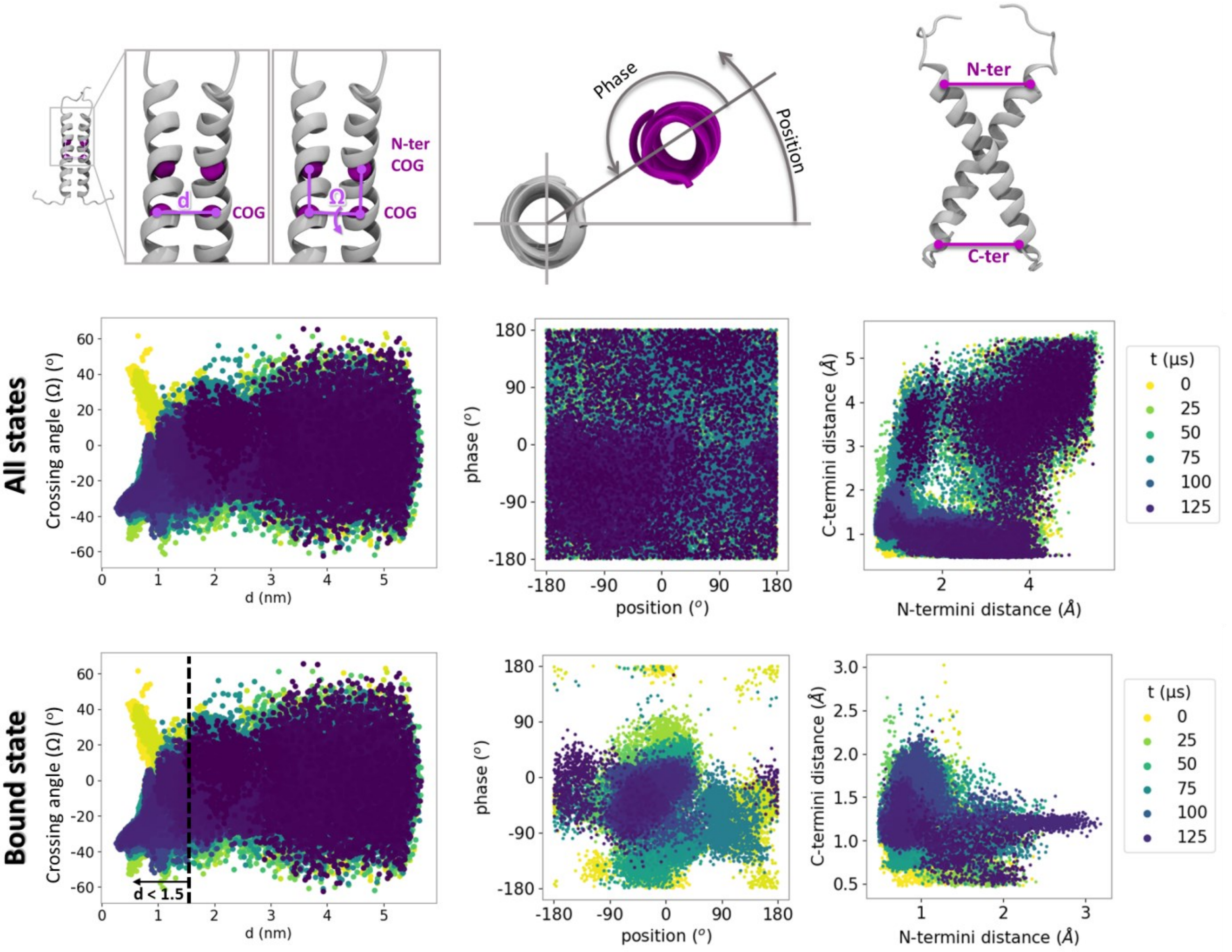

Figure 5.10: Analysis of the p75-C257A TM arrangements during the CG-MetaD simulation. 2D plots of the six geometric parameters of the TM arrangements and their time evolution. The 1st row plots show all the states (bound and unbound) of the TM helices that were sampled during the CG-MetaD simulation, while the 2nd row shows only the bound state arrangements, i.e. when d < 1.5 nm.

I then proceeded to the reconstruction of the FES from non-biasing CVs, i.e. from variables different than the interhelical distance. For this purpose, I performed a reweighting protocol that assigns a weight to each frame that depends on the bias potential deposited at that frame. This way the bias is removed from the simulation. I compared the FES as a function of the biasing CV (d) calculated from the MetaD bias and after reweighting and the two profiles were the same (Figure 5.11A) which indicates successful reweighting.

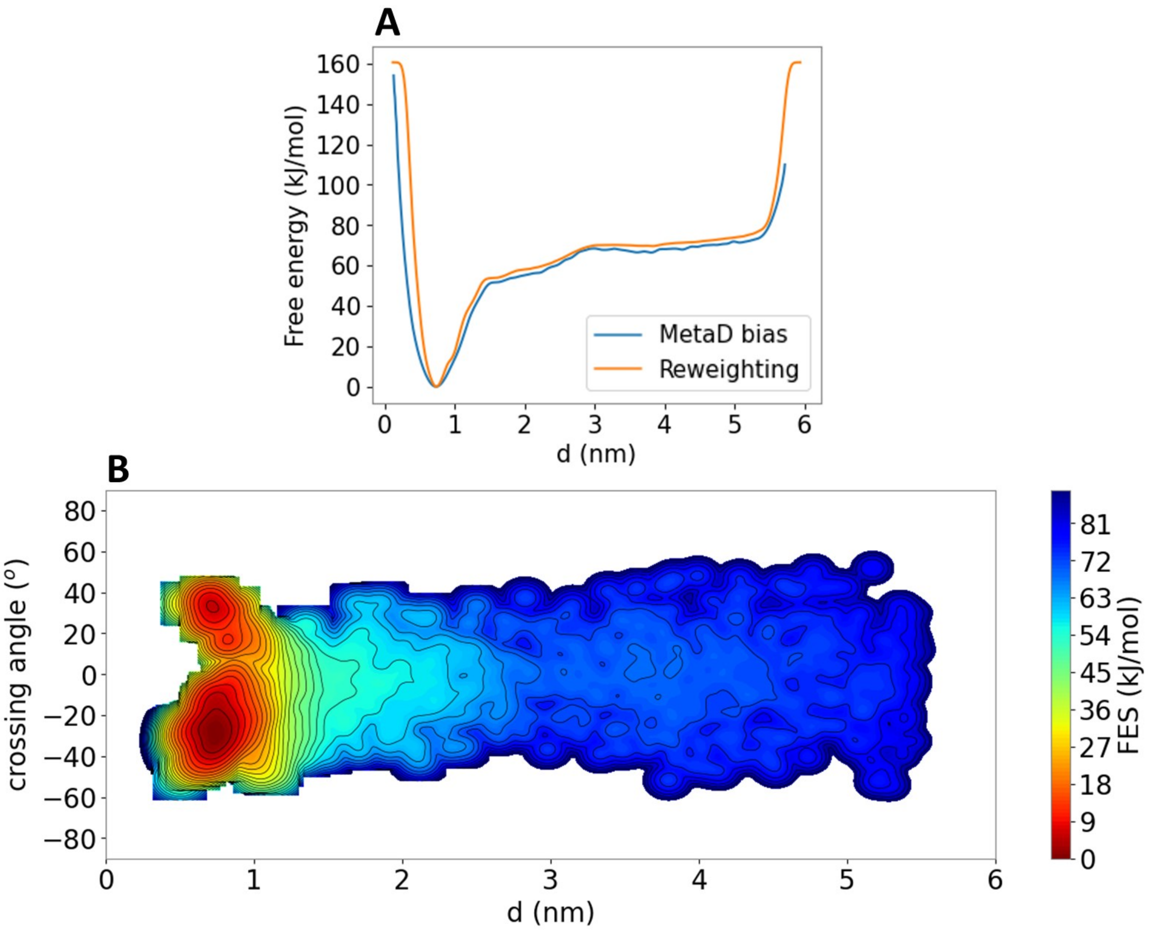

Figure 5.11: Free energy surfaces (FES) after reweighting. (A) FES as a function of the biasing CV (d) calculated from the MetaD bias and after reweighting for comparison. (B) FES as a function of the biasing CV (d) and the crossing angle after reweighting. Isosurfaces are plotted every 3 kJ/mol.

After the reweighting, I investigated the FES as a function of other CVs than the interhelical distance. I plotted the FES versus the CV (d) and the crossing angle after reweighting (Figure 5.11B). The FES shows that, the dimerization free energy is ca. -70 kJ/mol, which is in agreement with the 1D FES plot. From this 2D plot, it is also shown that there are two minima at around -30° and 30°, corresponding to right-handed and left-handed helical arrangements, similar to the two states sampled in the unbiased CG simulations. The two arrangements are degenerate for the interhelical distance, as they both correspond to the same value of 0.8 nm for the distance.

Finally, using the reweighting protocol, I calculated the FES as a function of the six geometric parameters discussed before for the description of TM arrangements. The Ω-d FES shows the same two minima at ca. -30° and 30° crossing angle. The phase-position plot has minima at around 0°, as in the case of the unbiased CG simulations, indicating that the A262 residue of the AxxxG motif is at the interface. Additionally, two more minima occurred in this 2D space, at phase < 90° for the 1st, and position around 180° for the 2nd. These probably correspond to two additional stable arrangements.

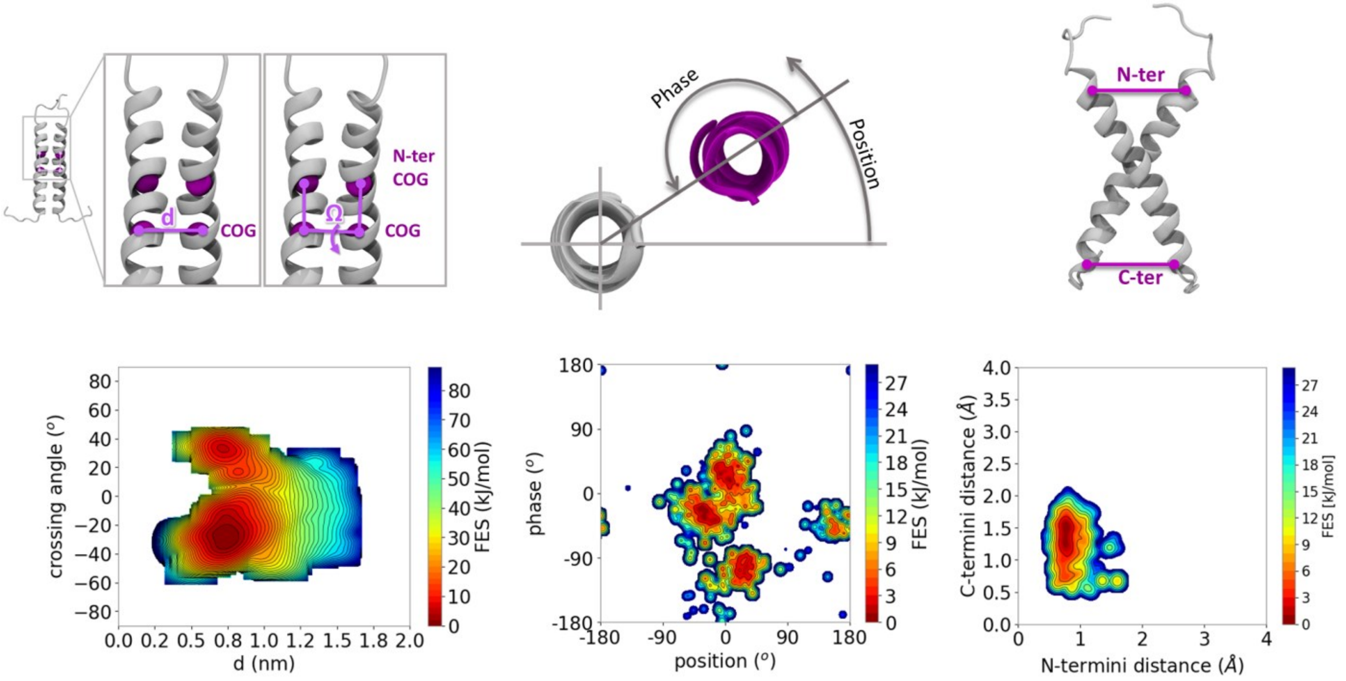

Figure 5.12: FES analysis on the six geometric parameters – interhelical distance, crossing angle (Ω), phase and position, and N- and C-termini distance – from the CG-MetaD simulation.[51] I created all subfigures and plots.

5.4 Conclusions

In this chapter, I studied the dimerization states of the TM domain of the p75-WT neurotrophin receptor and its mutant p75-C257A. The TM helices of p75-WT are covalently bonded with a disulfide bridge at C257, which holds the receptor in a dimeric state even prior to activation.[57] This disulfide bond is necessary for neurotrophin-dependent receptor activation.[57] The NMR structure of the disulfide-linked p75-WT TM homodimer has been solved with NMR in DPC micelles, as well as that of the p75-C257A mutant, in which the helices are not covalently bonded.[59] Here, I performed molecular dynamics

(MD) simulations of the p75-WT and p75-C257A TM dimers to further explore their configurational landscape.

I performed coarse-grained (CG) MD simulations for both p75-WT and p75-C257A TM dimers, starting from their NMR structures. The results showed that the p75-WT TM homodimer is quite stable due to the presence of the disulfide bond. Interhelical crossing angles of -45^o to -30^o were monitored, which corresponded to 9-13 Å C-ter distances. This scissors-like movement of the TM helices might be important for transferring the activation signal intracellularly. Contact analysis that I performed showed that the homotypic interactions that were present in the NMR structure were preserved during the simulations.

The CG simulations of the p75-C257A TM dimers showed that the NMR structure is not stable and instead two other right-handed and left-handed helical arrangements occurred with smaller crossing angles than the NMR arrangement. On the other hand, the $A^{262}xxxG^{266}$ dimerization motif which is located at the NMR interface, is also present at the interface of the two new arrangements. This shows the importance of the interactions in this motif when the C257 residue is not present in the TM sequence. However, since this mutant does not occur physiologically, the arrangements that were sampled may not correspond to any biological state.

Due to the fact that the NMR structure of the p75-C257A mutant was unstable in the CG level of representation, I decided to test its behavior in atomistic detail in DPC micelles and bilayers. In both cases the TM helices lost their initial NMR arrangement, which shows that the loss of the NMR arrangement is not due to the more approximate nature of the CG force field in modeling interactions. Consequently, the instability of the NMR structure raises questions about under which conditions it was solved.

Finally, I performed CG metadynamics simulations on the p75-C257A mutant to test the sampling efficiency of the unbiased CG simulations and calculate the free energy of dimerization. The metadynamics simulations verified the two arrangements that had been sampled in the unbiased CG simulations for this mutant and predicted a ΔG_{bind} of -16.7 ± 0.1 kcal/mol. The binding free energy in this case was overestimated, since the experimental one has been measured at -1.8 kcal/mol. This probably corresponds to the over-aggregating tendency in the Martini 2.2 force field for protein-protein interactions, which was used in the CG metadynamics simulations.

Overall, I showed the CG MD simulations that the p75-WT TM dimer, even though covalently bonded, it can adopt arrangements of varying C-terminal interhelical distance. This behavior is in agreement with what has been previously suggested in the literature for p75 TM to undergo a scissors-like movement in response to NGF binding, with the disulfide bond acting as the fulcrum.[57] In this work, the authors saw with FRET experiments a separation of the p75 death domains upon NGF binding, which they believe happens through a "snail-tong" mechanism, in which the EC domains come closer and the IC domain detach. The various C-terminal distances of the TM helices, that were observed here, constitute the first evidence that this mechanism is possible from a structural perspective. The next step would be to assess if this change in the C-termini distance can lead to signal propagation intracellularly, which is investigated in the next chapter of the thesis.

6 Full-length p75 in a neuronal membrane

6.1 p75 action in neuronal membranes

NT binding to the p75 receptor elicits an activating response on the receptor, which results in a conformational change in the structure of the full-length p75 receptor. As mentioned before, fluorescence resonance energy transfer (FRET) experiments, with the fluorophore tags placed at the C-terminus of p75, showed that p75 undergoes a conformational change when NT binds, in which C257 plays a key role.[57] Decrease in FRET upon NT binding indicated dissociation of the death domains, and it is proposed that p75 undergoes a scissors-like movement in which the C257-C257 bond plays the role of the fulcrum.[57] In this chapter, I have modeled the full-length p75 receptor homodimer with the NT-3 bound to the EC domains, aiming to get insights into the mechanism of the p75 activation.

The lipid environment in which p75 is localized plays an important role in receptor function. p75 acts in neuronal membranes that have a different composition from common plasma membranes, i.e. they have higher concentrations of cholesterol and sphingolipids, such as sphingomyelin.[400–402] The effect of the membrane becomes more apparent on NT receptors that tend to localize to lipid rafts which are membrane microdomains with even higher cholesterol concentrations.[139,141,143] The p75 receptor localizes within lipid rafts, regulated by the cAMP-dependent protein kinase A (PKA).[139] Moreover, the cleavage of p75-EC is influenced by lipid rafts, disordering of which enhances p75 cleavage and its pathways.[140] In summary, lipid rafts can modulate and fine-tune neuronal signaling.[403] This shows that the membrane environment can modulate receptor function, and thus here I have used a newly created model of a neuronal-like membrane for the simulations of the full-length p75 receptor.

6.2 Methodology

Protein model

For the modeling of the full-length human p75 receptor, I used two crystal structures of proteins from other species as templates for the EC and TM domains. I selected the species Rattus norvegicus (rat) due to the high sequence identity of ca. 92% for p75. I performed the sequence alignment using Clustal Omega 1.2.4[362] via UniProt.[363] For the EC domain, I used the crystal structure of the complex of the rat p75-EC domain homodimer and the human NT-3 homodimer (PDB ID: 3BUK), which contains the rat p75-EC domain residues 32-190 (31-189 in human — corresponding to UniProt entries P07174 and P08138, respectively), an N71S mutation in the rat p75-EC domain, which results in the serine residue present in the human sequence, and the human NT-3 residues 143-253. It thus comprises (with a few missing residues) the full length of the structured parts of the p75-EC domain and NT-3. For the TM domain, I used the NMR structure of the rat p75-TM domain homodimer (PDB ID: 2MIC),[387] which contains the residues 245-284 (244-283 in human), an initiating methionine (M), and a C279S mutation, thus comprising (with some extra residues) the full length p75-TM helix. For the IC domain, I used the NMR structure of the human p75-IC domain homodimer (PDB ID: 2N97),[70] which contains the residues 334-427, thus comprising the p75 death domain (DD). I processed the structures using the Schrödinger Suite 2020,[351] by mutating the residues that were different in rat to the human ones using Maestro, and then I prepared the proteins (addition of hydrogen atoms, formation of double bonds, optimization of hydrogen-bond network, restrained minimization) using the Protein Preparation Wizard,[351] and the three domains were aligned to one another and exported as a single structure. This combined structure was missing the p75-EC residues 29-30 and 190-243 (EC linker), the p75-IC residues 284-333 (IC linker), and the NT-3 residues 139-142 and 254-257, per monomer. These are all known to be loop regions and therefore I modelled them as such using MODELLER 9.23.[364] The resulting model lacked hydrogen atoms, so I predicted the protonation states using PROPKA 3.4.0[365] via PDB2PQR 3.4.0.[366] Regarding the glycosylation of p75, it is known that each monomer has one N-glycan of composition $Hex_5HexNac_4dHex_1NeuAc_2$ at Asn60 and 4-7 O-glycans of composition $Hex_1HexNac_1NeuAc_1$ at undefined positions on the EC-linker.[84] For this reason, I performed a prediction of the O-glycosylation sites using NetOGlyc 4.0.[404] Based on the scores and positions, I selected four residues for the O-glycans to be linked to residues: S199, S207, S211 and S239. For the building of the glycans I used CHARMM-GUI[368] and the final model is shown in Figure 6.1.

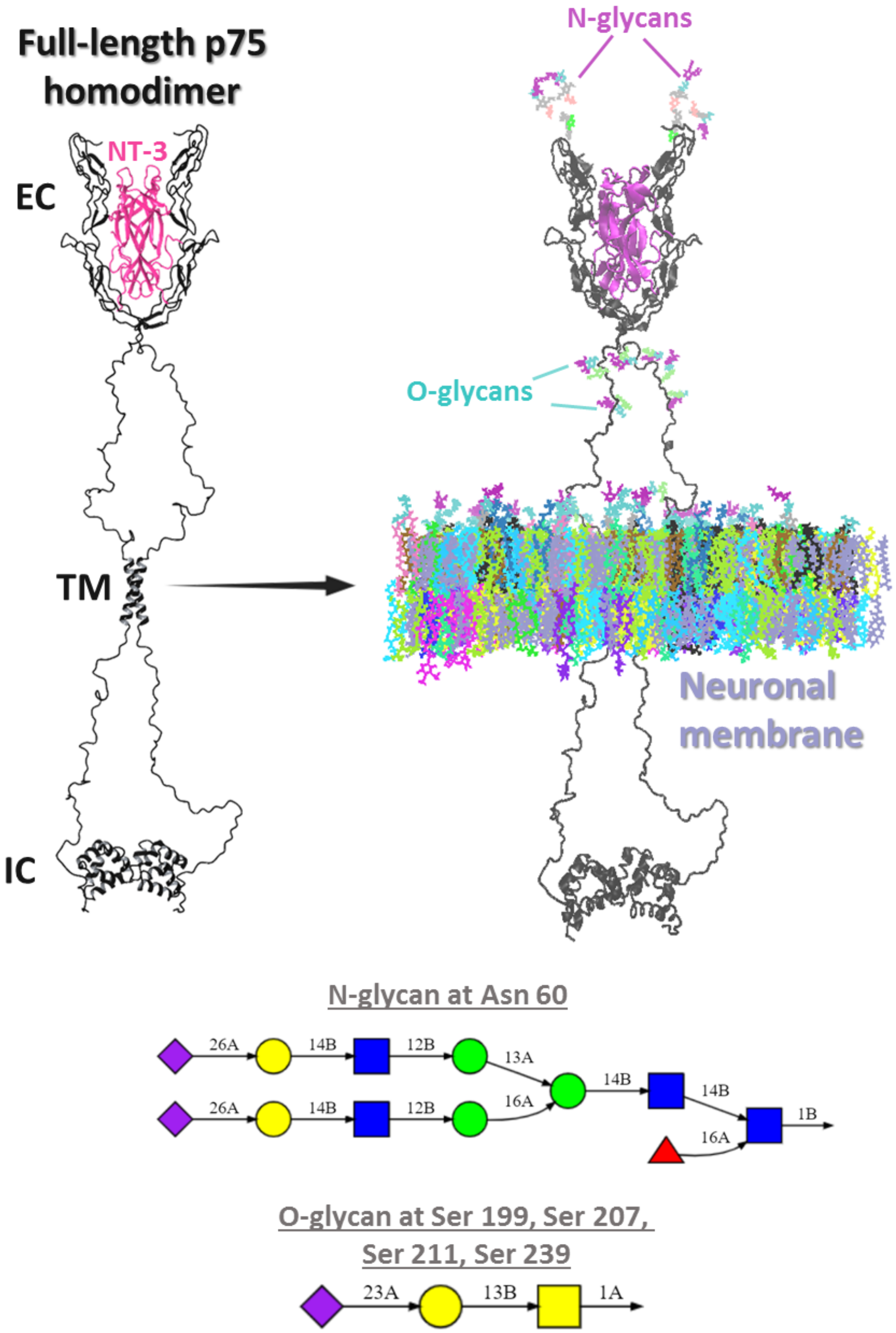

Figure 6.1: Model of the full-length p75 receptor homodimer bound to the NT-3 homodimer. The initial protein model and the final one after the modeling of the N- and O-glycans and the embedding of the TM domain in the neuronal membrane are shown in comparison.

Neuronal membrane model

I incorporated the full-length p75 receptor in a neuronal membrane model created by Christina Athanasiou from the MCM group at HITS.[72] The model was based on a 90-lipid neuronal membrane model,[400] and it was simplified to reduce the number of lipids, and consequently the size of the membrane, while maintaining the headgroup and lipid tail saturation composition (Table 6.1, Figure 6.2).

Table 6.1: Neuronal membrane composition made by Christina Athanasiou.[72] The lipid tail type is presented in the form "[*C atoms of 1st tail*] **:** [*number of unsaturated bonds in the 1st tail*] **/** [*C atoms of 2nd tail*] **:** [*number of unsaturated bonds in the 2nd tail*]". The exact numbers of the lipids that were included in the outer and inner leaflets are presented in the 3rd and 4th columns. The lipid name codes are: 1,2-dipalmitoyl-sn-glycero-3-phosphocholine (DPPC), 1-palmitoyl-2-oleoyl-sn-glycero-3-phosphocholine (POPC), 1-palmitoyl-2-arachidonoyl-sn- glycero-3-phosphocholine (PAPC), 1,2-dipalmitoyl-sn-glycero-3-phosphoethanolamine (DPPE), 1-palmitoyl-2-oleoyl-sn-glycero-3-phosphoethanolamine (POPE), 2-linoleoyl-sn- glycero-3-phosphoethanolamine (LLPE), 1-palmitoyl-2-oleoyl-sn-glycero-3-phospho-L-serine (POPS), 1-palmitoyl-2-linoleoyl-sn-glycero-3-phospho-L-serine (PLPS), 1-palmitoyl-2-oleoyl-sn-glycero-3-phosphoinositol (POPI), 1-palmitoyl-2-oleoyl-sn-glycero-3-phosphoinositol 4,5-bisphosphate (POPI25 or PIP2), 1-stearoyl-2-arachidonoyl-sn-glycero-3-phosphoinositol (SAPI), N-stearoyl sphingomyelin (SSM), neutral sphingomyelin (NSM), ceramide 18:0 (CER180), monosialo-tetrahexosyl-ganglioside (GM1), monosialo-dihexosyl-ganglioside (GM3), galactosyl-ceramide 18:0 (GalCER180), galactosyl-ceramide 24:1 (GalCER241). The last two are cerebrosides.

Lipid	Lipid tails	Outer leaflet	Inner leaflet
Cholesterol	-	336	332
DPPC	16:0/16:0	18	12
POPC	16:0/18:1	108	56
PAPC	16:0/20:4	57	33
DPPE	16:0/16:0	27	51
POPE	16:0/18:1	21	39
LLPE	18:2/18:3	36	72
POPS	16:0/18:1	0	24
PLPS	16:0/18:2	0	48
POPI	16:0/18:1	0	15
POPI25 (PIP2)	16:0/18:1	0	15
SAPI	18:0/20:4	0	30
SSM	18:1/18:0	45	18

NSM	18:1/24:1	18	0
CER180	18:1/18:0	9	9
GM1	18:1/18:0	12	0
GM3	18:1/18:0	12	0
GalCER180	18:1/18:0	42	0
GalCER241	18:1/24:1	15	0

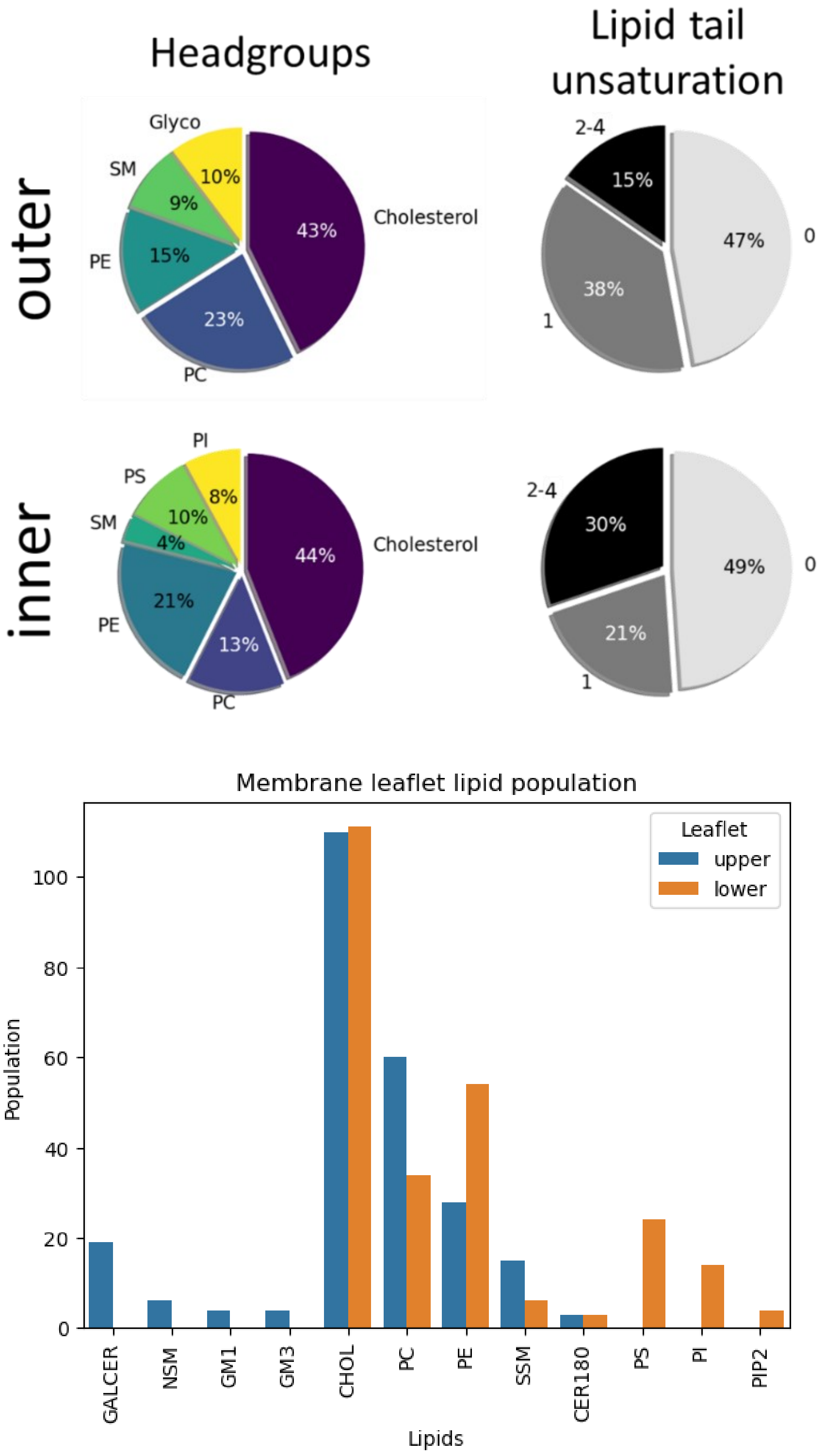

Figure 6.2: Neuronal membrane composition built by Christina Athanasiou in headgroup and lipid tail populations.[72] The lipid types are cholesterol, phosphocholine (PC), phosphoethanolamine (PE), sphingomyelin (SM), glycolipids (Glyco) including GM1, GM3, GalCER180, GalCER241, phospho-L-serine

(PS), phosphoinositol (PI). The bar plot shows the population of headgroup lipid types per leaflet. Figure adapted from Christina Athanasiou.[72]

Molecular dynamics (MD) simulations

I built the neuronal membrane model with the Membrane Builder of CHARMM-GUI,[394] with which I also added NaCl at neutralization and ionic strength 150 mM. I used GROMACS v.2020[369] for all simulations and the CHARMM36m force field.[370] I ran several equilibration steps for proper membrane behavior, consisting of two energy minimizations with steepest descent and conjugate gradient, one NVT equilibration at 310 K for 200 ps with 1 fs time step, and 4 NPT equilibrations at 310 K, 1 bar for 1, 2, 4 and 5 ns each with 1 fs time step for the 1st NVT and 2 fs for the rest (Table 6.2). In all equilibration steps, I used restraints on protein backbone, side chain heavy atoms and on the z direction of the P atoms of phospholipids (to keep them on the plane of the membrane) and an equivalent atom for the gangliosides, as well as on the lipid improper dihedrals that were gradually decreased in the various steps, from 4000 kJ/(mol nm^2) to 0 kJ/(mol nm^2) at the production step (Table 6.2). For thermostat and barostat I used Berendsen[392] for all equilibration steps and Nose-Hoover[371,372] and Parrinello-Rahman,[373,374] respectively, for production. I used semi-isotropic pressure coupling every 5 ps with $4.5 \cdot 10^{-5}$ bar^{-1} compressibility. I used the Linear Constraint Solver (LINCS) algorithm[377] to fix the length of bonds with hydrogens. For Coulomb interactions, I employed the Particle Mesh Ewald (PME)[375,376] summation for the treatment of long range electrostatics with a cutoff distance of 1.2 nm, and for van der Waals interactions I used a force-switch function, that changes the shape of the force between the range of 1.0 and 1.2 nm. I ran 6 replica simulations of 500 ns production step with the system fully unrestrained.

Table 6.2: Equilibration steps for the p75 simulations in neuronal membrane.

Step	Type	Steps/Time	Time step	Restraints (kJ/(mol nm^2) Backbone/Side chains/Lipid	Thermostat/ Barostat
Step 1: minimization	Steepest descent	10000	-	4000/2000/1000	-
Step 2: minimization	Conjugate gradient	10000	-	4000/2000/1000	-

Step 3: equilibration	NVT	200 ps	1 fs	4000/2000/1000	Berendsen
Step 4: equilibration	NPT	1 ns	1 fs	4000/2000/1000	Berendsen/ Berendsen
Step 5: equilibration	NPT	2ns	2 fs	2000/1000/500	Berendsen/ Berendsen
Step 6: equilibration	NPT	4 ns	2 fs	1000/500/200	Berendsen/ Berendsen
Step 7: equilibration	NPT	5 ns	2 fs	1000/500/0	Berendsen/ Berendsen
Step 8: production	NPT	500 ns	2 fs	0/0/0	Nose-Hoover/ Parrinello-Rahman

Analysis of simulations

At the end of each replica simulation I performed a set of post-processing analyses, with the fixing of periodic effects being with the *gmx trjconv* tool of GROMACS being the first step. I also performed a rigid-body alignment to the backbone of one of the TM helices in the 1st frame of the simulations. I rendered all protein structures presented in this thesis with VMD 1.9.3.[355]

Root mean square deviation (RMSD), root mean square fluctuation (RMSF) & radius of gyration (Rg)

I performed RMSD calculations on the protein structures with the MDAnalysis Python library.[378,379] Specifically, I calculated the RMSD of each protein backbone during the simulations with respect to the initial structure, after having aligned first all frames to protein backbone of the first frame. I also calculated the internal RMSD of each subdomain backbone of p75, after alignment to the backbone of the same sub-domain at the first frame. I plotted the RMSD values with the Matplotlib Python library,[380] while I calculated and plotted their density distributions with the Seaborn Python library.[381]

To monitor the residue fluctuations during the simulations, I performed RMSF calculations with MDAnalysis. For this, I aligned first the Cα atoms of the protein to an average structure from the simulations and then I calculated the RMSF of each residue Cα from that average structure. I plotted the RMSF values with Matplotlib.

I performed a radius of gyration calculation of the full-length p75 again with MDAnalysis, after having aligned each of the systems to the backbone of p75 at the 1st frame of the simulations. I performed the plotting with Seaborn.

Distances and angles between EC segment and membrane

I estimated the distance between the EC segment of the full-length p75 and the membrane during the simulations. For this, I defined the center of mass (COM) of the NT atoms and the z-coordinate of the COM of the membrane P atoms and the calculated the distance between the two points. I also estimated the relative orientation of the EC segment with respect to the membrane. For this, I defined a vector corresponding to the long axis of the NT and the membrane normal, and calculated the angle between the two. I did this with MDAnalysis for the whole of the simulations and after the first 150 ns when the system was more equilibrated. I performed the plotting with Seaborn.

Contact analysis

I analyzed the contacts between all the residues of the TM helices, the kinase domains (in the homodimer), and between the receptor domains and the membrane with MDAnalysis. I defined a contact when two non-hydrogen atoms were within 4.5 Å distance. I ran this analysis after the 1st 150 ns, when the system had equilibrated, while I processed and visualized the data with Pandas[397,398] and Matplotlib.

Principal component analysis (PCA)

I chose to quantify this intrinsic motion of the full-length p75 receptor in the neuronal membrane, for which I ran a principal component analysis (PCA) with the built-in class in MDAnalysis. I did the analysis after the 1st 150 ns, in the equilibrated systems, while I aligned the trajectories to the structure at 150 ns before running PCA. I plotted the values of the 1st and 2nd principal components with Seaborn. Moreover, I used the numpy.dot function of Numpy to calculate the dot products of all PC1 and PC2 combinations from the different replicas.

TM helix geometric parameters

As in chapter 5, for the analysis of the helical arrangements during the simulations I used six geometric parameters: (1) the interhelical distance (d) defined by the centers of geometry (COG) of the backbone atoms, (2) the interhelical crossing angle (Ω) defined as a dihedral by COGs of the helix backbone atoms and the COGs of the N-terminal halves of the helices, (3), (4) the rotation around the axis of each helix, mentioned later as phase and position, defined as a dihedral by the COG of the N-terminal half of one of the helices, the COGs of the backbone atoms of the two helices and the COG of Cys 256, and finally (5), (6) the distance between the N- and C-termini of the helices. I calculated these parameters in all simulation frames using the MDAnalysis and the numpy.linalg.norm function of the Numpy library.[382] I visualized the geometric parameter distributions during the simulations with Kernel Density Estimation (KDE) plots using the seaborn.kdeplot function of Seaborn.

Secondary structure calculation

I ran secondary structure calculations for the EC and IC linkers of p75 to see if their initial unstructured form remains during the simulations. I calculated this with the Timeline plugin of VMD and I ran it every 10 frames after the 1st 150 ns, when the system had equilibrated.

6.3 Results

I modeled and simulated the glycosylated full-length p75 receptor homodimer with NT-3 bound in the EC domain, inserted in the neuronal membrane. For the modeling of the EC, TM and IC domains of p75 I used available X-ray and NMR structures, while for the EC and IC linkers, which were predicted as unstructured by webservers, I modeled them as extended loops. I ran 6 replica simulations staring from the same p75 structure with different initial velocities and I first monitored the large scale changes from the initial model structure with RMSD calculations.

I calculated the RMSD of the different domains of p75 as well as the full-length p75 and the NT-3, with respect to the initial model structure (Figure A.13). The RMSD calculations showed high values (backbone RMSD > 3 Å) for the EC domain, which originate from the D1 domain, as shown from the RMSD calculations for each of the EC domains (Figure A.13A). Domains D2-D4 have RMSD less than 3 Å, which means that their conformation from the crystal structure is preserved. The high RMSD values for the D1 domain could be due to the partial unfolding of the N-terminal domain, as shown before in the simulations of p75-EC in chapter 4 (Figure A.3). This is supported by the high RMSF values for the N-terminal residues of D1 domain in both monomers (Figure A.14A).

For the EC and IC linkers, the RMSD reaches very high values, suggesting big conformational changes in these disordered domains (Figure A.13B,D). These conformational changes seem to happen in the whole length of the linkers, as suggested by the high RMSF values in all residues of the linkers (Figure A.14B,D). The TM domain (TMD) helical conformation is retained throughout the simulations with RMSD values less than 1.5 Å (Figure A.13C), which is reflected also in the low RMSF values for this domain (Figure A.14C). The intracellular death domains (ICDs) have also high RMSD values (Figure A.13E), for which the C-terminal part of the DDs is responsible according to the high RMSF values of that region which is disordered (Figure A.14E). Finally, the N- and C-terminal regions of the NT, which are disordered, fluctuate a lot (Figure A.14F), which leads to high RMSD values (Figure A.13F).

The high conformational changes in the EC and IC linkers, as suggested by the high RMSD and RMSF values, seem to be the biggest changes in the simulated systems and thus they were further investigated. Specifically, I examined visually the simulation trajectories, which revealed that the p75 homodimer contracts in the EC and IC linkers and approaches the membrane during the course of the simulation (Figure 6.3). This contraction was observed in all replica simulations. The contraction of the EC linkers is accompanied by a bending of the p75-EC domains bound to NT-3 towards the membrane and in some replica simulations they even interact with it (Figure 6.3).

To quantify the contraction of the EC linkers and the EC domain bending, I calculated the distance between the center of geometry (CoG) of the NT and the upper leaflet of the membrane, as well as the angle between the 1st principal axis of the ECD-NT3 complex and the membrane normal, which coincides with the Z-axis in the simulation box (Figure 6.4). The distance analysis showed that, in the first 150 ns of the replica simulations, the EC domain approaches the membrane and then it is mostly stabilized in a distance that varies among the different replicas (Figure 6.4A). This means that the first 150 ns correspond to an equilibration period for the p75 linkers. Calculation of the probability density of distance for the equilibrated part of the simulation (after the first 150 ns) showed that distances mostly at ~ 85 and 110 Å were sampled (Figure 6.4B).

The analysis of the angle between the ECD and the membrane normal showed that it starts from very low values (ECD perpendicular to membrane normal) and increases very fast in the equilibration period of the first 150 ns (Figure 6.4C). The probability density of the angle corresponds to ranges between 20-60° (Figure 6.4D).

Upon visualizing the trajectories, I saw that in some replicas the EC linkers seem to fold and form globular subdomains. This led to the calculation of the radius of gyration (R_g) of the different p75 domains including the linkers (Figure A.15). The calculations showed that in several replicas the EC linkers sample low R_g values during the equilibrated phase of the simulations (Figure A.15B). Similar low

R_g values were observed for IC linkers which also contract and approach the membrane intracellularly (Figure A.15D). For the rest of the domains smaller R_g changes were observed during the course of the simulations.

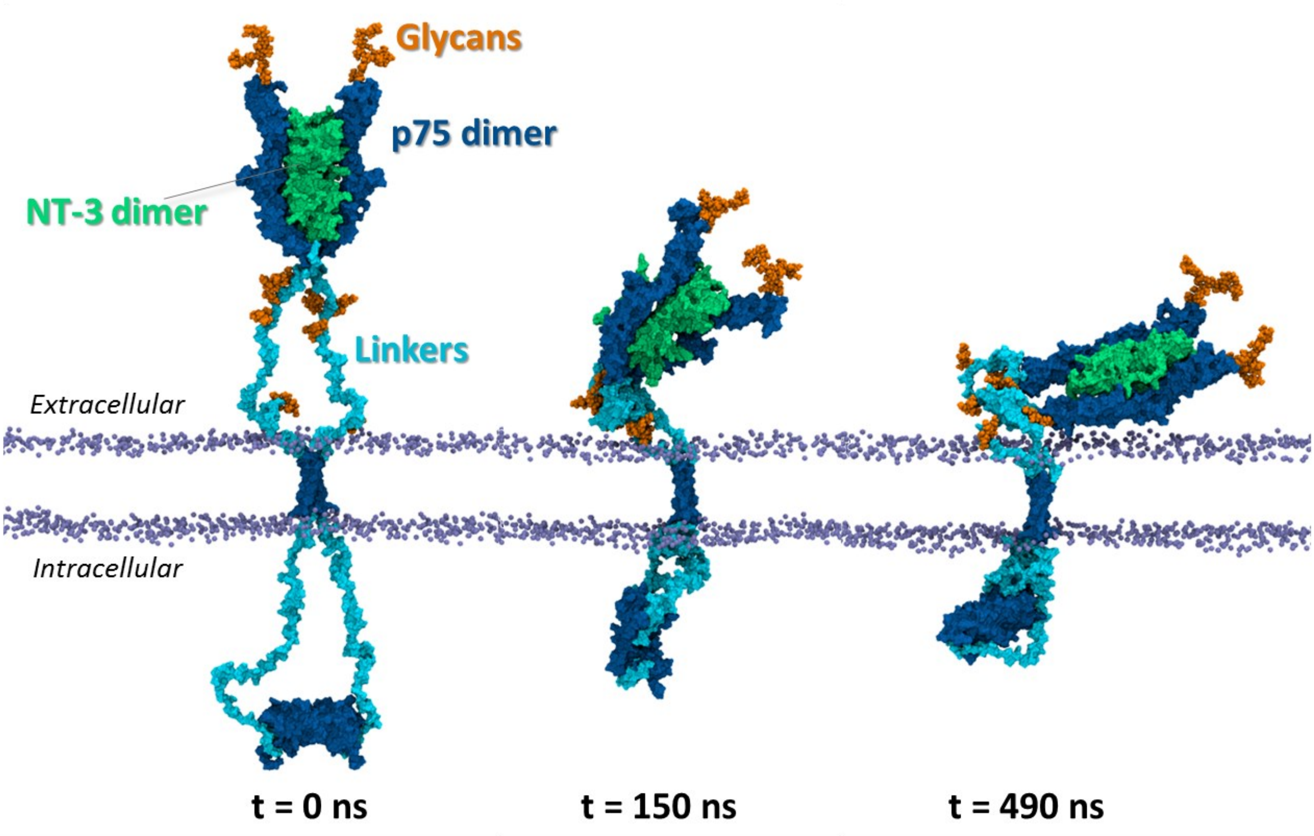

Figure 6.3: Conformational contraction of the full-length p75 system. The p75 homodimer with the NT-3 bound is shown in three different time steps; at 0 ns in the beginning of the simulation, at 150 ns when the contraction of the linkers has been completed, and at 490 ns when the bending towards the membrane has been completed.

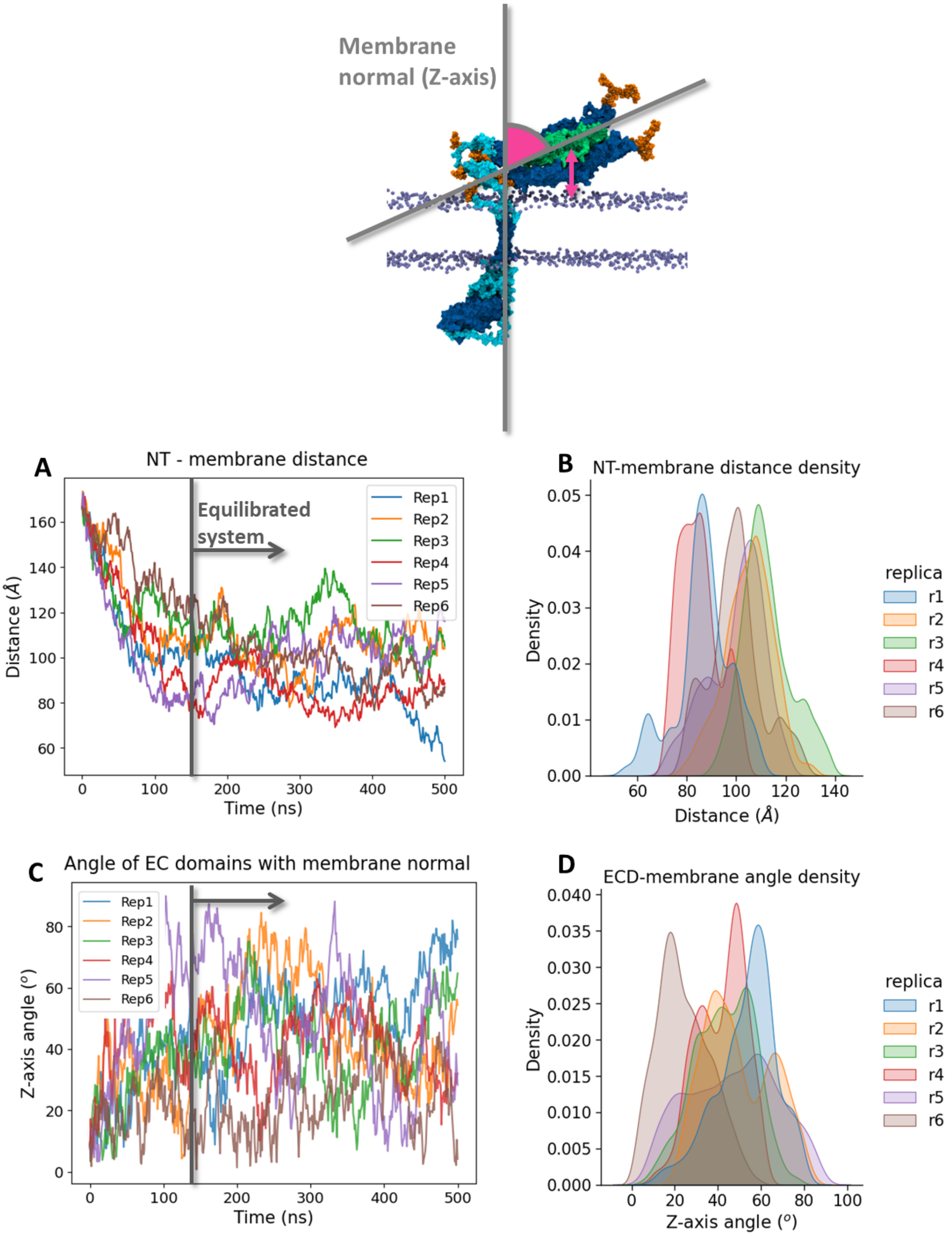

Figure 6.4: Distance and angle calculations between NT- membrane and NT-membrane normal. The 1st 150 ns, indicated with a vertical line, show that the system equilibrates and reaches stable distance angles. Distance and angle distribution densities are also shown per replica for the equilibrated systems after the first 150 ns.

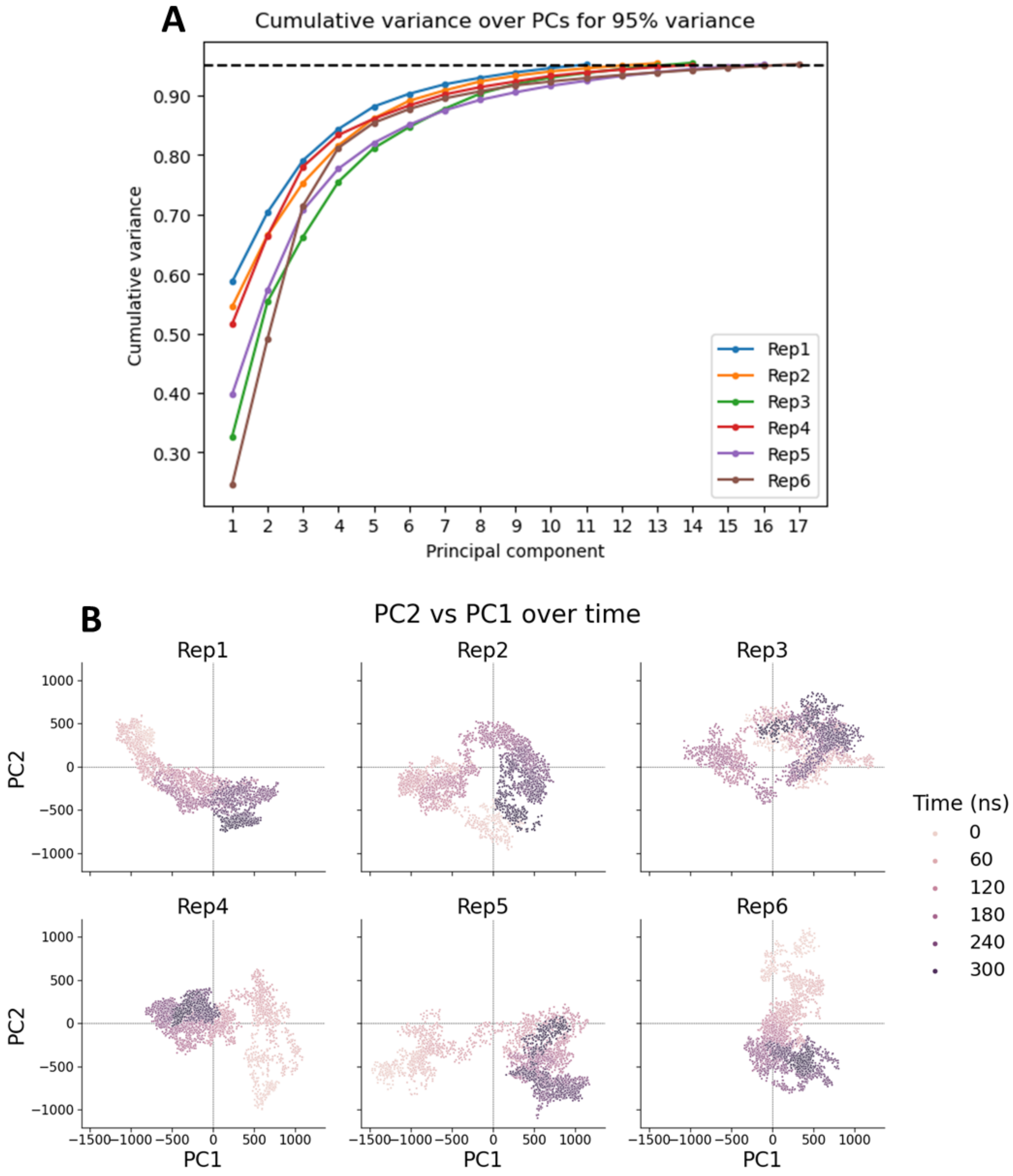

Figure 6.5: Principal component analysis (PCA) of the p75 full-length system. (A) Number of principal components that offer up to 95% cumulative variance for the six replica simulations. (B) Projections of the simulation configurations of the 2D space of the 1st and 2nd principal components over time, after the 1st 150 ns. The PCA was performed for the full-length p75 structure.

As mentioned before, I modeled the EC and IC linkers as extended loops, since they were predicted to be unstructured by webservers. I monitored during the simulations whether they remain unstructured or if they adopt any specific secondary structure (Figure A.16). The results showed that they remain disordered with only the C-terminal residues 250-254 of ECL2 forming a helical conformation, thus extending the TM helix a bit outside the membrane plane.

Next, I performed PCA to investigate the large-scale motions of the full-length p75. Calculation of the cumulative variance showed that many principal components are needed (up to 17) to describe the 95% variance of the p75 motions (Figure 6.5A). This is indicative of quite complex receptor movements. Visualization of the system evolution in the 2D space of the 1st and 2nd principal components (PC1 and PC2) shows different behaviors for each replica (Figure 6.5B). Because PC1 and PC2 can be different on different replicas, I calculated the dot products of the PC1s from different replicas, the PC2s from different replicas and the PC1s and PC2s for each replica (Figure A.17A-C). Most of the dot products are very close to 0, which means orthogonal vectors. The 3rd principal component (PC3) was also taken into account with a root mean squared inner product (RMSIP)[405,406] of PC1, PC2 and PC3, which showed only partial similarity among those 3 PCs (Figure A.17D).

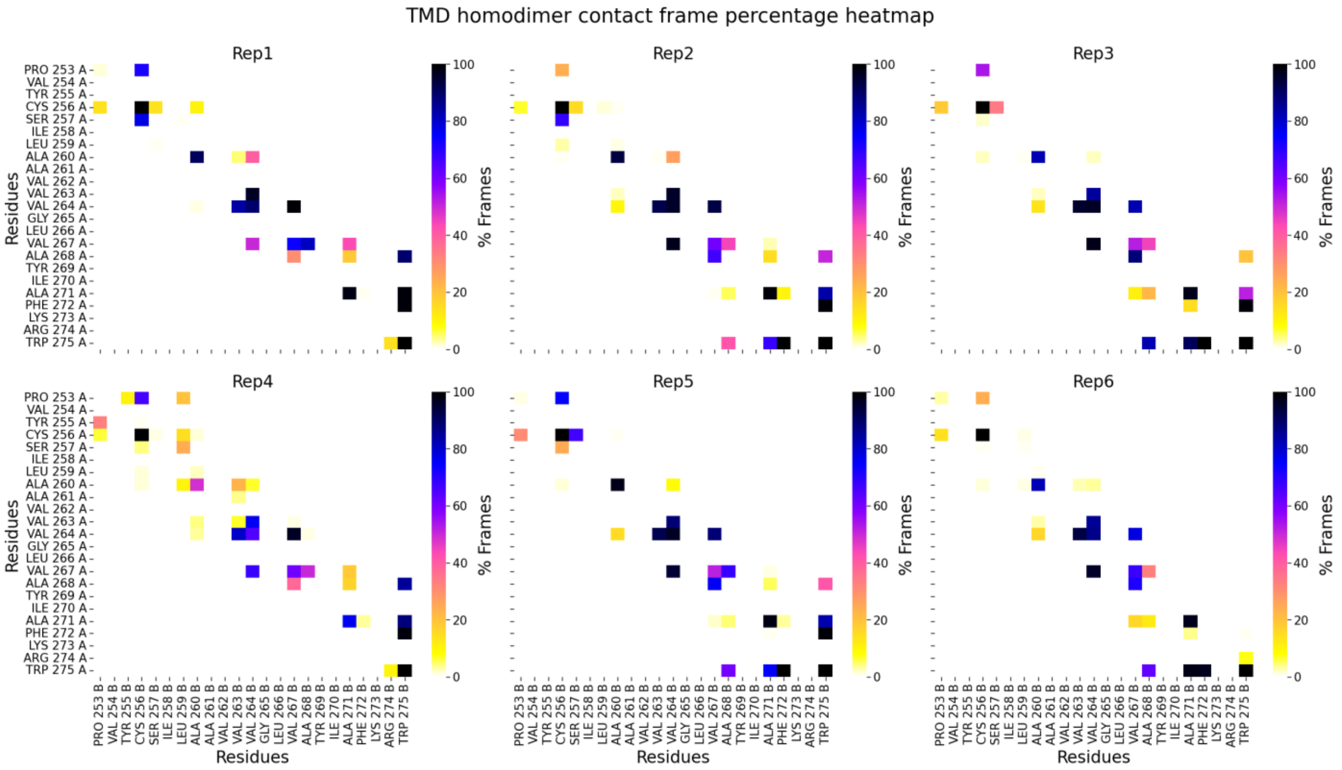

Figure 6.6: Contact maps of the TM helix residues during the 6 replica simulations.

Subsequently, I calculated the contacts between the two monomers of the TM helices of p75 (Figure 6.6). The main goal was to monitor whether the interaction interface of the p75-TM homodimer from the NMR structure (PDB ID: 2MIC)[387] changes when incorporated in the full-length p75 structure. In all replicas the TM helices interact in their whole length with the interface containing the motif C^{256}xxxA^{260}xxV^{263}V^{264}xxV^{267}A^{268}xxA^{271}F^{272}xxW^{275}. C256 (C257 for rat) is the disulfide linked residue in the TM homodimer and thus it is always at the interface. The rest of the interfacial residues have also been reported in the NMR structure, which means that it is preserved also in the full-length system.

I also examined the six geometric parameters that describe TM helix motion, described in Chapter 5. The results show similar density maxima sampled in the six replicas (Figure A.18). An exception to this is the C-termini distance, which has a maximum at ~8 Å in replicas 1, 4 and 6, and at ~3.5 Å in replicas 2, 3 and 5. The NMR structure C-termini distance is 10 Å. It has been previously proposed that p75 undergoes a scissors-like movement upon NT binding, in which the C257-C257 disulfide bond plays the role of the fulcrum.[57] This difference in the C-termini distance might be related to the activation of the p75 receptor which is expected to lead to dissociation of the IC death domains according to fluorescence resonance energy transfer (FRET) data.[57]

In light of this, I examined visually the behavior of the death domains (DDs) during the simulations. Interestingly, the two DD monomers which are initially bound to each other, in a presumably inactive state, dissociate from each other in replicas 2 and 5. These are two of the three replicas where a smaller C-termini distance of the TM domains was observed. This suggests that reduction of the TM C-termini distance might lead to dissociation of the DDs and thus activation of the p75 receptor. For the rest of the replica simulations, where the DDs remain in contact, I calculated the preservation of the DD-DD contacts from the initial bound state, which corresponds to the NMR structure (PDB ID: 2N97).[70] Specifically, I calculated the fraction of the NMR interface contacts that was preserved during the simulations (Figure A.19A). This analysis showed that only very few (maximum 20%) of the NMR DD contacts were actually preserved during the trajectories. The actual contacts of the DDs were also calculated revealing to some extent homotypic interactions (Figure A.19B-E).

Next, I analyzed the interactions between p75 and the lipids of the neuronal membrane (Figure 6.7). In each of the replica simulations, the membrane was remodeled ensuring a random distribution of lipids around the protein. The results revealed that the p75-EC domain rarely has contacts with the membrane (replicas 1 and 4), and this happens through interactions with the GM1 and GM3 gangliosides, which have long extended headgroups. The EC linker interacts with the PC and PE headgroups of lipids, with the sphingolipids GalCER, GM1, GM3, NSM, SSM, but also with cholesterol. The TM domain p75, which has a Cholesterol Recognition Amino acid Consensus (CRAC) motif **VVV**GLVA**Y**IAF**KR**, interacts a lot with cholesterol, PC, PE, SSM, PS and in some cases with PIP2. The IC linker interacts for the majority of the frames with the negatively charged PS, PI and PIP2, but also with the abundant PC and PE lipids. The DDs interact less with the membrane, with most of the interactions being with PS, PI, PE and PC.

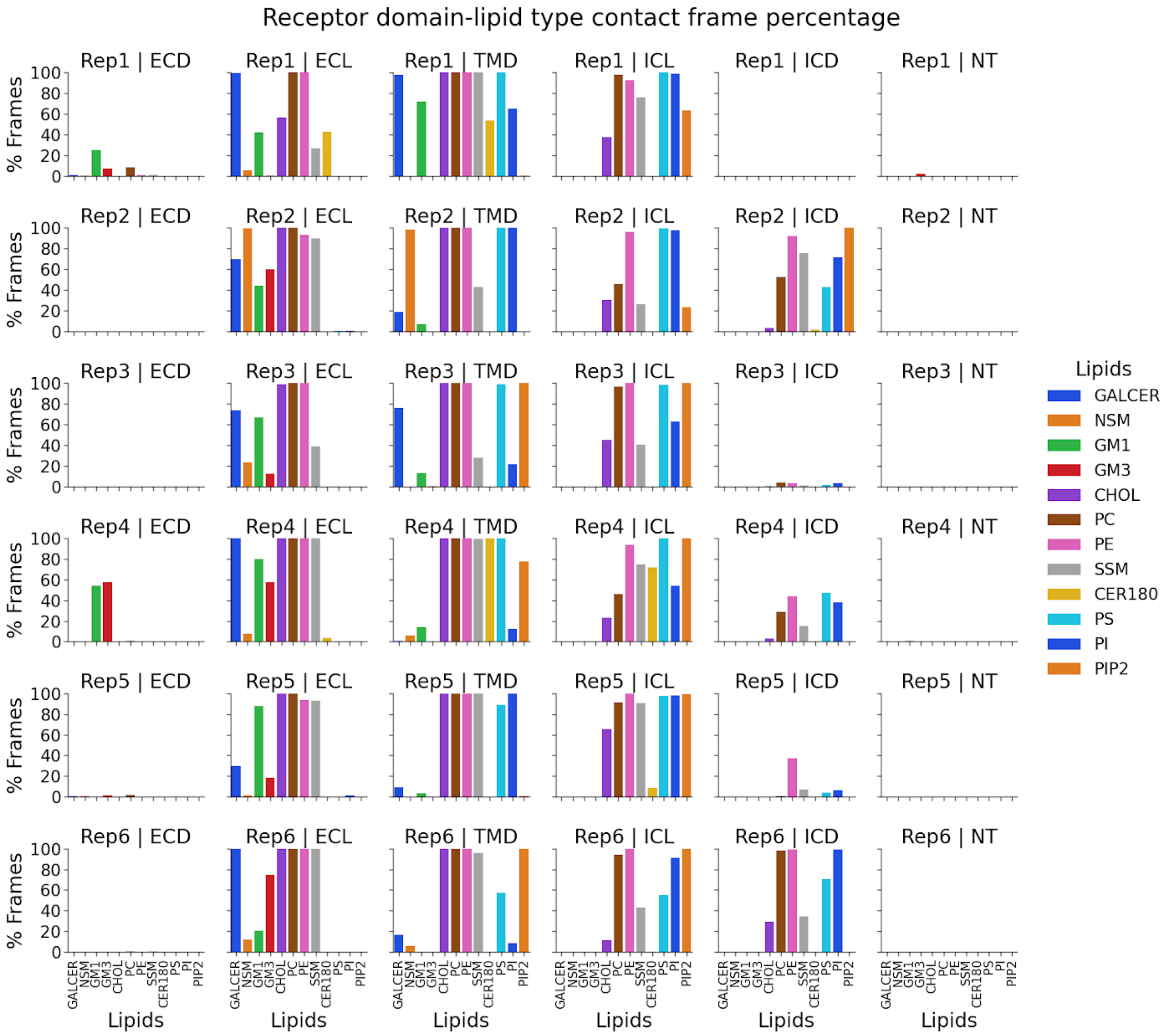

Figure 6.7: Contact analysis between the different domains of p75 and membrane lipids. The domains are as follows: extracellular domain (ECD), extracellular linker (ECL), transmembrane domain (TMD), intracellular linker (ICL), intracellular domain (ICD).

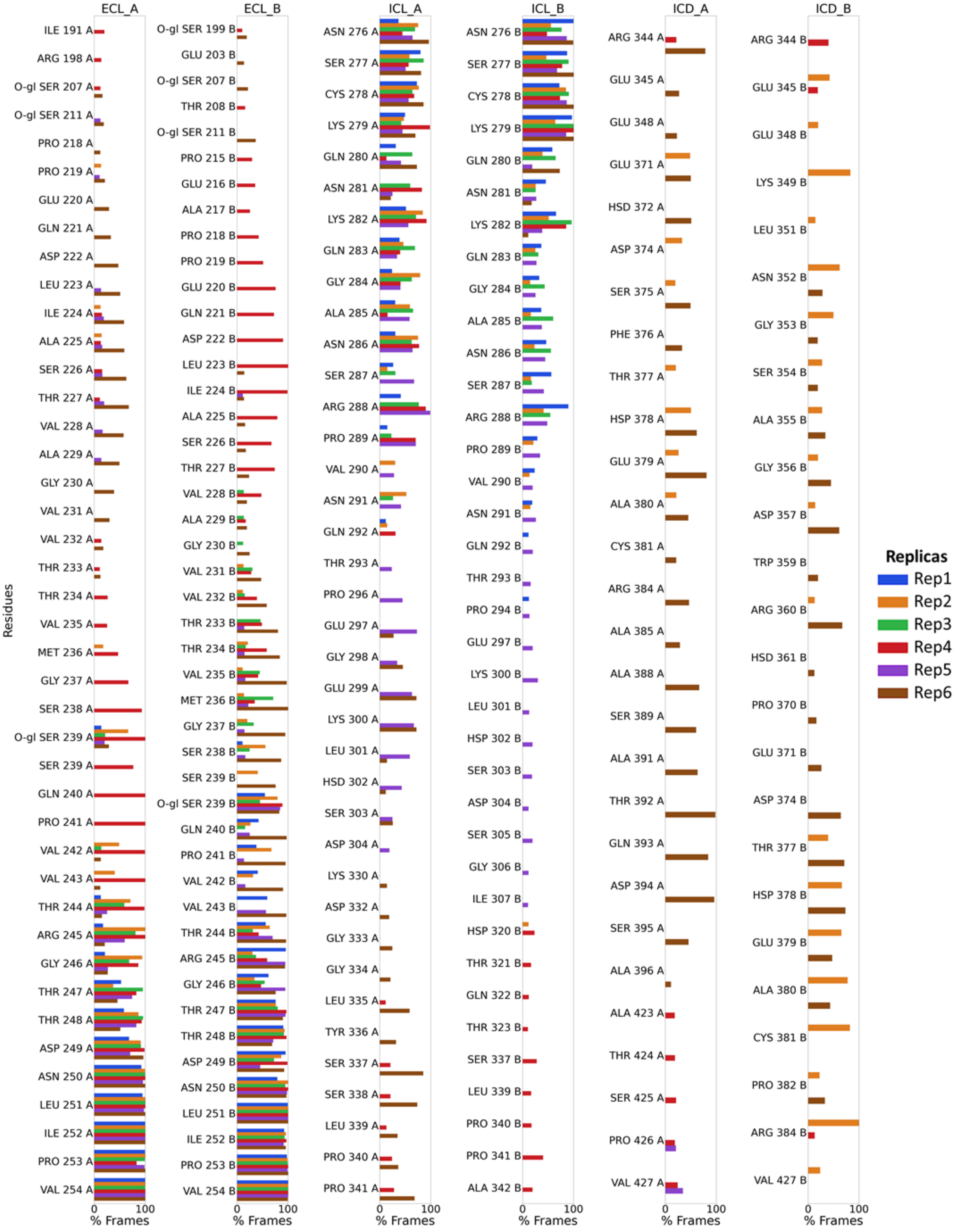

Figure 6.8: Contact analysis between the EC and IC linker (ECL and ICL), as well as the intracellular death domain (ICD) residues with lipids of the neuronal membrane. The O-glycans in the EC linkers have also been included in the calculation. The different colors correspond to different replicas.

Finally, I calculated the residues of the EC and IC linkers as well as the DDs that interact with the membrane (Figure 6.8). This analysis showed that the linkers interact with the membrane mostly through the parts that are closer to it; the C-terminus for the EC linker and the N-terminus for the IC linker. In the EC linker, the O-glycan at S239 from both p75 monomers interacts with the membrane in all replicas. The N-terminus of the EC linker seems to come closer to the membrane and interact with it in replicas 4 and 6. In the same replicas but also replica 5, where the DDs dissociate, the IC linker C-terminus interacts with the inner leaflet of the membrane. The DDs interact with the membrane in replicas 2 and 6, with the former being a replica in which the DDs dissociate.

6.4 Conclusions

In this chapter, I modeled and simulated the full-length structure of p75 in a complex asymmetric neuronal membrane model. For this purpose, I created a model of the full-length p75 homodimer structure, with all the EC, TM and IC domains connected with linkers, and the TM helices disulfide-bonded. In the model, NT-3 is bound to the EC D1-D4 domains of p75. I also added N- and O-glycans in the EC D1 domain and the EC linker, respectively. It has been shown experimentally that p75 is localized and modulated by lipid rafts,[139,140] which have high concentration of cholesterol and sphingolipids. For this reason, I also used a complex model of an asymmetric neuronal bilayer as the membrane environment of the receptor, which is closer to the lipid raft composition, compared to simpler, commonly used membranes.

I performed several atomistic simulations with the modeled system which showed that the disordered EC and IC linkers undergo large conformational changes. Specifically, the p75 homodimer contracts in these linkers, bringing the EC and IC domains closer to the membrane, and even interacting with it in some simulations. In the EC segment, the contraction of the EC linkers is accompanied by a bending of the p75-EC domains bound to NT-3 towards the membrane. The bent EC domains appear to be stable throughout the length of the simulations, however the distance of the EC domain from the outer leaflet of the membrane varies through the different replica simulations. The IC death domains also approach the membrane and interact with it in some replicas. Secondary structure analysis of the linkers showed that they remain mostly unstructured during the simulations. PCA analysis on the full-length p75 was indicative of quite complex receptor movements, which were different throughout the different replica simulations.

The TM helices retained the initial NMR structure interface, which is probably enforced by the presence of the disulfide cross-linking of the helices. Interestingly, the C-termini distance of the TM helices sampled two different states at ~8 and 3.5 Å in different replicas. In two out of three replicas where the shorter distance occurred, the death domains (DDs), which are initially bound to each other, in a presumably inactive state, dissociate from each other; an event expected to occur upon p75 activation. The correlation of the TM C-terminal distance and the dissociation of the DDs is in agreement with experimental data which propose that NT binding induces a scissors-like movement of disulfide-linked p75-TM domain, with the C257-C257 disulfide bond acting as the fulcrum.[57] Thus, in two out of six replica simulations, p75 possibly passes from an inactive to an active state. Analysis of the DD-DD contacts showed that they vary during the simulations, with the input NMR structure being unstable in the context of the full-length p75 structure.

Finally, I analyzed the interactions of the different domains of p75 with lipids of the neuronal membrane model. This analysis showed that the IC linker interacts for the majority of the frames with the negatively charged PS, PI and PIP2. In the two replicas where the dissociation of the DDs occurs, the IC segment interacts with the membrane either through the IC linker or the DD itself. This suggests a potential role of the membrane in the activation mechanism of p75.

The apparent correlation of the TM C-termini distance with the p75 death domain dissociation should be further probed with both computational and experimental methods. Enhanced sampling MD simulation methods can be used to bias the movement of the TM C-termini and study their influence on the IC domains with better statistics. Also, experimental studies, such as FRET assays, can be used to probe the changes of the TM C-termini upon NGF binding, through attachment of the fluorophores directly after the TM domains instead of at the end of the IC domains.

7 Conclusions and future perspectives

In this thesis, I set out to study and design novel neurotrophin (NT) mimetics and explore the mechanism of action of the p75 receptor. I have described the molecular modeling and design of NT mimetics and their interaction with the TrkA and TrkB NT receptors. I have also performed extensive mechanistic studies on the different domains of p75 receptor, i.e. the extracellular (EC), transmembrane (TM), as well as the full-length p75 receptor. Specifically, by employing molecular dynamics (MD) simulations, I investigated: (i) the glycosylation influence on the dynamics of p75-EC, (ii) the dimeric state of p75-TM, and finally (iii) the conformations of the full-length glycosylated p75 in a neuronal membrane model. The main conclusions of each mechanistic study are presented below.

Design and mechanistic studies of small molecule NT mimetics

I undertook the computer-aided design and molecular modeling of the NT mimetics developed by the EuroNeurotrophin collaborators. Specifically, I investigated the binding mode of the steroidal lead compound BNN27, for which I validated the two previously suggested binding pockets 1a and 1b at the interface of TrkA-D5 with NGF by STD-NMR.[270] Molecular docking tests showed that conventional rigid protein docking was sufficient to place the lead compound at site 1b, while for site 1a I employed a docking protocol which allowed for flexibility of the protein side chains and accommodation of the compound in the pocket. Also, I identified site 1b as the most plausible, accounting for the selectivity of BNN27 for TrkA over TrkB.

The determination of the two possible binding sites and the docking protocols allowed the study of BNN27 derivatives. I performed modeling of BNN27 analogues with three- and six-membered-17-spiro substitutions bound at the interface of TrkA-D5 and NGF and suggested to medicinal chemists in the project which compounds to prioritize in organic synthesis. From this work, I also identified that a phenol group at the C17 substitution position of the steroidal core of BNN27 would form favorable interactions with the proteins. This led to the start of a quest for other possible fragments that could be attached to position C17 and increase the affinity of the lead compound for the TrkA receptor.

In this framework, I performed virtual screening of a library of 9200 compounds synthesized in UNICAEN. Eleven compound fragments that came out of this screening were tested via STD-NMR for

TrkA-D5 binding, and eight fragments were identified as binders. Subsequently, I further optimized the fragment binder that had the best docking score. I did this with R-group enumeration, which generated 226 derivatives, which I tested for TrkA over TrkB selectivity with molecular docking calculations. I proposed the six most promising compounds for organic synthesis, which was not completed during the course of the current PhD thesis and should be included in future work on this project.

Additionally to the molecular design of novel BNN27 analogues, I performed mechanistic studies on small-molecule BNN27 derivatives that have been identified by the consortium as agonists of TrkA and TrkB. I used molecular docking and MD simulations to investigate the binding of the compounds to the EC domain of TrkA, and compared with the equivalent calculations performed on TrkB by Christina Athanasiou. The simulations indicated that the predicted binding modes were unstable, as relatively fast detachment of the small molecules from the receptors took place. This indicates weak binding to these sites which is not in agreement with the receptor selectivity of the compounds.

Since the docking and MD simulations of the compounds in the EC domains of TrkA and TrkB did not produce clear results on the compound binding site, together with consideration of the steroid core of the compounds, similar to that of cholesterol that is naturally found on cell membranes, I investigated the compound tendency to penetrate the membrane. I performed MD simulations with compounds close to the membrane which showed spontaneous incorporation of the compounds to the membrane bilayer either as single molecules (simulations by Christina Athanasiou) or as aggregates which then diffuse within the membrane. Control simulations with cholesterol showed that the compounds have a tendency to penetrate the membrane faster than cholesterol. The propensity of the compounds to readily penetrate the cell membrane suggests that they might act on the NT receptor TM domain, similarly to the antidepressant drug fluoxetine or psychedelic drugs that were found to bind to the TM domain of TrkB.[294,296] Simulations with the TM domains of TrkA and TrkB showed non-specific transient interactions with the compounds.

The mechanistic study results show that there are still open questions regarding the mode of action of these neurosteroid analogues. A potential explanation could be that the compounds bind to more than one region on the receptors and several binding events act synergistically. Also, accumulation of high compound concentrations in the cell membrane might alter the microenvironment of the membrane, which in turn leads to activation of the receptors. In fact it is known that NT receptors translocate to lipid rafts upon activation,[139,141,143] which shows that the lipid background plays a role in receptor function. Finally, the experimentally observed activity of NT mimetics on NT receptors might be an indirect effect resulting from binding to other proteins that interact with NT receptors. This could explain why the single binding sites that were tested here cannot provide a conclusive mechanism. This dictates that further experiments regarding the mode of action of these compounds with STD-NMR, X-ray crystallography, mutagenesis and membrane permeability assays need to be carried out for the development of analogues with greater affinity and selectivity. Also, the synthesis and testing of the six optimized fragments, which have been designed to specifically bind at the interface of TrkA-D5 with NGF could further validate the currently proposed binding sites.

Glycosylation in the p75-EC dynamics

In this thesis, I investigated the dynamical behavior of the EC domains of the p75 receptor in the presence and absence of glycosylation moieties covalently attached to the domains. The EC segment of p75 has been identified to have a single complex N-glycan at position N60 of CRD1.[76,77,367] I performed MD simulations of the glycosylated and non-glycosylated p75-EC as homodimers bound to NT-3, as monomers bound to NT-3, and as single monomers.

The results showed that only the very N-terminal part of the p75-EC can be shielded by the single glycan, which can partially interact with NT-3. The cloud of glycan conformations appears to block the entrance at the N-terminal region of the receptor, which might affect NT binding kinetics, which have been experimentally indicated to be different for the p75 compared to the Trk receptors.[383] The glycan shielding of the proteins was low and the binding of larger proteins, e.g. antibodies, rather than small molecules in the area proximal to the glycan may be more disturbed.

The EC domains of p75 were particularly stable during the simulations even though they have several loops present. This seems to be achieved by 12 disulfide bonds which form a disulfide “ladder” throughout the length of the EC domain. The N-terminal CRD1 domain that contains the single glycan was relatively more flexible because it has more disordered regions. The simulations also showed that the two p75 monomers are placed further apart in the presence of glycans, which interact with each other and are placed between the two monomers. The interacting glycans might help with the overall avidity of the complex and stabilize it in this homodimeric state or block the NT from dissociating from p75, which might affect its binding kinetics.

The results presented here regarding the glycosylation of the p75 receptor need to be corroborated experimentally. One direction would be to perform binding kinetic studies of the NTs bound to the glycosylated and non-glycosylated p75 receptor and estimate the effect of the glycans on kinetic properties. These effects could also potentially be studied with enhanced sampling simulations to acieve better statistics. Structural biology techniques could also provide valuable structural insights, although the flexible nature of glycans would make it challenging to achieve high resolution. The conclusions from this part of the thesis highlight the importance glycosylation, which should be considered in experimental and computational studies of the NT receptors.

TM helix dimerization of p75 receptor

I investigated the dimerization states of the TM helices of the p75-WT receptor, where the helices are covalently bonded at C257, and of the p75-C257A mutant which is incapable of NT-dependent receptor activation.[57] Both TM helix homodimers have been solved with NMR in DPC micelles.[59] I performed coarse-grained (CG) MD simulations using both NMR structures in DPC micelles, which showed that the p75-WT TM homodimer is quite stable due to the presence of the disulfide bond. It has been suggested previously that p75 might be activated by NTs with the TM helices undergoing a scissors-like movement. Here interhelical crossing angles of -45^o to -30^o were observed for the p75-WT simulations, corresponding to various interhelical TM C-terminal distances, which is in agreement to this scissors-like movement.

The simulations of the mutant p75-C257A showed that the NMR structure is not stable and instead two other right-handed and left-handed helical arrangements occurred with smaller crossing angles than the NMR arrangement. This was validated with atomistic simulations. However, the $A^{262}xxxG^{266}$ dimerization motif which is located at the NMR interface, is also present at the interface of the two new arrangements. This shows the importance of the interactions in this motif when the C257 residue is not present in the TM sequence. However, since this mutant does not occur physiologically, the arrangements that were sampled are probably not relevant to any biological state. I subsequently ran enhanced sampling CG metadynamics simulations in POPC bilayers, which further validated the two arrangements that had been sampled in the unbiased CG simulations for this mutant.

A limitation of the simulations that I performed for the identification of the TM arrangements of p75 is the lipid environment, which was DPC micelles in this case. The cell membrane environment in which p75 is found physiologically has different physicochemical properties and could induce the formation of different arrangements than those sampled here. The metadynamics simulations were run in a POPC membrane, which also differs from the real neuronal membrane. Additionally, detailed steric effects at the interface of the TM helices might be underestimated by the coarse grained nature of the Martini force field. More detailed long scale atomistic simulations could further validate the p75-TM arrangements proposed here, and thus their ability to eventually explain receptor function.

Full-length p75 receptor in the neuronal membrane

In this thesis, I also studied the dynamics of the full-length glycosylated p75 receptor in a neuronal membrane model. For this, I created for the first time a model of the full-length p75 homodimer structure, with all the EC, TM and IC domains connected with linkers, and the TM helices disulfide-bonded. In the model, NT-3 is bound to the EC D1-D4 domains of p75. I also added N- and O-glycans in the EC D1 domain and the EC linker, respectively. I embedded the p75 receptor model to an asymmetric neuronal bilayer, which is closer to the lipid raft composition where p75 localizes, compared to simpler, commonly-used membranes.

Atomistic simulations of this complex system showed that the disordered EC and IC linkers undergo large conformational changes. Specifically, the p75 homodimer contracted in these linkers, bringing the EC and IC domains closer to the membrane, and even interacting with it in some simulations. In the EC segment, the contraction of the EC linkers was accompanied by a bending of the p75-EC domains bound to NT-3 towards the membrane. The IC death domains also approached the membrane and interacted with it in some replicas.

The disulfide-bonded TM helices retained the initial NMR structure interface during the simulations, while their inter-termini distance (defined by the last TM residue backbone atoms) sampled two different states at ca. 8 and 3.5 Å, in different replicas. Interestingly, in two out of three replicas where the shorter distance occurred, the death domains (DDs), which are initially bound to each other, in a presumably inactive state, dissociate from each other, an event expected to occur upon p75 activation. The correlation of the TM C-terminal distance and the dissociation of the DDs is in agreement with experimental data which propose that NT binding induces a scissors-like movement of the disulfide-linked p75-TM domain, with the C257-C257 disulfide bond acting as the fulcrum.[57] Thus, in this thesis, a potential activation event of the p75 receptor is presented for the first time in atomic-detail, with an allosteric signal propagated through the TM helices to the IC domains. In the two replicas where the dissociation of the DDs occurs, the IC segment interacts with the membrane either through the IC linker or the DD itself. This suggests a potential role of the membrane in the activation mechanism of p75.

This thesis presents for the first time a model of the fully-glycosylated full-length p75 receptor bound to NT-3 in a neuronal membrane environment, as well as the potential activation mechanism of the receptor in atomic detail. Additional enhanced sampling simulations could be used to better characterize the events that lead to activation. Also, potential force field limitations could be tested by simulating the system with different force fields. It is important for the findings presented here to be explored experimentally, such as the TM helix distance before and after NT binding. Another test could be the use of different membrane systems to investigate the role of membrane in receptor activation. Cryo-electron microscopy might also be able to provide structural insights of the overall conformation of the receptor in a membrane and validate the bended conformations observed here. However, the flexible nature of the EC and IC linkers might prove challenging to create high resolution structures. Overall, the results presented here provide new insights into the dynamical behavior of p75.

Acknowledgements

The work presented herein was performed in the Molecular and Cellular Modelling (MCM) group of the Heidelberg Institute of Theoretical Studies (HITS), under the supervision of Prof. Dr. Rebecca Wade, whom I would like to thank for giving me the opportunity to work in her group and in this interesting project, as well as for her guidance and mentoring through the years of the PhD.

I would also like to thank my second supervisor and Thesis Advisory Committee (TAC) member, Prof. Dr. Christian Klein, and my third TAC-committee and defense-committee member, Prof. Dr. Robert Russell, for agreeing to and providing valuable feedback throughout the PhD work. Furthermore, I would like to thank my fourth defense-committee member, Dr. Jirka Peschek, for agreeing to be part of my examination-committee.

Additionally, I would like to thank the members of the MCM group for all the scientific discussions, and especially Christina Athanasiou, who also did her PhD on the EuroNeurotrophin project, for the extensive collaboration and discussion on all the aspects of the project, and Dr. Stefan Richter for his assistance in technical issues faced throughout the PhD work.

My PhD was part of the EuroNeurotrophin consortium, and I would like to thank all the partners for their collaboration. This work has received funding from the European Union's Horizon 2020 research and innovation programme "Euroneurotrophin", under the Marie Skłodowska-Curie grant agreement No. 765704, and the Klaus Tschira Foundation. The computations performed as part of this thesis were supported by the state of Baden-Württemberg through bwHPC and the German Research Foundation (DFG) through Grant INST 35/1134-1 FUGG.

Appendix

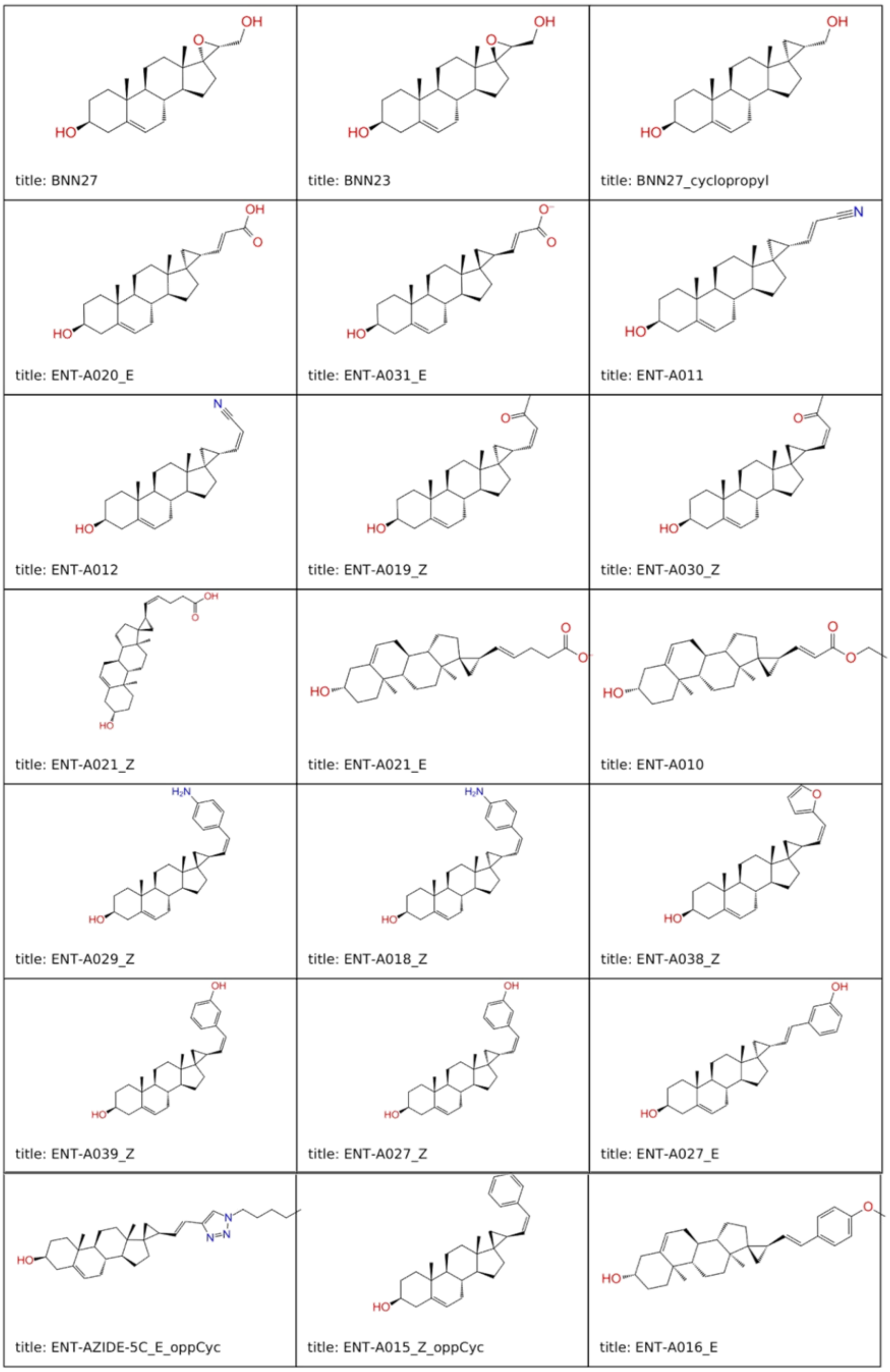

Figure A.1: 2D structures of the best-scoring compounds of the library with cyclopropyl BNN-27 analogues.

Table A.1: UNICAEN fragments with best docking scores and binding poses.

# Fragment	Library ID	2D Structure	Docking score (kcal/mol)
1	CNevoteccermn2019.3430	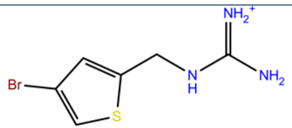	-4.342
2	CNevoteccermn2019.3102 (R)	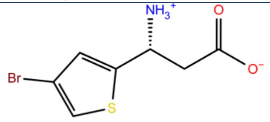	-6.060
3	CNevoteccermn2019.2110 (S)	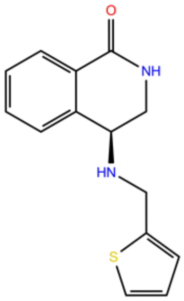	-5.599
4	CNevoteccermn2019.892 (S)	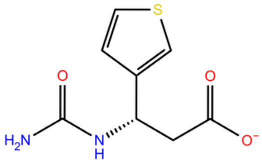	-5.196
5	CNevoteccermn2019.1870	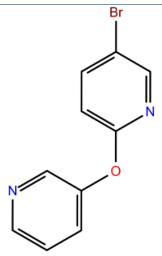	-4.369
6	CNevoteccermn2019.1398	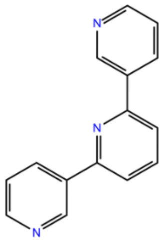	-4.479
7	CNevoteccermn2019.728	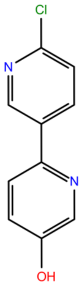	-4.507

8	CNevoteccermn2019.212	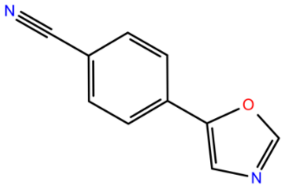	-4.089
9	cermn217peseseetsolubilise2018.137	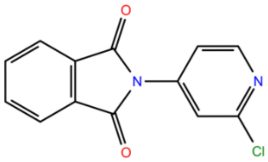	-4.227
10	CNevoteccermn2019.3365	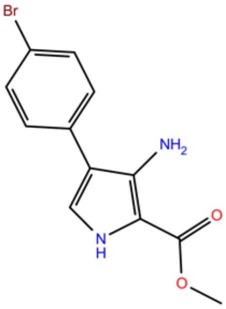	-4.222
11	CNevoteccermn2019.1956	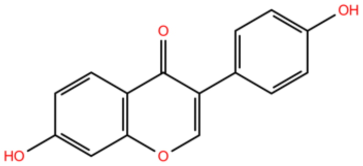	-4.891
12	CNevoteccermn2019.1504 (R)	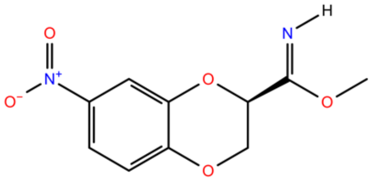	-4.146
13	CNevoteccermn2019.3116	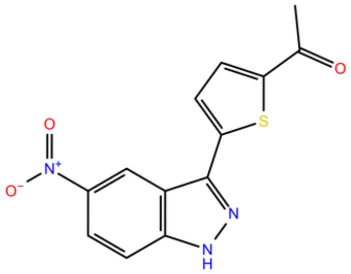	-4.690
14	CNevoteccermn2019.2259	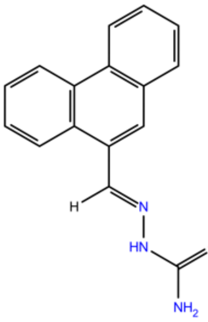	-5.157

15	CNevoteccermn2019.1990	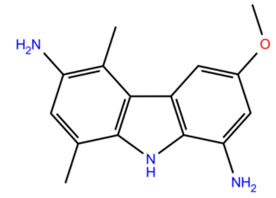	-4.007
16	CNevoteccermn2019.771 (R)	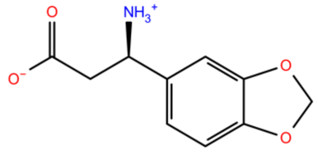	-4.708
17	CNevoteccermn2019.1179	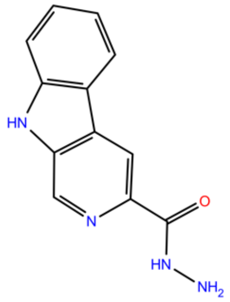	-4.596
18	CNevoteccermn2019.1830	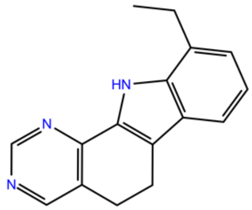	-4.858
19	CNevoteccermn2019.386	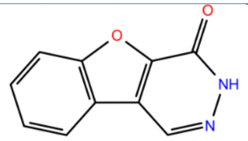	-4.508
20	CNevoteccermn2019.2808	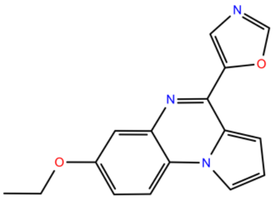	-4.577
21	CNevoteccermn2019.2981	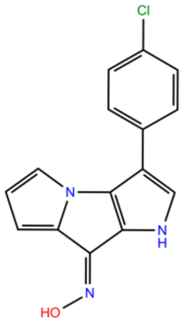	-4.817

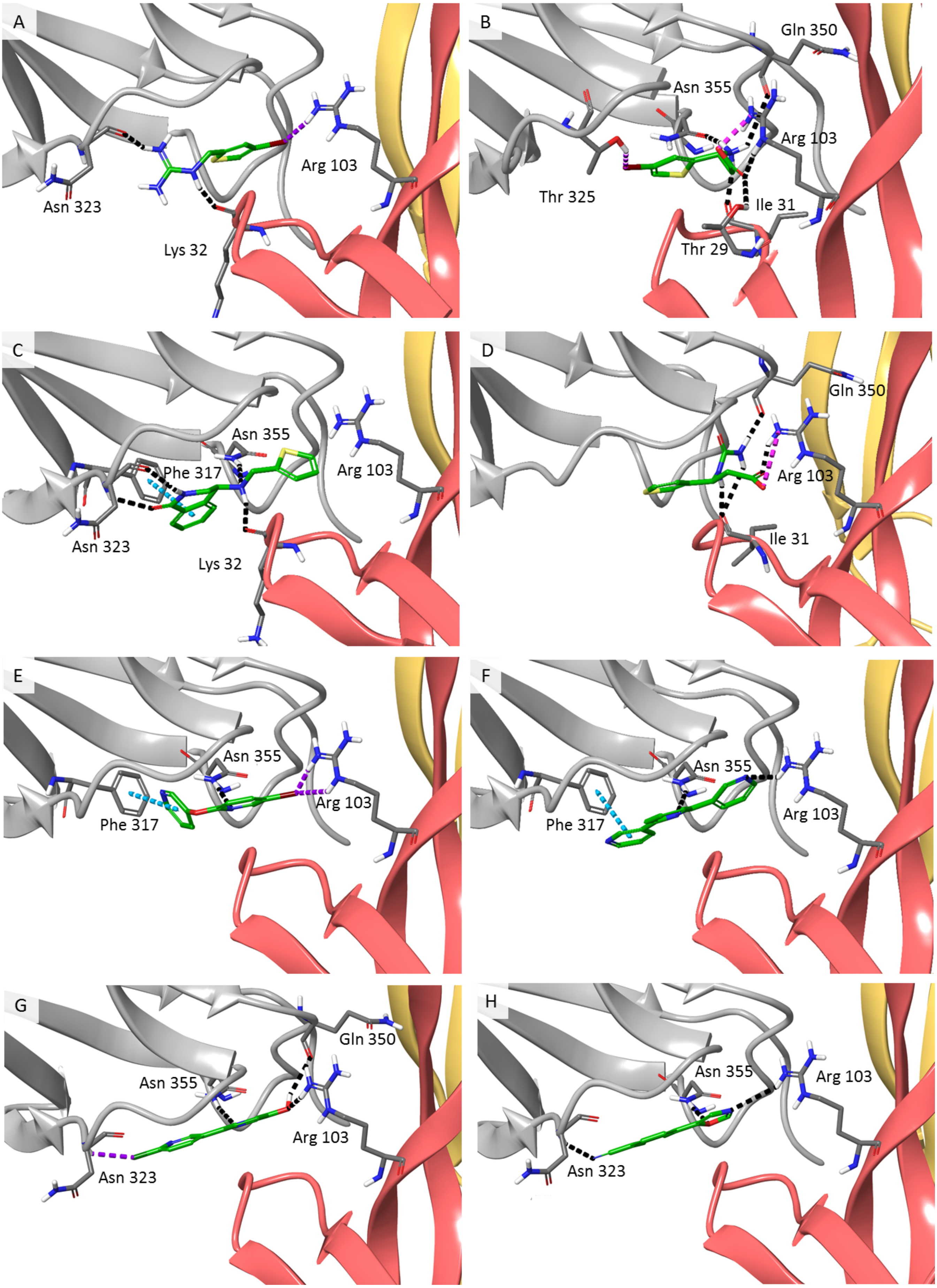
A
Asn 323
Arg 103
Lys 32
B
Gln 350
Asn 355
Arg 103
Thr 325
Ile 31
Thr 29
C
Asn 355
Phe 317
Arg 103
Asn 323
Lys 32
D
Gln 350
Arg 103
Ile 31
E
Asn 355
Arg 103
Phe 317
F
Asn 355
Arg 103
Phe 317
G
Gln 350
Asn 355
Arg 103
Asn 323
H
Asn 355
Arg 103
Asn 323

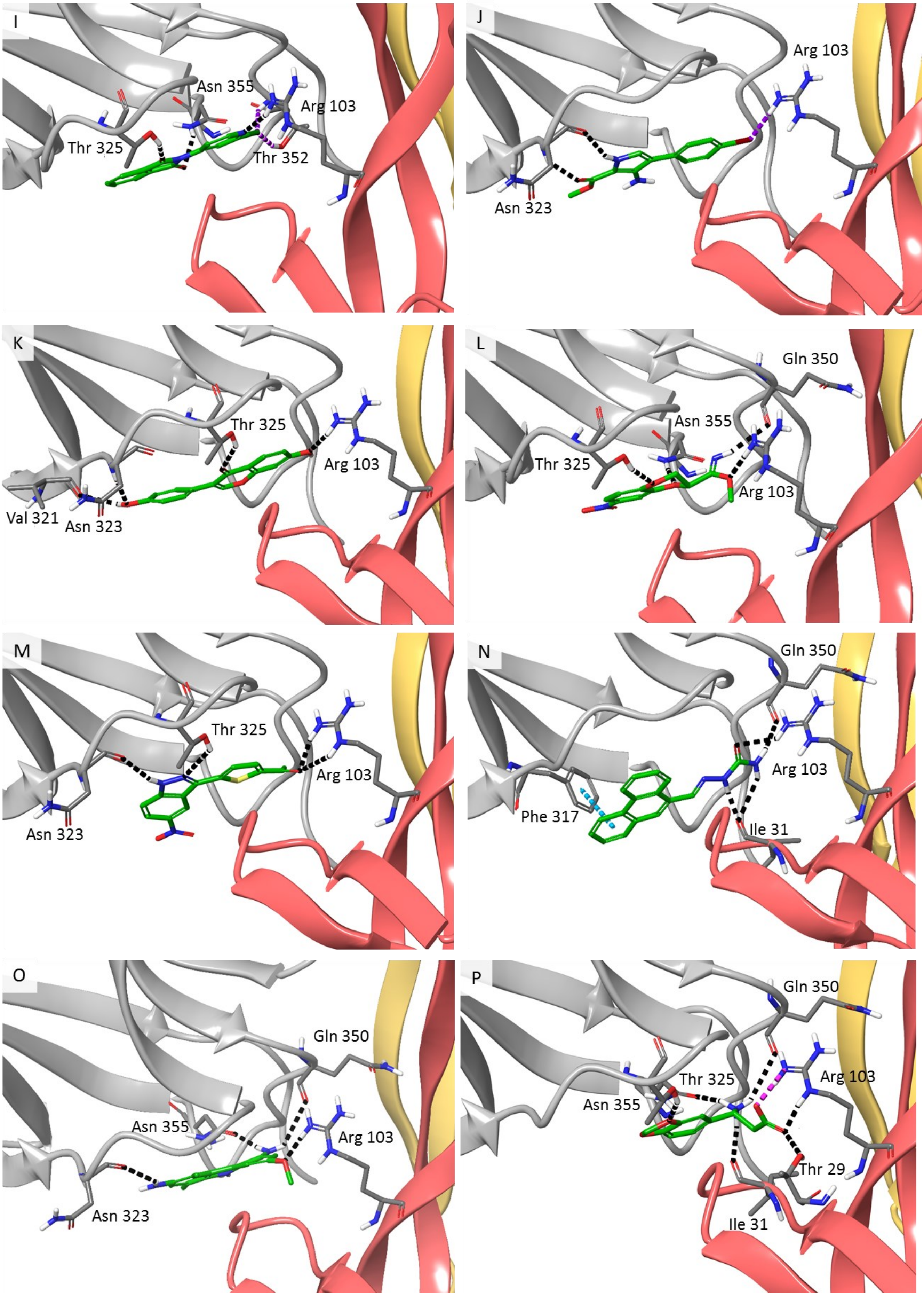
I
Asn 355
Arg 103
Thr 325
Thr 352
J
Arg 103
Asn 323
K
Thr 325
Arg 103
Val 321
Asn 323
L
Gln 350
Asn 355
Thr 325
Arg 103
M
Thr 325
Arg 103
Asn 323
N
Gln 350
Arg 103
Phe 317
Ile 31
O
Gln 350
Asn 355
Arg 103
Asn 323
P
Gln 350
Thr 325
Arg 103
Asn 355
Thr 29
Ile 31

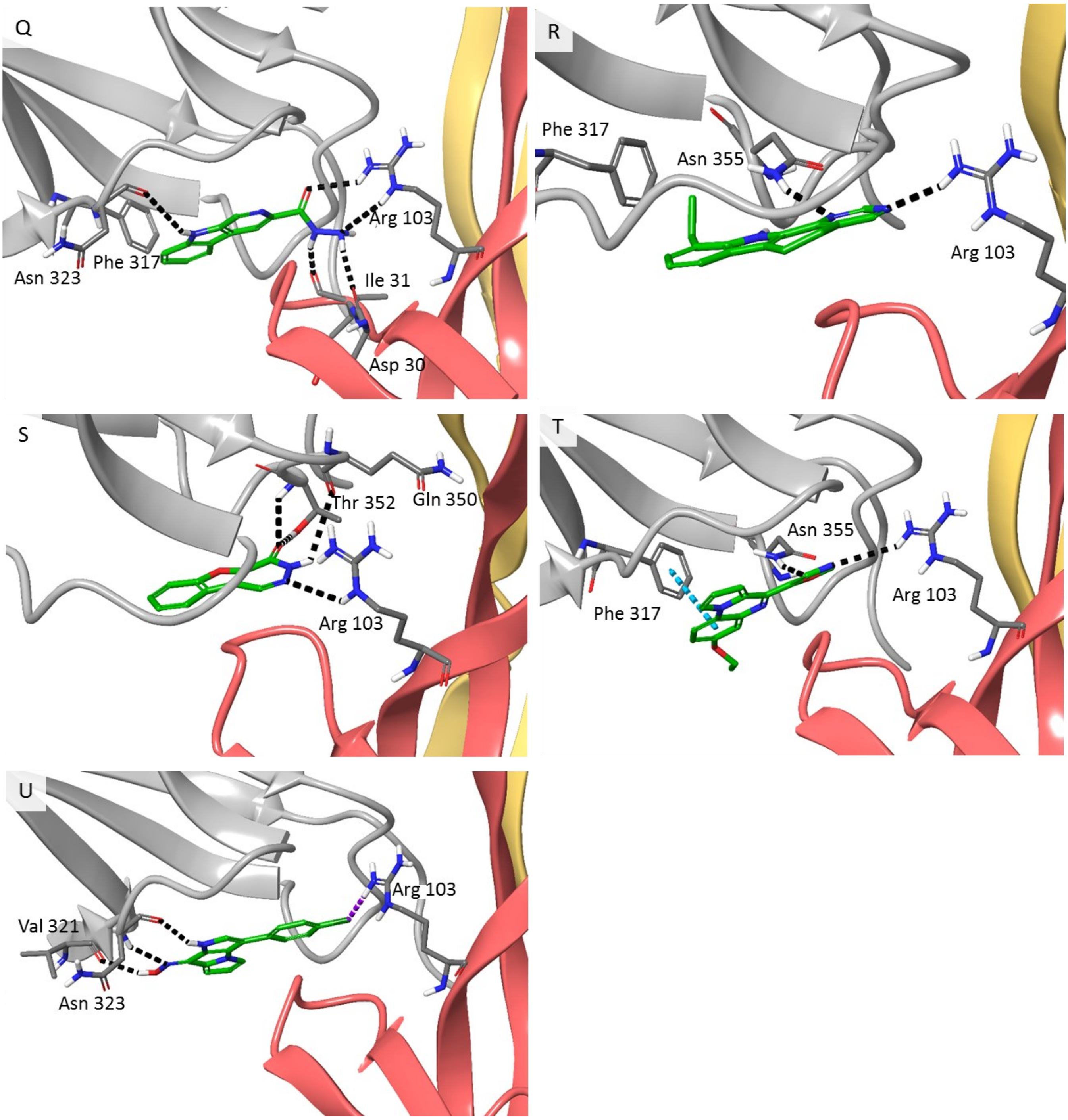

Figure A.2: Binding poses of best-scoring UNICAEN fragment compounds. The order of the compounds in the figures is the same as that in Table A.1.

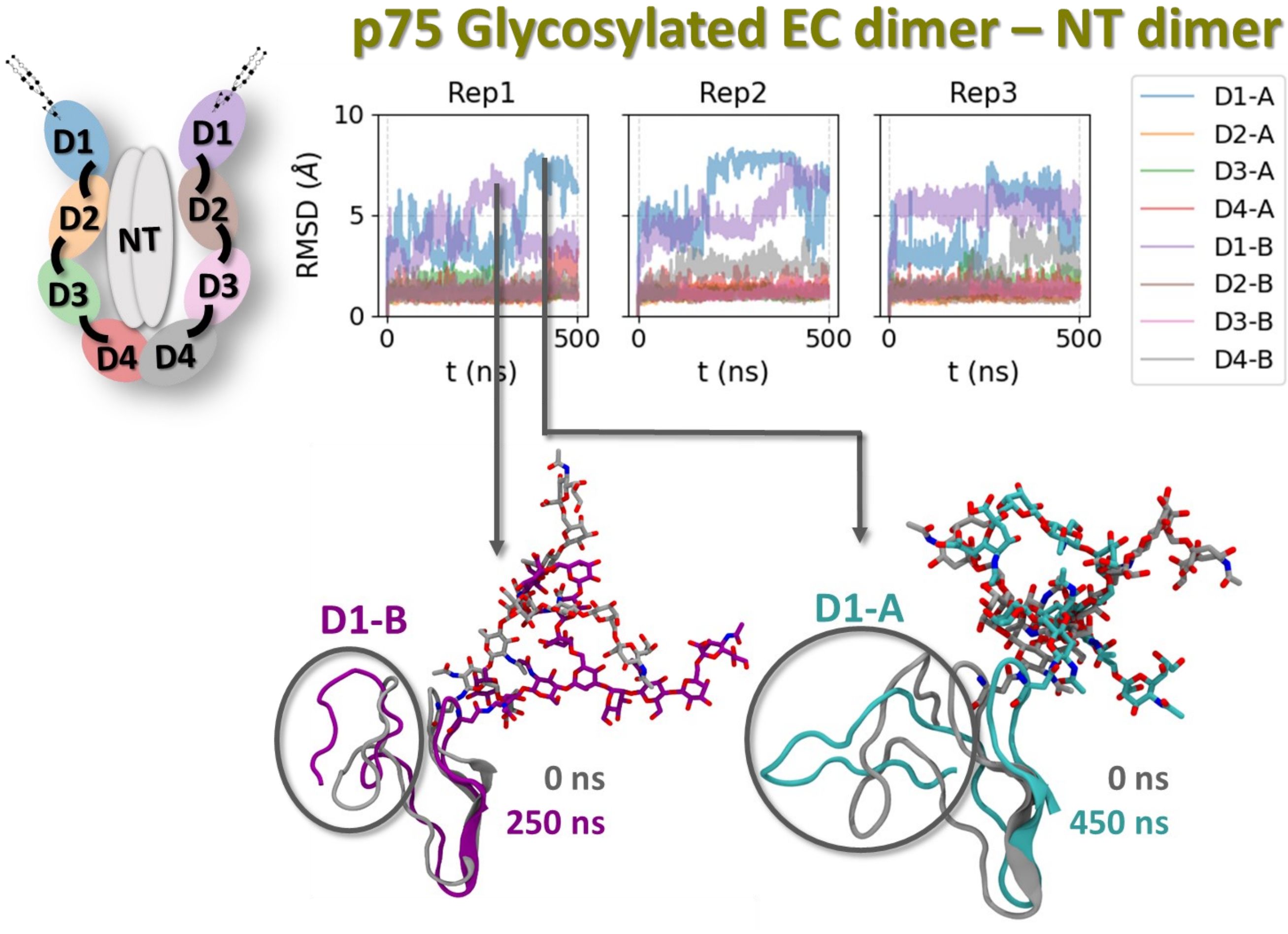

Figure A.3: Closer examination of conformations of the D1 domain of p75-EC with the glycan at Asn 60 which is covalently attached to the D1 domain. Two example representations of high RMSD values are shown with D1-glycan aligned to the input structure from X-ray. The high RMSD conformations are shown in purple and cyan for the two D1 monomers and the initial structures in grey. The D1 domain is shown in cartoon representation, while the glycan is shown in stick representation.

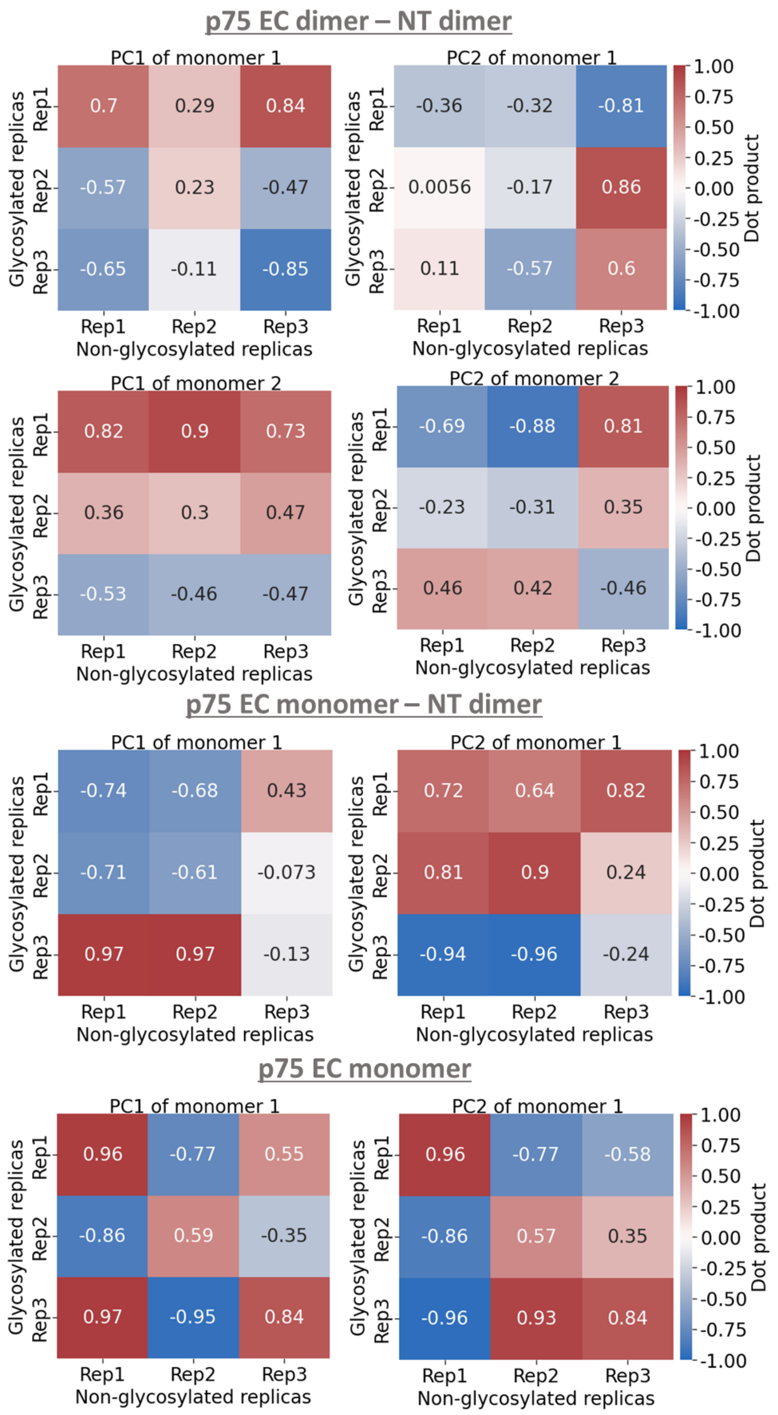

Figure A.4: Dot products of the 1st and 2nd principal components from the various replicas and systems with and without glycans. The dot product values are also color-coded with heatmaps, with values equal to 1 showing parallel vectors, values of -1 showing antiparallel vector and 0 meaning vertical vectors.

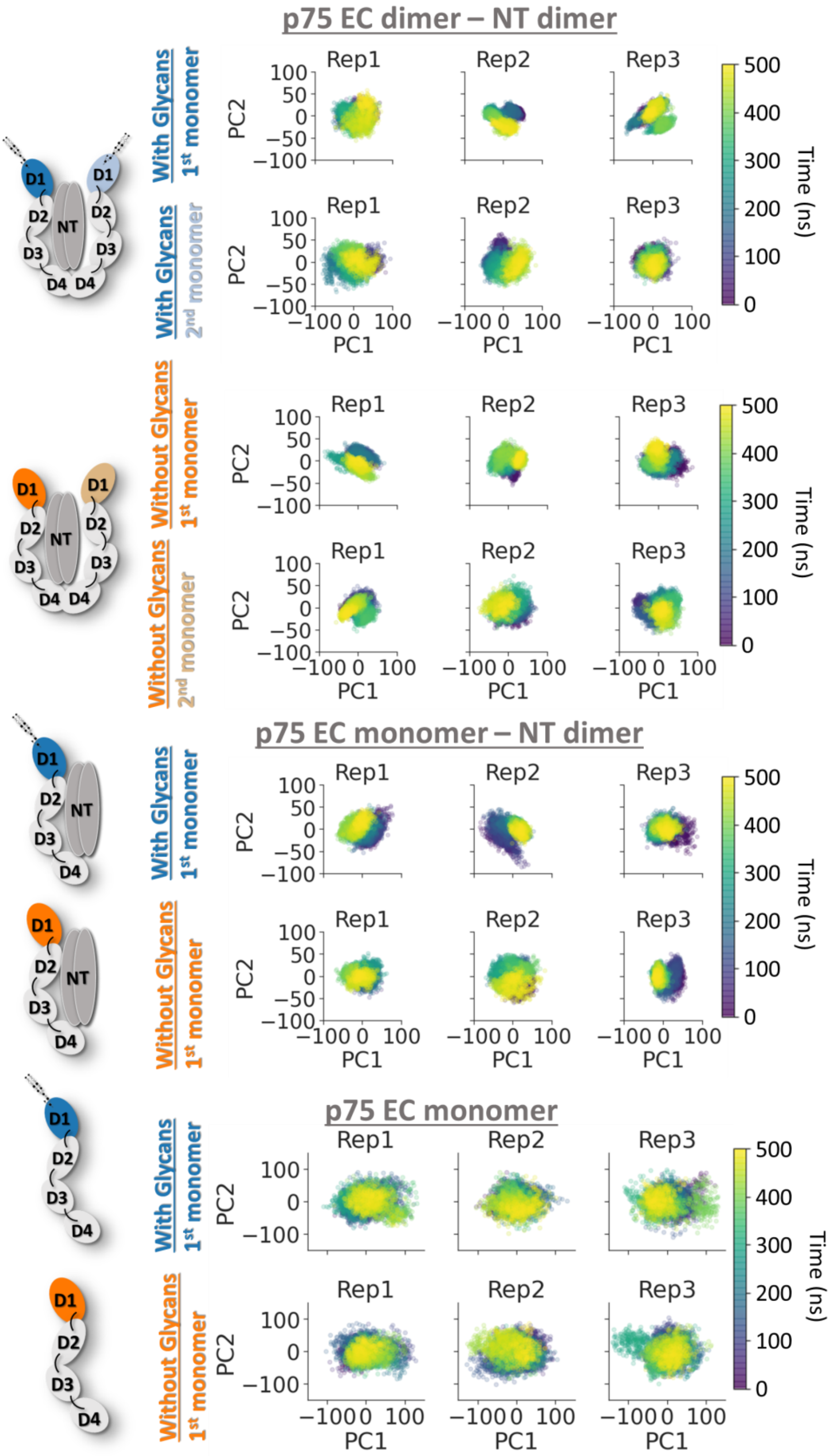

Figure A.5: Principal component analysis (PCA) of the D1 domain of p75-EC as a time evolution after alignment to the rest of the domains, for the glycosylated or not systems. Only the 1st and 2nd principal components are visualized.

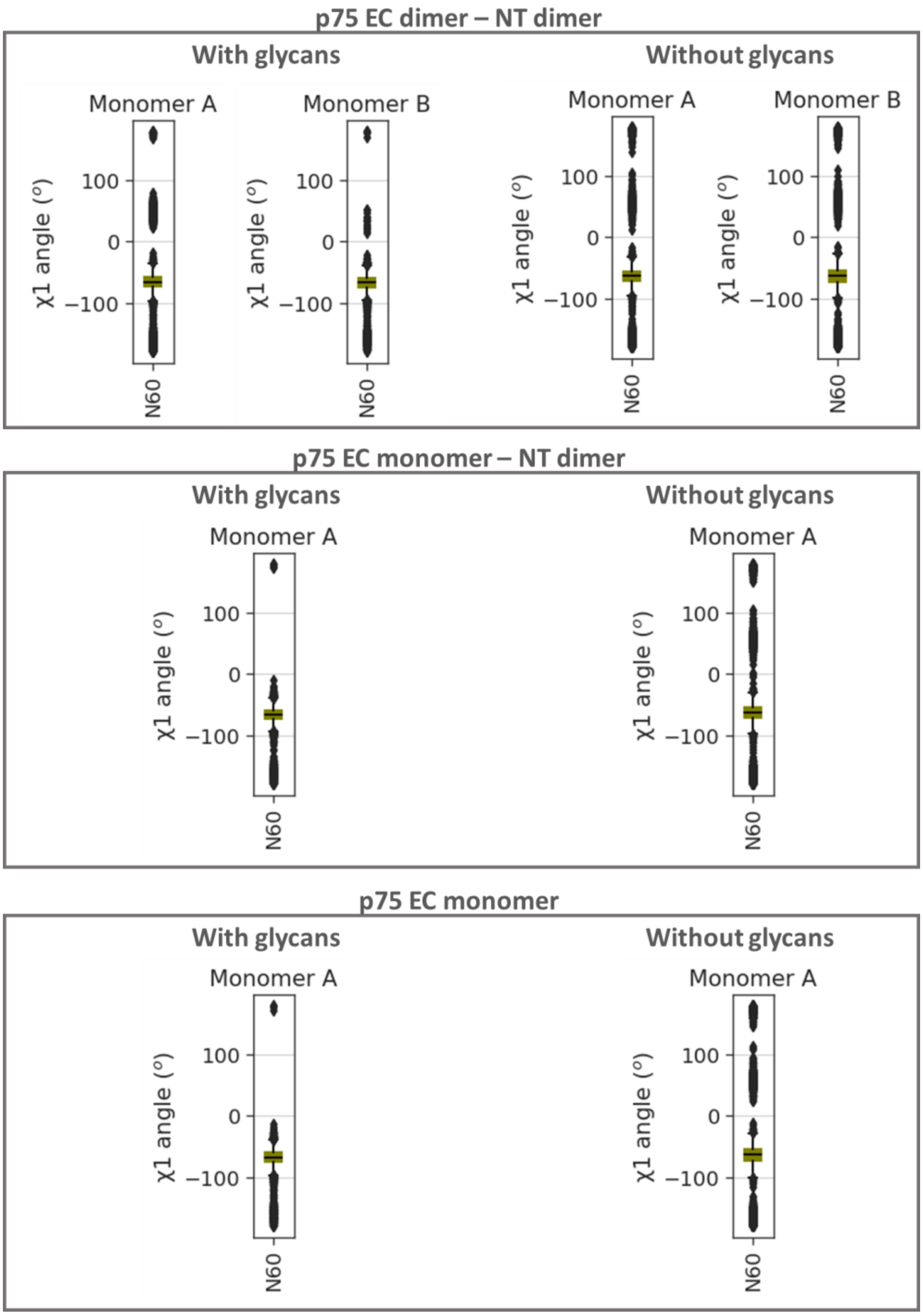
p75 EC dimer – NT dimer

p75 EC monomer – NT dimer

p75 EC monomer

Figure A.6: Distribution calculations of the χ1 dihedral angle of N60 for the three p75-EC systems with and without the glycans present.

p75-WT

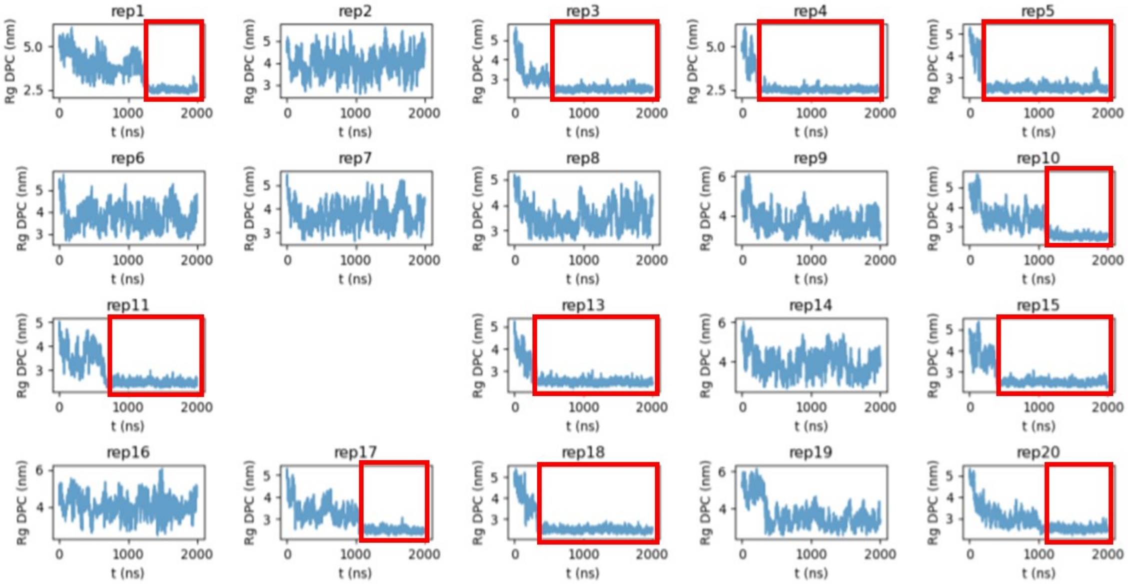

p75-C257A

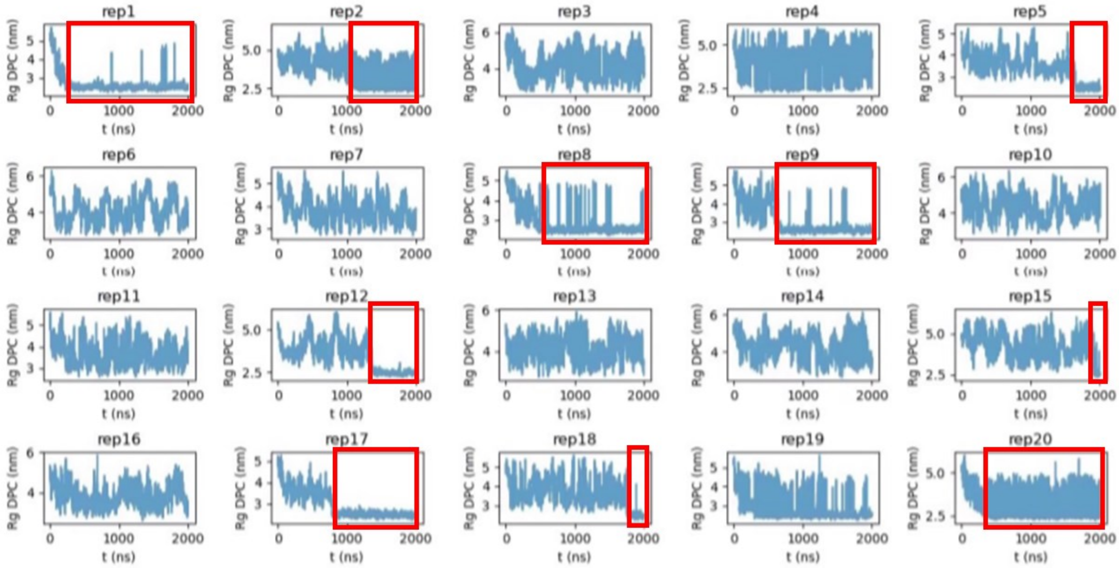

Figure A.7: Radius of gyration (Rg) of DPC lipids at the NPT equilibration of CG simulations. Low and constant Rg values suggest that the micelle has been formed, while the crossing of the periodic box can be visualized as “jumps” in the Rg values. Red boxes show micelle formation. The p75-WT replica 12 simulation did not finish successfully and was thus omitted from being plotted.

```
[ molecule ]
DPC
[ martini ]
NC3 PO4 C1 C2 C3
[ mapping ]
charmm36
[ atoms ]
; Terminal head group (choline)
1     N   NC3
2   C13   NC3
3  H13A   NC3
4  H13B   NC3
5  H13C   NC3
6   C14   NC3
7  H14A   NC3
8  H14B   NC3
9  H14C   NC3
10   C15   NC3
11  H15A   NC3
12  H15B   NC3
13  H15C   NC3
14   C12   NC3 NC3 NC3 PO4
15  H12A   NC3 NC3 NC3 PO4
16  H12B   NC3 NC3 NC3 PO4
17   C11   NC3 PO4
18  H11A   NC3 PO4
19  H11B   NC3 PO4
; Phosphate group
20     P   PO4
21   O13   PO4
22   O14   PO4
23   O11   PO4 PO4 C1
24   O12   PO4 PO4 PO4 NC3
; Acyl chain
25   C31   C1 PO4
26   H1X   C1 PO4
27   H1Y   C1 PO4
28   C32   C1 C1 PO4
29   H2X   C1 C1 PO4
30   H2Y   C1 C1 PO4
31   C33   C1 C1 C1 PO4
32   H3X   C1 C1 C1 PO4
33   H3Y   C1 C1 C1 PO4
34   C34   C1
35   H4X   C1
36   H4Y   C1
37   C35   C1 C1 C2
```

```
38   H5X   C1 C1 C2
39   H5Y   C1 C1 C2
40   C36   C2 C1
41   H6X   C2 C1
42   H6Y   C2 C1
43   C37   C2 C2 C1
44   H7X   C2 C2 C1
45   H7Y   C2 C2 C1
46   C38   C2
47   H8X   C2
48   H8Y   C2
49   C39   C2 C2 C3
50   H9X   C2 C2 C3
51   H9Y   C2 C2 C3
52  C310   C3 C2
53  H10X   C3 C2
54  H10Y   C3 C2
55  C311   C3 C3 C2
56  H11X   C3 C3 C2
57  H11Y   C3 C3 C2
58  C312   C3
59  H12X   C3
60  H12Y   C3
61  H12Z   C3
;;;making a choline group
[out]
C14 N C13 C12
H14A N C13 C12
H14B N C13 C12
H14C N C13 C12
[ chiral ]
C15 N C12 C13 C14
H15A N C12 C13 C14
H15B N C12 C13 C14
H15C N C12 C13 C14
```

Figure A.8: CG-to-AA map for the backward.py script.[393]

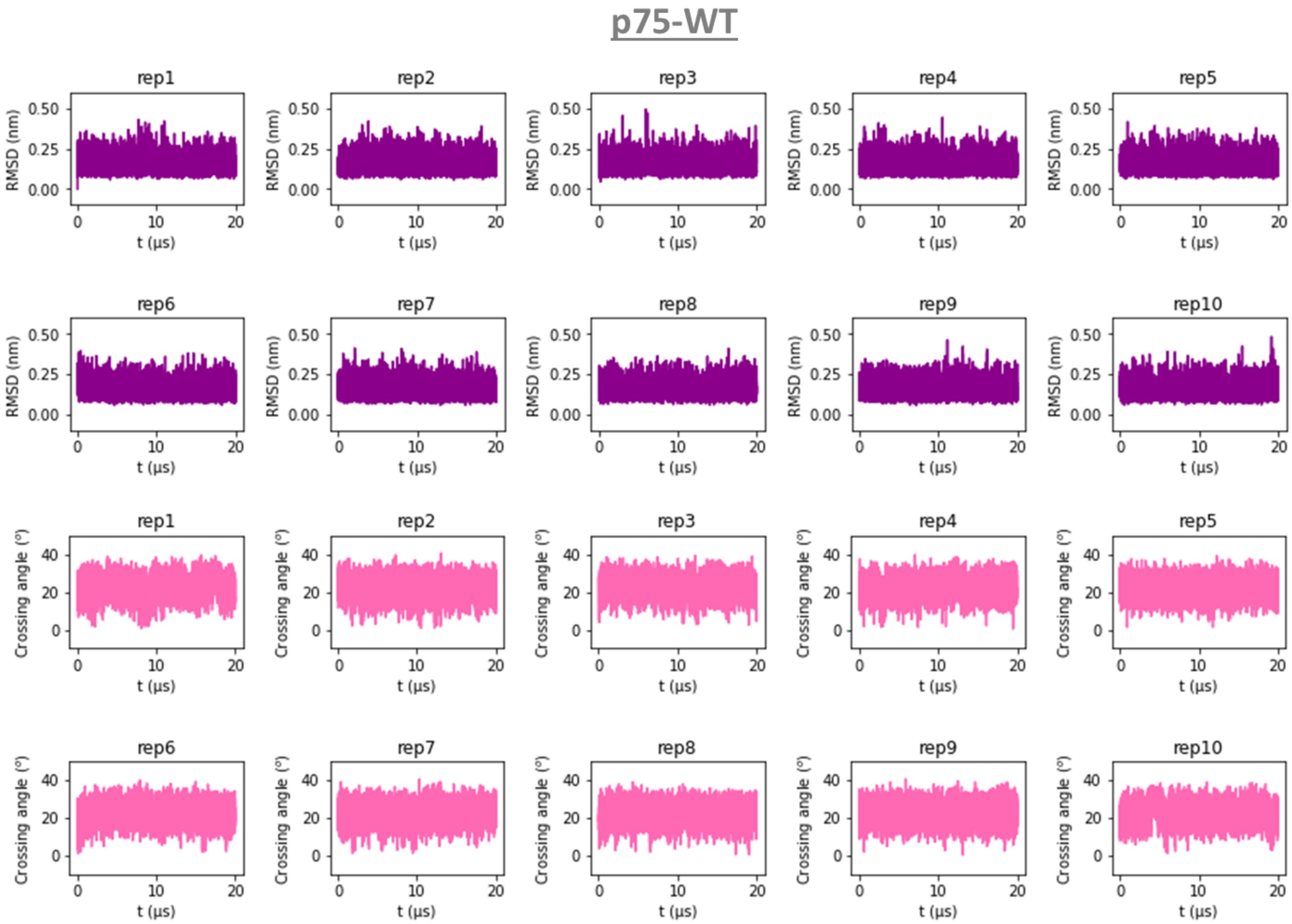

Figure A.9: RMSD and absolute crossing angle calculations for the p75-WT CG simulations.

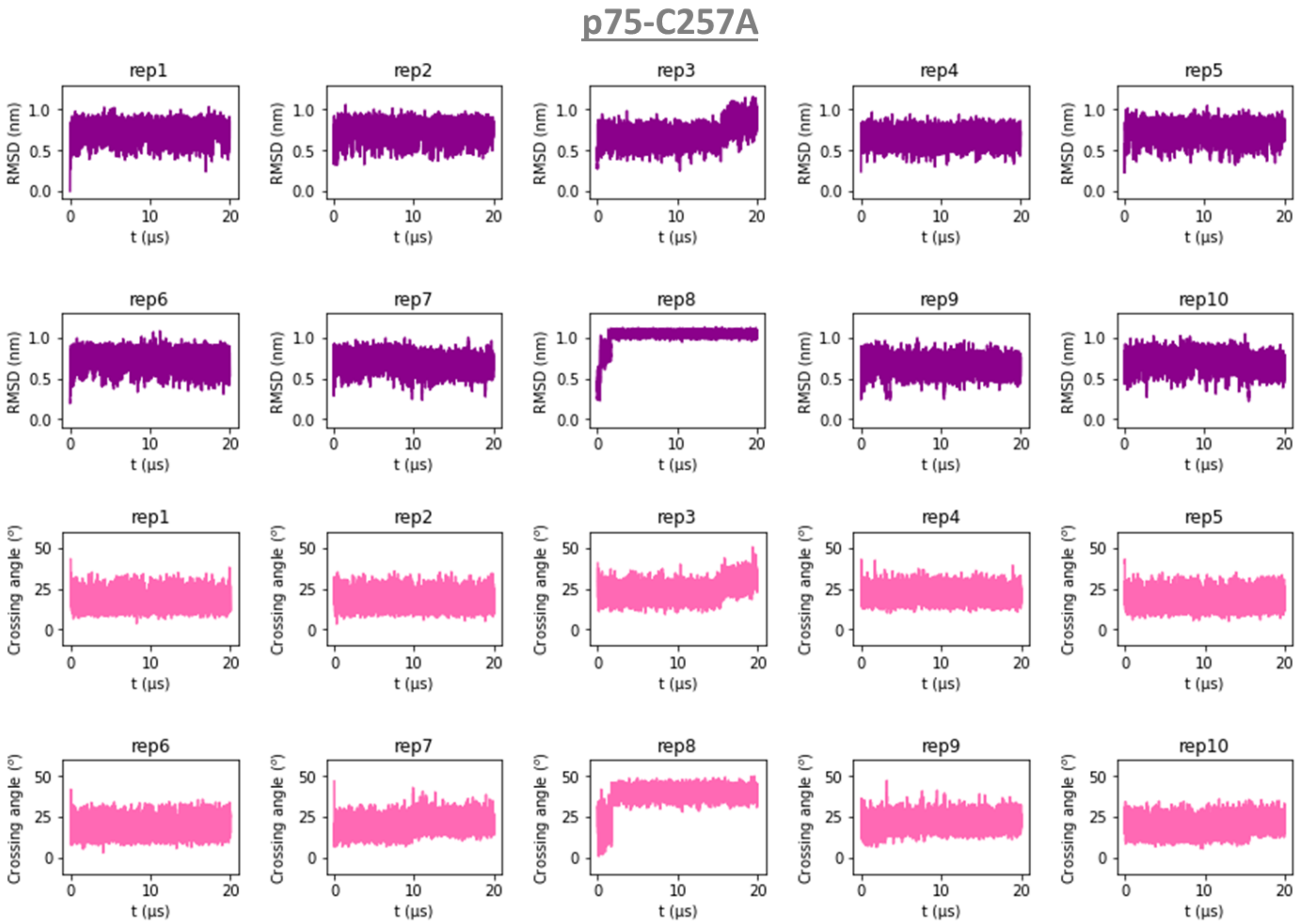

Figure A.10: RMSD and absolute crossing angle calculations for the p75-C257A CG simulations.

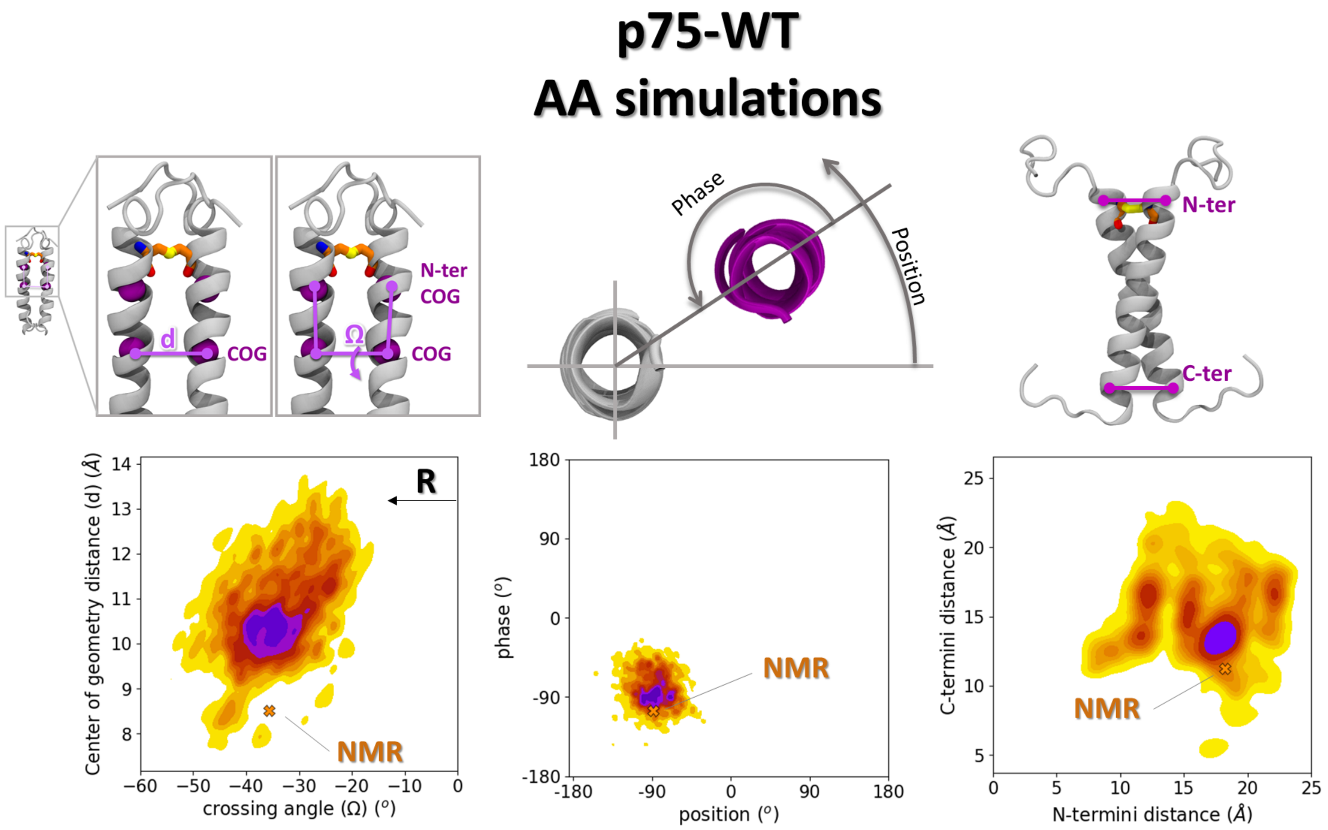

Figure A.11: Analysis of p75-WT TM homodimer arrangements from AA simulations. Density distribution plots are shown for the six geometric parameters that I chose to describe the TM helix arrangements: interhelical distance and crossing angle (Ω), phase and position, N- and C-termini distance. Negative crossing angle values correspond to right-handed helical arrangements ("R"). The NMR structure is shown in the orange cross.

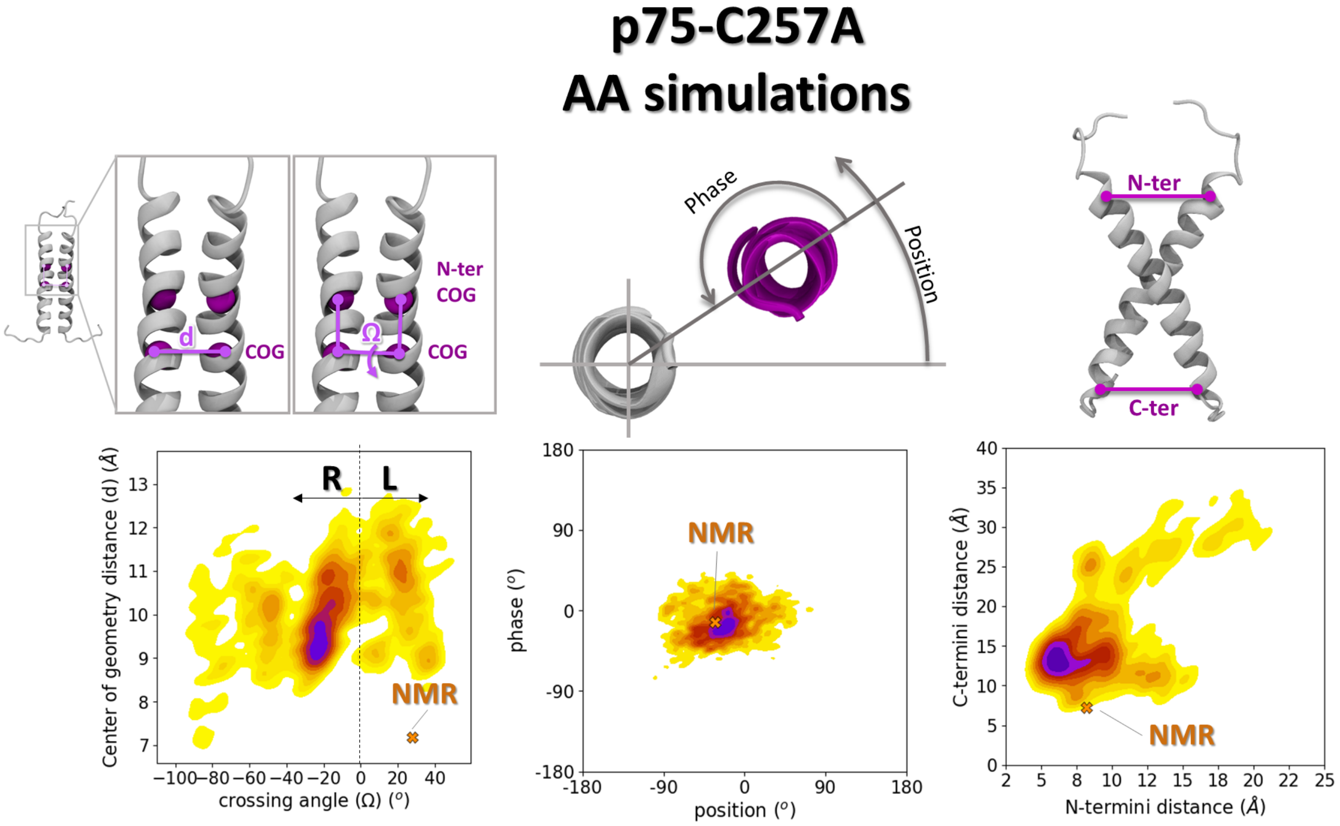

Figure A.12: Analysis of p75-C257A TM homodimer arrangements from AA simulations. Density distribution plots are shown for the six geometric parameters that I chose to describe the TM helix arrangements: interhelical distance and crossing angle (Ω), phase and position, N- and C-termini distance. Negative crossing angle values correspond to right-handed helical arrangements ("R") and positive values to left-handed helical arrangements ("L"). The NMR structure is shown in the orange cross.

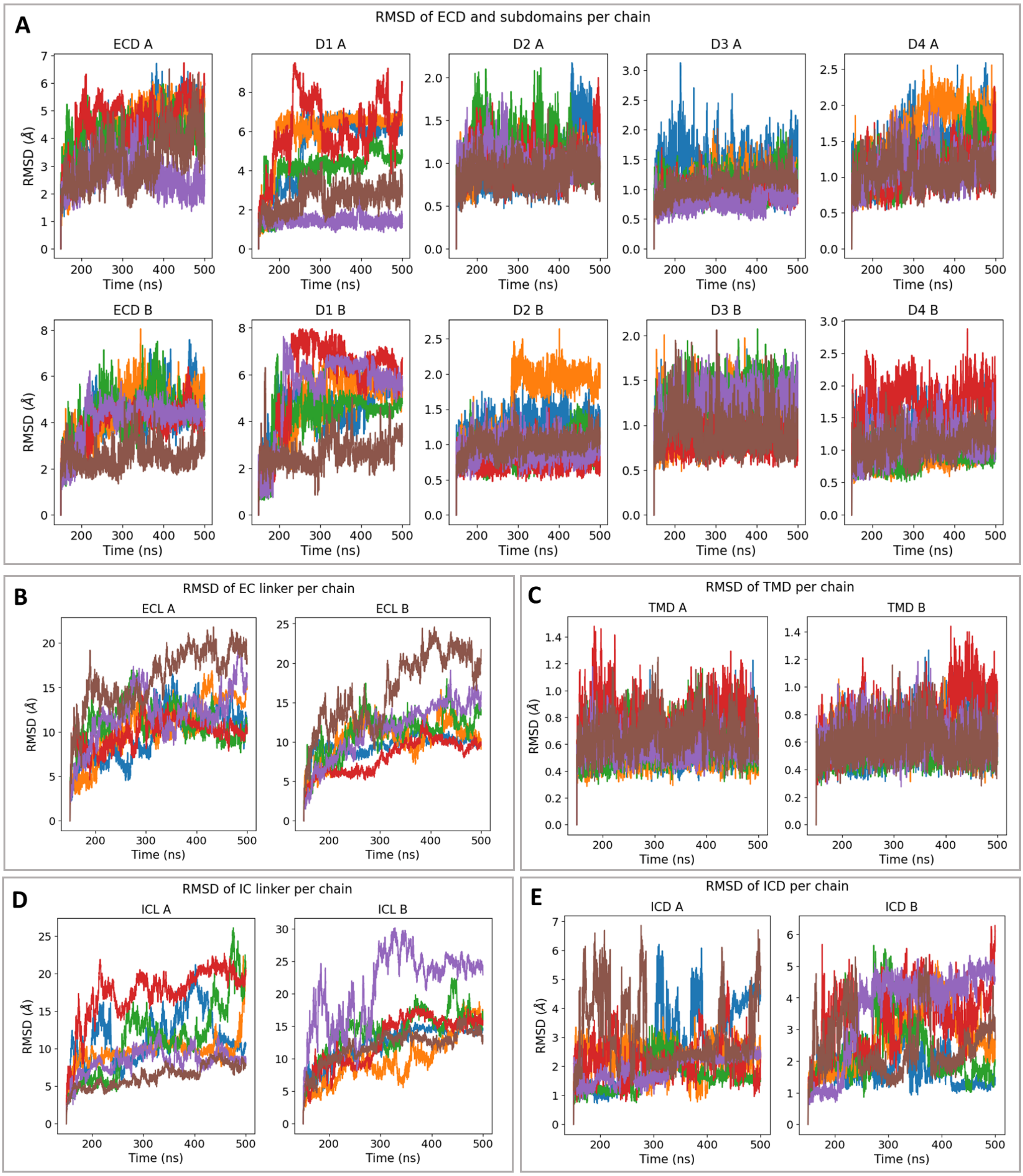
A
RMSD of ECD and subdomains per chain
ECD A
D1 A
D2 A
D3 A
D4 A
ECD B
D1 B
D2 B
D3 B
D4 B
RMSD (Å)
Time (ns)
200
300
400
500
B
RMSD of EC linker per chain
ECL A
ECL B
C
RMSD of TMD per chain
TMD A
TMD B
D
RMSD of IC linker per chain
ICL A
ICL B
E
RMSD of ICD per chain
ICD A
ICD B

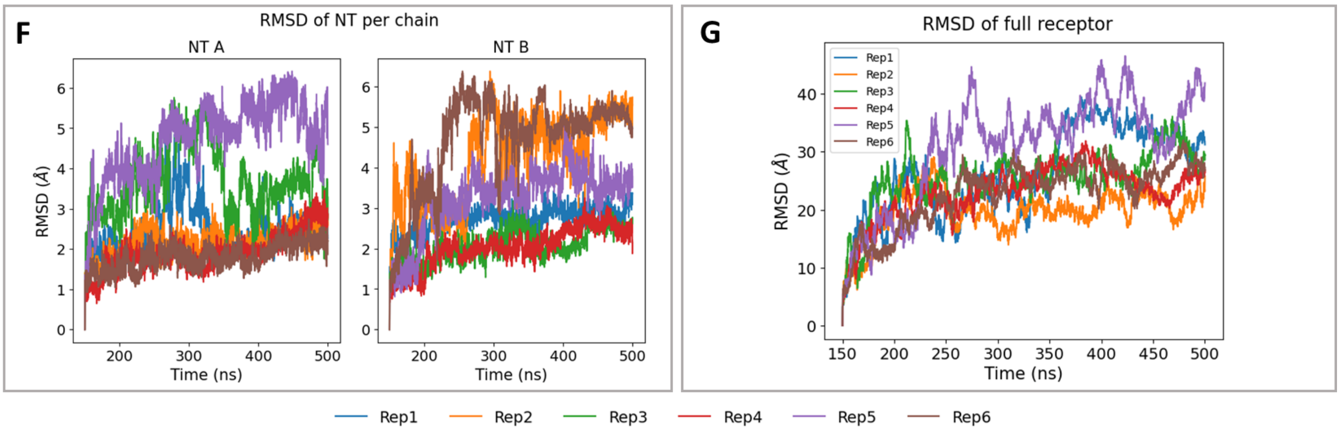

Figure A.13: RMSD calculations in the full-length p75 simulations.

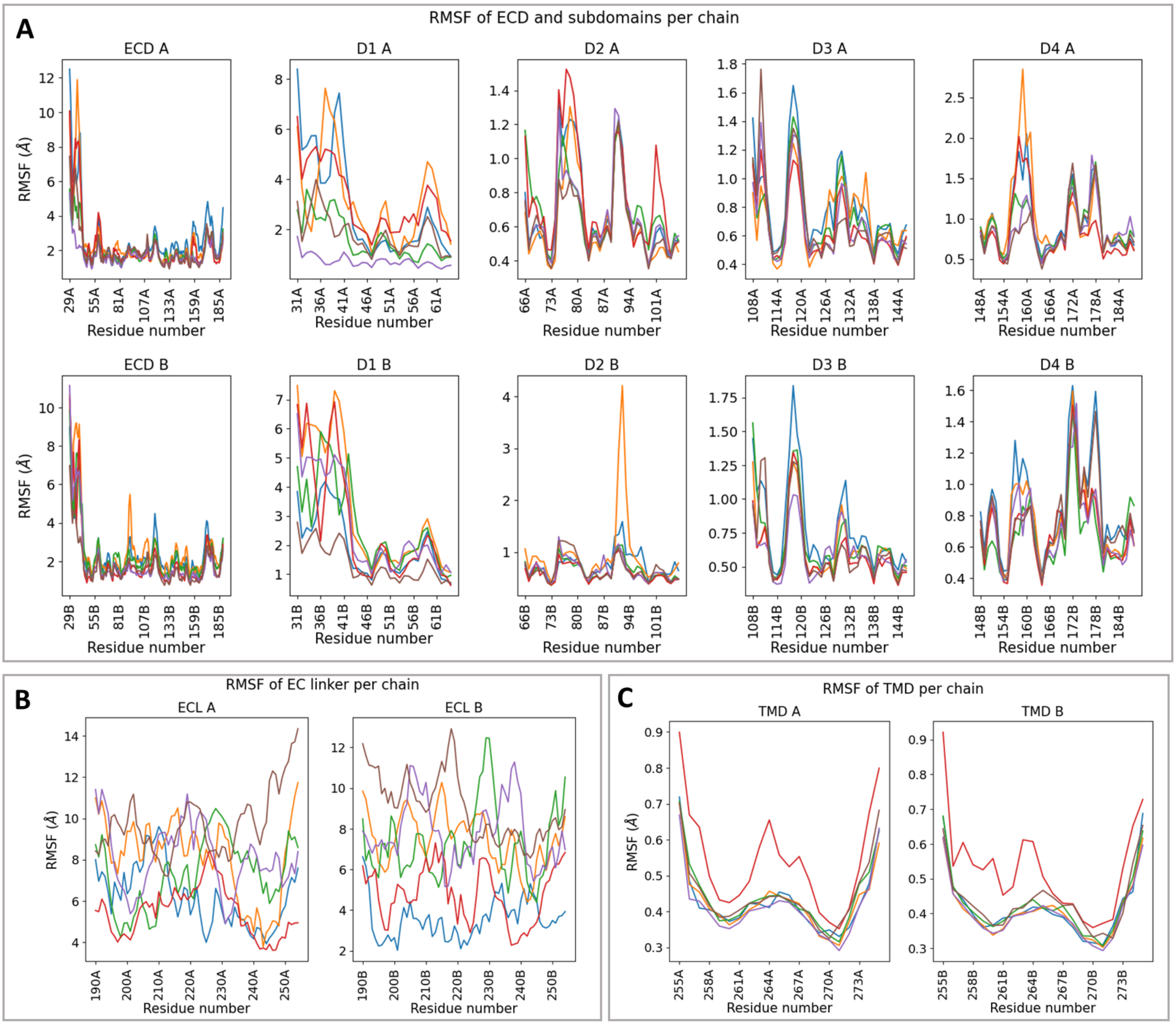

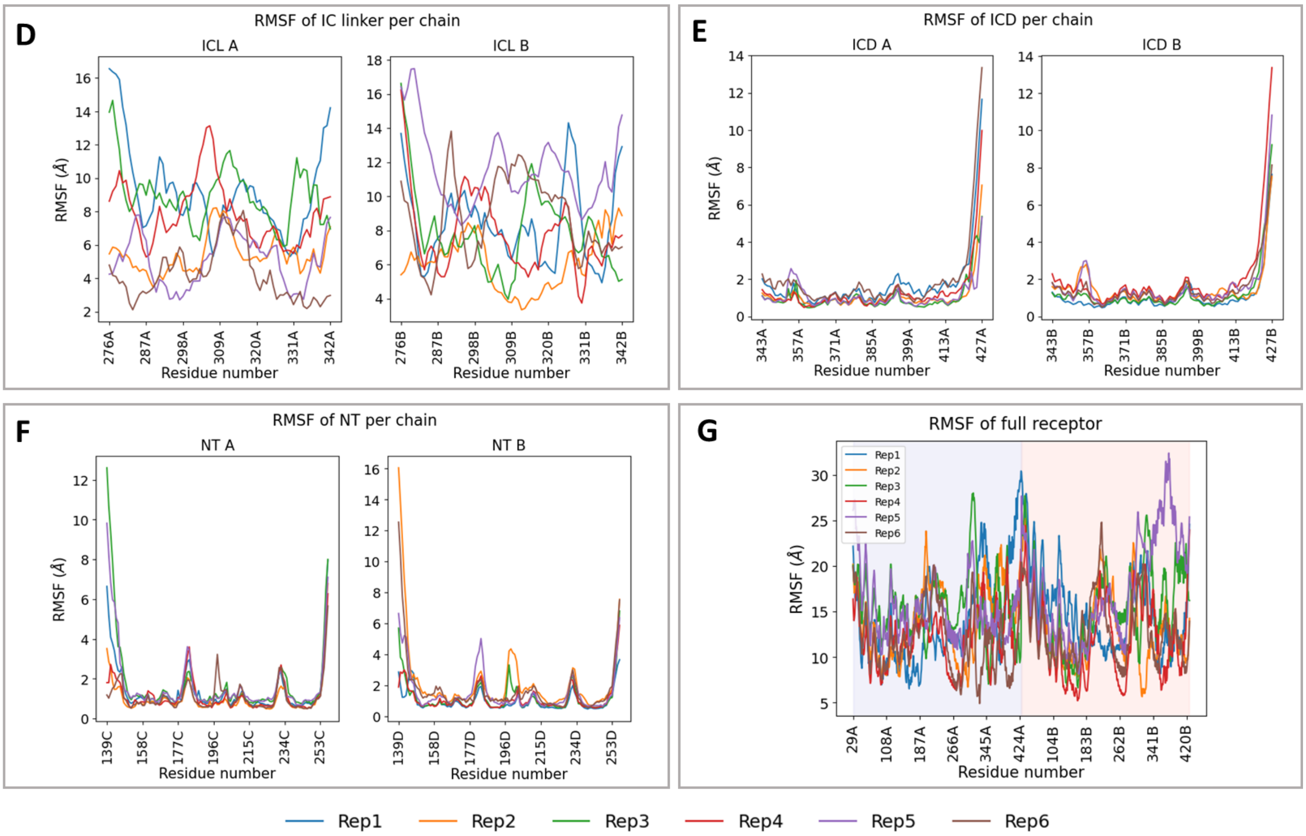

Figure A.14: RMSF calculations in the full-length p75 simulations.

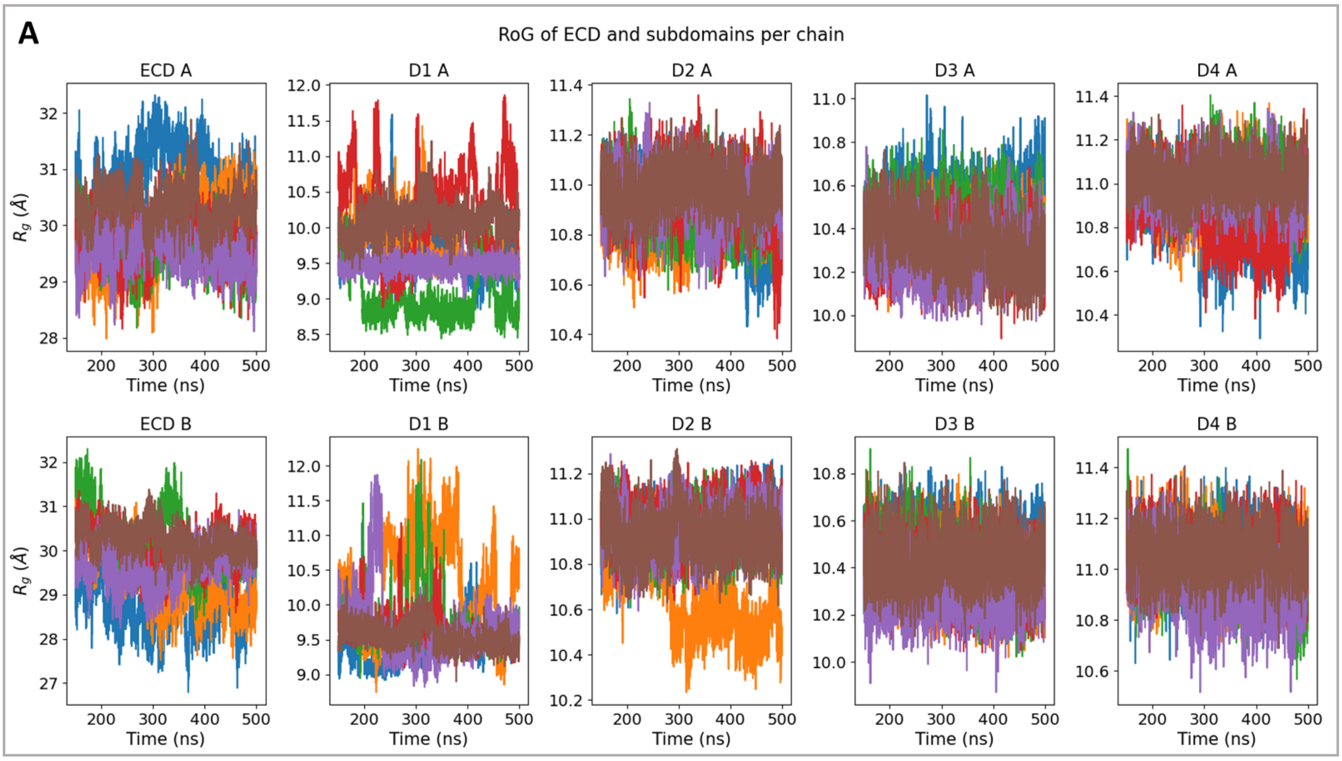

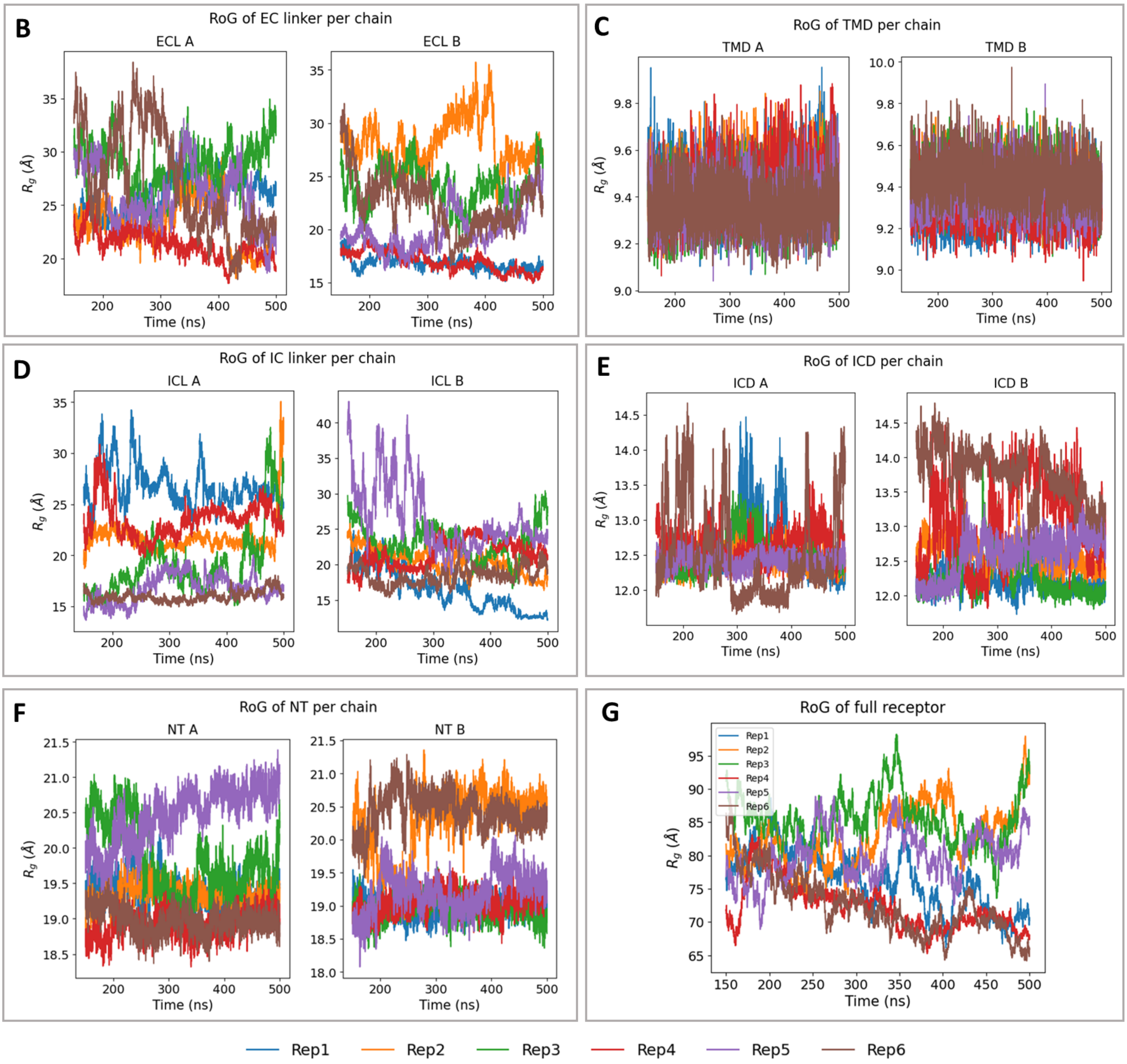

Figure A.15: Radius of gyration (R_g) calculations in the full-length p75 simulations.

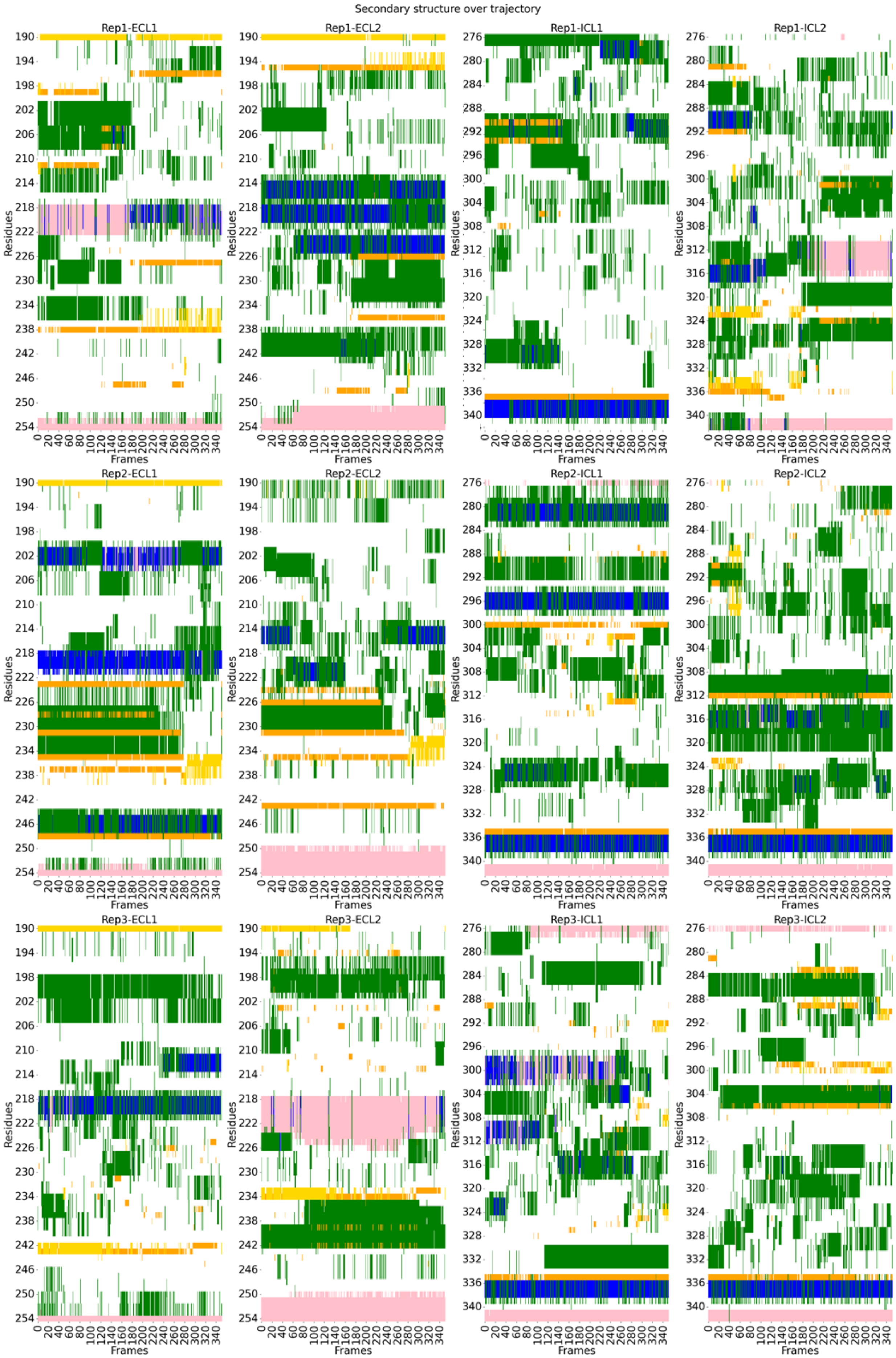
Secondary structure over trajectory
Rep1-ECL1
Rep1-ECL2
Rep1-ICL1
Rep1-ICL2
Rep2-ECL1
Rep2-ECL2
Rep2-ICL1
Rep2-ICL2
Rep3-ECL1
Rep3-ECL2
Rep3-ICL1
Rep3-ICL2
Residues
190 194 198 202 206 210 214 218 222 226 230 234 238 242 246 250 254
276 280 284 288 292 296 300 304 308 312 316 320 324 328 332 336 340
Frames
0 20 40 60 80 100 120 140 160 180 200 220 240 260 280 300 320 340

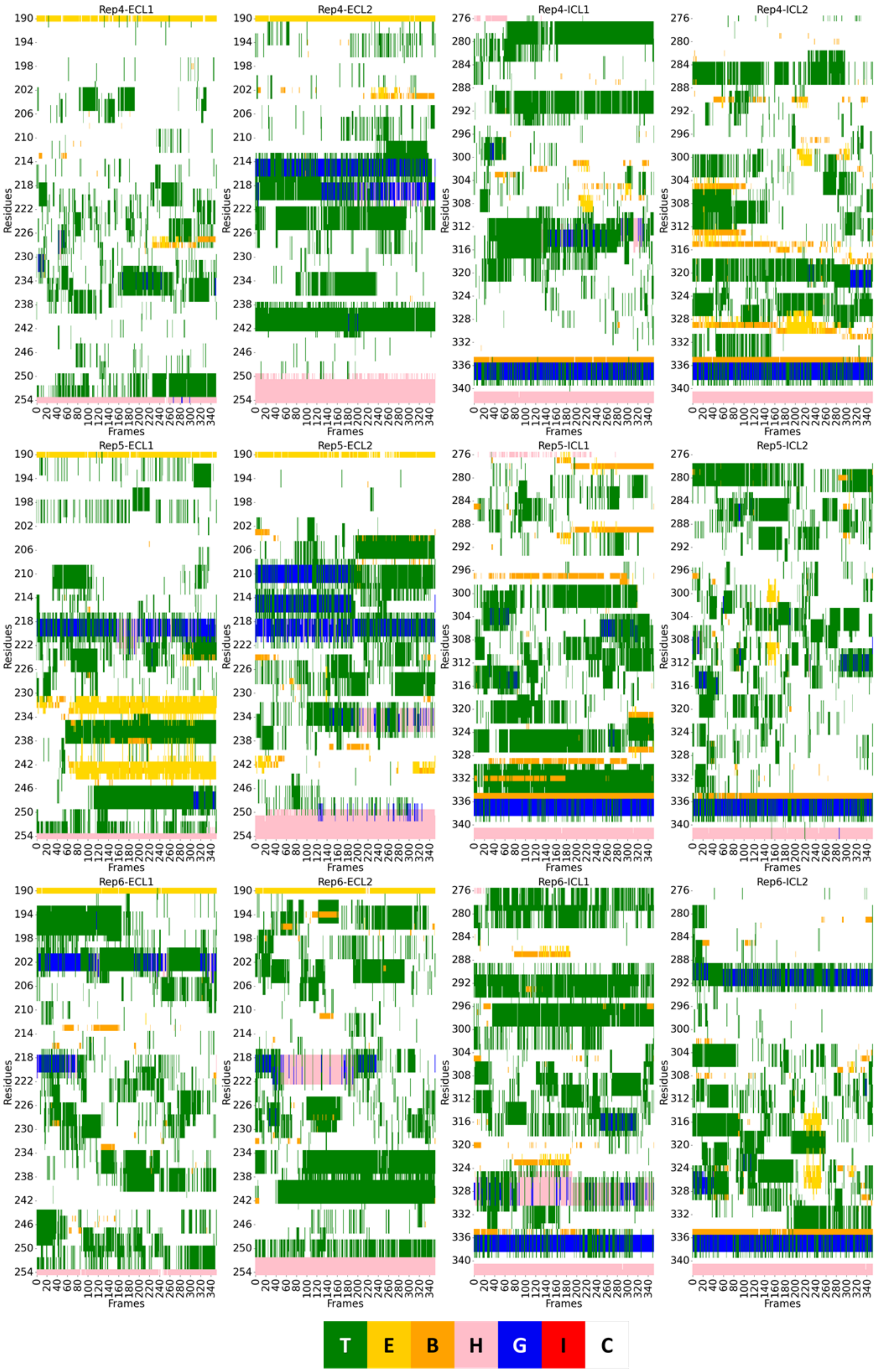
Rep4-ECL1
Rep4-ECL2
Rep4-ICL1
Rep4-ICL2
Rep5-ECL1
Rep5-ECL2
Rep5-ICL1
Rep5-ICL2
Rep6-ECL1
Rep6-ECL2
Rep6-ICL1
Rep6-ICL2
Residues
190 194 198 202 206 210 214 218 222 226 230 234 238 242 246 250 254
276 280 284 288 292 296 300 304 308 312 316 320 324 328 332 336 340
Frames
0 20 40 60 80 100 120 140 160 180 200 220 240 260 280 300 320 340
T
E
B
H
G
I
C

Figure A.16: Secondary structure of the two monomer EC and IC linkers after the 1st 150 ns, when the system is more equilibrated. The letters in the legend correspond to: T: turn, E: extended configuration, B: isolated bridge, H: alpha helix, G: 3-10 helix, I: pi-helix, C: random coil.

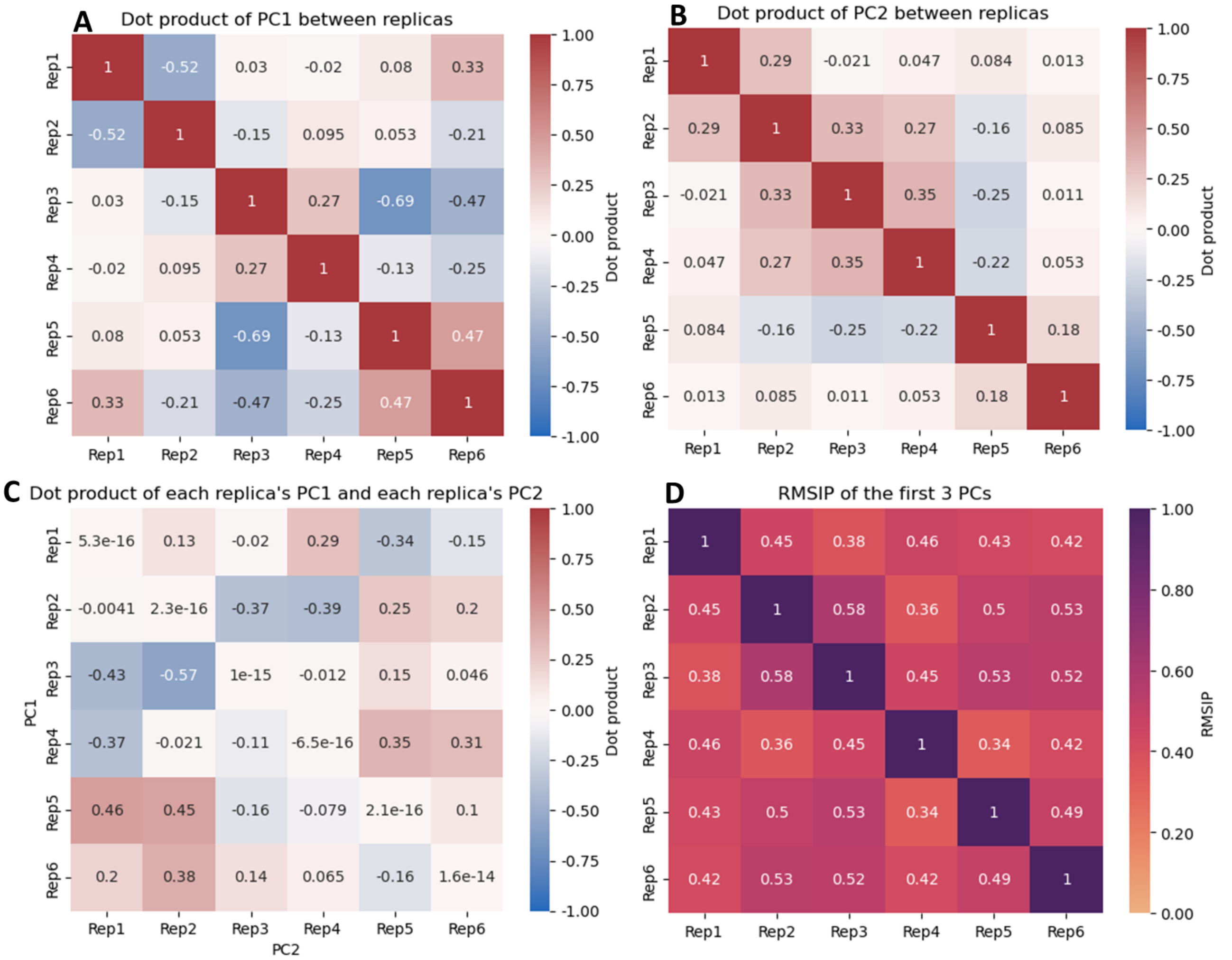

Figure A.17: Calculation of the dot products of principal components from p75 full-length simulations. (A) Dot products of the 1st principal components (PC1) from the different replica systems. (B) Dot products of the 2nd principal components (PC2) from the different replica systems. (C) Heatmap of the dot products between the PC1 and PC2 from the different replicas. The values correspond to: [1] parallel vectors, [-1] anti-parallel vectors and [0] perpendicular (or orthogonal) vectors. (D) Root mean squared inner product (RMSIP)[405,406] of the first 3 PCs. Values closer to 1 indicate similarity in PCs, while values closer to 0 indicate dissimilarity.

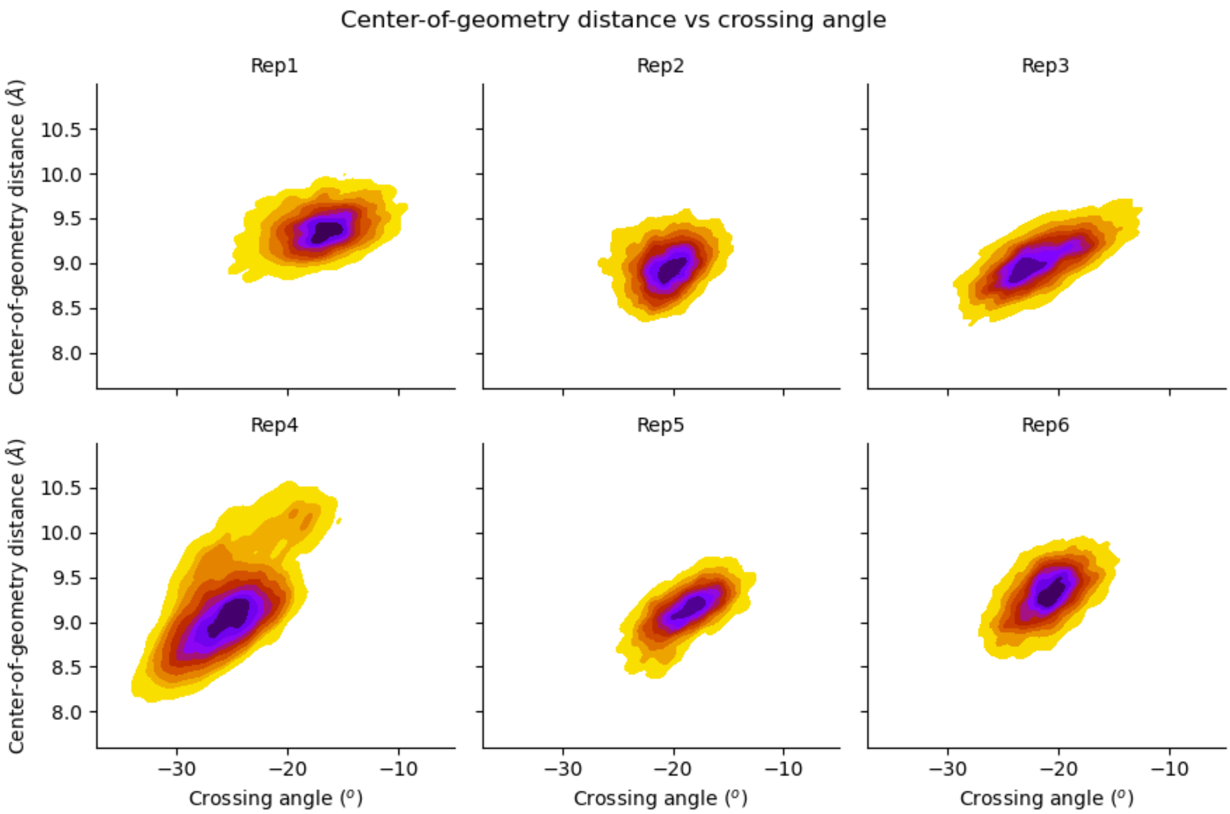
Center-of-geometry distance vs crossing angle
Rep1
Rep2
Rep3
Rep4
Rep5
Rep6
Center-of-geometry distance (Å)
10.5
10.0
9.5
9.0
8.5
8.0
−30
−20
−10
Crossing angle (°)

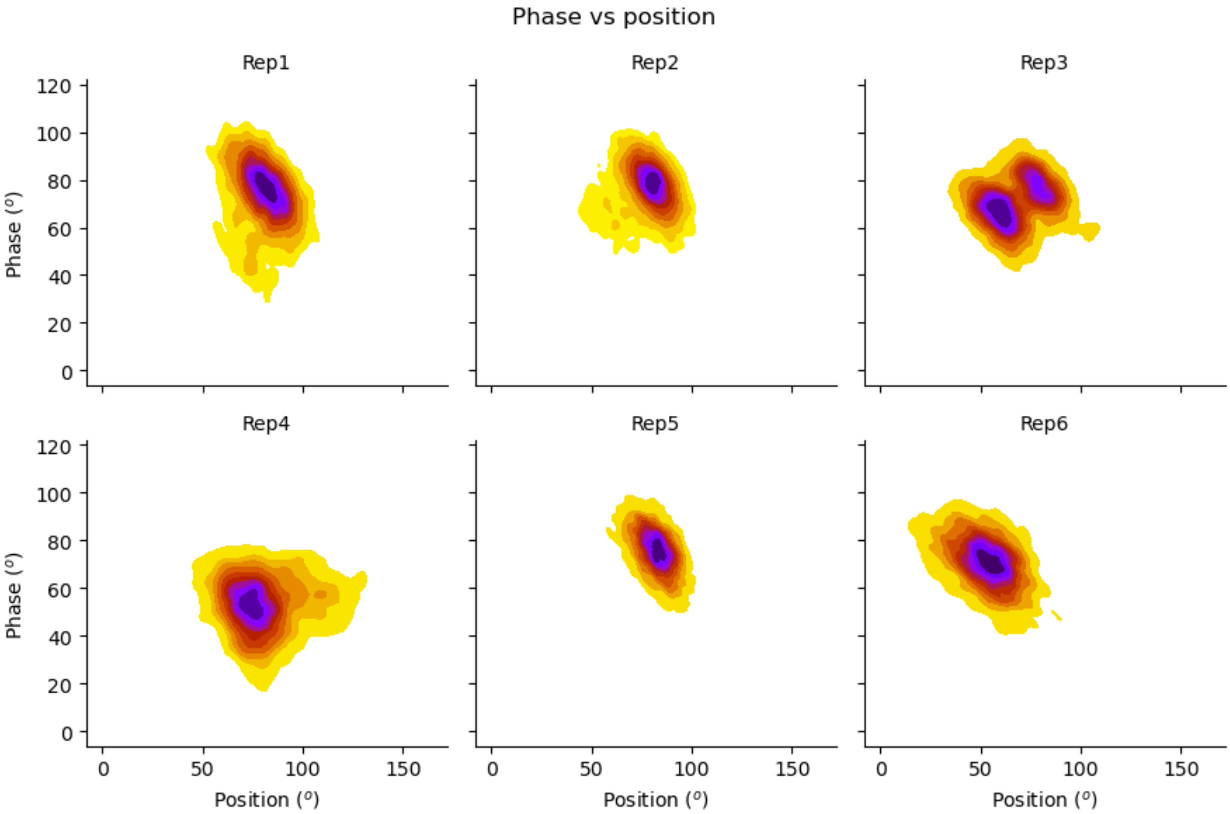
Phase vs position
Rep1
Rep2
Rep3
Rep4
Rep5
Rep6
Phase (°)
120
100
80
60
40
20
0
50
100
150
Position (°)

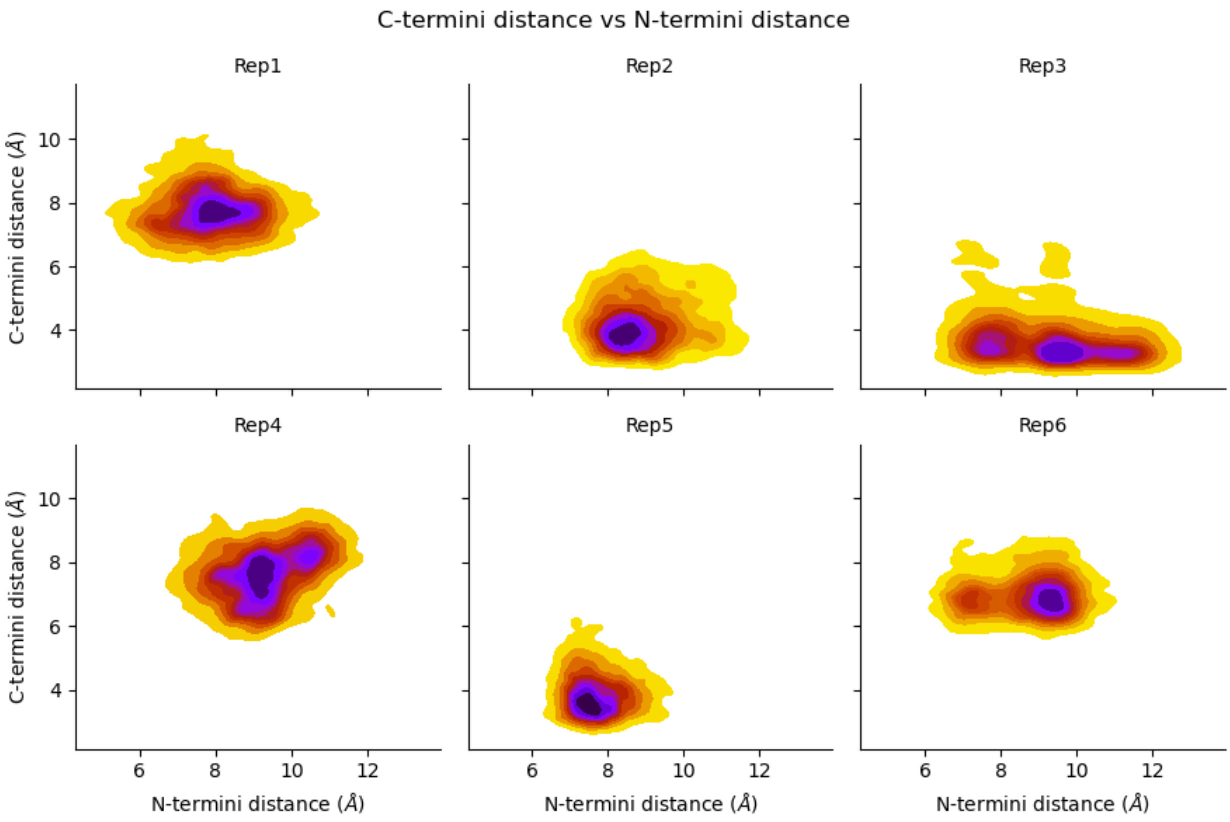

Figure A.18: Density distribution plots for the six geometric parameters that describe the TM helix arrangements: interhelical distance and crossing angle (Ω), phase and position, N- and C-termini distance. The distribution is shown for each replica.

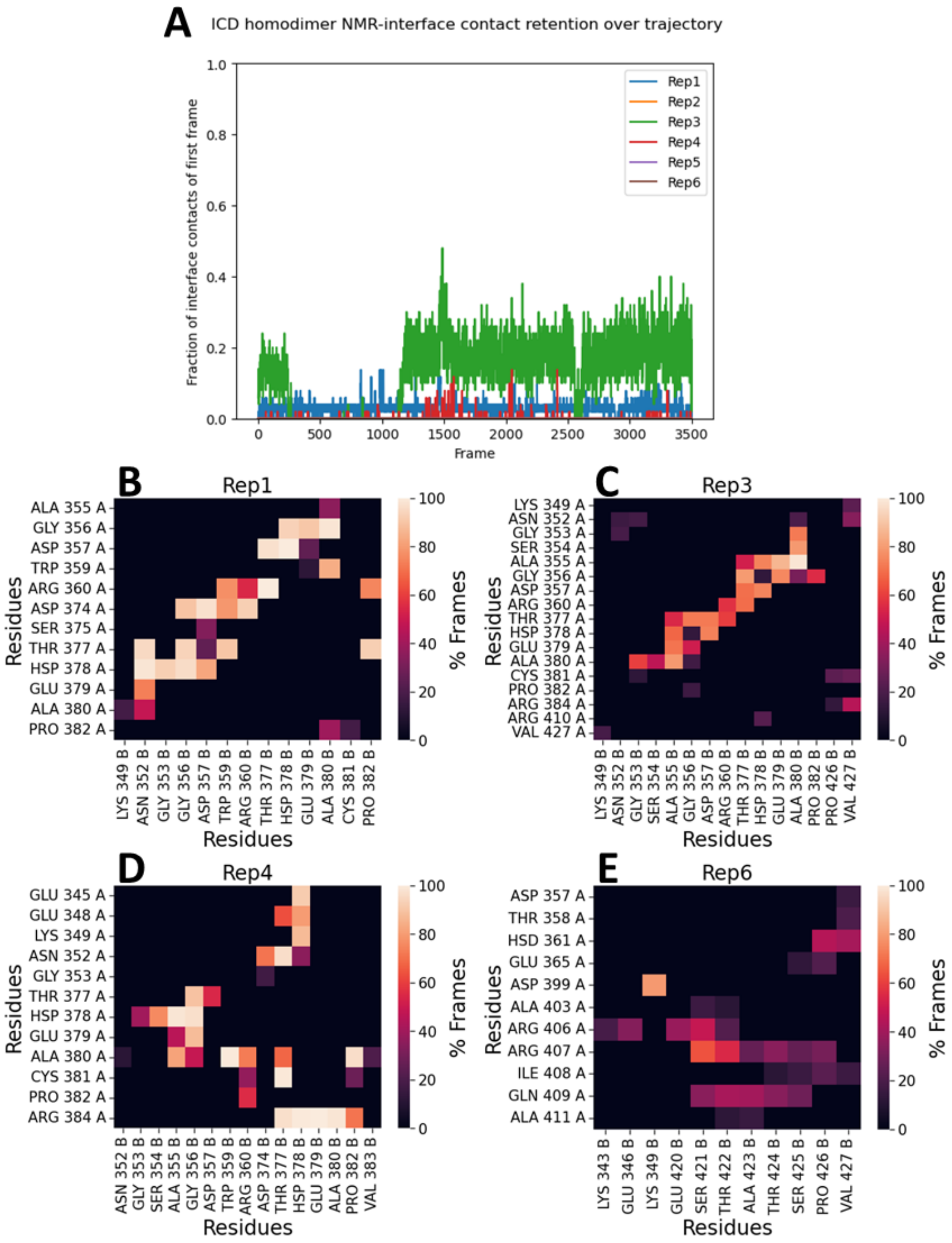

Figure A.19: Contact analysis of the two death domain (DD) (intracellular domains – ICD) monomer interactions during the simulations. (A) Calculation of the DD-DD fraction of contacts, present in the initial NMR structure, which are preserved during the simulations. (B)-(E) Contact maps between the two DD monomers with the contact occupancies shown as a percentage of simulation frames for replicas 1, 3, 4 and 6. Only contacts of >10% are shown. Replicas 2 and 5 have less than 10% contact occupancy, because the two domains dissociate, and that is why they are not shown here. A contact is defined when two heavy atoms are within 4.5 Å distance. The contact analyses were conducted after the 1st 150 ns of the simulations, when the system had equilibrated.

List of Publications

- C. Athanasiou, A. Claveras Cabezudo, **A. Tsengenes**, R. C. Wade, *Simulation of neurotrophin receptor transmembrane helix interactions reveals active states and distinct signaling mechanisms,* JACS Au*,* 2025, DOI: 10.1021/jacsau.5c00174

In this publication, I performed unbiased coarse-grained molecular dynamics simulations with the Martini 2.2 force field of the p75 WT and C257A mutant transmembrane helices in DPC micelles. For this work, I created an automation script that sets up the molecular system and submits multiple replica simulations. I also analyzed the arrangements of the transmembrane helices from the simulations with Python scripts that I created together with Christina Athanasiou. I also performed coarse-grained metadynamics molecular dynamics simulations of the p75 C257A mutant in a POPC lipid bilayer using the Martini 2.2 force field and calculated the binding free energy of the two helices. Most of the data in Chapter 5 of the current thesis are published in this manuscript.

- D. Charou, T. Rogdakis, A. Latorrata, M. Valcarcel, V. Papadogiannis, C. Athanasiou, **A. Tsengenes**, M. A. Papadopoulou, D. Lypitkas, M. D. Lavigne, T. Katsila, R. C. Wade, M. Z. Cader, T. Calogeropoulou, A. Gravanis and I. Charalampopoulos, *Comprehensive characterization of the neurogenic and neuroprotective action of a novel TrkB agonist using mouse and human stem cell models of Alzheimer's disease,* Stem Cell Res. Ther., 2024, 15, 200, DOI: 10.1186/s13287-024-03818-w

For this publication, I performed molecular docking calculations of the ENT-A011 neurotrophin mimetic identified in the EuroNeurotrophin consortium to two *in silico* detected binding sites at the interface of TrkA and NGF and compared them with the docking on TrkB-NT-4/5 performed by Christina Athanasiou. The relevant data are presented in Chapter 3 of the thesis.

- A. Claveras Cabezudo, C. Athanasiou, **A. Tsengenes**, R. C. Wade, *Scaling protein-water interactions in the Martini 3 coarse-grained force field to simulate transmembrane helix dimers in different lipid environments*, J. Chem. Theory Comput. 2023, 19, 7, DOI: 10.1021/acs.jctc.2c00950

In this publication, I contributed with co-supervision of Ainara Cabezudo who performed the molecular dynamics simulations presented in this work. For this work, Ainara used an automation script of mine that sets up the molecular system and submits multiple replica simulations, as well as Python analysis scripts that I created together with Christina Athanasiou. The results of this paper are not presented in the current thesis.

- T. Rogdakis, D. Charou, A. Latorrata, E. Papadimitriou**, A. Tsengenes**, C. Athanasiou, M. Papadopoulou, C. Chalikiopoulou, T. Katsila, I. Ramos, K. C. Prousis, R. C. Wade, K. Sidiropoulou, T. Calogeropoulou, A. Gravanis, I. Charalampopoulos, *Development and Biological Characterization of a Novel Selective TrkA Agonist with Neuroprotective Properties against Amyloid Toxicity*, Biomedicines, 2022, 10, 614, DOI: 10.3390/biomedicines10030614

For this publication, I performed molecular docking calculations of ENT-A013E and ENT-A013Z neurotrophin mimetics identified in the EuroNeurotrophin consortium to two *in silico* detected binding sites at the interface of TrkA and NGF and compared them with the docking on TrkB-NT-4/5 performed by Christina Athanasiou. The relevant data are presented in Chapter 3 of the thesis.

List of Tables

List of Figures

References

1. Kraemer, B. R. *et al.* A role for the p75 neurotrophin receptor in axonal degeneration and apoptosis induced by oxidative stress. *J. Biol. Chem.* **289**, 21205–16 (2014).
2. Sofroniew, M. V, Howe, C. L. & Mobley, W. C. Nerve growth factor signaling, neuroprotection, and neural repair. *Annu. Rev. Neurosci.* **24**, 1217–81 (2001).
3. Huang, E. J. & Reichardt, L. F. Trk receptors: roles in neuronal signal transduction. *Annu. Rev. Biochem.* **72**, 609–42 (2003).
4. Poon, V. Y., Choi, S. & Park, M. Growth factors in synaptic function. *Front. Synaptic Neurosci.* **5**, (2013).
5. Levi-Montalcini, R. & Hamburger, V. A diffusible agent of mouse sarcoma, producing hyperplasia of sympathetic ganglia and hyperneurotization of viscera in the chick embryo. *J. Exp. Zool.* **123**, 233–287 (1953).
6. Levi-Montalcini, R. & Hamburger, V. Selective growth stimulating effects of mouse sarcoma on the sensory and sympathetic nervous system of the chick embryo. *J. Exp. Zool.* **116**, 321–361 (1951).
7. Bothwell, M. NGF, BDNF, NT3, and NT4. in *Neurotrophic Factors. Handbook of Experimental Pharmacology* (ed. Lewin, G., Carter, B.) 3–15 (Springer Berlin Heidelberg, 2014). doi:10.1007/978-3-642-45106-5_1.
8. Barde, Y. A., Edgar, D. & Thoenen, H. Purification of a new neurotrophic factor from mammalian brain. *EMBO J.* **1**, 549–553 (1982).
9. Ernfors, P., Ibáñez, C. F., Ebendal, T., Olson, L. & Persson, H. Molecular cloning and neurotrophic activities of a protein with structural similarities to nerve growth factor: developmental and topographical expression in the brain. *Proc. Natl. Acad. Sci.* **87**, 5454–5458 (1990).
10. Hohn, A., Leibrock, J., Bailey, K. & Barde, Y.-A. Identification and characterization of a novel member of the nerve growth factor/brain-derived neurotrophic factor family. *Nature* **344**, 339–341 (1990).
11. Maisonpierre, P. *et al.* Neurotrophin-3: a neurotrophic factor related to NGF and BDNF. *Science (80-.).* **247**, 1446–1451 (1990).
12. Hallböök, F., Ibáñez, C. F. & Persson, H. Evolutionary studies of the nerve growth factor family reveal a novel member abundantly expressed in xenopus ovary. *Neuron* **6**, 845–858 (1991).
13. Berkemeier, L. R. *et al.* Neurotrophin-5: A novel neurotrophic factor that activates trk and trkB. *Neuron* **7**, 857–866 (1991).
14. Massague, J., Guillette, B. J., Czech, M. P., Morgan, C. J. & Bradshaw, R. A. Identification of a nerve growth factor receptor protein in sympathetic ganglia membranes by affinity labeling. *J. Biol. Chem.* **256**, 9419–9424 (1981).
15. Massague, J., Buxser, S., Johnson, G. L. & Czech, M. P. Affinity labeling of a nerve growth factor receptor component on rat pheochromocytoma (PC12) cells. *Biochim. Biophys. Acta - Biomembr.* **693**, 205–212 (1982).
16. Grob, P. M., Berlot, C. H. & Bothwell, M. A. Affinity labeling and partial purification of nerve growth factor receptors from rat pheochromocytoma and human melanoma cells. *Proc. Natl. Acad. Sci.* **80**, 6819–6823 (1983).
17. Johnson, D. *et al.* Expression and structure of the human NGF receptor. *Cell* **47**, 545–554 (1986).
18. Radeke, M. J., Misko, T. P., Hsu, C., Herzenberg, L. A. & Shooter, E. M. Gene transfer and molecular cloning of the rat nerve growth factor receptor. *Nature* **325**, 593–597 (1987).

19. Kaplan, D. R., Hempstead, B. L., Martin-Zanca, D., Chao, M. V. & Parada, L. F. The trk Proto-Oncogene Product: a Signal Transducing Receptor for Nerve Growth Factor. *Science (80-.).* **252**, 554–558 (1991).

20. Klein, R., Jing, S., Nanduri, V., O'Rourke, E. & Barbacid, M. The trk proto-oncogene encodes a receptor for nerve growth factor. *Cell* **65**, 189–197 (1991).

21. Klein, R., Parada, L. F., Coulier, F. & Barbacid, M. trkB, a novel tyrosine protein kinase receptor expressed during mouse neural development. *EMBO J.* **8**, 3701–3709 (1989).

22. Rodríguez-Tébar, A., Dechant, G., Götz, R. & Barde, Y. A. Binding of neurotrophin-3 to its neuronal receptors and interactions with nerve growth factor and brain-derived neurotrophic factor. *EMBO J.* **11**, 917–922 (1992).

23. Conroy, J. N. & Coulson, E. J. High-affinity TrkA and p75 neurotrophin receptor complexes: A twisted affair. *J. Biol. Chem.* **298**, 101568 (2022).

24. Wu, H. & Hymowitz, S. G. Structure and Function of Tumor Necrosis Factor (TNF) at the Cell Surface. in *Handbook of Cell Signaling* 265–275 (Elsevier, 2010). doi:10.1016/B978-0-12-374145-5.00040-1.

25. Litwack, G. *Neurotrophins*. (Elsevier, 2017).

26. Chao, M. V & Hempstead, B. L. p75 and Trk: a two-receptor system. *Trends Neurosci.* **18**, 321–6 (1995).

27. Ernfors, P. *et al.* The nerve growth factor receptor gene is expressed in both neuronal and non-neuronal tissues in the human fetus. *Int. J. Dev. Neurosci.* **9**, 57–66 (1991).

28. Cragnolini, A. B. & Friedman, W. J. The function of p75NTR in glia. *Trends Neurosci.* **31**, 99–104 (2008).

29. Wheeler, E. & Bothwell, M. Spatiotemporal patterns of expression of NGF and the low-affinity NGF receptor in rat embryos suggest functional roles in tissue morphogenesis and myogenesis. *J. Neurosci.* **12**, 930–945 (1992).

30. Beattie, M. S. *et al.* ProNGF Induces p75-Mediated Death of Oligodendrocytes following Spinal Cord Injury. *Neuron* **36**, 375–386 (2002).

31. Large, T. H. *et al.* Structure and developmental expression of the nerve growth factor receptor in the chicken central nervous system. *Neuron* **2**, 1123–1134 (1989).

32. Coulson, E. J. *et al.* Chopper, a New Death Domain of the p75 Neurotrophin Receptor That Mediates Rapid Neuronal Cell Death. *J. Biol. Chem.* **275**, 30537–30545 (2000).

33. Kraemer, B. R., Yoon, S. O. & Carter, B. D. The Biological Functions and Signaling Mechanisms of the p75 Neurotrophin Receptor. in *Neurotrophic Factors. Handbook of Experimental Pharmacology* (ed. Lewin, G., Carter, B.) 121–164 (Springer, Berlin, Heidelberg, 2014). doi:10.1007/978-3-642-45106-5_6.

34. Nykjaer, A. *et al.* Sortilin is essential for proNGF-induced neuronal cell death. *Nature* **427**, 843–848 (2004).

35. Hempstead, B. L., Martin-Zanca, D., Kaplan, D. R., Parada, L. F. & Chao, M. V. High-affinity NGF binding requires coexpression of the trk proto-oncogene and the low-affinity NGF receptor. *Nature* **350**, 678–683 (1991).

36. Skeldal, S. *et al.* Mapping of the Interaction Site between Sortilin and the p75 Neurotrophin Receptor Reveals a Regulatory Role for the Sortilin Intracellular Domain in p75 Neurotrophin Receptor Shedding and Apoptosis. *J. Biol. Chem.* **287**, 43798–43809 (2012).

37. McDonald, N. Q. *et al.* New protein fold revealed by a 2.3-Å resolution crystal structure of nerve growth factor. *Nature* **354**, 411–414 (1991).

38. Fandl, J. P. *et al.* Characterization and crystallization of recombinant human neurotrophin-4. *J. Biol. Chem.* **269**, 755–9 (1994).

39. Butte, M. J., Hwang, P. K., Mobley, W. C. & Fletterick, R. J. Crystal Structure of Neurotrophin-3 Homodimer Shows Distinct Regions Are Used To Bind Its Receptors ,. *Biochemistry* **37**, 16846–16852 (1998).

40. Robinson, R. C. *et al.* The structures of the neurotrophin 4 homodimer and the brain-derived neurotrophic factor/neurotrophin 4 heterodimer reveal a common Trk-binding site. *Protein Sci.* **8**, 2589–2597 (1999).

41. Robinson, R. C., Radziejewski, C., Stuart, D. I. & Jones, E. Y. Structure of the Brain-Derived Neurotrophic Factor/Neurotrophin 3 Heterodimer. *Biochemistry* **34**, 4139–4146 (1995).

42. Janssens, J. *et al.* Development of Precision Small-Molecule Proneurotrophic Therapies for Neurodegenerative Diseases. in *Neurotrophins* 263–311 (Elsevier, 2017). doi:10.1016/bs.vh.2016.10.006.

43. Bruno, M. A. & Cuello, A. C. Activity-dependent release of precursor nerve growth factor, conversion to mature nerve growth factor, and its degradation by a protease cascade. *Proc. Natl. Acad. Sci.* **103**, 6735–6740 (2006).

44. Sun, P. D. & Davies, D. R. The Cystine-Knot Growth-Factor Superfamily. *Annu. Rev. Biophys. Biomol. Struct.* **24**, 269–292 (1995).

45. Ivanisevic, L. & Saragovi, H. U. Neurotrophins. in *Handbook of Biologically Active Peptides* 1639–1646 (Elsevier, 2013). doi:10.1016/B978-0-12-385095-9.00224-4.

46. McDonald, N. Q. & Chao, M. V. Structural Determinants of Neurotrophin Action. *J. Biol. Chem.* **270**, 19669–19672 (1995).

47. Wehrman, T. *et al.* Structural and Mechanistic Insights into Nerve Growth Factor Interactions with the TrkA and p75 Receptors. *Neuron* **53**, 25–38 (2007).

48. Vilar, M. Structural Characterization of the p75 Neurotrophin Receptor. in *Neurotrophins* (ed. Litwack, G.) 57–87 (Elsevier, 2017). doi:10.1016/bs.vh.2016.10.007.

49. Underwood, C. K. & Coulson, E. J. The p75 neurotrophin receptor. *Int. J. Biochem. Cell Biol.* **40**, 1664–1668 (2008).

50. Almeida, R. D. & Duarte, C. B. p75NTR Processing and Signaling: Functional Role. in *Handbook of Neurotoxicity* 1899–1923 (Springer New York, 2014). doi:10.1007/978-1-4614-5836-4_25.

51. Athanasiou, C., Claveras Cabezudo, A., Tsengenes, A. & Wade, R. C. Simulation of Neurotrophin Receptor Transmembrane Helix Interactions Reveals Active States and Distinct Signaling Mechanisms. *JACS Au* (2025) doi:10.1021/jacsau.5c00174.

52. Baldwin, A. N., Bitler, C. M., Welcher, A. A. & Shooter, E. M. Studies on the structure and binding properties of the cysteine-rich domain of rat low affinity nerve growth factor receptor (p75NGFR). *J. Biol. Chem.* **267**, 8352–8359 (1992).

53. He, X. & Garcia, K. C. Structure of Nerve Growth Factor Complexed with the Shared Neurotrophin Receptor p75. *Science (80-.).* **304**, 870–875 (2004).

54. Aurikko, J. P. *et al.* Characterization of Symmetric Complexes of Nerve Growth Factor and the Ectodomain of the Pan-neurotrophin Receptor, p75NTR. *J. Biol. Chem.* **280**, 33453–33460 (2005).

55. Gong, Y., Cao, P., Yu, H. & Jiang, T. Crystal structure of the neurotrophin-3 and p75NTR symmetrical complex. *Nature* **454**, 789–793 (2008).

56. Feng, D. *et al.* Molecular and Structural Insight into proNGF Engagement of p75NTR and Sortilin. *J. Mol. Biol.* **396**, 967–984 (2010).

57. Vilar, M. *et al.* Activation of the p75 Neurotrophin Receptor through Conformational Rearrangement of Disulphide-Linked Receptor Dimers. *Neuron* **62**, 72–83 (2009).

58. Tran, T. S. & Yaron, A. *Wiring the Nervous System: Mechanisms of Axonal and Dendritic Remodelling in Health and Disease*. (River Publishers, 2023). doi:10.1201/9781032632698.

59. Nadezhdin, K. D. *et al.* Structural Basis of p75 Transmembrane Domain Dimerization. *J. Biol. Chem.* **291**, 12346–12357 (2016).

60. Mineev, K. S., Goncharuk, S. A., Kuzmichev, P. K., Vilar, M. & Arseniev, A. S. NMR Dynamics of Transmembrane and Intracellular Domains of p75NTR in Lipid-Protein Nanodiscs. *Biophys. J.* **109**, 772–782 (2015).

61. Casademunt, E. The zinc finger protein NRIF interacts with the neurotrophin receptor p75NTR and participates in programmed cell death. *EMBO J.* **18**, 6050–6061 (1999).

62. Chittka, A. & Chao, M. V. Identification of a zinc finger protein whose subcellular distribution is regulated by serum and nerve growth factor. *Proc. Natl. Acad. Sci.* **96**, 10705–10710 (1999).

63. Ye, X. *et al.* TRAF Family Proteins Interact with the Common Neurotrophin Receptor and Modulate Apoptosis Induction. *J. Biol. Chem.* **274**, 30202–30208 (1999).

64. Khursigara, G., Orlinick, J. R. & Chao, M. V. Association of the p75 Neurotrophin Receptor with TRAF6. *J. Biol. Chem.* **274**, 2597–2600 (1999).

65. Underwood, C. K., Reid, K., May, L. M., Bartlett, P. F. & Coulson, E. J. Palmitoylation of the C-terminal fragment of p75NTR regulates death signaling and is required for subsequent cleavage by γ-secretase. *Mol. Cell. Neurosci.* **37**, 346–358 (2008).

66. Liepinsh, E. NMR structure of the death domain of the p75 neurotrophin receptor. *EMBO J.* **16**, 4999–5005 (1997).

67. Yuan, W., Ibáñez, C. F. & Lin, Z. Death domain of p75 neurotrophin receptor: a structural perspective on an intracellular signalling hub. *Biol. Rev.* **94**, 1282–1293 (2019).

68. Qu, Q. *et al.* Structural Characterization of the Self-Association of the Death Domain of p75NTR. *PLoS One* **8**, e57839 (2013).

69. Vilar, M. *et al.* Heterodimerization of p45–p75 Modulates p75 Signaling: Structural Basis and Mechanism of Action. *PLoS Biol.* **12**, e1001918 (2014).

70. Lin, Z. *et al.* Structural basis of death domain signaling in the p75 neurotrophin receptor. *Elife* **4**, (2015).

71. Varki A, Cummings RD, Esko JD, Stanley P, Hart GW, Aebi M, Mohnen D, Kinoshita T, Packer NH, Prestegard JH, Schnaar RL, Seeberger PH, E. *Essentials of Glycobiology*. (Cold Spring Harbor (NY): Cold Spring Harbor Laboratory Press, 2022). doi:10.1101/9781621824213.

72. Athanasiou, C. Modeling of mechanistic effects of neurotrophin modulators. (PhD Thesis, University of Heidelberg, 2024). doi:10.11588/heidok.00033931.

73. Settineri, C. A. *et al.* Characterization of the Glycosylation on Recombinant Human Low-Affinity Nerve Growth Factor Receptor. in *Techniques in Protein Chemistry III* 295–301 (Elsevier, 1992). doi:10.1016/B978-0-12-058756-8.50035-3.

74. Haniu, M. *et al.* Interactions between Brain-derived Neurotrophic Factor and the TRKB Receptor. *J. Biol. Chem.* **272**, 25296–25303 (1997).

75. Yeaman, C. *et al.* The O-glycosylated Stalk Domain Is Required for Apical Sorting of Neurotrophin Receptors in Polarized MDCK Cells. *J. Cell Biol.* **139**, 929–940 (1997).

76. Monlauzeur, L., Breuza, L. & Le Bivic, A. Putative O-Glycosylation Sites and a Membrane Anchor Are Necessary for Apical Delivery of the Human Neurotrophin Receptor in Caco-2 Cells. *J. Biol. Chem.* **273**, 30263–30270 (1998).

77. Breuza, L., Garcia, M., Delgrossi, M.-H. & Bivic, A. Le. Role of the Membrane-Proximal O-glycosylation Site in Sorting of the Human Receptor for Neurotrophins to the Apical Membrane of MDCK Cells. *Exp. Cell Res.* **273**, 178–186 (2002).

78. Haniu, M. *et al.* Extracellular Domain of Neurotrophin Receptor trkB: Disulfide Structure, N-Glycosylation Sites, and Ligand Binding. *Arch. Biochem. Biophys.* **322**, 256–264 (1995).

79. Baldwin, A. N. & Shooter, E. M. Zone Mapping of the Binding Domain of the Rat Low Affinity Nerve Growth Factor Receptor by the Introduction of Novel N-Glycosylation Sites. *J. Biol. Chem.* **270**, 4594–4602 (1995).

80. Watson, F. L., Porcionatto, M. A., Bhattacharyya, A., Stiles, C. D. & Segal, R. A. TrkA glycosylation regulates receptor localization and activity. *J. Neurobiol.* **39**, 323–336 (1999).

81. Grob, P. M., Ross, A. H., Koprowski, H. & Bothwell, M. Characterization of the human melanoma nerve growth factor receptor. *J. Biol. Chem.* **260**, 8044–9 (1985).

82. Trabjerg, E., Kartberg, F., Christensen, S. & Rand, K. D. Conformational characterization of nerve growth factor-β reveals that its regulatory pro-part domain stabilizes three loop regions in its mature part. *J. Biol. Chem.* **292**, 16665–16676 (2017).

83. Benicky, J., Sanda, M., Brnakova Kennedy, Z. & Goldman, R. N-Glycosylation is required for secretion of the precursor to brain-derived neurotrophic factor (proBDNF) carrying sulfated LacdiNAc structures. *J. Biol. Chem.* **294**, 16816–16830 (2019).

84. Chapman, B. S., Eckart, M. R., Kaufman, S. E. & Lapointe, G. R. O-Linked Oligosaccharide on the 75-kDa Neurotrophin Receptor. *J. Neurochem.* **66**, 1707–1716 (2002).

85. Jullien, J., Guili, V., Reichardt, L. F. & Rudkin, B. B. Molecular Kinetics of Nerve Growth Factor Receptor Trafficking and Activation. *J. Biol. Chem.* **277**, 38700–38708 (2002).

86. Woronowicz, A. *et al.* Dependence of neurotrophic factor activation of Trk tyrosine kinase receptors on cellular sialidase. *Glycobiology* **17**, 10–24 (2007).

87. Sotthibundhu, A. *et al.* β-Amyloid 1–42 Induces Neuronal Death through the p75 Neurotrophin Receptor. *J. Neurosci.* **28**, 3941–3946 (2008).

88. Knowles, J. K. *et al.* The p75 Neurotrophin Receptor Promotes Amyloid-β(1-42)-Induced Neuritic Dystrophy In Vitro and In Vivo. *J. Neurosci.* **29**, 10627–10637 (2009).

89. Chao, M. V. Neurotrophins and their receptors: A convergence point for many signalling pathways. *Nat. Rev. Neurosci.* **4**, 299–309 (2003).

90. Yoon, S. O., Casaccia-Bonnefil, P., Carter, B. & Chao, M. V. Competitive Signaling Between TrkA and p75 Nerve Growth Factor Receptors Determines Cell Survival. *J. Neurosci.* **18**, 3273–3281 (1998).

91. PERRONE, L. *et al.* Functional interaction between p75NTR and TrkA: the endocytic trafficking of p75NTR is driven by TrkA and regulates TrkA-mediated signalling. *Biochem. J.* **385**, 233–241 (2005).

92. Ho, R. *et al.* The effect of P75 on Trk receptors in neuroblastomas. *Cancer Lett.* **305**, 76–85 (2011).

93. Lu, B., Pang, P. T. & Woo, N. H. The yin and yang of neurotrophin action. *Nat. Rev. Neurosci.* **6**, 603–614 (2005).

94. Berg, M. M., Sternberg, D. W., Hempstead, B. L. & Chao, M. V. The low-affinity p75 nerve growth factor (NGF) receptor mediates NGF-induced tyrosine phosphorylation. *Proc. Natl. Acad. Sci.* **88**, 7106–7110 (1991).

95. Landreth, G. E. & Shooter, E. M. Nerve growth factor receptors on PC12 cells: ligand-induced conversion from low- to high-affinity states. *Proc. Natl. Acad. Sci.* **77**, 4751–4755 (1980).

96. Bibel, M. Biochemical and functional interactions between the neurotrophin receptors trk and p75NTR. *EMBO J.* **18**, 616–622 (1999).

97. Makkerh, J. P. S. *et al.* p75 neurotrophin receptor reduces ligand-induced Trk receptor ubiquitination and delays Trk receptor internalization and degradation. *EMBO Rep.* **6**, 936–941 (2005).

98. Yamashita, T., Tucker, K. L. & Barde, Y.-A. Neurotrophin Binding to the p75 Receptor Modulates Rho Activity and Axonal Outgrowth. *Neuron* **24**, 585–593 (1999).

99. Deppmann, C. D. *et al.* A model for neuronal competition during development. *Science* **320**, 369–73 (2008).

100. Nykjaer, A., Willnow, T. E. & Petersen, C. M. p75NTR – live or let die. *Curr. Opin. Neurobiol.* **15**, 49–57 (2005).

101. Lee, H.-J. *et al.* Presenilin-dependent γ-Secretase-like Intramembrane Cleavage of ErbB4. *J. Biol. Chem.* **277**, 6318–6323 (2002).

102. DiStefano, P., Chelsea, D., Schick, C. & McKelvy, J. Involvement of a metalloprotease in low-affinity nerve growth factor receptor truncation: inhibition of truncation in vitro and in vivo. *J. Neurosci.* **13**, 2405–2414 (1993).

103. Kanning, K. C. *et al.* Proteolytic Processing of the p75 Neurotrophin Receptor and Two Homologs Generates C-Terminal Fragments with Signaling Capability. *J. Neurosci.* **23**, 5425–5436 (2003).

104. Brown, M. S., Ye, J., Rawson, R. B. & Goldstein, J. L. Regulated Intramembrane Proteolysis. *Cell* **100**, 391–398 (2000).

105. Matusica, D. *et al.* Inhibition of motor neuron death in vitro and in vivo by a p75 neurotrophin receptor intracellular domain fragment. *J. Cell Sci.* (2015) doi:10.1242/jcs.173864.

106. Matusica, D. *et al.* An Intracellular Domain Fragment of the p75 Neurotrophin Receptor (p75NTR) Enhances Tropomyosin Receptor Kinase A (TrkA) Receptor Function. *J. Biol. Chem.* **288**, 11144–11154 (2013).

107. Ceni, C. *et al.* The p75NTR intracellular domain generated by neurotrophin-induced receptor cleavage potentiates Trk signaling. *J. Cell Sci.* **123**, 2299–2307 (2010).

108. Kommaddi, R. P., Thomas, R., Ceni, C., Daigneault, K. & Barker, P. A. Trk-dependent ADAM17 activation facilitates neurotrophin survival signaling. *FASEB J.* **25**, 2061–2070 (2011).

109. Frade, J. M. Nuclear Translocation of the p75 Neurotrophin Receptor Cytoplasmic Domain in Response to Neurotrophin Binding. *J. Neurosci.* **25**, 1407–1411 (2005).

110. Kenchappa, R. S. *et al.* Ligand-Dependent Cleavage of the P75 Neurotrophin Receptor Is Necessary for NRIF Nuclear Translocation and Apoptosis in Sympathetic Neurons. *Neuron* **50**, 219–232 (2006).

111. Urra, S. *et al.* TrkA Receptor Activation by Nerve Growth Factor Induces Shedding of the p75 Neurotrophin Receptor Followed by Endosomal γ-Secretase-mediated Release of the p75 Intracellular Domain. *J. Biol. Chem.* **282**, 7606–7615 (2007).

112. Coulson, E. J. *et al.* p75 Neurotrophin Receptor Mediates Neuronal Cell Death by Activating GIRK Channels through Phosphatidylinositol 4,5-Bisphosphate. *J. Neurosci.* **28**, 315–324 (2008).

113. Marchetti, L. *et al.* Fast-diffusing p75 NTR monomers support apoptosis and growth cone collapse by neurotrophin ligands. *Proc. Natl. Acad. Sci.* **116**, 21563–21572 (2019).

114. Bradshaw, R. A. *et al.* Nerve growth factor: Structure/function relationships. *Protein Sci.* **3**, 1901–1913 (1994).

115. Chao, M. V. Stoichiometry counts. *Proc. Natl. Acad. Sci.* **116**, 21343–21345 (2019).

116. Puma, P., Buxser, S. E., Watson, L., Kelleher, D. J. & Johnson, G. L. Purification of the receptor for nerve growth factor from A875 melanoma cells by affinity chromatography. *J. Biol. Chem.* **258**, 3370–3375 (1983).

117. Skeldal, S., Matusica, D., Nykjaer, A. & Coulson, E. J. Proteolytic processing of the p75 neurotrophin receptor: A prerequisite for signalling? *BioEssays* **33**, 614–625 (2011).

118. Sykes, A. M. *et al.* The Effects of Transmembrane Sequence and Dimerization on Cleavage of the p75 Neurotrophin Receptor by γ-Secretase. *J. Biol. Chem.* **287**, 43810–43824 (2012).

119. Goncharuk, S. A., Artemieva, L. E., Nadezhdin, K. D., Arseniev, A. S. & Mineev, K. S. Revising the mechanism of p75NTR activation: intrinsically monomeric state of death domains invokes the 'helper' hypothesis. *Sci. Rep.* **10**, 13686 (2020).

120. Verdi, J. M. *et al.* p75LNGFR regulates Trk signal transduction and NGF-induced neuronal differentiation in MAH cells. *Neuron* **12**, 733–745 (1994).

121. Gentry, J. J., Barker, P. A. & Carter, B. D. The p75 neurotrophin receptor: multiple interactors and numerous functions. in *NGF and Related Molecules in Health and Disease* (ed. Aloe, L. Calza, L.) 25–39 (Elsevier, 2004). doi:10.1016/S0079-6123(03)46002-0.

122. Tanaka, K., Kelly, C. E., Goh, K. Y., Lim, K. B. & Ibáñez, C. F. Death Domain Signaling by Disulfide-Linked Dimers of the p75 Neurotrophin Receptor Mediates Neuronal Death in the CNS. *J. Neurosci.* **36**, 5587–5595 (2016).

123. Coulson, E. J. *et al.* The role of neurotransmission and the Chopper domain in p75 neurotrophin receptor death signaling. in *NGF and Related Molecules in Health and Disease* 41–62 (Elsevier, 2004). doi:10.1016/S0079-6123(03)46003-2.

124. Zhang, N. *et al.* Structural basis of NF-κB signaling by the p75 neurotrophin receptor interaction with adaptor protein TRADD through their respective death domains. *J. Biol. Chem.* **297**, 100916 (2021).

125. Papoff, G. *et al.* N-Terminal and C-Terminal Domains of Calmodulin Mediate FADD and TRADD Interaction. *PLoS One* **10**, e0116251 (2015).

126. Zhang, N., Yuan, W., Fan, J.-S. & Lin, Z. Structure of the C-terminal domain of TRADD reveals a novel fold in the death domain superfamily. *Sci. Rep.* **7**, 7073 (2017).

127. Xu, Z. *et al.* Dynamic expression of death receptor adapter proteins tradd and fadd in Eimeria tenella-induced host cell apoptosis. *Poult. Sci.* **96**, 1438–1444 (2017).

128. Xie, M. *et al.* Sublytic C5b-9 induces glomerular mesangial cell proliferation via ERK1/2-dependent SOX9 phosphorylation and acetylation by enhancing Cyclin D1 in rat Thy-1 nephritis. *Exp. Mol. Med.* **53**, 572–590 (2021).

129. Mazella, J. Deciphering Mechanisms of Action of Sortilin/Neurotensin Receptor-3 in the Proliferation Regulation of Colorectal and Other Cancers. *Int. J. Mol. Sci.* **23**, 11888 (2022).

130. Dedoni, S., Marras, L., Olianas, M. C., Ingianni, A. & Onali, P. Valproic acid upregulates the expression of the p75NTR/sortilin receptor complex to induce neuronal apoptosis. *Apoptosis* **25**, 697–714 (2020).

131. Teng, H. K. *et al.* ProBDNF Induces Neuronal Apoptosis via Activation of a Receptor Complex of p75 NTR and Sortilin. *J. Neurosci.* **25**, 5455–5463 (2005).

132. Eggert, S., Kins, S., Endres, K. & Brigadski, T. Brothers in arms: proBDNF/BDNF and sAPPα/Aβ-signaling and their common interplay with ADAM10, TrkB, p75NTR, sortilin, and sorLA in the progression of Alzheimer's disease. *Biol. Chem.* **403**, 43–71 (2022).

133. Saha, N., Kolev, M. & Nikolov, D. B. Structural features of the Nogo receptor signaling complexes at the neuron/myelin interface. *Neurosci. Res.* **87**, 1–7 (2014).

134. Egawa, J., Pearn, M. L., Lemkuil, B. P., Patel, P. M. & Head, B. P. Membrane lipid rafts and neurobiology: age-related changes in membrane lipids and loss of neuronal function. *J. Physiol.* **594**, 4565–4579 (2016).

135. Lorent, J. H. & Levental, I. Structural determinants of protein partitioning into ordered membrane domains and lipid rafts. *Chem. Phys. Lipids* **192**, 23–32 (2015).

136. Sezgin, E., Levental, I., Mayor, S. & Eggeling, C. The mystery of membrane organization: composition, regulation and roles of lipid rafts. *Nat. Rev. Mol. Cell Biol.* **18**, 361–374 (2017).

137. Levental, I., Levental, K. R. & Heberle, F. A. Lipid Rafts: Controversies Resolved, Mysteries Remain. *Trends Cell Biol.* **30**, 341–353 (2020).

138. Moll, T. *et al.* Membrane lipid raft homeostasis is directly linked to neurodegeneration. *Essays Biochem.* **65**, 999–1011 (2021).

139. Higuchi, H. PKA phosphorylates the p75 receptor and regulates its localization to lipid rafts. *EMBO J.* **22**, 1790–1800 (2003).

140. Gil, C., Cubí, R. & Aguilera, J. Shedding of the p75 NTR neurotrophin receptor is modulated by lipid rafts. *FEBS Lett.* **581**, 1851–1858 (2007).

141. Limpert, A. S., Karlo, J. C. & Landreth, G. E. Nerve Growth Factor Stimulates the Concentration of TrkA within Lipid Rafts and Extracellular Signal-Regulated Kinase Activation through c-Cbl-Associated Protein. *Mol. Cell. Biol.* **27**, 5686–5698 (2007).

142. Spencer, A. *et al.* Nerve Growth Factor Signaling from Membrane Microdomains to the Nucleus: Differential Regulation by Caveolins. *Int. J. Mol. Sci.* **18**, 693 (2017).

143. Suzuki, S. *et al.* BDNF-induced recruitment of TrkB receptor into neuronal lipid rafts. *J. Cell Biol.* **167**, 1205–1215 (2004).

144. Sharma, D. *et al.* Hypoxia-mediated alteration in cholesterol oxidation and raft dynamics regulates BDNF signalling and neurodegeneration in hippocampus. *J. Neurochem.* **148**, 238–251 (2019).

145. Duchemin, A.-M., Ren, Q., Mo, L., Neff, N. H. & Hadjiconstantinou, M. GM1 ganglioside induces phosphorylation and activation of Trk and Erk in brain. *J. Neurochem.* **81**, 696–707 (2002).

146. Kimura, M., Hidari, K. I.-P. J., Suzuki, T., Miyamoto, D. & Suzuki, Y. Engagement of endogenous ganglioside GM1a induces tyrosine phosphorylation involved in neuron-like differentiation of PC12 cells. *Glycobiology* **11**, 335–343 (2001).

147. Rabin, S. J. & Mocchetti, I. GM1 Ganglioside Activates the High-Affinity Nerve Growth Factor Receptor trkA. *J. Neurochem.* **65**, 347–354 (2002).

148. Mutoh, T., Tokuda, A., Miyadai, T., Hamaguchi, M. & Fujiki, N. Ganglioside GM1 binds to the Trk protein and regulates receptor function. *Proc. Natl. Acad. Sci.* **92**, 5087–5091 (1995).

149. MacPhee, I. & Barker, P. A. Extended Ceramide Exposure Activates the trkA Receptor by Increasing Receptor Homodimer Formation. *J. Neurochem.* **72**, 1423–1430 (2001).

150. Mutoh, T. *et al.* Stable transfection of GM1 synthase gene into GM1-deficient NG108-15 cells, CR-72 cells, rescues the responsiveness of Trk-neurotrophin receptor to its ligand, NGF. *Neurochem. Res.* **27**, 801–6 (2002).

151. Mutoh, T., Hamano, T., Tokuda, A. & Kuriyama, M. Unglycosylated Trk protein does not co-localize nor associate with ganglioside GM1 in stable clone of PC12 cells overexpressing Trk (PCtrk cells). *Glycoconj. J.* **17**, 233–7.

152. Chiricozzi, E. *et al.* Role of the GM1 ganglioside oligosaccharide portion in the TrkA-dependent neurite sprouting in neuroblastoma cells. *J. Neurochem.* **143**, 645–659 (2017).

153. Bachis, A., Rabin, S. J., Fiacco, M. & Mocchetti, I. Gangliosides prevent excitotoxicity through activation of TrkB receptor. *Neurotox. Res.* **4**, 225–234 (2002).

154. Rabin, S. J., Bachis, A. & Mocchetti, I. Gangliosides Activate Trk Receptors by Inducing the Release of Neurotrophins. *J. Biol. Chem.* **277**, 49466–49472 (2002).

155. Roux, P. Neurotrophin signaling through the p75 neurotrophin receptor. *Prog. Neurobiol.* **67**, 203–233 (2002).

156. Kuruvilla, R. *et al.* A Neurotrophin Signaling Cascade Coordinates Sympathetic Neuron Development through Differential Control of TrkA Trafficking and Retrograde Signaling. *Cell* **118**, 243–255 (2004).

157. Lad, S. P., Peterson, D. A., Bradshaw, R. A. & Neet, K. E. Individual and Combined Effects of TrkA and p75NTR Nerve Growth Factor Receptors. *J. Biol. Chem.* **278**, 24808–24817 (2003).

158. DeFreitas, M. F., McQuillen, P. S. & Shatz, C. J. A Novel p75NTR Signaling Pathway Promotes Survival, Not

Death, of Immunopurified Neocortical Subplate Neurons. *J. Neurosci.* **21**, 5121–5129 (2001).

159. Hamanoue, M. *et al.* p75-Mediated NF-κB Activation Enhances the Survival Response of Developing Sensory Neurons to Nerve Growth Factor. *Mol. Cell. Neurosci.* **14**, 28–40 (1999).

160. Khursigara, G. *et al.* A Prosurvival Function for the p75 Receptor Death Domain Mediated via the Caspase Recruitment Domain Receptor-Interacting Protein 2. *J. Neurosci.* **21**, 5854–5863 (2001).

161. Kane, L. P., Shapiro, V. S., Stokoe, D. & Weiss, A. Induction of NF-κB by the Akt/PKB kinase. *Curr. Biol.* **9**, 601-S1 (1999).

162. Miller, F. D. & Kaplan, D. R. Neurotrophin signalling pathways regulating neuronal apoptosis. *Cell. Mol. Life Sci.* **58**, 1045–1053 (2001).

163. Bamji, S. X. *et al.* The p75 Neurotrophin Receptor Mediates Neuronal Apoptosis and Is Essential for Naturally Occurring Sympathetic Neuron Death. *J. Cell Biol.* **140**, 911–923 (1998).

164. Linggi, M. S. *et al.* Neurotrophin Receptor Interacting Factor (NRIF) Is an Essential Mediator of Apoptotic Signaling by the p75 Neurotrophin Receptor. *J. Biol. Chem.* **280**, 13801–13808 (2005).

165. Sedel, F., Béchade, C. & Triller, A. Nerve growth factor (NGF) induces motoneuron apoptosis in rat embryonic spinal cord in vitro. *Eur. J. Neurosci.* **11**, 3904–3912 (1999).

166. Volosin, M. *et al.* Induction of Proneurotrophins and Activation of p75 NTR -Mediated Apoptosis via Neurotrophin Receptor-Interacting Factor in Hippocampal Neurons after Seizures. *J. Neurosci.* **28**, 9870–9879 (2008).

167. Casaccia-Bonnefil, P., Carter, B. D., Dobrowsky, R. T. & Chao, M. V. Death of oligodendrocytes mediated by the interaction of nerve growth factor with its receptor p75. *Nature* **383**, 716–719 (1996).

168. Syroid, D. E. *et al.* Induction of Postnatal Schwann Cell Death by the Low-Affinity Neurotrophin Receptor In Vitro and after Axotomy. *J. Neurosci.* **20**, 5741–5747 (2000).

169. Volosin, M. *et al.* Interaction of Survival and Death Signaling in Basal Forebrain Neurons: Roles of Neurotrophins and Proneurotrophins. *J. Neurosci.* **26**, 7756–7766 (2006).

170. Wang, S. *et al.* p75NTR Mediates Neurotrophin-Induced Apoptosis of Vascular Smooth Muscle Cells. *Am. J. Pathol.* **157**, 1247–1258 (2000).

171. Naumann, T. *et al.* Complete Deletion of the Neurotrophin Receptor p75 NTR Leads to Long-Lasting Increases in the Number of Basal Forebrain Cholinergic Neurons. *J. Neurosci.* **22**, 2409–2418 (2002).

172. MarÍa Frade, J. & Barde, Y.-A. Genetic evidence for cell death mediated by nerve growth factor and the neurotrophin receptor p75 in the developing mouse retina and spinal cord. *Development* **126**, 683–690 (1999).

173. Harrington, A. W., Kim, J. Y. & Yoon, S. O. Activation of Rac GTPase by p75 Is Necessary for c- jun N-Terminal Kinase-Mediated Apoptosis. *J. Neurosci.* **22**, 156–166 (2002).

174. Kraemer, B. R. & Carter, B. D. Receptors | Neurotrophin Receptor Signaling. in *Encyclopedia of Biological Chemistry III* 187–200 (Elsevier, 2021). doi:10.1016/B978-0-12-819460-7.00310-8.

175. Yeiser, E. C., Rutkoski, N. J., Naito, A., Inoue, J. & Carter, B. D. Neurotrophin Signaling through the p75 Receptor Is Deficient in traf6 -/- Mice. *J. Neurosci.* **24**, 10521–10529 (2004).

176. Dhanasekaran, D. N. & Reddy, E. P. JNK signaling in apoptosis. *Oncogene* **27**, 6245–6251 (2008).

177. Toshiyuki, M. & Reed, J. C. Tumor suppressor p53 is a direct transcriptional activator of the human bax gene. *Cell* **80**, 293–299 (1995).

178. Bhakar, A. L. *et al.* Apoptosis Induced by p75NTR Overexpression Requires Jun Kinase-Dependent Phosphorylation of Bad. *J. Neurosci.* **23**, 11373–11381 (2003).

179. Okuno, S., Saito, A., Hayashi, T. & Chan, P. H. The c-Jun N-Terminal Protein Kinase Signaling Pathway Mediates Bax Activation and Subsequent Neuronal Apoptosis through Interaction with Bim after Transient Focal Cerebral Ischemia. *J. Neurosci.* **24**, 7879–7887 (2004).

180. Barker, P. A. p75NTR Is Positively Promiscuous. *Neuron* **42**, 529–533 (2004).

181. Becker, E. B. E., Howell, J., Kodama, Y., Barker, P. A. & Bonni, A. Characterization of the c-Jun N-Terminal Kinase-Bim EL Signaling Pathway in Neuronal Apoptosis. *J. Neurosci.* **24**, 8762–8770 (2004).

182. Yamamoto, K., Ichijo, H. & Korsmeyer, S. J. BCL-2 Is Phosphorylated and Inactivated by an ASK1/Jun N-Terminal Protein Kinase Pathway Normally Activated at G 2 /M. *Mol. Cell. Biol.* **19**, 8469–8478 (1999).

183. Lei, K. & Davis, R. J. JNK phosphorylation of Bim-related members of the Bcl2 family induces Bax-dependent apoptosis. *Proc. Natl. Acad. Sci.* **100**, 2432–2437 (2003).

184. Donovan, N., Becker, E. B. E., Konishi, Y. & Bonni, A. JNK Phosphorylation and Activation of BAD Couples the Stress-activated Signaling Pathway to the Cell Death Machinery. *J. Biol. Chem.* **277**, 40944–40949 (2002).

185. Bogoyevitch, M. A. & Kobe, B. Uses for JNK: the Many and Varied Substrates of the c-Jun N-Terminal Kinases. *Microbiol. Mol. Biol. Rev.* **70**, 1061–1095 (2006).

186. Dobrowsky, R. T., Werner, M. H., Castellino, A. M., Chao, M. V. & Hannun, Y. A. Activation of the Sphingomyelin Cycle Through the Low-Affinity Neurotrophin Receptor. *Science (80-.).* **265**, 1596–1599 (1994).

187. Westwick, J. K., Bielawska, A. E., Dbaibo, G., Hannun, Y. A. & Brenner, D. A. Ceramide Activates the Stress-activated Protein Kinases. *J. Biol. Chem.* **270**, 22689–22692 (1995).

188. Brann, A. B., Tcherpakov, M., Williams, I. M., Futerman, A. H. & Fainzilber, M. Nerve Growth Factor-induced p75-mediated Death of Cultured Hippocampal Neurons Is Age-dependent and Transduced through Ceramide Generated by Neutral Sphingomyelinase. *J. Biol. Chem.* **277**, 9812–9818 (2002).

189. Mukai, J. *et al.* NADE, a p75NTR-associated Cell Death Executor, Is Involved in Signal Transduction Mediated by the Common Neurotrophin Receptor p75NTR. *J. Biol. Chem.* **275**, 17566–17570 (2000).

190. Kuwako, K., Taniura, H. & Yoshikawa, K. Necdin-related MAGE Proteins Differentially Interact with the E2F1 Transcription Factor and the p75 Neurotrophin Receptor. *J. Biol. Chem.* **279**, 1703–1712 (2004).

191. Jung, K.-M. *et al.* Regulated Intramembrane Proteolysis of the p75 Neurotrophin Receptor Modulates Its Association with the TrkA Receptor. *J. Biol. Chem.* **278**, 42161–42169 (2003).

192. Weskamp, G. *et al.* Evidence for a Critical Role of the Tumor Necrosis Factor α Convertase (TACE) in Ectodomain Shedding of the p75 Neurotrophin Receptor (p75NTR). *J. Biol. Chem.* **279**, 4241–4249 (2004).

193. Zampieri, N., Xu, C.-F., Neubert, T. A. & Chao, M. V. Cleavage of p75 Neurotrophin Receptor by α-Secretase and γ-Secretase Requires Specific Receptor Domains. *J. Biol. Chem.* **280**, 14563–14571 (2005).

194. Kenchappa, R. S. *et al.* p75 Neurotrophin Receptor-mediated Apoptosis in Sympathetic Neurons Involves a Biphasic Activation of JNK and Up-regulation of Tumor Necrosis Factor-α-converting Enzyme/ADAM17. *J. Biol. Chem.* **285**, 20358–20368 (2010).

195. Domeniconi, M. *et al.* MAG Induces Regulated Intramembrane Proteolysis of the p75 Neurotrophin Receptor to Inhibit Neurite Outgrowth. *Neuron* **46**, 849–855 (2005).

196. Geetha, T., Kenchappa, R. S., Wooten, M. W. & Carter, B. D. TRAF6-mediated ubiquitination regulates nuclear translocation of NRIF, the p75 receptor interactor. *EMBO J.* **24**, 3859–3868 (2005).

197. Forsyth, P. A. *et al.* p75 Neurotrophin Receptor Cleavage by α- and γ-Secretases Is Required for Neurotrophin-mediated Proliferation of Brain Tumor-initiating Cells. *J. Biol. Chem.* **289**, 8067–8085 (2014).

198. Molloy, N., Read, D. & Gorman, A. Nerve Growth Factor in Cancer Cell Death and Survival. *Cancers (Basel).*

3, 510–530 (2011).

199. Lee, R., Kermani, P., Teng, K. K. & Hempstead, B. L. Regulation of Cell Survival by Secreted Proneurotrophins. *Science (80-.).* **294**, 1945–1948 (2001).

200. Lebrun-Julien, F. *et al.* ProNGF induces TNFα-dependent death of retinal ganglion cells through a p75 NTR non-cell-autonomous signaling pathway. *Proc. Natl. Acad. Sci.* **107**, 3817–3822 (2010).

201. Harrington, A. W. *et al.* Secreted proNGF is a pathophysiological death-inducing ligand after adult CNS injury. *Proc. Natl. Acad. Sci.* **101**, 6226–6230 (2004).

202. Willnow, T. E., Petersen, C. M. & Nykjaer, A. VPS10P-domain receptors — regulators of neuronal viability and function. *Nat. Rev. Neurosci.* **9**, 899–909 (2008).

203. Jansen, P. *et al.* Roles for the pro-neurotrophin receptor sortilin in neuronal development, aging and brain injury. *Nat. Neurosci.* **10**, 1449–1457 (2007).

204. Franco, M. L., Comaposada-Baró, R. & Vilar, M. Neurotrophins and Neurotrophin Receptors. in *Hormonal Signaling in Biology and Medicine* 83–106 (Elsevier, 2020). doi:10.1016/B978-0-12-813814-4.00005-5.

205. Bronfman, F. C., Tcherpakov, M., Jovin, T. M. & Fainzilber, M. Ligand-Induced Internalization of the p75 Neurotrophin Receptor: A Slow Route to the Signaling Endosome. *J. Neurosci.* **23**, 3209–3220 (2003).

206. Wang, X. *et al.* BDNF-TrkB and proBDNF-p75NTR/Sortilin Signaling Pathways are Involved in Mitochondria-Mediated Neuronal Apoptosis in Dorsal Root Ganglia after Sciatic Nerve Transection. *CNS Neurol. Disord. - Drug Targets* **19**, 66–82 (2020).

207. Wong, S. T. *et al.* A p75NTR and Nogo receptor complex mediates repulsive signaling by myelin-associated glycoprotein. *Nat. Neurosci.* **5**, 1302–1308 (2002).

208. Wang, K. C., Kim, J. A., Sivasankaran, R., Segal, R. & He, Z. p75 interacts with the Nogo receptor as a co-receptor for Nogo, MAG and OMgp. *Nature* **420**, 74–78 (2002).

209. Mi, S. *et al.* LINGO-1 is a component of the Nogo-66 receptor/p75 signaling complex. *Nat. Neurosci.* **7**, 221–228 (2004).

210. Yamashita, T. & Tohyama, M. The p75 receptor acts as a displacement factor that releases Rho from Rho-GDI. *Nat. Neurosci.* **6**, 461–467 (2003).

211. Schwab, M. E. Nogo and axon regeneration. *Curr. Opin. Neurobiol.* **14**, 118–124 (2004).

212. Hou, Y. *et al.* Ageing as a risk factor for neurodegenerative disease. *Nat. Rev. Neurol.* **15**, 565–581 (2019).

213. Pöyhönen, S., Er, S., Domanskyi, A. & Airavaara, M. Effects of Neurotrophic Factors in Glial Cells in the Central Nervous System: Expression and Properties in Neurodegeneration and Injury. *Front. Physiol.* **10**, (2019).

214. Blesch, A. Neurotrophic Factors in Neurodegeneration. *Brain Pathol.* **16**, 295–303 (2006).

215. Xiao, Q., Chen, J., Fang, C., Su, Z. & Wang, T. Neurotrophins-3 plays a vital role in anti-apoptosis associated with NGF and BDNF regulation in neonatal rats with hypoxic-ischemic brain injury. *Ibrain* **6**, 12–17 (2020).

216. Shen, L.-L. *et al.* The ProNGF/p75NTR pathway induces tau pathology and is a therapeutic target for FTLD-tau. *Mol. Psychiatry* **23**, 1813–1824 (2018).

217. Xiong, L., Chen, L., Deng, I. B., Zhou, X. & Wang, T. P75 neurotrophin receptor as a therapeutic target for drug development to treat neurological diseases. *Eur. J. Neurosci.* **56**, 5299–5318 (2022).

218. Becker, K., Cana, A., Baumgärtner, W. & Spitzbarth, I. p75 Neurotrophin Receptor: A Double-Edged Sword in Pathology and Regeneration of the Central Nervous System. *Vet. Pathol.* **55**, 786–801 (2018).

219. Meeker, R. & Williams, K. Dynamic Nature of the p75 Neurotrophin Receptor in Response to Injury and Disease. *J. Neuroimmune Pharmacol.* **9**, 615–628 (2014).

220. Ibáñez, C. F. & Simi, A. p75 neurotrophin receptor signaling in nervous system injury and degeneration: paradox and opportunity. *Trends Neurosci.* **35**, 431–440 (2012).

221. Uzdensky, A. B. Apoptosis regulation in the penumbra after ischemic stroke: expression of pro- and antiapoptotic proteins. *Apoptosis* **24**, 687–702 (2019).

222. Fujii, T. & Kunugi, H. p75NTR as a Therapeutic Target for Neuropsychiatric Diseases. *Curr. Mol. Pharmacol.* **2**, 70–76 (2009).

223. Wang, Q., Fang, C., Huang, X. & Xue, L. Research progress of the CXCR4 mechanism in Alzheimer's disease. *Ibrain* **8**, 3–14 (2022).

224. Mufson, E. J. & Kordower, J. H. Cortical neurons express nerve growth factor receptors in advanced age and Alzheimer disease. *Proc. Natl. Acad. Sci.* **89**, 569–573 (1992).

225. Chakravarthy, B. *et al.* Hippocampal Membrane-Associated p75NTR Levels are Increased in Alzheimer's Disease. *J. Alzheimer's Dis.* **30**, 675–684 (2012).

226. Yeo, T. T. *et al.* Absence of p75 NTR Causes Increased Basal Forebrain Cholinergic Neuron Size, Choline Acetyltransferase Activity, and Target Innervation. *J. Neurosci.* **17**, 7594–7605 (1997).

227. Dechant, G. & Barde, Y.-A. The neurotrophin receptor p75NTR: novel functions and implications for diseases of the nervous system. *Nat. Neurosci.* **5**, 1131–1136 (2002).

228. Jiao, S.-S. *et al.* Differential levels of p75NTR ectodomain in CSF and blood in patients with Alzheimer's disease: a novel diagnostic marker. *Transl. Psychiatry* **5**, e650–e650 (2015).

229. Wang, Y.-J. *et al.* p75NTR Regulates Aβ Deposition by Increasing Aβ Production But Inhibiting Aβ Aggregation with Its Extracellular Domain. *J. Neurosci.* **31**, 2292–2304 (2011).

230. Wong, L.-W., Wang, Z., Ang, S. R. X. & Sajikumar, S. Fading memories in aging and neurodegeneration: Is p75 neurotrophin receptor a culprit? *Ageing Res. Rev.* **75**, 101567 (2022).

231. Brown, R. H. & Al-Chalabi, A. Amyotrophic Lateral Sclerosis. *N. Engl. J. Med.* **377**, 162–172 (2017).

232. Haase, G., Pettmann, B., Raoul, C. & Henderson, C. E. Signaling by death receptors in the nervous system. *Curr. Opin. Neurobiol.* **18**, 284–291 (2008).

233. Shepheard, S. R., Chataway, T., Schultz, D. W., Rush, R. A. & Rogers, M.-L. The Extracellular Domain of Neurotrophin Receptor p75 as a Candidate Biomarker for Amyotrophic Lateral Sclerosis. *PLoS One* **9**, e87398 (2014).

234. Beitz, J. M. Parkinson s disease a review. *Front. Biosci.* **S6**, S415 (2014).

235. Li, W.-W. *et al.* Genetic Association Between NGFR, ADAM17 Gene Polymorphism, and Parkinson's Disease in the Chinese Han Population. *Neurotox. Res.* **36**, 463–471 (2019).

236. Brito, V. *et al.* Imbalance of p75NTR/TrkB protein expression in Huntington's disease: implication for neuroprotective therapies. *Cell Death Dis.* **4**, e595–e595 (2013).

237. Lemiere, J., Decruyenaere, M., Evers-Kiebooms, G., Vandenbussche, E. & Dom, R. Cognitive changes in patients with Huntington's disease (HD) and asymptomatic carriers of the HD mutation. *J. Neurol.* **251**, (2004).

238. Majerová, V. *et al.* Disturbance of real space navigation in moderately advanced but not in early Huntington's disease. *J. Neurol. Sci.* **312**, 86–91 (2012).

239. Plotkin, J. L. *et al.* Impaired TrkB Receptor Signaling Underlies Corticostriatal Dysfunction in Huntington's Disease. *Neuron* **83**, 178–188 (2014).

240. Andsberg, G., Kokaia, Z. & Lindvall, O. Upregulation of p75 Neurotrophin Receptor after Stroke in Mice Does Not Contribute to Differential Vulnerability of Striatal Neurons. *Exp. Neurol.* **169**, 351–363 (2001).

241. Lazarovici, P. *et al.* Multimodal Neuroprotection Induced by PACAP38 in Oxygen–Glucose Deprivation and Middle Cerebral Artery Occlusion Stroke Models. *J. Mol. Neurosci.* **48**, 526–540 (2012).

242. Delbary-Gossart, S. *et al.* A novel inhibitor of p75-neurotrophin receptor improves functional outcomes in two models of traumatic brain injury. *Brain* **139**, 1762–1782 (2016).

243. Liu, L. *et al.* Panax notoginseng Saponins Promotes Stroke Recovery by Influencing Expression of Nogo-A, NgR and p75NGF, in Vitro and in Vivo. *Biol. Pharm. Bull.* **37**, 560–568 (2014).

244. Wang, Y. & Yuan, H. Research progress of endogenous neural stem cells in spinal cord injury. *Ibrain* **8**, 199–209 (2022).

245. Meldolesi, J. Neurotrophin receptors in the pathogenesis, diagnosis and therapy of neurodegenerative diseases. *Pharmacol. Res.* **121**, 129–137 (2017).

246. Tep, C. *et al.* Oral Administration of a Small Molecule Targeted to Block proNGF Binding to p75 Promotes Myelin Sparing and Functional Recovery after Spinal Cord Injury. *J. Neurosci.* **33**, 397–410 (2013).

247. Yamada, K. *et al.* Genetic analysis of the calcineurin pathway identifies members of the EGR gene family, specifically EGR3 , as potential susceptibility candidates in schizophrenia. *Proc. Natl. Acad. Sci.* **104**, 2815–2820 (2007).

248. Weickert, C. S. *et al.* Reduced brain-derived neurotrophic factor in prefrontal cortex of patients with schizophrenia. *Mol. Psychiatry* **8**, 592–610 (2003).

249. Neves-Pereira, M. *et al.* BDNF gene is a risk factor for schizophrenia in a Scottish population. *Mol. Psychiatry* **10**, 208–212 (2005).

250. Egan, M. F. *et al.* The BDNF val66met Polymorphism Affects Activity-Dependent Secretion of BDNF and Human Memory and Hippocampal Function. *Cell* **112**, 257–269 (2003).

251. Fernandez-Enright, F., Andrews, J. L., Newell, K. A., Pantelis, C. & Huang, X. F. Novel implications of Lingo-1 and its signaling partners in schizophrenia. *Transl. Psychiatry* **4**, e348–e348 (2014).

252. Gao, X., Daugherty, R. L. & Tourtellotte, W. G. Regulation of low affinity neurotrophin receptor (p75NTR) by early growth response (Egr) transcriptional regulators. *Mol. Cell. Neurosci.* **36**, 501–514 (2007).

253. Ochs, G. *et al.* A phase I/II trial of recombinant methionyl human brain derived neurotrophic factor administered by intrathecal infusion to patients with amyotrophic lateral sclerosis. *Amyotroph. Lateral Scler. Other Mot. Neuron Disord.* **1**, 201–206 (2000).

254. Dey, N. D. *et al.* Genetically engineered mesenchymal stem cells reduce behavioral deficits in the YAC 128 mouse model of Huntington's disease. *Behav. Brain Res.* **214**, 193–200 (2010).

255. Cao, L. *et al.* Molecular therapy of obesity and diabetes by a physiological autoregulatory approach. *Nat. Med.* **15**, 447–454 (2009).

256. Williams, L. R. Hypophagia is induced by intracerebroventricular administration of nerve growth factor. *Exp. Neurol.* **113**, 31–37 (1991).

257. Apfel, S. C. Nerve growth factor for the treatment of diabetic neuropathy: What went wrong, what went right, and what does the future hold? in *Neurobiology of Diabetic Neuropathy* (ed. Tomlinson, D.) 393–413 (Elsevier, 2002). doi:10.1016/S0074-7742(02)50083-0.

258. Birch, A. M. & Kelly, Á. M. Chronic intracerebroventricular infusion of nerve growth factor improves recognition memory in the rat. *Neuropharmacology* **75**, 255–261 (2013).

259. Winkler, J. *et al.* Reversible schwann cell hyperplasia and sprouting of sensory and sympathetic neurites after intraventricular administration of nerve growth factor. *Ann. Neurol.* **41**, 82–93 (1997).

260. Isaacson, L. G., Saffran, B. N. & Crutcher, K. A. Intracerebral NGF infusion induces hyperinnervation of cerebral blood vessels. *Neurobiol. Aging* **11**, 51–55 (1990).

261. Weissmiller, A. M. & Wu, C. Current advances in using neurotrophic factors to treat neurodegenerative disorders. *Transl. Neurodegener.* **1**, 14 (2012).

262. Schlachetzki, J. C. M., Pizzo, D. P., Morrissette, D. A. & Winkler, J. Intracerebroventricular Administration of Nerve Growth Factor Induces Gliogenesis in Sensory Ganglia, Dorsal Root, and within the Dorsal Root Entry Zone. *Biomed Res. Int.* **2014**, 1–9 (2014).

263. Dyck, P. J. *et al.* Intradermal recombinant human nerve growth factor induces pressure allodynia and lowered heat-pain threshold in humans. *Neurology* **48**, 501–505 (1997).

264. Eriksdotter Jönhagen, M. *et al.* Intracerebroventricular Infusion of Nerve Growth Factor in Three Patients with Alzheimer's Disease. *Dement. Geriatr. Cogn. Disord.* **9**, 246–257 (1998).

265. Apfel, S. C. *et al.* Efficacy and Safety of Recombinant Human Nerve Growth Factor in Patients With Diabetic Polyneuropathy. *JAMA* **284**, 2215 (2000).

266. Massa, S. M. Small, Nonpeptide p75NTR Ligands Induce Survival Signaling and Inhibit proNGF-Induced Death. *J. Neurosci.* **26**, 5288–5300 (2006).

267. Bai, Y. *et al.* Chronic and Acute Models of Retinal Neurodegeneration TrkA Activity Are Neuroprotective whereas p75NTR Activity Is Neurotoxic through a Paracrine Mechanism. *J. Biol. Chem.* **285**, 39392–39400 (2010).

268. Pediaditakis, I. *et al.* BNN27, a 17-spiroepoxy steroid derivative, interacts with and activates p75 neurotrophin receptor, rescuing cerebellar granule neurons from apoptosis. *Front. Pharmacol.* **7**, 1–14 (2016).

269. Calogeropoulou, T. *et al.* Novel dehydroepiandrosterone derivatives with antiapoptotic, neuroprotective activity. *J. Med. Chem.* **52**, 6569–6587 (2009).

270. Pediaditakis, I. *et al.* Selective and differential interactions of BNN27, a novel C17-spiroepoxy steroid derivative, with TrkA receptors, regulating neuronal survival and differentiation. *Neuropharmacology* **111**, 266–282 (2016).

271. Yilmaz, C. *et al.* ENT-A010, a Novel Steroid Derivative, Displays Neuroprotective Functions and Modulates Microglial Responses. *Biomolecules* **12**, 424 (2022).

272. Rogdakis, T. *et al.* Development and Biological Characterization of a Novel Selective TrkA Agonist with Neuroprotective Properties against Amyloid Toxicity. *Biomedicines* **10**, 614 (2022).

273. Charou, D. *et al.* Comprehensive characterization of the neurogenic and neuroprotective action of a novel TrkB agonist using mouse and human stem cell models of Alzheimer's disease. *Stem Cell Res. Ther.* **15**, 200 (2024).

274. Botsakis, K. *et al.* BNN-20, a synthetic microneurotrophin, strongly protects dopaminergic neurons in the "weaver" mouse, a genetic model of dopamine-denervation, acting through the TrkB neurotrophin receptor. *Neuropharmacology* **121**, 140–157 (2017).

275. Scarpi, D. *et al.* Low molecular weight, non-peptidic agonists of TrkA receptor with NGF-mimetic activity. *Cell Death Dis.* **3**, e339-13 (2012).

276. Jang, S.-W. *et al.* Gambogic amide, a selective agonist for TrkA receptor that possesses robust neurotrophic activity, prevents neuronal cell death. *Proc. Natl. Acad. Sci.* **104**, 16329–16334 (2007).

277. Harada, K., Kubo, M. & Fukuyama, Y. Chemistry and Neurotrophic Activities of (–)-Talaumidin and Its Derivatives. *Front. Chem.* **8**, (2020).

278. Sisti, F. M., dos Santos, N. A. G., do Amaral, L. & dos Santos, A. C. The Neurotrophic-Like Effect of Carvacrol: Perspective for Axonal and Synaptic Regeneration. *Neurotox. Res.* **39**, 886–896 (2021).

279. Bruno, M. A. Long-Lasting Rescue of Age-Associated Deficits in Cognition and the CNS Cholinergic

Phenotype by a Partial Agonist Peptidomimetic Ligand of TrkA. *J. Neurosci.* **24**, 8009–8018 (2004).

280. O'Leary, P. D. & Hughes, R. A. Design of Potent Peptide Mimetics of Brain-derived Neurotrophic Factor. *J. Biol. Chem.* **278**, 25738–25744 (2003).

281. Jang, S.-W. *et al.* A selective TrkB agonist with potent neurotrophic activities by 7,8-dihydroxyflavone. *Proc. Natl. Acad. Sci.* **107**, 2687–2692 (2010).

282. Jiang, M. *et al.* Small-molecule TrkB receptor agonists improve motor function and extend survival in a mouse model of Huntington's disease. *Hum. Mol. Genet.* **22**, 2462–2470 (2013).

283. Gudasheva, T. A., Logvinov, I. O., Antipova, T. A. & Seredenin, S. B. Brain-derived neurotrophic factor loop 4 dipeptide mimetic GSB-106 activates TrkB, Erk, and Akt and promotes neuronal survival in vitro. *Dokl. Biochem. Biophys.* **451**, 212–214 (2013).

284. English, A. W., Liu, K., Nicolini, J. M., Mulligan, A. M. & Ye, K. Small-molecule trkB agonists promote axon regeneration in cut peripheral nerves. *Proc. Natl. Acad. Sci.* **110**, 16217–16222 (2013).

285. Zainullina, L. F., Vakhitova, Y. V., Lusta, A. Y., Gudasheva, T. A. & Seredenin, S. B. Dimeric mimetic of BDNF loop 4 promotes survival of serum-deprived cell through TrkB-dependent apoptosis suppression. *Sci. Rep.* **11**, 7781 (2021).

286. Longo, F. M. & Massa, S. M. Small-molecule modulation of neurotrophin receptors: a strategy for the treatment of neurological disease. *Nat. Rev. Drug Discov.* **12**, 507–525 (2013).

287. Boltaev, U. *et al.* Multiplex quantitative assays indicate a need for reevaluating reported small-molecule TrkB agonists. *Sci. Signal.* **10**, (2017).

288. Berrera, M., Cattaneo, A. & Carloni, P. Molecular Simulation of the Binding of Nerve Growth Factor Peptide Mimics to the Receptor Tyrosine Kinase A. *Biophys. J.* **91**, 2063–2071 (2006).

289. Settanni, G., Cattaneo, A. & Carloni, P. Molecular Dynamics Simulations of the NGF-TrkA Domain 5 Complex and Comparison with Biological Data. *Biophys. J.* **84**, 2282–2292 (2003).

290. Wang, Z. *et al.* Coaction of Electrostatic and Hydrophobic Interactions: Dynamic Constraints on Disordered TrkA Juxtamembrane Domain. *J. Phys. Chem. B* **123**, 10709–10717 (2019).

291. Wu, X., Li, Q., Wan, S. & Zhang, J. Molecular dynamics simulation and free energy calculation studies of the binding mechanism of allosteric inhibitors with TrkA kinase. *J. Biomol. Struct. Dyn.* **39**, 202–208 (2021).

292. Paoletti, F. *et al.* Endogenous modulators of neurotrophin signaling: Landscape of the transient ATP-NGF interactions. *Comput. Struct. Biotechnol. J.* **19**, 2938–2949 (2021).

293. Franco, M. L. *et al.* Interaction between the transmembrane domains of neurotrophin receptors p75 and TrkA mediates their reciprocal activation. *J. Biol. Chem.* **297**, 100926 (2021).

294. Casarotto, P. C. *et al.* Antidepressant drugs act by directly binding to TRKB neurotrophin receptors. *Cell* **184**, 1299-1313.e19 (2021).

295. Cannarozzo, C. *et al.* Cholesterol-recognition motifs in the transmembrane domain of the tyrosine kinase receptor family: The case of TRKB. *Eur. J. Neurosci.* **53**, 3311–3322 (2021).

296. Moliner, R. *et al.* Psychedelics promote plasticity by directly binding to BDNF receptor TrkB. *Nat. Neurosci.* **26**, 1032–1041 (2023).

297. Resende-Lara, P. T., Perahia, D., Scott, A. L. & Braz, A. S. K. Unveiling functional motions based on point mutations in biased signaling systems: A normal mode study on nerve growth factor bound to TrkA. *PLoS One* **15**, e0231542 (2020).

298. Pietropaolo, A. *et al.* Binding of Zn(II) to Tropomyosin Receptor Kinase A in Complex with Its Cognate Nerve Growth Factor: Insights from Molecular Simulation and in Vitro Essays. *ACS Chem. Neurosci.* **9**, 1095–1103 (2018).

299. EuroNeurotrophin - a European training network for the discovery of neurotrophins small molecule mimetics as potential therapeutic agents for neurodegeneration and neuroinflammation.

300. Schlick, T. *Molecular Modeling and Simulation: An Interdisciplinary Guide*. vol. 21 (Springer New York, 2010).

301. Hinchliffe, A. *Molecular Modelling for Beginners, 2nd Edition*. (Wiley, 2008).

302. Leach, A. R. *Molecular Modelling: Principles and Applications*. (Longman, 1996).

303. Cramer, C. J. *Essentials of Computational Chemistry: Theories and Models, 2nd Edition*. (Wiley, 2004).

304. Jensen, J. H. *Molecular Modeling Basics*. (CRC Press, 2010). doi:10.1201/9781420075274.

305. Alessandri, R. *et al.* Martini 3 Coarse-Grained Force Field: Small Molecules. *Adv. Theory Simulations* **5**, (2022).

306. Grünewald, F. *et al.* Martini 3 Coarse-Grained Force Field for Carbohydrates. *J. Chem. Theory Comput.* **18**, 7555–7569 (2022).

307. Uusitalo, J. J., Ingólfsson, H. I., Akhshi, P., Tieleman, D. P. & Marrink, S. J. Martini Coarse-Grained Force Field: Extension to DNA. *J. Chem. Theory Comput.* **11**, 3932–3945 (2015).

308. Marrink, S. J. *et al.* Computational Modeling of Realistic Cell Membranes. *Chem. Rev.* **119**, 6184–6226 (2019).

309. Monticelli, L. *et al.* The MARTINI Coarse-Grained Force Field: Extension to Proteins. *J. Chem. Theory Comput.* **4**, 819–834 (2008).

310. Marrink, S. J., Risselada, H. J., Yefimov, S., Tieleman, D. P. & de Vries, A. H. The MARTINI Force Field: Coarse Grained Model for Biomolecular Simulations. *J. Phys. Chem. B* **111**, 7812–7824 (2007).

311. Dominguez, L., Foster, L., Meredith, S. C., Straub, J. E. & Thirumalai, D. Structural Heterogeneity in Transmembrane Amyloid Precursor Protein Homodimer Is a Consequence of Environmental Selection. *J. Am. Chem. Soc.* **136**, 9619–9626 (2014).

312. Majumder, A., Kwon, S. & Straub, J. E. On Computing Equilibrium Binding Constants for Protein-Protein Association in Membranes. *J. Chem. Theory Comput.* (2022) doi:10.1021/acs.jctc.2c00106.

313. Wassenaar, T. A. *et al.* High-Throughput Simulations of Dimer and Trimer Assembly of Membrane Proteins. The DAFT Approach. *J. Chem. Theory Comput.* **11**, 2278–2291 (2015).

314. Lelimousin, M., Limongelli, V. & Sansom, M. S. P. Conformational Changes in the Epidermal Growth Factor Receptor: Role of the Transmembrane Domain Investigated by Coarse-Grained MetaDynamics Free Energy Calculations. *J. Am. Chem. Soc.* **138**, 10611–10622 (2016).

315. Bond, P. J. & Sansom, M. S. P. Insertion and Assembly of Membrane Proteins via Simulation. *J. Am. Chem. Soc.* **128**, 2697–2704 (2006).

316. de Jong, D. H. *et al.* Improved Parameters for the Martini Coarse-Grained Protein Force Field. *J. Chem. Theory Comput.* **9**, 687–697 (2013).

317. Souza, P. C. T. *et al.* Martini 3: a general purpose force field for coarse-grained molecular dynamics. *Nat. Methods* **18**, 382–388 (2021).

318. Claveras Cabezudo, A., Athanasiou, C., Tsengenes, A. & Wade, R. C. Scaling Protein–Water Interactions in the Martini 3 Coarse-Grained Force Field to Simulate Transmembrane Helix Dimers in Different Lipid Environments. *J. Chem. Theory Comput.* **19**, 2109–2119 (2023).

319. Laio, A. & Parrinello, M. Escaping free-energy minima. *Proc. Natl. Acad. Sci.* **99**, 12562–12566 (2002).

320. Barducci, A., Bussi, G. & Parrinello, M. Well-Tempered Metadynamics: A Smoothly Converging and Tunable Free-Energy Method. *Phys. Rev. Lett.* **100**, 020603 (2008).

321. Friesner, R. A. *et al.* Glide: A New Approach for Rapid, Accurate Docking and Scoring. 1. Method and Assessment of Docking Accuracy. *J. Med. Chem.* **47**, 1739–1749 (2004).

322. Halgren, T. A. *et al.* Glide: a new approach for rapid, accurate docking and scoring. 2. Enrichment factors in database screening. *J. Med. Chem.* **47**, 1750–9 (2004).

323. Friesner, R. A. *et al.* Extra Precision Glide: Docking and Scoring Incorporating a Model of Hydrophobic Enclosure for Protein−Ligand Complexes. *J. Med. Chem.* **49**, 6177–6196 (2006).

324. Schrödinger Release 2020-2: Glide, Schrödinger, LLC, New York, NY, 2020.

325. Jorgensen, W. L., Maxwell, D. S. & Tirado-Rives, J. Development and Testing of the OPLS All-Atom Force Field on Conformational Energetics and Properties of Organic Liquids. *J. Am. Chem. Soc.* **118**, 11225–11236 (1996).

326. Lu, C. *et al.* OPLS4: Improving Force Field Accuracy on Challenging Regimes of Chemical Space. *J. Chem. Theory Comput.* **17**, 4291–4300 (2021).

327. Schödinger Release 2020-2. (2020).

328. Halgren, T. A. Identifying and Characterizing Binding Sites and Assessing Druggability. *J. Chem. Inf. Model.* **49**, 377–389 (2009).

329. Halgren, T. New Method for Fast and Accurate Binding-site Identification and Analysis. *Chem. Biol. Drug Des.* **69**, 146–148 (2007).

330. Halgren, T. A. *et al.* Glide: A New Approach for Rapid, Accurate Docking and Scoring. 2. Enrichment Factors in Database Screening. *J. Med. Chem.* **47**, 1750–1759 (2004).

331. Sherman, W., Beard, H. S. & Farid, R. Use of an Induced Fit Receptor Structure in Virtual Screening. *Chem. Biol. Drug Des.* **67**, 83–84 (2006).

332. Sherman, W., Day, T., Jacobson, M. P., Friesner, R. A. & Farid, R. Novel Procedure for Modeling Ligand/Receptor Induced Fit Effects. *J. Med. Chem.* **49**, 534–553 (2006).

333. Farid, R., Day, T., Friesner, R. A. & Pearlstein, R. A. New insights about HERG blockade obtained from protein modeling, potential energy mapping, and docking studies. *Bioorg. Med. Chem.* **14**, 3160–3173 (2006).

334. Schrödinger Release 2020: LigPrep, Schrödinger, LLC, New York, NY, 2020.

335. Johnston, R. C. *et al.* Epik: pKa and Protonation State Prediction through Machine Learning. *J. Chem. Theory Comput.* **19**, 2380–2388 (2023).

336. Schrödinger Release 2020: QikProp, Schrödinger, LLC, New York, NY, 2020.

337. Wiesmann, C., Ultsch, M. H., Bass, S. H. & de Vos, A. M. Crystal structure of nerve growth factor in complex with the ligand-binding domain of the TrkA receptor. *Nature* **401**, 184–188 (1999).

338. Banfield, M. J. *et al.* Specificity in Trk Receptor:Neurotrophin Interactions. *Structure* **9**, 1191–1199 (2001).

339. Schrödinger Release 2020: Desmond Molecular Dynamics System, D. E. Shaw Research, New York, NY, 2020. Maestro-Desmond Interoperability Tools, Schrödinger, New York, NY, 2020.

340. Duan, J., Dixon, S. L., Lowrie, J. F. & Sherman, W. Analysis and comparison of 2D fingerprints: Insights into database screening performance using eight fingerprint methods. *J. Mol. Graph. Model.* **29**, 157–170 (2010).

341. Sastry, M., Lowrie, J. F., Dixon, S. L. & Sherman, W. Large-Scale Systematic Analysis of 2D Fingerprint Methods and Parameters to Improve Virtual Screening Enrichments. *J. Chem. Inf. Model.* **50**, 771–784 (2010).

342. Sali, A. & Blundell, T. L. Comparative protein modelling by satisfaction of spatial restraints. *J. Mol. Biol.* **234**,

779–815 (1993).

343. Dobson, C. L. *et al.* Engineering the surface properties of a human monoclonal antibody prevents self-association and rapid clearance in vivo. *Sci. Rep.* **6**, 38644 (2016).

344. Robinson, R. C. *et al.* The structures of the neurotrophin 4 homodimer and the brain-derived neurotrophic factor/neurotrophin 4 heterodimer reveal a common Trk-binding site. *Protein Sci.* **8**, 2589–2597 (2008).

345. Madhavi Sastry, G., Adzhigirey, M., Day, T., Annabhimoju, R. & Sherman, W. Protein and ligand preparation: parameters, protocols, and influence on virtual screening enrichments. *J. Comput. Aided. Mol. Des.* **27**, 221–234 (2013).

346. Schrödinger Release 2020-2: Protein Preparation Wizard; Epik, Schrödinger, LLC, New York, NY, 2020; Impact, Schrödinger, LLC, New York, NY; Prime, Schrödinger, LLC, New York, NY, 2020.

347. Olsson, M. H. M., Søndergaard, C. R., Rostkowski, M. & Jensen, J. H. PROPKA3: Consistent Treatment of Internal and Surface Residues in Empirical pKa Predictions. *J. Chem. Theory Comput.* **7**, 525–37 (2011).

348. Harder, E. *et al.* OPLS3: A Force Field Providing Broad Coverage of Drug-like Small Molecules and Proteins. *J. Chem. Theory Comput.* **12**, 281–296 (2016).

349. Schrödinger Release 2020-2: SiteMap, Schrödinger, LLC, New York, NY, 2020.

350. Halgren, T. New Method for Fast and Accurate Binding-site Identification and Analysis. *Chem. Biol. Drug Des.* **69**, 146–148 (2007).

351. Schrödinger Release 2020-2: Maestro, Schrödinger, LLC, New York, NY, 2020.

352. Schrödinger Release 2020-2: LigPrep, Schrödinger, LLC, New York, NY, 2020.

353. Farid, R., Day, T., Friesner, R. A. & Pearlstein, R. A. New insights about HERG blockade obtained from protein modeling, potential energy mapping, and docking studies. *Bioorg. Med. Chem.* **14**, 3160–73 (2006).

354. Schrödinger Release 2020-2: Induced Fit Docking protocol; Glide, Schrödinger, LLC, New York, NY, 2020; Prime, Schrödinger, LLC, New York, NY, 2020.

355. Humphrey, W., Dalke, A. & Schulten, K. VMD: Visual molecular dynamics. *J. Mol. Graph.* **14**, 33–38 (1996).

356. Davis, S. J. & Crispin, M. Solutions to the Glycosylation Problem for Low- and High-Throughput Structural Glycoproteomics. in *Functional and Structural Proteomics of Glycoproteins* 127–158 (Springer Netherlands, 2010). doi:10.1007/978-90-481-9355-4_6.

357. Kozak, S. *et al.* Homogeneously N -glycosylated proteins derived from the GlycoDelete HEK293 cell line enable diffraction-quality crystallogenesis. *Acta Crystallogr. Sect. D Struct. Biol.* **76**, 1244–1255 (2020).

358. Casalino, L. *et al.* Beyond Shielding: The Roles of Glycans in the SARS-CoV-2 Spike Protein. *ACS Cent. Sci.* **6**, 1722–1734 (2020).

359. Harbison, A. M. *et al.* Fine-tuning the spike: role of the nature and topology of the glycan shield in the structure and dynamics of the SARS-CoV-2 S. *Chem. Sci.* **13**, 386–395 (2022).

360. Vuorio, J. *et al.* N-Glycosylation can selectively block or foster different receptor–ligand binding modes. *Sci. Rep.* **11**, 5239 (2021).

361. Mehdipour, A. R. & Hummer, G. Dual nature of human ACE2 glycosylation in binding to SARS-CoV-2 spike. *Proc. Natl. Acad. Sci.* **118**, (2021).

362. Sievers, F. *et al.* Fast, scalable generation of high-quality protein multiple sequence alignments using Clustal Omega. *Mol. Syst. Biol.* **7**, (2011).

363. UniProt: a worldwide hub of protein knowledge. *Nucleic Acids Res.* **47**, D506–D515 (2019).

364. Šali, A. & Blundell, T. L. Comparative Protein Modelling by Satisfaction of Spatial Restraints. *J. Mol. Biol.* **234**, 779–815 (1993).

365. Olsson, M. H. M., Søndergaard, C. R., Rostkowski, M. & Jensen, J. H. PROPKA3: Consistent Treatment of Internal and Surface Residues in Empirical p K a Predictions. *J. Chem. Theory Comput.* **7**, 525–537 (2011).

366. Jurrus, E. *et al.* Improvements to the APBS biomolecular solvation software suite. *Protein Sci.* **27**, 112–128 (2018).

367. Yeaman, C. *et al.* The O -glycosylated Stalk Domain Is Required for Apical Sorting of Neurotrophin Receptors in Polarized MDCK Cells. *J. Cell Biol.* **139**, 929–940 (1997).

368. Park, S.-J. *et al.* CHARMM-GUI Glycan Modeler for modeling and simulation of carbohydrates and glycoconjugates. *Glycobiology* **29**, 320–331 (2019).

369. Abraham, M. J. *et al.* GROMACS: High performance molecular simulations through multi-level parallelism from laptops to supercomputers. *SoftwareX* **1**–**2**, 19–25 (2015).

370. Huang, J. *et al.* CHARMM36m: an improved force field for folded and intrinsically disordered proteins. *Nat. Methods* **14**, 71–73 (2017).

371. Nosé, S. A molecular dynamics method for simulations in the canonical ensemble. *Mol. Phys.* **52**, 255–268 (1984).

372. Hoover, W. G. Canonical dynamics: Equilibrium phase-space distributions. *Phys. Rev. A* **31**, 1695–1697 (1985).

373. Parrinello, M. & Rahman, A. Polymorphic transitions in single crystals: A new molecular dynamics method. *J. Appl. Phys.* **52**, 7182–7190 (1981).

374. Nosé, S. & Klein, M. L. Constant pressure molecular dynamics for molecular systems. *Mol. Phys.* **50**, 1055–1076 (1983).

375. Darden, T., York, D. & Pedersen, L. Particle mesh Ewald: An N ·log(N) method for Ewald sums in large systems. *J. Chem. Phys.* **98**, 10089–10092 (1993).

376. Essmann, U. *et al.* A smooth particle mesh Ewald method. *J. Chem. Phys.* **103**, 8577–8593 (1995).

377. Hess, B., Bekker, H., Berendsen, H. J. C. & Fraaije, J. G. E. M. LINCS: A linear constraint solver for molecular simulations. *J. Comput. Chem.* **18**, 1463–1472 (1997).

378. Gowers, R. *et al.* MDAnalysis: A Python Package for the Rapid Analysis of Molecular Dynamics Simulations. in *SciPy Proceedings* 98–105 (2016). doi:10.25080/Majora-629e541a-00e.

379. Michaud-Agrawal, N., Denning, E. J., Woolf, T. B. & Beckstein, O. MDAnalysis: A toolkit for the analysis of molecular dynamics simulations. *J. Comput. Chem.* **32**, 2319–2327 (2011).

380. Hunter, J. D. Matplotlib: A 2D Graphics Environment. *Comput. Sci. Eng.* **9**, 90–95 (2007).

381. Waskom, M. Seaborn: statistical data visualization. *J. Open Source Softw.* **6**, 3021 (2021).

382. Harris, C. R. *et al.* Array programming with NumPy. *Nature* **585**, 357–362 (2020).

383. Bothwell, M. Functional interactions of neurotrophins and neurotrophin receptors. *Annu. Rev. Neurosci.* **18**, 223–253 (1995).

384. Vilar, M. *et al.* Ligand-independent signaling by disulfide-crosslinked dimers of the p75 neurotrophin receptor. *J. Cell Sci.* **122**, 3351–3357 (2009).

385. Anastasia, A., Barker, P. A., Chao, M. V & Hempstead, B. L. Detection of p75NTR Trimers: Implications for Receptor Stoichiometry and Activation. *J. Neurosci.* **35**, 11911–11920 (2015).

386. Yaar, M. *et al.* Amyloid β Binds Trimers as Well as Monomers of the 75-kDa Neurotrophin Receptor and Activates Receptor Signaling. *J. Biol. Chem.* **277**, 7720–7725 (2002).

387. Nadezhdin, K. D. *et al.* Structural Basis of p75 Transmembrane Domain Dimerization. *J. Biol. Chem.* **291**, 12346–12357 (2016).

388. Russ, W. P. & Engelman, D. M. The GxxxG motif: A framework for transmembrane helix-helix association. *J. Mol. Biol.* **296**, 911–919 (2000).

389. Walters, R. F. S. & DeGrado, W. F. Helix-packing motifs in membrane proteins. *Proc. Natl. Acad. Sci.* **103**, 13658–13663 (2006).

390. Moore, D. T., Berger, B. W. & DeGrado, W. F. Protein-Protein Interactions in the Membrane: Sequence, Structural, and Biological Motifs. *Structure* **16**, 991–1001 (2008).

391. Bussi, G., Donadio, D. & Parrinello, M. Canonical sampling through velocity rescaling. *J. Chem. Phys.* **126**, (2007).

392. Berendsen, H. J. C., Postma, J. P. M., van Gunsteren, W. F., DiNola, A. & Haak, J. R. Molecular dynamics with coupling to an external bath. *J. Chem. Phys.* **81**, 3684–3690 (1984).

393. Wassenaar, T. A., Pluhackova, K., Böckmann, R. A., Marrink, S. J. & Tieleman, D. P. Going Backward: A Flexible Geometric Approach to Reverse Transformation from Coarse Grained to Atomistic Models. *J. Chem. Theory Comput.* **10**, 676–690 (2014).

394. Lee, J. *et al.* CHARMM-GUI Membrane Builder for Complex Biological Membrane Simulations with Glycolipids and Lipoglycans. *J. Chem. Theory Comput.* **15**, 775–786 (2019).

395. Wassenaar, T. A., Ingólfsson, H. I., Böckmann, R. A., Tieleman, D. P. & Marrink, S. J. Computational Lipidomics with insane : A Versatile Tool for Generating Custom Membranes for Molecular Simulations. *J. Chem. Theory Comput.* **11**, 2144–2155 (2015).

396. Tribello, G. A., Bonomi, M., Branduardi, D., Camilloni, C. & Bussi, G. PLUMED 2: New feathers for an old bird. *Comput. Phys. Commun.* **185**, 604–613 (2014).

397. McKinney, W. Data Structures for Statistical Computing in Python. in *SciPy Proceedings* 56–61 (2010). doi:10.25080/Majora-92bf1922-00a.

398. pandas development team, T. pandas-dev/pandas: Pandas. (2020) doi:10.5281/zenodo.3509134.

399. Psachoulia, E., Fowler, P. W., Bond, P. J. & Sansom, M. S. P. Helix−Helix Interactions in Membrane Proteins: Coarse-Grained Simulations of Glycophorin A Helix Dimerization. *Biochemistry* **47**, 10503–10512 (2008).

400. Ingólfsson, H. I. *et al.* Computational Lipidomics of the Neuronal Plasma Membrane. *Biophys. J.* **113**, 2271–2280 (2017).

401. Niemelä, P. S., Ollila, S., Hyvönen, M. T., Karttunen, M. & Vattulainen, I. Assessing the nature of lipid raft membranes. *PLoS Comput. Biol.* **3**, e34 (2007).

402. Chan, R. B. *et al.* Comparative Lipidomic Analysis of Mouse and Human Brain with Alzheimer Disease. *J. Biol. Chem.* **287**, 2678–2688 (2012).

403. Zonta, B. & Minichiello, L. Synaptic membrane rafts: traffic lights for local neurotrophin signaling? *Front. Synaptic Neurosci.* **5**, (2013).

404. Steentoft, C. *et al.* Precision mapping of the human O-GalNAc glycoproteome through SimpleCell technology. *EMBO J.* **32**, 1478–1488 (2013).

405. Leo-Macias, A., Lopez-Romero, P., Lupyan, D., Zerbino, D. & Ortiz, A. R. An Analysis of Core Deformations in Protein Superfamilies. *Biophys. J.* **88**, 1291–1299 (2005).

406. Amadei, A., Ceruso, M. A. & Di Nola, A. On the convergence of the conformational coordinates basis set obtained by the essential dynamics analysis of proteins’ molecular dynamics simulations. *Proteins Struct. Funct. Genet.* **36**, 419–424 (1999).